

UNIVERSITÉ DU QUÉBEC

THÈSE PRESENTÉE À  
L'UNIVERSITÉ DU QUÉBEC À CHICOUTIMI  
COMME EXIGENCE PARTIELLE  
DU DOCTORAT EN INGÉNIERIE

PAR

KLÁRA VÉKONY

LARGE BUBBLE MOVING UNDER A SOLID SURFACE

APRIL 2009



### **Mise en garde/Advice**

Afin de rendre accessible au plus grand nombre le résultat des travaux de recherche menés par ses étudiants gradués et dans l'esprit des règles qui régissent le dépôt et la diffusion des mémoires et thèses produits dans cette Institution, **l'Université du Québec à Chicoutimi (UQAC)** est fière de rendre accessible une version complète et gratuite de cette œuvre.

Motivated by a desire to make the results of its graduate students' research accessible to all, and in accordance with the rules governing the acceptance and diffusion of dissertations and theses in this Institution, the **Université du Québec à Chicoutimi (UQAC)** is proud to make a complete version of this work available at no cost to the reader.

L'auteur conserve néanmoins la propriété du droit d'auteur qui protège ce mémoire ou cette thèse. Ni le mémoire ou la thèse ni des extraits substantiels de ceux-ci ne peuvent être imprimés ou autrement reproduits sans son autorisation.

The author retains ownership of the copyright of this dissertation or thesis. Neither the dissertation or thesis, nor substantial extracts from it, may be printed or otherwise reproduced without the author's permission.

## ABSTRACT

The formation and movement of large Fortin shaped bubbles are studied through physical experiments and numerical simulations. The role these Fortin bubbles play in the aluminium electrolysis process and their effect on the formation of the bubble layer is also examined.

The physics of the Fortin bubbles is investigated for the first time in this field using an air-water set-up and by numerical simulations. Fortin bubbles form under slightly inclined solid surfaces. It is found to be induced by a gravity wave. The dimensions and the velocity of the large Fortin bubble are measured as a function of the angle of inclination and the volume of the bubble. Two approximations are developed to calculate the volume of a Fortin bubble as a function of a few measured parameters. An arbitrary shaped large bubble gliding under a solid surface is numerically simulated for the first time in the literature. The results agree with the measurements. The formation and movement of large carbon-dioxide bubbles moving in molten cryolite is also simulated.

The formation and movement of the bubble layer and the effect of the Fortin bubbles on this layer and on the flow field induced in the cell are investigated in a real-size air-water model of an electrolysis cell. Three different flow regimes were observed under the anode depending on the gas generation rate. A correlation between the average height of the entire bubble layer and the position under the anode is determined in order to calculate the volume of the accumulated gas. The maximum height of the bubbles is found to be up to 2 cm due to the presence of the so called Fortin bubbles. Also, the mean height of the bubble layer is found to be much higher than previously published. The large bubbles always break up into smaller parts right before escaping from under the anode. The escape of a large bubble leads to a large momentum transfer in the bath. The movement of the liquid layer in the cell is examined using PIV techniques. Results show that the size and shape of the single bubbles are very important. Large Fortin bubbles are found to be even more important for momentum transfer than small bubbles. These large bubbles transfer a high

amount of momentum to the fluid, helping to homogenize the temperature field and increase mass transport in the bath.



## RÉSUMÉ

Durant ces années doctorales, la formation et le mouvement des grandes bulles « Fortin » ont été étudiés par l'entremise de la modélisation physique et numérique. L'influence de ce type de bulles sur la couche gazeuse présente dans le procédé d'électrolyse de l'aluminium a aussi été quantifiée.

Dans un premier temps, la morphologie de la bulle « Fortin », qui se forme sous une surface solide légèrement inclinée, a été étudiée dans un modèle physique à eau ainsi que par modélisation numérique. Cette étude a permis de découvrir que la bulle « Fortin » était formée par une onde gravitationnelle. Les dimensions et la vitesse de la bulle « Fortin » ont été mesurées en fonction du volume de la bulle et de l'angle d'inclinaison de la surface. Deux équations ont été développées afin de prédire le volume d'une bulle « Fortin ». Lors de ces études, une large bulle se mouvant sous une surface inclinée fut, pour une première fois dans la littérature, simulée numériquement. Les résultats obtenus concordent avec les mesures expérimentales. D'autre part, la formation et le mouvement de larges bulles de dioxyde de carbone, se déplaçant dans la cryolithe liquide, ont aussi été simulés.

L'effet de la bulle « Fortin » sur la couche gazeuse et sur l'écoulement engendré par les bulles a été étudié expérimentalement dans un modèle physique à eau. Trois régimes d'écoulement sous l'anode, différenciés par le taux de génération de gaz, ont été déterminés. Une corrélation entre la hauteur moyenne de la couche gazeuse et la position sous l'anode a été développée. Le volume de gaz accumulé sous l'anode peut être calculé avec cette équation. La hauteur maximale de la couche gazeuse a été mesurée et ce chiffre à 2 cm en raison de la présence de la bulle « Fortin ». De plus, la hauteur moyenne de la couche gazeuse a été mesurée et s'est avérée supérieure aux valeurs présentes dans la littérature. Il a été possible d'observer que les grandes bulles se fractionnent toujours en deux ou plusieurs bulles juste avant de quitter la surface de l'anode. La sortie des grandes bulles engendre une augmentation du transfert de quantité de mouvement dans la cuve. Le

mouvement de la couche liquide dans la cuve a été étudié par la technique PIV. Ces expérimentations démontrèrent que la taille et la forme des bulles jouent un rôle très important sur le transfert de quantité de mouvement. L'influence des bulles « Fortin » sur le transfert de quantité de mouvement est plus importante que celle des petits bulles. Les bulles de type « Fortin » engendrent un intense transfert de quantité de mouvement dans le liquide, lequel participe à l'homogénéisation du champ de température et à l'augmentation du transport de masse dans la cuve.

## ACKNOWLEDGEMENT

I would like to express my thanks to the director of my Ph.D. program, Professor László I. Kiss, for his guidance, supervision, support and his generous help during my Ph.D. studies. I am also grateful for numerous professors at the university, especially in the Department of Applied Science, and numerous other staff members who helped and encouraged me during my thesis.

I also would like to express my gratitude to Pascal Vandal and Patrice Paquette who helped me in the laboratory. I greatly appreciate the help of Emmanuel de Varennes who spent long hours with me in the laboratory and helped me observe and record the different phenomena I investigated.

The financial support of the Ministry of Education of Québec and Rio Tinto Alcan in the form of scholarships is gratefully acknowledged.

I have been happy to spend three and a half year in the same office with Sébastien Bolduc who did not only help me to adapt to Québec culture but also taught me numerous Québécois expressions. I am also grateful for the long conversations we had during numerous nights spent together working at the university. I am also very grateful for the friendship of Véronique Dassylva-Raymond who, in addition to being my friend, also helped me out a lot with my French.

I would like to express my thanks to my partner in life, Manel da Silva, who had the “chance” to support me only at the end, but then he indeed did, to my family and friends who are not named here but who helped me and encouraged me.

At least, but most importantly, nothing is remotely possible without my parents, Vékonyné J. Klára and Vékony Sándor, whose love, attention, encouragement, support and genes let me be whoever I wanted to be and led me wherever I wanted to go. There is not enough time nor chance in my life to thank them for all they gave and still give to me.

## LIST OF PUBLICATIONS

The work presented in this thesis is based on the following four articles which have been submitted to refereed journals and on one conference publications and presentations.

### Articles:

Vékony, K. and Kiss, L., *Velocity measurements in a real size model of an aluminium electrolysis cell using PIV techniques*, submitted to Journal of Applied Electrochemistry

Vékony, K. and Kiss, L., *Morphology of two-phase layers with large bubbles*, submitted to Journal of Metallurgical Transactions

Vékony, K. and Kiss, L., *Experimental study of the morphology and dynamics of gas-laden layers under the anodes of aluminium reduction cells*, submitted to Journal of Metallurgical Transactions

Vékony, K. and Kiss, L., *A large bubble moving under a slightly inclined solid surface*, submitted to International Journal of Multiphase Flow

### Conference:

Kiss, L. and Vékony, K., *Dynamics of the Gas Emission from Aluminum Electrolysis Cells*, Light Metals 2007, pp. 425

## TABLE OF CONTENTS

Abstract.....	ii
Résumé.....	iv
Acknowledgement.....	vi
List of publications.....	vii
Table of Contents.....	viii
Nomenclature.....	xiii
List of figures.....	xvii
List of tables.....	xxiv
1. INTRODUCTION.....	1
1.1 Aluminium production.....	1
1.2 Motivation.....	3
1.3 Structure of this thesis.....	5
1.4 References.....	6
2. THE BUBBLE PHENOMENON.....	7
2.1 Introduction.....	7
2.2 Gas-liquid two-phase flow.....	8
2.2.1 Interfacial phenomena.....	9
2.2.2 Stability of the gas-liquid interface.....	12
2.2.3 Characteristics of standing and freely moving bubbles.....	15
2.2.3.1 Standing bubbles.....	15
2.2.3.2 Freely moving bubbles.....	18
2.3 Bubbles in the Hall-Héroult electrolysis cell.....	40
2.3.1 Nucleation and motion of the bubbles in an electrolysis cell.....	40

2.3.2 Formation of the bubble layer and the bubble induced flow.....	43
2.3.3 Fortin shaped bubbles in the cell.....	48
2.3.4 The importance of bubbles in the process of aluminium electrolysis.....	50
2.4 Objectives of this thesis.....	52
2.5 References.....	54
3. METHODOLOGY.....	60
3.1 Introduction.....	60
3.2 Physical modeling.....	62
3.2.1 Objectives of physical modeling.....	63
3.2.2 Air-water model.....	63
3.2.3 Measurement techniques.....	70
3.2.3.1 Digital image recording.....	71
3.2.3.2 High speed camera.....	75
3.2.3.3 Particle Image Velocimetry.....	76
3.2.4 Digital image processing.....	80
3.3 Mathematical modeling.....	92
3.3.1 Objectives.....	93
3.3.2 Available numerical methods for two-phase bubbly flows.....	94
3.3.2.1 Physical models.....	94
3.3.2.2 Mathematical methods.....	100
3.3.2.3 Surface handling methods.....	103
3.4 References.....	108
4. A LARGE BUBBLE MOVING UNDER A SLIGHTLY INCLINED SURFACE.....	111
4.1 Objectives.....	111
4.2 Series of experiments.....	112
4.3 Results and discussion.....	113
4.3.1 Characterization of the Fortin shape.....	113
4.3.2 Effect of the inclination and volume on the bubble dimensions and shape.....	120

4.3.3 Bubble movement along irregularities on the solid surface.....	126
4.3.4 Effect of the bubble volume and surface inclination on the terminal velocity.....	128
4.3.5 Effect of the inclination angle and bubble volume on the drag coefficient.....	133
4.3.6 Correlation between the contact size and cross section size.....	136
4.3.6.1 Approximation with equivalent height.....	137
4.3.6.2 Exact form approximation with head and tail.....	140
4.3.7 Forces acting on a moving bubble.....	143
4.3.8 Fortin shape induced by a gravity wave.....	146
4.3.9 Special shape and height of a Fortin bubble.....	147
4.3.10 Momentum transported by a Fortin bubble.....	152
4.3.11 Theory of similarity.....	153
4.4 Conclusions.....	156
4.5 References.....	159
5. BUBBLE LAYER AND FLOW INDUCED BY A BUBBLE LAYER IN A REAL-SIZE ELECTROLYSIS CELL MODEL.....	160
5.1 Objectives.....	161
5.2 Series of experiments.....	162
5.3 Bubble layer under a solid surface.....	162
5.3.1 Flow regimes under the anode.....	163
5.3.2 Covering factor as a function of the gas generation and angle of inclination.....	165
5.3.3 Contact size as a function of the current density and angle of inclination.....	173
5.3.4 Height of the bubble layer and bubbles.....	178
5.3.4.1 Local average height and terminal value of the average height of the bubble layer.....	179
5.3.4.2 Local maximum height of the bubble layer.....	184

5.3.4.3 Ratio of the local maximum height to the local average height.....	185
5.3.5 Height of the bubble layer as a function of the gas generation rate.....	187
5.3.6 Calculation of the volume of a bubble from its contact size.....	189
5.3.7 Formation of the Fortin bubble.....	196
5.3.7.1 Dynamic formation of the Fortin head.....	198
5.3.7.2 Onset of the Fortin shape as a function of different parameters.....	200
5.3.8 Escape of large bubbles.....	201
5.3.9 Momentum transfer by the escaping large bubbles.....	203
5.3.10 Sweeping effect.....	205
5.3.11 Bubble layer in a real electrolysis cell.....	206
5.4 Bubble layer induced flow.....	207
5.4.1 Fluid flow induced by discrete bubbles and by the bubble layer.....	207
5.4.1.1 Vertical motion of the bath.....	208
5.4.1.2 Fortin head as a gravity wave.....	210
5.4.1.3 Backflow caused by escaping bubbles.....	216
5.4.1.4 Momentum transferred by an escaping bubble.....	220
5.4.2 Movement in the centre channel.....	222
5.4.3 Flow pattern under the anode.....	223
5.4.4 The impact of the anodes on each other.....	225
5.4.5 Effect of the inclination angle of the anode on the flow pattern.....	226
5.4.6 Bubble induced flow in a real electrolysis cell.....	228
5.5 Conclusions.....	229
5.5.1 Bubble layer formed under the anode.....	229
5.5.2 Bubble layer induced flow.....	233
5.6 References.....	235



<b>6. NUMERICAL SIMULATIONS OF A SINGLE LARGE BUBBLE MOVING UNDER A SLIGHTLY INCLINED SURFACE.....</b>	<b>237</b>
6.1 Introduction.....	237
6.2 Objectives.....	241
6.3 Simulations using the openFOAM code.....	243
6.3.1 Model, mesh and simulations.....	243
6.3.2 Results and discussion.....	250
6.3.2.1 Shape forming from the initial gas pocket.....	250
6.3.2.2 Formation of the final Fortin shape.....	252
6.3.2.3 Effect of the angle of inclination on the bubble shape and movement.....	257
6.3.2.4 Effect of the liquid properties on the bubble shape and movement.....	259
6.3.2.5 Effect of the bubble volume on the bubble shape and movement.....	262
6.3.2.6 Air bubble in water vs. carbon-dioxide bubble in molten cryolite.....	265
6.3.2.7 Comparing measurements with the results from the simulations.....	266
6.4 Conclusions.....	267
6.5 References.....	269
<b>7. CONCLUSIONS.....</b>	<b>270</b>
7.1 Conclusions.....	270
7.2 Suggestion for future work.....	275
 Appendix A - Derivation of the correlation to calculate the volume of a large Fortin bubble using the exact form approximation.....	 278
 Appendix B - Derivation of the correlation to calculate the wave velocity for two substances.....	 282

## NOMENCLATURE

### Abbreviations

<i>ACD</i>	Anode-Cathode Distance	
<i>Ar</i>	Archimedes number	$Ar = \frac{g \cdot \rho \cdot \Delta \rho \cdot d_c^3}{\mu^2}$
<i>Bo</i>	Bond number	$Bo = \frac{\rho_l \cdot d_c^2 \cdot g}{\sigma}$
<i>Ca</i>	Capillary number	$Ca = \frac{\mu \cdot u}{\sigma}$
<i>Eö</i>	Eötvös number	$Eö = \frac{g \cdot \Delta \rho \cdot d_c^2}{\sigma}$
<i>Fr</i>	Froude number	$Fr = \frac{u_T}{\sqrt{g \cdot d_c \cdot \sin \alpha}}$
<i>M</i>	Mach number	$M = \frac{u_{source}}{u_{sound}}$
<i>Mo</i>	Morton number	$Mo = \frac{g \cdot \nu_l^4 \cdot \rho_l^3}{\sigma^3}$
<i>Re</i>	Reynolds number	$Re = \frac{d_c \cdot u_T}{\nu_l}$
<i>We</i>	Weber number	$We = \frac{\rho \cdot v^2 \cdot L_c}{\sigma}$

### Roman letters

<i>a</i>	acceleration	[m/s <sup>2</sup> ]
<i>a</i>	spherical, undisturbed bubble radius	[m]

$a$	semi-major axis	[m]
$a, B$	parameters in equation (5.6)	[-, $1/\text{m}^{1-a}$ ]
$air_{inlet}$	volume flow rate of air	[lpm]
$A$	surface area	[m <sup>2</sup> ]
$A_T$	frontal area	[m <sup>2</sup> ]
$A, B, C$	constants of the parabola	[1/m, -, m]
$b$	semi-minor axis	[m]
$c$	wave velocity	[m/s]
$C$	covering factor	[-]
$C_D$	drag coefficient	[-]
$d$	distance	[m]
$d, D$	diameter	[m]
$e$	eccentricity	[-]
$f_c$	maximal turbulence frequency	[Hz]
$F$	Faraday constant	[C/mol]
$g$	gravitational acceleration	[m/s <sup>2</sup> ]
$h, H$	thickness	[m]
$H$	mean curvature	[1/m]
$i$	current density	[A/cm <sup>2</sup> ]
$i$	length of arc	[m]
$k$	turbulence kinetic energy	[m <sup>2</sup> /s <sup>2</sup> ]
$k$	smoothing factor	[-]
$k$	wave number	[1/m]
$L$	length	[m]
$L_c$	characteristic length	[m]
$n, N$	number of samples	[-]
$P$	pressure	[Pa]
$r$	aspect ratio	[-]

$\vec{r}$	point vector	[m]
$R$	radius	[m]
$R_1, R_2$	the principal radii of curvature of the surface	[m]
$R_{gas}$	gas constant	[J/K mol]
$s$	curvature	[1/m]
$t$	variable of line equation	[-]
$t$	time	[s]
$T$	temperature	[K]
$u$	velocity	[m/s]
$\hat{u}$	turbulence intensity	[-]
$\bar{u}$	mean velocity	[m/s]
$\bar{v}$	direction vector	[m]
$V_p$	equivalent volume	[m <sup>3</sup> ]
$W$	width	[m]
$x, y, z$	coordinate	[m]
$z$	number of charged electrons	[-]

### Greek letters

$\alpha$	angle	[°]
$\beta$	angle	[°]
$\phi$	angle at the nose of a bubble	[°]
$\kappa$	viscosity ratio of two immiscible fluids	[-]
$\lambda$	diameter ratio	[-]
$\lambda$	wavelength	[m]
$\mu$	dynamic viscosity	[kg/m s]
$\theta_c$	contact angle	[°]
$\ominus$	angle	[°]

$\rho$	density	[kg/m <sup>3</sup> ]
$\sigma$	standard deviation of velocity	[m/s]
$\sigma$	standard deviation of covering factor	[-]
$\sigma$	surface or interfacial tension	[N/m]
$\tau$	stress	[N/m <sup>2</sup> ]
$\nu$	kinematic viscosity	[m <sup>2</sup> /s]
$\omega$	wave frequency	[1/s]

## Indexes

$C$	contact zone
$e$	equivalent
$f$	frontal
$g$	gas
$h$	head
$l$	liquid
lim	limiting value
max	maximum value
$nn$	normal component
$nt$	tangential component
$p$	particle
$s$	surface
$St$	Stokes
$t$	tail
$T$	terminal value
$\infty$	undisturbed quantity

## LIST OF FIGURES

### CHAPTER 1

Figure 1.1 - Hall-Héroult electrolysis cell. After <i>Grjotheim et al (1993)</i> .....	2
--	---

### CHAPTER 2

Figure 2.1 – Sessile, pendant and floating bubbles.....	16
Figure 2.2 – Limiting and maximum height of a bubble under a surface.....	17
Figure 2.3 - Shape regimes of freely rising bubbles. After <i>Clift et al (1978)</i> .....	19
Figure 2.4 - Terminal velocity as a function of the equivalent diameter and angle of inclination. After <i>Perron et al (2006a)</i> .....	35
Figure 2.5 - Bubble volume vs. aspect ratio at a given inclination. After <i>Perron et al (2006a)</i> .....	36
Figure 2.6 - Bubble shapes in the contact zone. After <i>Perron et al (2006a)</i> .....	37
Figure 2.7 – Fortin bubble with the special “head and tail” shape.....	49

### CHAPTER 3

Figure 3.1 – Dimensions of the real-size model.....	65
Figure 3.2 – Dimensions of the setup for single bubbles.....	69
Figure 3.3 – Device used to inject the bubble under the surface.....	69
Figure 3.4 – Showing colour difference between air and water in the recorded videos.....	72
Figure 3.5 – Recording the bubbles from the side.....	73
Figure 3.6 – Recording the bubbles from the bottom.....	74
Figure 3.7 – Recording the bubbles in the single bubble setup with the movable cameras.....	74
Figure 3.8 – Example from the video made with the high speed camera.....	75
Figure 3.9 – PIV measurement in the real-size model.....	77
Figure 3.10 – Different coordinate systems used with the video recorded from the side....	82

Figure 3.11 – Different coordinate systems used with the video recorded from the bottom.....	82
Figure 3.12 – Interlaced image (top) and the two unfolded fields (bottom).....	84
Figure 3.13 – Image before and after using the threshold filter.....	85
Figure 3.14 – Interpretation of a digital image in MATLAB® .....	86
Figure 3.15 – Method to determine the contour of the bubbles.....	87
Figure 3.16 – Fortin head approximated by a 2 <sup>nd</sup> order parabola.....	89

#### CHAPTER 4

Figure 4.1 – Illustration of the different geometrical parameters used to describe a Fortin bubble.....	114
Figure 4.2 – Contact shapes at different inclinations and bubble volumes.....	115
Figure 4.3 – Side views at different inclinations and bubble volumes.....	116
Figure 4.4 – Cross sections for different bubble volumes at 2° of inclination.....	117
Figure 4.5 – Initial contact shape.....	118
Figure 4.6 – Definition of the length of the Fortin head.....	119
Figure 4.7 – Bubble length measured for all angles and bubble volumes.....	120
Figure 4.8 – Bubble width measured for all angles and bubble volumes.....	120
Figure 4.9 – Maximum height of the head measured for all angles and bubble volumes.....	121
Figure 4.10 – Maximum length of the head measured for all angles and bubble volumes.....	121
Figure 4.11 – Mean thickness of the tail measured for bubble volumes.....	122
Figure 4.12 – Aspect ratio of width to length as a function of the volume and angle.....	123
Figure 4.13 – Aspect ratio of mean thickness of the tail to height of the head as a function of the volume and angle.....	124
Figure 4.14 – Aspect ratio of width to height of the head as a function of the volume and angle.....	124
Figure 4.15 – Bubble radii of curvatures as a function of the bubble volume and angle of inclination.....	125

Figure 4.16 – Bubble angles of the front and head as a function of the bubble volume and angle of inclination.....	126
Figure 4.17 – Snapshots of the evolution of the shape of a bubble running on a dry spot.....	128
Figure 4.18 – Terminal velocity as a function of bubble volume and inclination angle.....	129
Figure 4.19 – Terminal velocity as a function of the equivalent diameter and angle of inclination.....	131
Figure 4.20 – Froude number as a function of the angle and bubble volume.....	132
Figure 4.21 – Froude number as a function of the angle and Bond number.....	133
Figure 4.22 – Drag coefficient as a function of the volume and inclination.....	134
Figure 4.23 – Drag coefficient as a function of the Reynolds number and inclination.....	135
Figure 4.24 – Drag coefficient as a function of the Bond number and inclination.....	136
Figure 4.25 – Form approach to the Fortin bubble.....	137
Figure 4.26 – Contact sizes.....	138
Figure 4.27 – Equivalent height.....	139
Figure 4.28 – Equivalent height as a function of the contact size.....	139
Figure 4.29 – Scheme for the exact form approximation with head and tail.....	141
Figure 4.30 – Measured and calculated volumes using the exact form approach.....	142
Figure 4.31 – Buoyancy force as a function of the inclination and equivalent diameter.....	144
Figure 4.32 – Buoyancy force and limit of the force at head onsets.....	145
Figure 4.33 – Fortin shape and forces inducing the head.....	148
Figure 4.34 – Deep water wave velocity as a function of the wave length.....	150
Figure 4.35 – Kinetic energy as a function of the volume of the bubble and the angle of inclination of the surface.....	153

## CHAPTER 5

Figure 5.1 – Flow patterns under the anode.....	164
---	-----



Figure 5.2 – Minimum covering factor as a function of the current density and angle of inclination.....	167
Figure 5.3 – Minimum covering factor as a function of the position under the anode at 1° .....	169
Figure 5.4 – Maximum covering factor as a function of the current density and angle of inclination.....	170
Figure 5.5 – Maximum covering factor as a function of the position under the anode at 1° .....	170
Figure 5.6 – Difference between the minimum and maximum covering factors as a function of the current density and angle of inclination.....	171
Figure 5.7 – Fluctuation of the covering factor under the outer edge of the anode at the highest current density.....	172
Figure 5.8 – Mean covering factor and standard deviation from its arithmetic mean value (RMS) at 1° of inclination.....	173
Figure 5.9 – Local average, local maximum heights and their ratio at 105 lpm gas generation rate and 1° of inclination.....	180
Figure 5.10 – Local average, local maximum heights and their ratio at 75 lpm gas generation rate and 1° of inclination.....	181
Figure 5.11 – Local average, local maximum heights and their ratio at 51 lpm gas generation rate and 1° of inclination.....	181
Figure 5.12 – Local average, local maximum heights and their ratio at 24.75 lpm gas generation rate and 1° of inclination.....	182
Figure 5.13 – Local average, local maximum heights and their ratio at 18 lpm gas generation rate and 1° of inclination.....	182
Figure 5.14 – Local average, local maximum heights and their ratio at 6 lpm gas generation rate and 1° of inclination.....	183
Figure 5.15 – Local maximum/local average height ratios for the six cases.....	186
Figure 5.16 – Height distribution at 105 lpm volume flow rate of air.....	188

Figure 5.17 – Mean height of the entire bubble layer as a function of the volume flow rate of air.....	189
Figure 5.18 – Two parameters to calculate the average height as a function of the volume flow rate of air at 1° of inclination.....	191
Figure 5.19– Accumulated gas volume under the anode (sum of 60x60 frames).....	192
Figure 5.20 – Specific bubble volume under the outer edge of the anode at 1° and at 1.0 A/cm <sup>2</sup> current density.....	193
Figure 5.21 – Specific bubble volume under the third section of the anode bottom at 1° and at 1.0 A/cm <sup>2</sup> current density.....	193
Figure 5.22 – Specific bubble volume under the second section of the anode bottom at 1° and at 1.0 A/cm <sup>2</sup> current density.....	194
Figure 5.23 – Specific bubble volume under the inner edge of the anode at 1° and at 1.0 A/cm <sup>2</sup> current density.....	194
Figure 5.24 – Mean specific bubble volume as a function of the position under the anode at 1° and at 1.0 A/cm <sup>2</sup> current density.....	194
Figure 5.25 – Specific bubble volume under the whole anode at 1° and at 1.0 A/cm <sup>2</sup> current density.....	195
Figure 5.26 – Specific bubble volume under the whole anode at 1° and at 0.72 A/cm <sup>2</sup> current density.....	195
Figure 5.27 – Specific bubble volume under the whole anode at 1° and at 0.49 A/cm <sup>2</sup> current density.....	195
Figure 5.28 – Specific bubble volume under the whole anode at 1° and at 0.24 A/cm <sup>2</sup> current density.....	196
Figure 5.29 – Mean specific bubble volume for the whole anode as a function of the volume flow rate of air at 1°.....	196
Figure 5.30 – Cross-section of a Fortin bubble.....	197
Figure 5.31 - Escape and break-up of a large bubble.....	202
Figure 5.32– Effect of the escape of large bubbles.....	204
Figure 5.33 – Snapshot showing the sweeping effect of large bubbles.....	205

Figure 5.34 – Instantaneous velocity field close to the side channel.....	209
Figure 5.35 - Instantaneous velocity field close to the centre channel.....	209
Figure 5.36 – Instantaneous velocity field showing the large vortex created by a Fortin head at 0 and 0.026 seconds.....	212
Figure 5.37 – Instantaneous velocity field showing the large vortex created by a Fortin head at 0.078 and 0.104 seconds.....	213
Figure 5.38 – Instantaneous velocity field showing the large vortex created by a Fortin head at 0.13 and 0.286 seconds.....	214
Figure 5.39 – Time-average vertical velocity under the anode showing the mixing effect of Fortin bubbles.....	216
Figure 5.40 – Instantaneous velocity field induced by the escape of the first part of a large bubble.....	217
Figure 5.41 – Instantaneous velocity field induced by the escape of the second part of a large bubble.....	218
Figure 5.42 – Mean horizontal velocity close to the side channel.....	219
Figure 5.43 – Mean horizontal velocity in the centre channel.....	222
Figure 5.44 – Mean velocity in the cell. The right legend applies to images b-f.....	224
Figure 5.45 – Flow pattern under the anodes.....	225
Figure 5.46 – Mean velocity close to the side channel at 1° of angle of inclination.....	227
Figure 5.47 – Mean velocity close to the side channel at 2° of angle of inclination.....	227

## CHAPTER 6

Figure 6.1 - Simulation of bubbles under the anode. After <i>Kiss et al (2005)</i> .....	240
Figure 6.2 - Computational domain.....	244
Figure 6.3 - Boundary conditions.....	246
Figure 6.4 – Vertex and block numbers.....	247
Figure 6.5 – Close up of the mesh used in the simulations.....	247
Figure 6.6 – Initial gas phase under the initial surface.....	251
Figure 6.7 – Snapshots of the initial bubble shape evolution.....	252

Figure 6.8 – Snapshots of the Fortin shape formation.....	253
Figure 6.9 – Duration of the formation of the final shape as a function of the bubble volume.....	254
Figure 6.10 – Duration of the formation of the final shape as a function of the angle of inclination.....	255
Figure 6.11 – Length of a 490 ml large bubble as a function of the angle of inclination.....	257
Figure 6.12 – Terminal velocity of a 490 ml large bubble as a function of the angle of inclination.....	257
Figure 6.13 – Relationship between the simulated and the real bubble.....	258
Figure 6.14 – Effect of bubble volume on the dimensions of the gliding bubble.....	263
Figure 6.15 – Terminal velocity as a function of the bubble volume.....	264
Figure 6.16 – Effect of the material properties on the duration of the formation of a bubble.....	265
Figure 6.17 – Cross-section of air bubble gliding under an inclined surface in water.....	267
Figure 6.18 – Cross-section of a numerically simulated air bubble gliding under an inclined surface in water.....	267

## APPENDIX A

Figure A.1 – Cross-section of the exact approximation.....	278
--	-----

## APPENDIX B

Figure B.1 – Wave onset at the interface of two substances.....	282
---	-----

## LIST OF TABLES

### CHAPTER 3

Table 3.1 – Volume flow rates used in the experiments.....	67
Table 3.2 – Parameters of the experiments in the real-size set-up.....	68
Table 3.3 - Parameters of the experiments in the single bubble set-up.....	70
Table 3.4 – Parameters of the camera.....	72

### CHAPTER 4

Table 4.1 – Parameters in the model and in the real systems.....	155
--	-----

### CHAPTER 5

Table 5.1 – Contact size [ $\text{cm}^2$ ] distribution under the anode bottom (current density= $1.0 \text{ A/cm}^2$ ; angle= $1^\circ$ ).....	175
Table 5.2 – Contact size [ $\text{cm}^2$ ] distribution under the anode bottom (angle= $1^\circ$ ).....	176
Table 5.3 – Contact size [ $\text{cm}^2$ ] distribution under the outer edge as a function of the angle of inclination (current density= $1.0 \text{ A/cm}^2$ ).....	177
Table 5.4 – Contact size [ $\text{cm}^2$ ] distribution under the whole anode as a function of the angle of inclination (current density= $1.0 \text{ A/cm}^2$ ).....	178

### CHAPTER 6

Table 6.1 – Parameters used during the simulations.....	249
Table 6.2 – Control parameters of the simulations.....	249

# Chapter 1

## INTRODUCTION

### 1.1 Aluminium production

Pure aluminium does not occur in nature, it occurs only in combined forms such as oxides and silicates. Today primary aluminium is produced by electrically decomposing alumina. Since its invention more than a hundred years ago, the only industrially used process for aluminium reduction is the Hall-Héroult electrolysis cell. Several new improvements have been proposed, but the original process is still used more or less unchanged.

The electrolysis process takes place at around 960°C. In an electrolysis cell the carbon anodes are suspended in the molten cryolite ( $\text{Na}_3\text{AlF}_6$ ) bath where the alumina powder ( $\text{Al}_2\text{O}_3$ ) is dissolved. The reduced liquid aluminium forms a 15 to 20 cm thick layer at the bottom of the cell above the cathode, and it too acts as the cathode. The distance between the liquid aluminium layer and the anode bottom is 4 to 5 cm and called the Anode Cathode Distance (ACD).

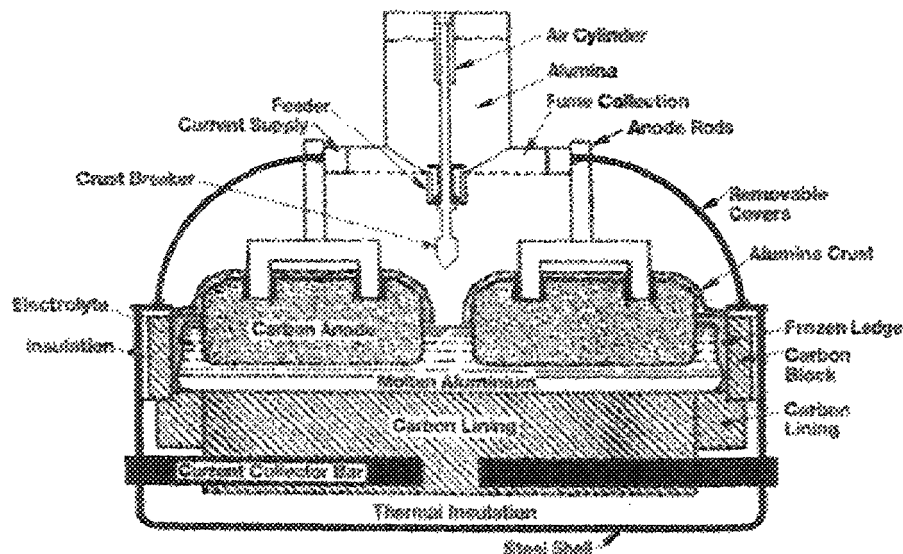


Figure 1.1 – Hall-Héroult electrolysis cell. After Grjotheim et al (1993)

The top of the electrolysis cells are covered by a solid, frozen electrolyte crust. The alumina powder is fed into the bath through small holes in this crust. After alimentation, the dissolved alumina particles are transported to the nucleation sites, where the oxygen is discharged electrically onto the surface of the anode. The discharged oxygen molecules instantly enter into reaction with the carbon anode and form gaseous carbon-dioxide ( $\text{CO}_2$ ). This reaction consumes the anode and nucleates a large number of bubbles under the surface of the anode. The overall chemical reaction in the bath is as follows:



The nucleated bubbles regularly detach from the nucleation sites and start to glide under the anode. After detaching, the size of the bubbles grows only by collision and coalescence with other bubbles. This coalescence creates a more or less continuous bubble layer under the anode. The bubbles range in size from a few micrometers up to dozens of centimetres. The shape of a bubble strongly depends on its volume. The small bubbles are spherical, while the large bubbles are highly deformed due to the forces acting upon them. When a bubble moving under a solid surface becomes large enough, it can form an unusual shape. The shape is characterized by a head that is taller than the tail. This shape will be referred to as a Fortin bubble, or shape, in this thesis after the person who first noted this feature (*Fortin et al, 1984*).

## 1.2 Motivation

The low energy efficiency of the Hall-Héroult process (below 50 %) has been motivating people to improve on the aluminium reduction method. Even though the materials used have been significantly improved over the years, the process itself is used more or less unchanged. Technology has reached a level where further improvements require a still deeper understanding of the underlying mechanisms. Nowadays the principal research themes in this domain are geared to a better knowledge and understanding of the complex chemical and physical phenomena which take place during aluminium electrolysis.



Since the current efficiency of the process is already excellent, around 90-95%, the energy consumption and thus the cost of the aluminium production can be efficiently reduced by lowering cell voltage and avoiding parasite voltage drops. However, both have their limits. The applicable cell voltage is influenced by the current density, the ACD and the bath temperature and composition. The temperature and composition of the bath are the subject of ongoing chemical research, while the reduction of the ACD is limited by the presence of the bubble layer. This bubble layer, the magnetic field and the temperature gradient induce a continuous flow in the bath. This flow helps to homogenize the temperature field and transport the alumina to the reaction sites. Unfortunately, this homogenized temperature field leads to a thinner solid ledge that increases the heat loss from the cell through the side walls. Moreover, the bubbles create unwanted instabilities in the cell and significantly increase the electrical resistance of the cell by having a much lower conductivity than the gas free electrolyte. Thus an understanding and detailed knowledge of the bubble layer and its role in the aluminium electrolysis process are essential in order to understand completely, and eventually improve, the Hall-Héroult process.

The direct physical observation and measurement of the bubble layer in real cells are almost impossible, because of the hostile environment and non-transparent nature of the cell. Generally indirect methods, such as numerical modelling and experiments using an air-water model, for example, can give detailed information about this phenomenon.

### 1.3 Structure of this thesis

In the next chapter the phenomenon of bubbles and of the bubble layer formed under the anode in an electrolysis cell are reviewed. The importance of the bubbles in the electrolysis process is explained. A literature review of different experiments with bubbles moving under solid surfaces is also presented. This is followed by the objectives of this thesis. The applied methodologies are reviewed in detail in the third chapter. The exact physical set-up and the applied measuring techniques along with the analytical methods developed for this study are described. This is followed by the description of the available numerical methods and the created algorithm which was solved numerically in order to simulate the motion and formation of a single large bubble moving under a solid surface.

The fourth chapter presents the results of the experiments with a single large bubble and the theoretical explanation of the mechanism of formation of a Fortin bubble. The fifth chapter is linked closely to the fourth one. It presents the effect of the large bubbles on the aluminium electrolysis cell and gives the connection between the formation of the bubble layer, the angle of the anode, the current density of the cell and the bubble induced flow under the anode. The sixth chapter reviews the results of different numerical simulations of a single large bubble.

The seventh chapter contains the conclusions and suggestions for future work.

#### 1.4 References

- Burkin, A.R., Critical Reports on Applied Chemistry Volume 20, *Production of aluminium and alumina*, Society of Chemical Industry (1987)
- Fortin, S., Gerhardt, M. and Gesing, A. J., *Physical modelling of bubble behaviour and gas release from aluminium reduction cell anodes*, TMS Light Metals, pp. 721-741 (1984)
- Grjotheim, K. and Kvande, H., *Introduction to aluminium electrolysis*, 2<sup>nd</sup> edition, Aluminium-Verlag, Düsseldorf (1993)
- Thonstad, J., Fellner, P., Haarberg, G.M., Hives, J., Kvande, H. and Sterten, A., *Aluminium electrolysis: Fundamentals of the Hall-Héroult process*, 3<sup>rd</sup> edition, Aluminium-Verlag, Düsseldorf (2001)

## **Chapter 2**

# **THE BUBBLE PHENOMENON**

### **2.1 Introduction**

We are surrounded by multiphase flows everywhere in nature just as in several industrial processes. These flows are complex and frequently play a significant role both in nature and industry. During aluminium reduction in a Hall-Héroult electrolysis cell several multiphase flows can be observed. The complexity of these two-phase flows in the electrolysis cell and their role in aluminium production cannot be underestimated. The solid alumina powder is fed into the bath through holes in the crust. The powder is then mixed into the liquid cryolite forming a solid-liquid two-phase flow. The extracted aluminium, having a higher density than the molten alumina-cryolite bath, settles to the bottom of the cell. It creates a separated liquid layer between the cathode and the cryolite bath, thus forming a liquid-liquid two-phase flow. Moreover, the freed oxygen molecules react with the carbon molecules of the anode during the reduction and create carbon-dioxide molecules, which form small bubbles. These bubbles glide under the anode on a thin

wetting film immersed in the cryolite bath, thus forming a bubbly liquid-gas two-phase flow. The bubbles gliding under the anode form a bubble layer and the shape and volume of the bubbles have an effect on the layer itself. The movement of the layer induces a flow in the liquid electrolyte. Since this flow is induced by the bubbles, their shape, volume, velocity and their effect on the induced flow is very important. Small single bubbles moving in different liquids have been observed widely. The results of the experiments with freely rising bubbles, bubbles rising in tubes or small bubbles moving under solid surfaces are reviewed in the first part of this chapter. This review focuses on such parameters of the moving bubbles as shape, velocity and the relationship between them. A short review of bubble nucleation in a Hall-Héroult cell, the bubble layer, bubble induced flow and the importance of the bubbles in the aluminium electrolysis process follows.

## **2.2 Gas-liquid two-phase flow**

As its name indicates, a gas-liquid two-phase flow is formed by a lighter and less dense gas phase and a heavier and denser liquid phase. Depending on the direction of the flows, the velocity difference between the two phases and the volume fraction of the phases, different flow regimes can be observed. For example, in a horizontal, vertical or inclined tube with a high gas fraction the gas phase occupies most of the volume while the liquid flows on the wall as a thin film. The continuous gas phase diminishes in volume as the

liquid fraction increases and the gas phase breaks into various sized bubbles. At high liquid fraction and low gas fraction the gas phase forms small bubbles which either move along with the liquid phase or rise due to the buoyancy. This regime is called bubbly flow.

In a horizontal tube with approximately equal quantities of gas and liquid, the so called *stratified* or *stratified wavy* flow can be observed. In this regime the gas fraction is high enough to maintain a continuous gas volume. Due to the higher density of the liquid phase, it occupies the bottom of the tube while the gas fraction occupies the top. This phenomenon can be observed in a Hall-Héroult cell, where the nucleated bubbles form a semi-continuous gas layer under the anode and above the molten cryolite.

### 2.2.1 Interfacial phenomena

Additional to the volume fraction of the two phases, their movement and consequently their different velocities, the momentum, energy and mass transport occurring at the phase interfaces have a strong effect on the formation and movement of the phases. For example, a fast moving gas phase can induce waves in the gas-liquid interface thus inducing a flow in the previously standing fluid phase.

Interfacial phenomena are all processes where momentum, energy and mass transfer occur at phase interfaces. A phase interface is a finite but very thin layer which separates

two phases whose physical and mechanical properties are different. In practice, we consider the interface as an infinitely thin layer where the properties vary sharply, but in reality the interface may be several molecular diameters or more where the physical properties vary continuously.

The molecules near the interface have a different environment than the molecules inside the phase. Inside the phase there are molecules in every direction around a molecule and thus the forces acting on the molecule are balanced. Therefore, over a certain time the sum of acting forces is zero. While near the interface there are fewer molecules of the given phase and thus the short range force is not well balanced. The molecules in the denser phase, but near the interface experience less force than inside the phase and thus the non-equilibrium forces try to pull the molecules back into their own phase. The effect of the interface is opposite in the lighter fluid. The molecules close to the interface experience a pulling force. The effect of this phenomenon is that the lighter free fluid at rest, where a free fluid is subjected only to internal attractive forces, tries to reduce its interfacial area and its density close to the interface. Thus a small bubble is always shaped like a sphere. This phenomenon is represented by the presence of the surface or interfacial tension which is the surface free energy per unit area at constant temperature and can be calculated by the Laplace-Young equation. This equation gives the excess pressure across a curved surface.

$$\Delta p = \sigma \left( \frac{1}{R_1} + \frac{1}{R_2} \right) \quad (2.1)$$

The tension along the interface between a liquid and a vapour phase is referred to as surface tension, while between two fluids it is called interfacial tension.

Considering that the gas-liquid two-phase flow consists of a lighter gas phase and a denser liquid phase, the boundary conditions at the interface of these two phases have the same form:

- i. If the interface between the two phases is stable, there is no jump in the normal components of the velocity, thus the normal components of the velocity at the two sides of the interface are equal and they are also equal to the normal component of the velocity of the interface.
- ii. There is a jump in the tangential component of the velocity. This is called the free slip condition.
- iii. If the two phases are immiscible, a fluid particle stays on the interface once it is there (kinematic boundary condition). Hence the motion of the interface can be given by the total time derivative of the position of the interface particles.
- iv. Certain amount of energy is needed at the boundary of the two phases in order to create the interface. This energy is proportional to the surface or interfacial tension. The higher pressure inside the dispersed phase is balanced by this tension, given by the Laplace-Young equation (2.1).



- v. According to Newton's third law, the normal and tangential components of stress must be balanced at the interface.

If surface viscosities are neglected, the normal stress condition takes the form:

$$p_p + (\tau_{nn})_p - p - \tau_{nn} = \sigma \cdot \left[ \frac{1}{R_1} + \frac{1}{R_2} \right] \quad (2.2)$$

while the tangential stress condition is:

$$\tau_{nt} - (\tau_{nt})_p = \nabla_{(s)} \sigma \quad (2.3)$$

If the surface or interfacial tension is uniform, there is no jump in the tangential component of the stress. If there is no jump in the normal component of the stress, then (2.2) reduces to the Laplace-Young equation (2.1).

### 2.2.2 Stability of the gas-liquid interface

The surface and interfacial tensions have a large influence on the hydrodynamic stability of mobile interfaces. Surface instability can occur because of local small-scale or non-local large-scale reasons. The non-homogeneous distribution of the surface or interface tension

due to non-uniform heat and/or mass transfer in the interface itself, leads to a motion inside this layer; this is the so called Marangoni effect. The motion in a small part of the interface layer can induce motion in the whole layer. It can induce the movement of the layer itself or even lead to a local break-up in the interface.

On the other hand, non-local, large scale changes, such as a change in the fluid flow, mass or heat transfer, can also induce the movement of the interface. For a standing liquid with gas flowing above it, the stability of the interface depends on the value of the Mach number of the gas flow. If  $M > 1$ , the interface cannot be stable. While in a subsonic flow ( $M < 1$ ), the interface is stable if the gravity force vector is directed from the lighter to the heavier phase, that is to say that the gas phase is above the liquid phase. Due to the moderate velocities, our experiments are always in the  $M < 1$  range, the gas phase is above the liquid, and our interface is always stable. If disturbances occur at the interface, the stability depends on the wavelength of the disturbance. If the wavelength of the disturbance is smaller than a critical value, the disturbance will be damped; otherwise it will increase without limit. The travelling disturbance of the interface is called a surface wave.

A surface wave always occurs at the interface of two different fluids. This kind of wave is frequently the result of wind or a geologic effect. The phenomenon is called wind where a large amount of gas moves with a velocity higher than the velocity of the liquid phase at and close to the interface. There are two different restoring forces which allow the surface waves to propagate. The first is the surface or interfacial tension, the second is the gravity or buoyancy. A tension propagated wave dies instantly away if its restoring force stops

working, while a gravity wave lives longer than the force which caused the wave. Gravity surface waves are caused by a displacement of liquid parcels which causes a disturbance in the liquid, a perturbation in the equilibrium of the surface. The force which caused the disturbance transfers energy from the gas to the liquid phase. The restoring force tries to restore the displaced parcels toward equilibrium, leading to an oscillation around the equilibrium state. In a continuous medium this causes a travelling disturbance which is called a gravity wave.

The path of the individual fluid parcels under a gravitational wave is circular in deep fluids and elliptical in shallow fluids, where the depth of the water is less than half of the wavelength of the wave. There is only a small forward motion in the fluid and the movement of the individual liquid parcels at a depth of half a wavelength decreases to zero. The momentum and energy is carried forward by the wave not the mass. Shallow water waves are not dispersive, meaning that the phase velocity of the wave is constant and independent of the wavelength, but it depends on the depth of the wave. Thus the crest of a shallow water wave always propagates faster than the trough. In open fluids the top of the first wave passes over the bottom and breaks into a foaming front. The onset of the foaming front depends on the ratio between the top and bottom of the wave. If this ratio is smaller than 1.3, than the wave front acquires a smooth profile, stable against further change and no foaming front forms.

### **2.2.3 Characteristics of standing and freely moving bubbles**

The shape of a bubble is controlled by the physical properties of the continuous and dispersed phases and the properties of the flow. The shape of an immobile bubble immersed in an immobile liquid is controlled by the surface tension and buoyancy. Whereas the shape of a moving bubble or an immobile bubble immersed in a flowing liquid is controlled by the above mentioned forces and by the hydrodynamic forces induced by the flow or the movement of the bubble. The shape of immobile bubbles attached to upward or downward surfaces can be calculated from the Laplace-Young equation.

#### **2.2.3.1 Standing bubbles**

Depending on their response to the effect of gravity, we can distinguish 3 types of bubbles: sessile, pendant and floating. We call a bubble or drop sessile if in equilibrium the gravity tries to stick the particle to a surface while a pendant bubble tries to leave a surface under the influence of gravity. Floating bubbles rest at the interface of two fluids. The three types of bubbles can be seen in figure 2.1.

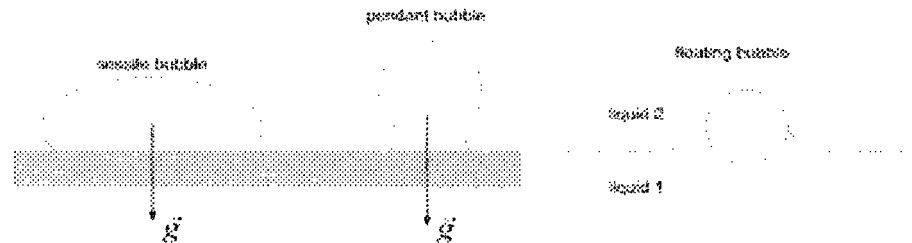


Figure 2.1 – Sessile, pendant and floating bubbles

*The shape of a sessile bubble under an upward facing surface*

When a bubble stands under a downward surface (figure 2.2), the gravitational force presses the bubble against the surface and thus only the small bubbles have a spherical shape. Under the influence of buoyancy, the larger bubbles have a flattened bottom surface, but the contact shape is always circular with radius  $R_c$ . Contact shape is the shape of the contact zone between the bubble and the surface, and it is independent of the volume of the bubble.

The height – which is in fact the depth, in order to be precise - increases with increasing bubble volume until it reaches a maximum value,  $h_{\max}$ . Further increase in the volume decreases the height slightly until it reaches  $h_{\lim}$ , the limiting height. When this limit is reached, an increase in the volume will not increase or decrease the height, but will change the dimensions perpendicular to the height. The shape of a bubble under a downward face can be seen in figure 2.2.

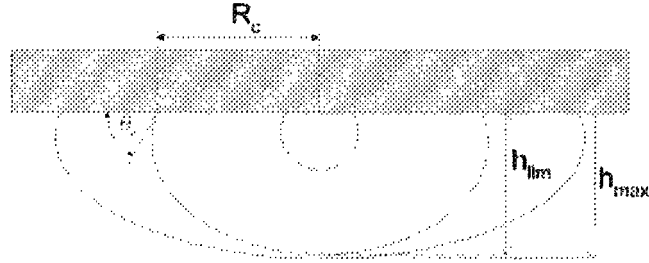


Figure 2.2 – Limiting and maximum height of a bubble under a surface

The maximum and limiting heights of a stationary bubble under a downward face are given by *Pruppacher and Klett (1978)* as:

$$h_{\max} = \left( -0.19 \cdot (\pi - \theta_c)^2 + 1.293 \cdot (\pi - \theta_c) - 0.053 \right) \cdot \sqrt{\frac{\sigma}{(\rho_l - \rho_g) \cdot g}} \quad (2.4)$$

and:

$$h_{\lim} = \sqrt{2 \cdot (1 - \cos(\pi - \theta_c)) \cdot \frac{\sigma}{(\rho_l - \rho_g) \cdot g}} \quad (2.5)$$

where  $\theta_c$  is the contact angle,  $\sigma$  is the surface tension,  $\rho_l$  and  $\rho_g$  are the densities of the liquid and gas phases, respectively and  $g$  is the gravitational acceleration. The maximum and limiting heights of carbon-dioxide bubbles in molten cryolite are 4.19 mm and 3.95 mm, respectively. These values are close to the heights of air bubbles in water standing under a Plexiglass® surface, where the maximum height is 4.44 mm, and the limiting height is 4.18 mm (*Perron et al, 2006a*).

### 2.2.3.2 Freely moving bubbles

Bubbles moving freely in liquids reach a steady state after certain time. In steady state the bubbles are moving with the so called terminal velocity. The terminal velocity is determined by the physical properties of the bubble and the liquid and the properties of the system the bubble is moving in. Several bubble shapes have been identified and numerous equations have been developed to calculate the velocity and dimensions of a moving bubble. This sub-chapter reviews these results.

#### Bubble rising in unbounded medium

The deformation of the shape of a bubble rising freely under gravity in a Newtonian liquid is caused by inertia (*Taylor and Acrivos, 1964*). These shapes can be classified as spherical, ellipsoidal or spherical cap. A bubble is spherical if it is rounded with a minimum height-to-width aspect ratio of about 0.9. A bubble is considered to be ellipsoidal when it has a concave surface (viewed from inside), even if the bubble has no real ellipsoidal shape. Large bubbles tend to have a shape with a flat base. Secondary motions, such as oscillation, dilation and wobbling, deform these shapes. The shape regimes can be seen in figure 2.3 as a function of the Eötvös, Reynolds and Morton numbers for cases  $0.01 < E\delta < 1000$ ,  $0.1 < Re < 10^5$  and  $-14 < \log Mo < 8$ .





### *Spherical regime*

In the spherical regime, the bubble behaves as a rigid sphere even in the absence of surfactants. The terminal velocity is mainly controlled by the viscous drag; the rising bubble path is rectilinear without secondary motion. By finding the solution to the Stokes stream functions, *Hadamard (1911)* and *Rybczynski (1911)* obtained the following expression for the terminal velocity of spherical bubbles:

$$u_T = \frac{2}{3} \cdot \frac{g \cdot a^2 \cdot \Delta\rho}{\mu} \cdot \frac{\kappa + 1}{3 \cdot \kappa + 2} \quad (2.6)$$

where  $\kappa = \frac{\mu_p}{\mu}$  is the dimensionless viscosity ratio of the bubble and the liquid.

They also found that at low Reynolds numbers, the surface tension does not have to be dominant for a bubble to be spherical. It was observed that small spherical bubbles do not tend to obey (2.6) (*Bond et al, 1928*). Instead, they follow Stoke's law, which gives the following expression for the terminal velocity:

$$u_{Ts} = \frac{ga^2\Delta\rho}{18\mu} \quad (2.7)$$

If the Reynolds and Eötvös numbers of the flow increase to a limit, the shape of the bubble begins to flatten. For bubbles rising freely in a liquid, significant deformation occurs for all  $Re > 600$ .

The circulation inside a bubble delays the onset of flow separation in the liquid the bubble is rising in and makes the surface vorticity and wake volume be smaller than for non-circulating spheres. As a consequence, the pressure drag and skin friction are reduced, thus the drag coefficient is also reduced. Therefore, the terminal velocity is increased for circulating bubbles. The high  $\kappa$  viscosity ratio damps the internal circulation because of the high viscosity inside the bubble. The internal circulation is small in a highly viscous flow even in the complete absence of surfactants, which also reduce the inner circulation. In practice, any deformation or surfactant at the surface of the bubble increases the drag coefficient.

For the case of  $0 \leq \kappa \leq \infty$  and  $2 < Re < 500$  *Rivkind and Ryskin (1976)* gives the drag coefficient as:

$$C_D = \frac{1}{\kappa + 1} \cdot \left[ \frac{14.9}{Re^{0.78}} + \kappa \cdot \left( \frac{24}{Re} + \frac{4}{Re^{1/3}} \right) \right] \quad (2.8)$$

For low  $\kappa$  *Levich (1962)* gave the next approximation as:

$$C_D = \frac{48}{Re} \quad (2.9)$$

*Moore's (1963)* improved the drag coefficient expression and obtained:

$$C_D = \frac{48}{Re} \left[ 1 - \frac{2.21}{\sqrt{Re}} + O(Re^{-5/6}) \right] \quad (2.10)$$

*Haas (1972)* gave a good fit to numerical prediction of drag of spherical bubbles in intermediate Reynolds number with the following equation:

$$C_D = 14.9 \text{Re}^{-0.78} \text{ for } \kappa \rightarrow 0, \text{Re} > 2 \quad (2.11)$$

### *Ellipsoidal regime*

The terminal velocity of ellipsoidal bubbles can be given for systems of normal purity by the experimental correlation. This correlation is based on 1483 experimental data points (drops and bubbles in liquid) and was developed by *Grace et al (1976)* (for systems with  $Mo < 10^{-3}$ ,  $\text{Re} > 0.1$  and  $E\sigma < 40$ ).

$$u_T = \frac{\mu}{\rho \cdot d_s} \cdot Mo^{-0.149} \cdot (J - 0.857) \quad (2.12)$$

$$\text{where} \quad J = 0.94 \cdot H^{0.757} \quad (2 < H \leq 59.3) \quad (2.13)$$

$$J = 3.42 \cdot H^{0.441} \quad (H > 59.3) \quad (2.14)$$

$$J = \text{Re} Mo^{0.149} + 0.857 \quad (2.15)$$

$$\text{where} \quad H = \frac{4}{3} \cdot E\sigma \cdot Mo^{-0.149} \cdot \left( \frac{\mu}{\mu_{\text{water}}} \right)^{-0.14} \quad (2.16)$$

While for a pure system the following modification was proposed (*Grace et al, 1976*):

$$(u_T)_{pure} = u_T \left[ 1 + \frac{\Gamma}{1 + \kappa} \right] \quad (2.17)$$

where  $\Gamma$  is obtained experimentally and

$u_T$  is calculated from (2.12).

Intermediate sized bubbles show two types of secondary motion; a rigid body motion such as zigzag, rocking or helical, and a shape oscillation. These motions always decrease the terminal velocity. The occurrence of secondary motion is most likely because of the weak shedding. The onset of weak shedding and so the onset of shape oscillation is delayed in a pure system with a relatively low  $\kappa$ . It is feasible to accept that the type of secondary motion depends on the way the bubble is released.

*Tomiyama et al (2002)* have concentrated on intermediate sized bubbles, where the surface tension plays a significant role and has given the following two correlations to calculate the terminal velocity at the nose of the bubble.

$$u_T = F(E_f) \sqrt{\frac{8\sigma E_f^{4/3}}{\rho_l d \gamma^{1/3}} + \frac{\Delta \rho g d \gamma^{1/3} E_f^{2/3}}{2\rho_l (1 - E_f^2)}} \quad (2.18)$$

$$\text{where } F(E_f) = \frac{\sin^{-1} \sqrt{1 - E_f^2} - E_f \sqrt{1 - E_f^2}}{1 - E_f^2} \quad (2.19)$$

$$E_f = \frac{b}{a} = \frac{2}{1+\beta} E = \gamma E \text{ is the aspect ratio for the frontal part} \quad (2.20)$$

$$\gamma = \frac{2}{1+\beta} \text{ is the distortion factor} \quad (2.21)$$

$$E = \frac{b + \beta b}{2a} \text{ is the aspect ratio} \quad (2.22)$$

For high Reynolds number flows, where the potential flow theory is valid up to a high angle  $\phi \cong 160^\circ$  at the nose of the bubble, the terminal velocity can be expressed as (Tomiyama et al, 2002):

$$u_T = \frac{f(m_A, E_f)}{\sqrt{(1-E_f^2)(1-m_A^2)}} F(E_f) \sqrt{\frac{4\sigma}{\rho_l d} \frac{E_f^{4/3}}{\gamma^{1/3}} \left[ \frac{1}{f(m_A, E_f)} + \frac{1}{f(m_A, E_f)^3} - 2 \right] + \frac{\Delta \rho g d}{\rho_l} \gamma^{1/3} E_f^{2/3} (1-m_A)} \quad (2.23)$$

$$\text{where } f(m_A, E_f) = \sqrt{m_A^2 + E_f^2 (1-m_A^2)} \quad (2.24)$$

$$m_A = \cos \phi_A \quad (2.25)$$

### *Spherical cap regime*

Two different spherical cap shapes can be observed. One has a spherical front and flat rear surface. In low Reynolds number flows ( $Re < 150$ ) the rear surface is also bent with

an oblate spherical surface. Spherical cap shape onset occurs in high Eötvös number flows ( $Eö > 40$ ), where  $d_e$ , the equivalent diameter,  $> 18\text{mm}$ . Due to the size of the bubble, the interfacial tension forces are neglected in this regime and the terminal velocity is derived using only the shape and motion near the nose.

*Davies and Taylor (1950)* gave an approximation for the terminal velocity for bubbles for  $Re > 150$ :

$$u_T = \frac{2}{3} \cdot \sqrt{\frac{g \cdot R_C \cdot \Delta\rho}{\rho}} \quad (2.26)$$

where  $R_C$  is the radius of curvature of the bubble surface at the nose.

While *Collins (1966)* used the same approach, he made  $R_C$  the average radius of curvature of the front surface. The terminal velocity can also be given in terms of the equivalent volume  $V_p$  or the equivalent diameter  $d_e$  of a bubble (for  $Re > 150$ ,  $Eö > 40$ ):

$$u_T = 0.792 \cdot \sqrt{\frac{g \cdot \Delta\rho}{\rho}} \cdot V_p^{1/6} \quad (2.27)$$

and

$$u_T = 0.711 \cdot \sqrt{\frac{g \cdot d_e \cdot \Delta\rho}{\rho}} \quad (2.28)$$

For low Reynolds number flows (  $Re < 150$  ) the terminal velocity is given by *Wairegi and Grace (1976)* as follows:

$$u_T = \left( \sin^{-1} e - e \cdot \sqrt{1 - e^2} \right) \cdot \frac{(g \cdot b \cdot \Delta \rho / \rho)^{1/2}}{e^3} \quad (2.29)$$

$$\text{where } e = \sqrt{1 - \left( \frac{b}{a} \right)^2} \quad \text{is the eccentricity}$$

$a$  and  $b$  are the semi-axis

*Bhaga and Weber (1981)* gave an empirical correlation for gas bubbles  $\left( \frac{\Delta \rho}{\rho} \approx 1 \right)$  for

$Re > 1.2$ ,  $Eö > 40$  and  $10^{-11} < Mo < 10^3$  as:

$$u_T = \frac{10^{6m} \cdot V_p^m}{4 + 1.32 \cdot Mo^{0.29}} \quad (2.30)$$

$$\text{where } m = 0.167 \cdot (1 + 0.34 \cdot Mo^{0.24}) \quad (2.31)$$

For a very viscous system (  $Mo > 2$  ) the terminal velocity can be calculated using the following correlation for the entire range of  $Re$  number flows (*Darton and Harrison, 1974*):

$$2 \cdot Re^2 + 6 \cdot Re \cdot \frac{2 + 3 \cdot \kappa}{1 + \kappa} - Ar = 0 \quad (2.32)$$

where  $Ar = E\delta^{3/2} \cdot Mo^{-1/2} = \frac{g \cdot \rho \cdot \Delta\rho \cdot d_e^3}{\mu^2}$  is the Archimedes number. (2.33)

*Joseph (2003)* developed a correlation for the terminal velocity of a freely rising bubble through a viscous liquid in the spherical cap regime. He assumed that the fluid is irrotational and his expression is given as:

$$\frac{u_T}{\sqrt{gD}} = -\frac{8}{3} \frac{\nu_l (1+8s)}{\sqrt{gD^3}} + \frac{\sqrt{2}}{3} \left[ 1 - 2s - \frac{16s\sigma}{\rho_l g D^2} + \frac{32\nu_l^2}{gD^3} (1+8s)^2 \right] \quad (2.34)$$

where  $D$  is the diameter of the cap,

$s$  is the curvature at the bubble nose ( $s = 0$  for spherical shape)

In the spherical cap regime, the bubble with  $Mo > 10^{-1}$  may trail a thin annular film called a skirt. This occurs when the viscous forces in that region overcome the retaining forces. The skirt has no effect on the terminal velocity but has an effect on the nature of the wake behind the bubble. Skirt formation depends on the Capillary and Reynolds numbers.

For a bubble, skirts exist for  $Re > 9$  and  $We/Re > 2.32 + \frac{11}{(Re-9)^{0.7}}$ . The skirts can be

steady or non-steady and symmetric or asymmetric. Its thickness increases with increasing  $Re$  and its maximal length is controlled by balance and stability. The width of the skirt is not uniform. It is wider close to the bubble and becomes thinner drawing away from it. Skirts behind bubbles are much thinner than behind drops.



*Formulas for all regimes*

Terminal velocity for air bubbles rising in water for all shape regimes but for  $d_e > 1.3 \text{ mm}$  can be approximated closely by expression (2.35). It is based on large number of experimental data (Gaudin, 1957).

$$u_T = \sqrt{\left(\frac{2.14\sigma}{\rho d_e}\right) + 0.505gd_e} \quad (2.35)$$

Bozzano et al (2001) assume that the shape of a rising bubble is the one minimizing the total energy associated with it. During the minimalization process they neglect the secondary motion of the bubble if there is any. They get the following equation for the terminal velocity:

$$u_T^2 = \frac{4}{3} \frac{gd_e}{C_D} \quad (2.36)$$

$$\text{where } C_D = f \cdot \left(\frac{a}{d_e/2}\right)^2 \quad (2.37)$$

$$f = \frac{48}{\text{Re}} \left( \frac{1 + 12Mo^{1/3}}{1 + 36Mo^{1/3}} \right) + 0.9 \frac{E\delta^{1/3}}{1.4(1 + 30Mo^{1/6}) + E\delta^{3/2}} \quad (2.38)$$

### Effect of the initial shape on the terminal velocity

If the initial shape is highly deformed, the terminal velocity will be high and the aspect ratio will be low; that is to say the shape will be greatly deformed. Whereas in the case of a small initial deformation, the velocity will be lower and the shape will be less deformed. The path of a bubble with small initial deformation will be a zigzag. However, the path of a bubble with great initial deformation changes from zigzag to helical motion (Tomiyama *et al*, 2002).

### Wall effect on bubbles rising in tubes

Bubbles rising between two walls or close to a wall may be retarded by the wall, thereby decreasing the terminal velocity. In the presence of a wall there is usually some elongation of the bubble shape in the vertical direction. The wall usually has an effect on the terminal velocity, the shape, the secondary motion and the wake structure.

Generally there are very few experimental and theoretical data available for particles moving in tubes with cross-section shapes other than circular. Wall effects on bubble movement can be treated in two groups: first, wall effects on small bubbles, where  $\lambda \leq 0.6$  and wall effects on large bubbles which form a slug in the tube.  $\lambda$  is the diameter ratio of the bubble diameter to that of the tube.

*Wall correction for  $\lambda \leq 0.6$*

For an intermediate bubble size ( $E\delta < 40$ ),  $\lambda \leq 0.6$  and  $Re > 200$  the deviation from the undisturbed terminal velocity can be given as:

$$\frac{u_T}{u_{T\infty}} = [1 - \lambda^2]^{1/2} \quad (2.39)$$

For large bubbles ( $E\delta \geq 40$ ) the wall effects are negligible in low Mo number liquids for  $\lambda \leq 0.125$ . Wallis (1969) proposed the following expression for higher diameter ratios:

$$\frac{u_T}{u_{T\infty}} = 1.13e^{-\lambda} \quad (0.125 \leq \lambda \leq 0.6) \quad (2.40)$$

*Wall correction for  $\lambda > 0.6$  (slug flow)*

A deformable bubble rising in a circular tube can maintain non-zero terminal velocity even if  $\lambda \gg 1$ . If  $\lambda > 0.6$ , then the diameter of the tube becomes the controlling length governing the terminal velocity of the bubble and its shape. In the regime of  $\lambda > 0.6$  a bubble is called a Taylor bubble or a slug. Its bullet like shape consists of a rounded nose region whose shape and dimensions are independent of the bubble volume and of a cylindrical section surrounded by an annular film of the surrounding liquid. If the length of the bubble is more than one and half times the diameter of the tube, the length of bubble has no further effect on the terminal velocity (Zukoski, 1966).

In some special cases the terminal velocity of the slug can be given by an expression.

These cases are:

- 1, when the viscosity and surface tension forces are negligible ( $Mo \leq 10^{-6}$  and  $Eö_D > 100$ ) (Dumitrescu, 1943)

$$Fr_D = \sqrt{\frac{\rho}{\Delta\rho}} \frac{u_T}{\sqrt{gd}} = 0.35 \quad (2.41)$$

- 2, in a surface tension dominant regime ( $Eö_D < 3.4$ ) the slug is motionless thus the terminal velocity is zero (White and Beardmore, 1962; Zukoski, 1966).

- 3, in a viscosity dominant regime ( $Eö_D > 70$  and  $Fr_D < 0.05$ ) (Wallis, 1969; White and Beardmore, 1962).

$$u_T = \frac{gL^2\Delta\rho}{102\mu} \quad (2.42)$$

The terminal velocity of a Taylor bubble in other cases can be estimated using the White and Beardmore (1962) graphical correlation. Bozzano et al (2001) also gave an expression for intermediate sized bubbles as follows:

$$u = \frac{u_T}{\left[ 1 + \frac{C_D/2}{(d_1/d_s)^2 - DEF} \right]} \quad (2.43)$$

$$\text{where } DEF = \left( \frac{a}{d_c/2} \right)^2 \cong \frac{10(1+1.3Mo^{1/6}) + 3.1E\delta}{10(1+1.3Mo^{1/6}) + E\delta} \quad (2.44)$$

*Funada et al (2005)* modelled the rising Taylor bubbles by an ovary ellipsoidal cap rising in viscous potential flow. They obtained the following expression for the dimensionless rise velocity:

$$-Fr^2 e^2 f_1'(e) + \frac{1}{2}(1-e^2) - \frac{8Fr}{Re_g} e \left[ f_2(e) \left( \frac{1}{2} + \frac{e^2}{1-e^2} \right) + \frac{e^2 f_1(e)}{1-e^2} \right] = \frac{8}{E\delta} \left( \frac{e^2}{1-e^2} \right) \quad (2.45)$$

$$\text{where } e = \frac{\sqrt{l^2 - b^2}}{l} \text{ is the eccentricity} \quad (2.46)$$

$$f_1(e) = \frac{e^2}{e + (1-e^2) \tanh^{-1}(e)} \quad (2.47)$$

$$f_2(e) = \frac{2e^2}{e + (1-e^2) \tanh^{-1}(e)} = 2f_1(e) \quad (2.48)$$

The shape of the slug depends also on the viscosity of the liquid the bubble is moving in and the inclination of the tube. *Zukoski (1966)* found that for  $Re > 200$  the velocity is independent of the viscosity effect and the tube properties had no influence on the movement of the bubble when the tube diameter was greater than 2 cm. The shape of the bubble changes gradually with an increase in the tube's angle of inclination. If the tube inclination decreases from vertical to horizontal, the liquid penetrates under the bottom of the bubble, and it is flattened gradually. When the tube is in horizontal position, all the

liquid is in the bottom part of the tube and the bubble is in the upper part of it. The velocity of the bubble increases from zero as the tube position changes from horizontal to  $\sim 45^\circ$  where it reaches its maximum. By further increasing the inclination angle the velocity decreases to the value of terminal velocity of a bubble rising in a closed tube.

#### Bubble rising under an inclined solid surface

The shape of a moving bubble under a surface depends on the volume of the bubble, the angle of inclination, the velocity of the bubble and the properties of the liquid and the bubble. Bubbles moving under an inclined surface have a complex, three dimensional shape and have not been widely investigated yet.

*Maneri and Zuber (1974)* investigated the rise of small bubbles under an inclined plate. The inclination angle varied from  $0^\circ$  to  $85^\circ$ , measured from the vertical axis. They reported three different regimes of movement. The first was between the vertical and  $10^\circ$  inclination of the plate. Inertia is the main force acting on the bubble in this regime. The terminal velocity of the bubble is independent of the physical properties of the liquid the bubbles are rising in. The second regime is from  $10^\circ$  to  $30^\circ$ . Here, the terminal velocity increases with the increasing angle. In the third regime, from  $30^\circ$  to the vertical plane, the terminal velocity depends on the fluid properties.

*Maxworthy (1991)* studied the movement of bubbles under an inclined surface. He found a critical angle of inclination at which the terminal velocity of the bubble reaches a

maximum. He used an air-water system, where the surface angle of inclination varied from 5° to 90° from the horizontal and the bubble volume ranged from 5 to 60 ml. He found that the non-dimensional velocity, namely the Froude number, depends only slightly on the bubble volume and thus depends only slightly on the shape of the rising bubble. He also found that the terminal velocity increases with bubble volume and reaches a maximum at about a 50° angle of inclination. All the cases investigated by him were controlled principally by inertia.

*Chen et al (1992)* also performed experiments to investigate the effect of surface inclination and bubble volume on terminal velocity. They found that the terminal velocity increases monotonously with the inclination angle. This is not in agreement with *Maxworthy's (1991)* and *Perron et al's (2006)* observations.

*Masliyah et al (1994)* studied the rise velocity of small bubbles under an inclined surface in high-Morton number liquids. They found that the rising velocity increases as the inclination angle increases to the vertical. But since they investigated small bubbles, the shape always stayed close to spherical. The experimental data for  $0 < Re_b < 130$  and  $0.4 < E\delta < 1.7$  of their study concluded that:

$$C_D = \frac{16}{Re_b} (1 + 0.007 Re_b^{0.65}) (1 + 1.31 (E\delta \cdot \cos \theta)^{0.51}) \quad (2.49)$$

*Perron et al (2005, 2006a, b, c)* made a wide range of experimental and theoretical studies on small bubbles rising in a liquid under a slightly inclined plate. They found that

the terminal velocity increases with increasing bubble volume and angle of inclination, but the increase is not monotonous. The terminal velocity highly depends on the shape of the bubble which in turn depends on the volume of the bubble and angle of inclination (figure 2.4). The terminal velocity seems to be independent of the bubble volume for large bubbles.

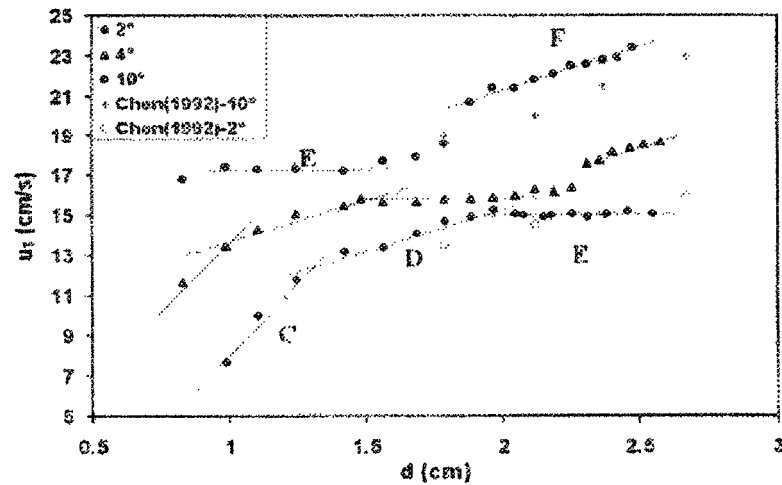


Figure 2.4 - Terminal velocity as a function of the equivalent diameter and angle of inclination. After Perron *et al* (2006a)

They reported two different regimes of movement if the buoyancy force overcomes the retarding surface tension forces. The first regime is the creeping motion when the bubble leaves its nucleation site and moves under the surface attached to it. Thus, there is a dry spot. If the bubble reaches a critical velocity, perturbation occurs at the equilibrium state and the liquid penetrates under the bubble. If the liquid film evolves, the bubble continues moving under the surface but now separated by a thin liquid film from it. The motion of a bubble moving under a solid surface is controlled by the inertia on the bottom of the bubble



while it is controlled by viscous dissipation on the upper side where the bubble is in contact with the wetting film. The film thickness monotonously increases with the bubble volume at a given inclination angle and also with the inclination angle at a given volume. The terminal velocity of the bubble gliding on the wetting film is reported to be an order of magnitude higher than that of the creeping bubble. The distance travelled in the creeping motion is inversely proportional to the bubble volume at a given inclination. If the volume of the bubble exceeds a limit, the bubble rises almost only in the wetting film regime and the distance travelled in the creeping motion tends to zero. With an increase in the bubble volume, the shape of the bubble in the moving plane, the contact zone of a moving bubble, is not a circle anymore. The tendency of the aspect ratio as a function of the bubble volume at a given inclination angle is given in figure 2.5, where the aspect ratio is defined as  $r = \text{width}/\text{length}$  and  $V$  is the volume, ranging from  $0.3 \text{ cm}^3$  to  $9 \text{ cm}^3$ .

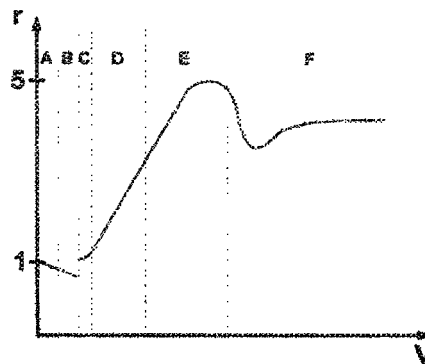


Figure 2.5 - Bubble volume vs. aspect ratio at a given inclination. After Perron *et al* (2006a)

The shape of this volume vs. aspect ratio function depends on the angle of inclination. They classified the observed shapes into 6 classes based on a volume increase (figure 2.6). At high angles some shapes can be disappear starting at A, while at low inclination angles shapes E and F might be missing. Shapes A and B are circular. Shape A is immobile, the bubble rests under the surface attached to it. The bubble remains in this regime until the receding and advancing contact angles reach their critical value. At this point the buoyancy force overcomes the surface tension and the bubble starts to creep under the surface. In regime B the bubble moves slowly with a nearly constant velocity. The contact zone is oval and the bigger axis lies in the direction of the motion.

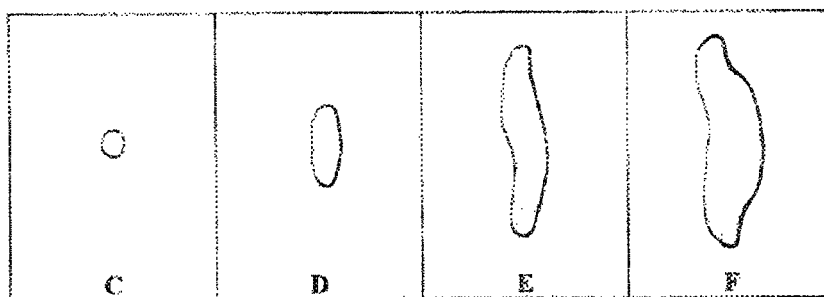


Figure 2.6 - Bubble shapes in the contact zone. After Perron *et al* (2006a)

If the velocity reaches a critical value, perturbation occurs at the nose of the bubble and the liquid starts to penetrate between the bubble and the surface. The front of the bubble is already gliding on the liquid layer where the restraining force of the surface tension is much smaller. Thus the velocity of the front part of the bubble is accelerated more than the rear part. This tendency tries to pull apart the bubble. If the liquid film evolves, the whole bubble glides on the liquid layer instead of gliding on the surface. During the wetting film

regime the bubble reaches its terminal velocity. At this time, the contact shape of the bubble depends on the terminal velocity, therefore on the volume of the bubble, but it is always elongated with the longer axis perpendicular to the direction of the motion. The main forces controlling this regime are inertia and buoyancy. Four different bubble shapes can be observed in the wetting film regime. The shape of the bubble depends on its volume and terminal velocity. With increasing bubble velocity and volume, the effect of inertia increases and the effects of the viscous force and surface tension decrease, though the effect of the surface tension is not evident. Surface tension tries to reduce bubble deformation caused by the motion of the liquid, which in turn is induced by the bubble itself. The bubble in regime C is called semi-rigid because its overall shape is mainly circular with a slightly larger radius of curvature at the nose than at the rear part. The path of the bubble is almost rectilinear. The shape of the bubble, called oval oscillating, is more elongated in regime D. Periodical oscillation of the shape does occur, but the path can still be assumed to be rectilinear. The curvature is positive at the front and it can be negative or zero at the rear part of the bubble. The hydraulic jump is observed in the vertical cross section at the end of this regime. All bubbles that have a larger volume than regime D bubbles have the hydraulic jump at the front. With increasing volume, the bubble deforms in all directions and the deformable bubble shape is reached, E. The longer axis is still perpendicular to the direction of motion. The path can hardly be observed because of the high oscillation, but it is mainly rectilinear. The radii of the curvature at the front and rear can be either negative or positive. Again, the hydraulic jump can always be observed in this regime. Oscillation of the shape can occur in the last regime. The leading curvature is always positive while the

rear curvature can be negative or zero. Two tails can be observed at the lateral ends of the bubble depending on the size of the bubble volume. The path is near to rectilinear. This kind of bubble is called a bulged bubble, F.

*Perron et al (2006c)* found that the bubble shape strongly depends on the liquid properties and thus the liquid properties have a strong influence on the onset of the hydraulic jump at the front part of the bubble. They reported that the bubbles moving in a low-Morton number liquid are more deformable than bubbles moving in a high-Morton number liquid. In the low-Morton number liquid the motion of the bubble is principally controlled by inertia, while in the high-Morton number liquid the motion is controlled by viscous dissipation due to the presence of the wetting film. In high-Morton number liquids, like glycerine and propanediol, the hydraulic jump was not noted even at high bubble volumes. Also, the terminal velocity increased with decreasing Morton number.

For low-Morton number liquids, they obtained the following expression for the dimensionless terminal velocity:

$$-Fr^2 f_1^2(e) e^2 (2 - e^2) + 2(\cot \phi + 1)(1 - e^2) - 4e \frac{Fr}{Re_G} \left[ f_1(e) \left( \frac{1}{2} + \frac{e^2}{1 - e^2} \right) + f_1(e) \frac{e^2}{1 - e^2} \right] = \frac{e^2}{Bo \sin \phi} \left( \frac{4 - e^2}{1 - e^2} \right) \quad (2.50)$$

where

$$f_1(e) = \frac{2e}{e(1 + e^2) - \sqrt{1 - e^2} \sin^{-1}(e)} \quad (2.51)$$

$$f_2(e) = \frac{2e^2(2-e^2)}{e(1+e^2) - \sqrt{1-e^2} \sin^{-1}(e)} \quad (2.52)$$

## 2.3 Bubbles in the Hall-Héroult electrolysis cell

### 2.3.1 Nucleation and motion of the bubbles in an electrolysis cell

During aluminium redaction in the Hall-Héroult cell, the freed oxygen molecules react with the carbon molecules of the anode and create carbon dioxide molecules, which form small gaseous bubbles. The rate of nucleation of the bubbles can be as high as  $0.002 \text{ m}^3/\text{m/s}$  (Zoriç *et al*, 2000).

The bubbles are nucleated periodically at certain preferred places at the bottom side of the anode, called nucleation sites (Poncsák *et al*, 2006). The bubbles nucleate at an increasing frequency with increasing current density. Increasing current density also leads to a larger number of nucleation sites (Aaberg, 1997). The nucleation and growth cycle starts with a slow, latent period. In this period the gas produced during the electrolysis and stored at the pores of the anode surface permeates into the nucleation sites. The pressure of the gas increases until it overcomes the restrictive force of the surface tension, which tries to minimize the surface of the bubble. The smaller the bubble, the higher the surface tension, thus the most excess pressure is needed at the beginning of the nucleation. When

the bubble reaches a certain diameter, its size rapidly expands. At this time the growth of the bubble is controlled by diffusion. The bubble is gradually freed from the nucleation site until it is only connected to it by a dry spot.

During the growth cycle the bubble is attached to the nucleation site. We consider a bubble attached to a surface if there is a dry spot between the bubble and the surface. In the case of a downward facing surface, a bubble can be statically 'attached' to the surface even in the presence of a thin liquid film between the bubble and the surface. In this case the bubble is not considered attached even if it reaches thermodynamic equilibrium. It is evident that a bubble cannot stay attached to an upward or inclined surface in the presence of liquid layer.

The detachment or departure of the nucleated bubble occurs when the forces trying to move the bubble overcome the forces tying the bubble to the nucleation site. Detachment and departure can be distinguished by the presence or absence of a dry spot. A bubble is considered detached from the surface when the dry spot between the surface and the bubble disappears. During air-water experiments it was found that a thin liquid layer exists between the bubble and the surface and the bubble glides on this layer. When the bubble starts gliding along the surface and leaves the nucleation site even though a dry spot remains between the surface and the bubble, it is called departure. Whether the bubble departs or detaches, the feed from the nucleation site is over and further growth of the bubble can occur only with coalescence. The exact physical mechanism of the detachment is not yet fully understood, though it is very important. *Kloucek and Romerio (2002)*

consider the detachment of a bubble under a surface in a motionless liquid as a first order transition where there is a discontinuity of the derivative of the free energy of the bubble. *Kiss et al (2004)* investigated the departure and detachment of bubbles experimentally and found that the angle of inclination where the departure occurs is inversely proportional to the bubble volume.

The detachment size of a bubble nucleated under a solid surface can be calculated from the dynamic conditions of the flow. The size is thus given by the balance of the forces acting on the bubble. The force tying the bubble to the surface is the surface tension and the forces tearing away the bubble are the buoyancy and hydrodynamic force exerted on the bubble by the liquid. The experimental data shows that during aluminium reduction the bubble departure size is about 5-6 mm horizontally and 2.5-3 mm vertically (*Cassayre et al, 2002*), but it depends also on the wetting angle. The wetting angle in the electrolysis cell depends on the composition of the bath, the physical properties of the carbon, the composition of the gas phase, the temperature and the current density. It has been reported to be lower than  $90^\circ$  in the presence of dissolved metallic aluminium in the melt (*Thonstad et al, 2001*). *Utigard et al (1994)* reported that the contact angle formed by liquid aluminium drop on graphite or alumina crucible bottom varied between  $150-170^\circ$  and observed that it did not change with current density or changes in the bath composition. *Vogt (1997)* assumed that the decrease of the contact angle might be caused by an increased bubble size. Because of poor wetting, the bubbles nucleating on a graphite anode stay stuck on the anode and grow before detachment.

After a bubble leaves the nucleation site, a new bubble growth cycle starts and new bubbles are nucleated.

When the bubble detaches from the surface and gains some velocity, the electrolyte penetrates between the anode and the bubble forming a thin liquid layer. The bubble glides on this film and does not touch the anode surface. This wetting film is thicker than the liquid layer in static conditions.

### **2.3.2 Formation of the bubble layer and the bubble induced flow**

After detachment, the size of the bubble can grow only by collision and coalescence with other bubbles (*Fortin et al, 1984*). The modelling and simulation of bubble collision is difficult and the phenomenon itself is not yet fully understood but we know that under the anode the faster bubbles catch up with the slower ones. The size of a bubble helps the collision; the larger bubbles grow faster than the smaller ones. As a bubble grows, it gains velocity further increasing its chance for collisions. The larger bubbles “eat” the smaller and slower bubbles leaving an empty spot behind. As the velocity increases, the transversal size of the large bubbles gets bigger than the longitudinal one. The bubble sizes range from a few micrometers up to dozens of centimetres. The shape of a bubble strongly depends on its volume; small bubbles are spherical, while large bubbles are highly deformed under the force of buoyancy and the dynamic effects in the bath.



As the bubbles glide under the anode, they reach the side of the anode and leave it. When a large bubble leaves the anode, it leaves the anode quite bubble free. Bubble coverage of the anode decreases intensely and can be close to zero (*Aaberg et al, 1997*). Anode coverage was found to range from 65.4% to 90.1% (*Aaberg et al, 1997*), from 30% to 60% (*Zhang, 1993*), from 20% to 35% (*Richards, 1998*), around 50% (*Poncsák et al, 2006*), around 50% (*Zoriç et al, 2000*) and 24-90% depending on the angle of inclination and current density (*Fortin et al, 1984*). Increasing the angle of inclination decreased the anode coverage slightly; the coverage of the anode was not uniform (*Poncsák et al, 2006*). A large number of small bubbles were found under the inner edge of the anode while the outer edge of it was covered by a few large bubbles. Despite the small number of the large bubbles, they covered a large fraction of the anode bottom. The unique size of the bubbles is important, since one large bubble covers a smaller area under the anode than several smaller bubbles with the same total volume. The size of the gas bubbles under the anode was estimated to be 400-700 cm<sup>3</sup> (*Richards, 1998*). The form of the anode also influences bubble distribution and movement. A commonly used technique to significantly decrease the bubble coverage of the anode bottom is using a grooved anode. Also, a slight inclination of the anode sets the bubbles into movement. An inclination as small as 0.3° is enough to start movement (*Fortin et al, 1984*).

At a high rate of bubble nucleation the nucleated bubbles form a more or less continuous bubble layer under the anode, forming really large bubbles or gas pockets. The height of the bubble layer was calculated to be between 0.4 to 0.6 cm and it ranges up to 0.71 cm before bubble release (*Aaberg et al, 1997*). *Xue and Øye (1995)* estimated it to be about 0.4 cm,

while *Haupin (1971)* and *Dewing (1991)* found it to be 0.5 cm. The height of the bubble layer under the anode decreases with decreasing current density from 5 mm to 4.2 mm (*Cassayre et al, 2002*).

Bubble nucleation with a bottom size of around 5-20 mm has been extensively observed in see-through-cells, but only with small anodes (*Cassayre et al, 2002*). These observations have shown that the bubbles collide and coalesce after detachment and then leave the anode. However, there are contradictory results about the relationship between bubble size and current density. While *Haupin et al (1975)* found increasing bubble size with increasing current density, *Utigard et al (1994)* found the opposite. Thus it is possible that cell geometry has an influence on bubble behaviour and the size of the bubbles formed depend on the alumina content of the bath. Bubble size increases as the alumina content decreases. *Cassayre et al (2002)* found that the release size of the bubbles depends on the current density; the size decreases with increasing current density. The bubble release frequency also depends on the current density. Measured release frequencies on their small experimental anodes were higher than those calculated by cell voltage analysis alone. However, the alumina content does not have a major effect on the bubble size.

In an electrolysis cell there are three sources of motion, the buoyancy, the Lorentz force as well as the temperature and concentration gradients. Recent technological improvements in cell design have reduced the effect of the Lorentz force significantly. For a long time the bubble layer was not considered as a source of momentum, but recent articles have shown that the bubbles do play a significant role in the heat and momentum transfer in the bath

(Solheim *et al*, 1989; Purdie *et al*, 1993; Bilek *et al*, 1994; Begunov *et Gromov*, 1994).

When the current passes through the conductor element of the aluminium electrolysis cell, a magnetic field is produced. This field induces a motion in the metal bath, at the metal-electrolyte interface and in the bath. The direction of these motions and the velocity field depend highly on the applied bus bar system, the anode and cathode geometry and the neighbouring cells (Grjotheim *et al*, 1993).

The motion of the electrolyte and the aluminium pad is very important in the process of electrolysis. As it was mentioned before, these movements have negative and positive effects. Negative effects are the induced instabilities and the increased re-oxidation of the aluminium. The distance between the aluminium pad and the anode is only about 4-5 cm. Due to the wavy motion of the aluminium pad, the system can short-circuit. The motion of the electrolyte and the aluminium pad is due to different effects. The motion of the aluminium pad is due to the electromagnetic action in the aluminium. The interfacial drag of the moving electrolyte also causes a small motion in the aluminium pad, but its effect is small compared to the electromagnetic effect. The movement of the electrolyte is induced by the movement of the bubble layer, the electromagnetic forces and the temperature and concentration gradients in the cell. The bubbles have the strongest effect, while the temperature gradient has the smallest.

These movements are also important for heat balance in the cell. A too intense movement of the electrolyte can lead to a significant change in the heat balance and an increase or decrease in the thickness of the frozen ledge.

There are several methods to calculate the magnetic field in the Hall-Héroult cell. Several improvements have been made to adjust or compensate for the magnetic fields (Grjotheim, 1993). It is important to adjust the transverse fields since it causes the curvature of the aluminium pad. It is also important to minimize the vertical magnetic fields since they create instabilities and swirls while interacting with the horizontal currents.

Several attempts have been made to simulate the flow field in the Hall-Héroult cells. Generally, a simulation is limited to one component of the controlling forces, such as the magnetic field, gas bubbles or temperature differences. ESTER (Electrolytic Smelter) is a PHOENIX based simulation program that claims to include all the above mentioned components, but only a very simplified example can be found (CHAM, Bakery House, 40 High St, Wimbledon, London, SW19 5AU England). There are several two-dimensional models using three-dimensional inputs of the magnetic field for example, to calculate the electrolyte and metal pad motion but to the best of the author's knowledge only the ESTER code and Robl (1975) claim to include the effect of gas bubbles which are really important for momentum transport and current distribution in the cell.

The velocity field of the bath has been measured and modelled numerically before. The measurements were performed in real-size air-water models where usually the bath velocity was measured in the side channels and in the anode-anode gaps, but not under the anodes (Chen et al, 1996; Solheim et al, 1989; Purdie et al, 1993; Bilek et al, 1994; Begunov and Gromov, 1994). These measurements were mostly concerned about the flow pattern in a complete electrolysis cell consisting of several anodes. The measured velocity differs in the

different parts in the cell and varies from 1 to 40 cm/s (*Chen et al, 1996*). The numerical simulation contained the effects of the MHD and/or the gas driven flow. Every numerical model seen by the author assumed the bubbles to be spherical and uniform in size (*Purdie et al, 1993; Bilek et al, 1994; Begunov and Gromov 1994*). It may be adequate for a general numerical model, but it misses the small scale momentum transport between the bubbles and the bath.

Gas layer induced wavy motion has been measured in the gap between anodes. Its frequency was measured to be around 0.5-1.0 second. Its amplitude depends on the current density, ACD and bath depth; it was around 7-35 mm (*Chesonis, 1990*).

### 2.3.3 Fortin shaped bubbles in the cell

When the volume of a moving bubble reaches a limit, a special shape can be observed. In real-size air-water models, at a slight inclination of the anode, large bubbles with a head penetrating up to 2 cm into the electrolyte and with a long tail are formed and moved under the anode (*Fortin, 1984; Solheim et al, 1989; Utigard, 1994; Zorić et al, 2000*). The bubble forms a so called “head” which is taller than the “tail”. This bubble shape was first reported by *Fortin et al (1984)* and from this point it will be referred as a **Fortin bubble** or **Fortin head**. They thought that this form occurs when the “bubble surface became horizontal and the bubble front collapsed”. This is not in agreement with our observations as it will be

shown later. This shape forms due to a variation in the hydrostatic and hydrodynamic pressures along the interface between the bubble and liquid. The height of the head is greater than the maximum thickness of a standing bubble or the mean height of a moving bubble layer. A bubble with the “head and tail” shape can be seen in figure 2.7.

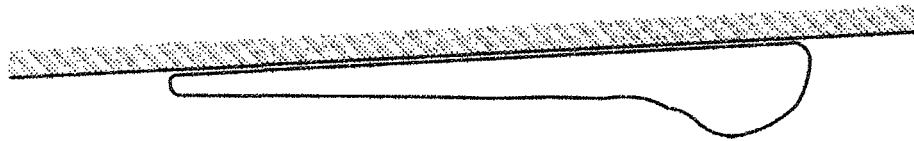


Figure 2.7 – Fortin bubble with the special “head and tail” shape

According to *Fortin et al (1984)*, the longitudinal dimension of the large bubbles varied from 2 to 128 cm and the dimension perpendicular to the motion of the bubble varied from 4 to 40 cm, where the 40 cm is the width of the anode. For any bubble having a width less than the width of the anode its transversal dimension was always larger than the longitudinal one. The height of the head varied from 0.8 to 2.4 cm while the height of the tail was about 0.5 cm.

Large bubbles do not interact with the bath the same way small ones do; there is a strong interaction between bubble size, shape, velocity and drag force (*Perron et al, 2006a; Perron et al, 2005; Kiss et al, 2004; Chen et al, 1992*). Based on measurements, the turbulence intensity in the wake of a bubble depends on its size and it increases with increasing size (*Choi et al, 2002*).

#### 2.3.4 The importance of bubbles in the process of aluminium electrolysis

The small and especially the large bubbles in the bubble layer formed under the anode play an important role in the productivity of the electrolysis cells because of their negative and positive impacts. Natural heat convection, the magnetic field and the bubbles induce a circulation in the cell under the anode and in the sidewall channels. The induced flow transports the alumina particles to the reaction sites and improves the mixing in the cell, thus helping to homogenize the temperature field and improving the dissolution rate of the alumina in the bath. After feeding the alumina into the bath, the alumina must be dissolved and mixed fast in order to avoid the formation of sludge or muck (*Grjotheim et al, 1993*). A too low alumina concentration can lead to the formation of a continuous gas layer under the anode, the so called anode effect. The continuous gas layer insulates the anodes and thus increases the cell voltage rapidly up to 30-50V and disrupts the normal process. However, the gas cover of the anode is only a secondary phenomenon and not the primary reason of the anode effect (*Calandra et al, 1979*). Other negative forces take place during the anode effect, such as an increase in the bath temperature, increase in the energy consumption, sidewall attack, among others. In the case of a horizontal anode, only the vertical sides of the anode are involved in the electrical process during the anode effect. The anode effect can be terminated by removing the gas layer and feeding alumina into the bath (*Grjotheim et al, 1993*).

On the other hand, the induced flow and the turbulences in the flow create unwanted instabilities in the bath. Because of the gas producing electrochemical reaction, the anode is consumed continuously. The regions with a mixture of electrolyte and bubbles have lower conductivity than the gas-free electrolyte. Hence the bubbles nucleated under the anode increase the resistance of the cell and thus increase the energy consumption of the process. According to *Haupin (1971)* the ohmic over voltage in the electrolyte due to the presence of the bubbles may be about 0.15 – 0.35 V. Resistance strongly depends on the size of the gas bubbles; the larger bubbles cause larger resistance. The bubbles gliding under the anode deform the electrical field in the bubble-free region and reduce the effective conducting area of the anode. The bigger the contact size of the bubble, the bigger the electrical resistance caused by the bubble. *Poncsak et al (2006)* used a full-size air-water model with horizontal and inclined anodes, both with and without groove. They observed that the anode was covered by a few large and many small bubbles. Increasing the inclination decreased the coverage slightly. The coverage of the anode was not uniform; a large number of small bubbles were found under the inner edge of the anode while the outer edge was covered by a few large bubbles. Despite the small number of large bubbles, they covered an important fraction of the anode bottom. Furthermore, as the large bubbles leave the anode they work as a siphon, inducing gravitational waves in the metal-bath interface. These waves strengthen the bubble induced flow and help the re-oxidation of the aluminium (*Dernedde, 1976*). The motion of the metal-bath interface is induced mainly by the bubble motion under the anode (*Bilek et al, 1994; Begunov and Gromov, 1994; Dernedde, 1976; Haarberg et al, 1998*).



A few experiments and numerical calculations were carried out in order to understand the bubble induced flow field and the movement of the bubbles nucleated under the anode in an electrolysis cell. Even though the bubble layer is more or less understood, the role of the single bubbles in the bubble layer is not; neither is their effect on the fluid. As mentioned before, the presence of the bubble layer increases the resistance of the cell and thus increases the energy consumption. One way to reduce consumption is to reduce the anode cathode distance (ACD) and the resistance created by the bubble layer. The limit of the ACD decrease is the bubble induced flow and the motion of the metal surface due to the magnetic effect, because these two induce flow in the bath and create vortexes. The flow and especially the turbulences can cause instabilities in the bath-aluminium interface and lead to the re-oxidation of the aluminium, significantly reducing the efficacy of the production. A strong connection has been found between the specific bubble volume and the cell voltage; a higher bubble volume causes higher cell voltage (*Aaberg, 1997*). *Perron et al (2006d)* and *Hyde and Welch (1997)* have found that the shape of the bubble does not have much effect on the total electrical resistance but the size does.

## 2.4 Objectives of this thesis

Nowadays the main areas of interest in the aluminium electrolysis domain are a still deeper understanding of the different phenomena which take place in the electrolysis cell. The main objective of this thesis is to understand the phenomenon of the so called Fortin

bubble completely, including its physical properties, formation and behaviour, to identify and understand the parameters which control their shape and movement, and also to understand their effect on the aluminium electrolysis process, on the bubble driven flow in the cell and most importantly on the aluminium extracting process. In order to achieve these goals, numerical simulations and experimental measurements will be carried out on single bubbles and complete bubble layers evolved under the anode in an electrolysis cell:

- To understand the role of large bubbles in the electrolysis cell and their effect on the process of aluminium electrolysis and most importantly on the resistance of the cell and on the bubble driven flow
- To characterize the movement of a single large bubble:
  - to observe and analyse the evolution of the shape of large bubbles,
  - to analyse their terminal velocity,
  - to study the correlation between their terminal velocity, volume and shape,
  - to determine their drag coefficient.
- To develop a mathematical model to calculate the movement of the arbitrary shaped large bubbles
- To optimize the mathematical model in order to be able to simulate a large number of arbitrary shaped bubbles

- To use the mathematical model to analyse the effect of single factors (such as density, viscosity, bubble size, angle of inclination, surface tension and velocity) on bubble shape and movement.

The work carried out and presented in this thesis gives detailed information about the bubbles and their roles in the cell. Detailed knowledge about the bubbles, the bubble layer and the bubble induced flow in the cell could lead to a better cell and anode design when combined with existing knowledge about magnetic force induced flow, temperature gradient driven flow, the electrolysis process, cell controlling methods and cell geometry.

## 2.5 References

- Aaberg, R.J., Ranum, V., Williamson, K. and Welch, B.J., in R. Huglen (ed.), *The gas under anodes in aluminium smelting cells. II. Gas volume and bubble layer characteristics*, TMS Light Metals, pp. 341-346 (1997)
- Aybers, N. M., and Tapucu, A., *The motion of gas bubbles rising through stagnant liquid*, Wärme- Stoffübertrag., vol. 2, pp. 118-128 (1969a)
- Aybers, N. M., and Tapucu, A., *Studies on the drag and shape of gas bubbles rising through a stagnant liquid*, Wärme- Stoffübertrag., vol. 2, pp. 171-177 (1969b)
- Begunov A. I. and Gromov, B. S., *Fluid dynamic effects of gas circulation in aluminium cells*, TMS Light Metals, pp. 295-304 (1994)
- Bhaga, D., and Weber, M. E., *Bubbles in viscous liquids: shapes, wakes and velocities*, J. Fluid Mech., vol. 105, pp. 61-85 (1981)
- Bilek, M. M., Zhang W.D. and Stevens, F. J., *Modeling of electrolyte flow and its related transport processes in aluminium reduction cells*, TMS Light Metals, pp. 323-331 (1994)

- Bond, W.N. and Newton, D.A., *Bubbles, drops and Stokes' law*, Philos. Mag., vol. 5, pp 794-800 (1928)
- Bozzano, G., and Dente, M., *Shape and terminal velocity of single bubble motion: a novel approach*, Computers and Chemical Engineering, vol. 25, pp. 571-576 (2001)
- Calandra, A.J, Castellano, C.E and Ferro, C.M., *The electrochemical behaviour of different graphite/cryolite alumina melt interfaces under potentiodynamic perturbations*, Electrochim. Acta, vol. 24, pp. 425-437 (1979)
- Cassayre, L., Utigard, T.A. and Bouvet, S., *Visualizing gas evolution on graphite and oxygen-evolving anodes*, JOM, vol. 54, pp. 41-45 (2002)
- Chen, J. J. J., Jianchao, Z., Kangxing, Q., Welch, B. J., and Taylor, M. P., *Rise velocity of air bubbles under a slightly inclined planed submerged in water*, The Fifth Asian Congress of Fluid Mechanics, pp. 1173-1176 (1992)
- Chen, J. J. J., Xianchun Shen, Taylor, M. P. and Welch, B.J., *A study of bath velocity distribution in a 3-D water model*, TMS Light Metals, pp. 343-350 (1996)
- Chesonis, D.C. and LaCamera, A.F., *The influence of gas-driven circulation on alumina distribution and interface motion in a Hall-Héroult cell*, TMS Light Metals, pp. 211-220 (1990)
- Choi, H.M., Kurihara, T., Monji, H. and Matsui, G., *Measurement of particle/bubble motion and turbulence around it by hybrid PIV*, Flow Measurement and Instrumentation, vol. 12, pp. 421-428 (2002)
- Clift, R., Grace, J. R., and Weber, M. E., *Bubbles, drops and particles*, Dover Publications, New York, 381 pages (1978)
- Collins, R., *A second approximation for the velocity of a large gas bubble rising in an infinite fluid*, J. Fluid Mech., vol. 25, pp. 469-480 (1966)
- Darton, R. C., and Harrison, D., *The rise of single gas bubbles in liquid fluidized beds*, Trans. Inst. Chem. Eng., vol. 52, pp. 301-306 (1974)
- Davies, R. M., and Taylor, G. I., *The mechanics of large bubbles rising through extended liquids and through liquids in tubes*, Proc. R. Soc. London Ser. A, vol. 200, pp. 375-390 (1950)
- Dernedde, E., *Gas induced circulation in prebaked and Soderberg cells*, TMS Light Metals, pp. 10-23 (1976)
- Dumitrescu, D.T., *Stromung an einer Luftblase im senkrechten Rohr*, Z. Andew. Math. Mech., vol. 23, pp. 139-149 (1943)

- Fortin, S., Gerhardt, M., and Gesing, A.J., *Physical modelling of bubble behavior and gas release from aluminium reduction cell anodes*, TMS Light Metals, pp 721-741 (1984)
- Funada, T., Joseph, D. D., Maehara, T. and Yamashita, S., *Ellipsoidal model of the rise of a Taylor bubble in a round tube*, International Journal of Multiphase Flow, vol. 31, pp. 473-491 (2005)
- Gaudin, A.M., *Flotation*, 2<sup>nd</sup> ed., McGraw-Hill, New York (1957)
- Grace, J. R., Wairegi, T., and Nguyen, T. H., *Shapes and velocities of single drops and bubbles moving freely through immiscible liquids*, Trans. Inst. Chem. Eng., vol. 54, pp. 167-173 (1976)
- Grjotheim, K., et al, *Aluminium electrolysis: Fundamentals of the Hall-Héroult process*, 2<sup>nd</sup> edition, p. 146 (1993)
- Haarberg, T., Solheim, A. and Johansen, S. T., *Effect of anodic gas release on current efficiency in Hall-Héroult cells*, TMS Light Metals, pp. 475-481 (1998)
- Haas, U., Schmidt-Traub, H., and Brauer, H., *Umströmung kugelförmiger Blasen mit innerer Zirkulation*, Chem. Ing. Tech., vol. 44, pp. 1060-1068 (1972)
- Hadamard, J. S., *Mouvement permanent lent d'une sphère liquide et visqueuse dans un liquide visqueux*, C. R. Acad. Sci., vol. 152, pp. 1735-1738 (1911)
- Haupin, W. and McGrew, W.C., *See-through Hall-Héroult Cell*, Aluminium, vol. 51, pp. 273-275 (1975)
- Haupin, W., *Scanning reference electrode for voltage contours in aluminum smelting cells*, J. Metal, vol. 23, pp. 46-49 (1971)
- Hyde, T.M. and Welch, B. J., *The gas under anodes in aluminium smelting cells. Part I: Measuring and modeling bubble resistance under horizontally oriented electrodes*, TMS Light Metals, pp. 333-340 (1997)
- Joseph, D. D., *Rise velocity of a spherical cap bubble*, J. Fluid. Mech., vol. 488, pp. 213-223 (2003)
- Kiss, L.I., Poncsák, S., Toulouse, D., Perron, A., Liedtke, A. and Mackowiak, V., *Detachment of bubbles from their nucleation sites*, TMS Light Metals, Multiphase Phenomena and CFD Modeling and Simulation in Materials Processes, pp. 159-167 (2004)
- Kloucek, P. and Romerio, M.V., *The detachment of bubbles under a porous rigid surface during aluminium electrolysis*, Mathematical Models and Methods in Electrolysis, vol. 12, no. 11, pp. 1617-1652 (2002)

- Levich, V. G., *Physicochemical Hydrodynamics*, Prentice-Hall, New York (1962)
- Maneri, C. C., and Zuber, N., *An experimental study of plane bubbles rising at inclination*, Int. J. Multiphase Flow, vol. 1, pp. 623-645 (1974)
- Masliyah, J., Jauhari, R., and Gray, M., *Drag coefficient for air bubbles rising along an inclined surface*, Chemical Engineering Science, vol. 49, pp. 1905-1911 (1994)
- Maxworthy, T., *Bubble rise under an inclined plate*, J. Fluid Mech., vol. 229, pp. 659-674 (1991)
- Moore, D. W., *The boundary layer on a spherical gas bubble*, J. Fluid Mech., vol. 16, pp. 161-176 (1963)
- Perron, A., Kiss, L. I. and Poncsák, S., *Regimes of the movement of bubbles under the anode in an aluminium electrolysis cell*, Light Metals 2005, pp. 565-570 (2005)
- Perron, A., Kiss, L. I. and Poncsák, S., *An experimental investigation of the motion of single bubbles under a slightly inclined surface*, Int. J. Multiphase Flow, vol. 32, pp. 606-622 (2006a)
- Perron, A., Kiss, L. I. and Poncsák, S., *Motion of single bubbles moving under a slightly inclined surface through stationary liquids*, Int. J. Multiphase Flow, vol. 32, pp. 1311-1325 (2006b)
- Perron, A. and Kiss, L. I., *Rise velocity of single bubbles moving under a slightly inclined surface in various liquids*, personal communication, UQAC (2006c)
- Perron, A., Kiss, L. I. And Poncsák, S., *The influence of bubble shape and the thickness of the wetting film on the incremental electrical resistance caused by the presence of a single bubble in Hall-Héroult cells*, J. Appl. Electrochemistry, vol. 36, pp. 1381-1389 (2006d)
- Poncsák, S., Kiss, L., Toulouse, D., Perron, A. and Perron, S., *Size distribution of the bubbles in the Hall-Héroult cells*, TMS Light Metals, pp. 457-462 (2006)
- Pruppacher, H. R., and Klett, J. D., *Microphysics of clouds and precipitation*, Boston, D. Reidel, 714 pages (1978)
- Purdie, J. M., Bilek, M., Taylor, M. P., Zhang, W.D., Welch, B. J. and Chen, J. J. J., *Impact of anode gas evolution on electrolyte flow and mixing in aluminium electrowinning cells*, TMS Light Metals, pp. 355-360 (1993)
- Richards, N.E., *The dynamics of components of the anodic overvoltage in the alumina reduction cell*, TMS Light Metals, pp. 521-528 (1998)

- Rivkind, V. Y., and Ryskin, G. M., *Flow structure in motion of a spherical drop in fluid medium at intermediate Reynolds number*, Fluid Dyn. (U.S.S.R.), vol. 11, pp. 5-12 (1976)
- Robl, R.F., *Molten aluminium circulation in Hall-Héroult cells*, TMS Light Metals, pp. 179-191 (1975)
- Ryzbzyński, W., *Über die fortschreitende bewegung einer flüssigen Kugel in einem zähen Medium*, Bull. Int. Acad. Sci. Cracovie A, pp. 40-46 (1911)
- Solheim, A., Johansen, S., Rolseth, S. and Thonstad, J., *Gas driven flow in Hall-Héroult cells*, TMS Light Metal, pp. 245-252 (1989)
- Taylor, T. D., and Acrivos, A., *On the deformation and drag of a falling viscous drop at low Reynolds number*, J. Fluid Mech., vol. 18., pp. 466-476 (1964)
- Thonstad, J., Fellner, P., Haarberg, G.M., Hives, J., Kvande, H. and Sterten, A., *Aluminium Electrolysis*, 3<sup>rd</sup> edition (2001)
- Tomiyama, A., Celata, G. P., Hosokawa, S., and Yoshida S., *Terminal velocity of single bubbles in surface tension dominant regime*, International Journal of Multiphase Flow, vol. 28, pp. 1497-1519 (2002)
- Utigard, T.A., Costa, H. and Popelar, P., *Visualization of the Hall-Héroult process*, TMS Light Metals, pp. 233-240 (1994)
- Vogt, H., *Contribution to the interpretation of the anode effect*, Electrochimica Acta, vol 42, pp. 2695 (1997)
- Wairegi, T., and Grace, J. R., *The behaviour of large drops in immiscible liquids*, Int. J. Multiphase Flow, vol. 3, pp. 67-77 (1976)
- Wallis, G. B., *One-dimensional two-phase flow*, McGraw-Hill, New York (1969)
- White, E. T., and Beardmore, R. H., *The velocity of rise of single cylindrical air bubbles through liquids contained in vertical tubes*, Chem. Eng. Sci., vol. 17, pp. 351-361 (1962)
- Xue, J. and Øye, H., *Bubble behavior – cell voltage oscillation during aluminium electrolysis and the effects of sound and ultrasound*, TMS Light Metals, pp. 265-271 (1995)
- Zhang, W.D., *Modelling of anode gas evacuation and current efficiency in Hall-Héroult cells*, PhD thesis, Dept. Of Chemical and Materials Eng., University of Auckland (1993)

Zorić, J. and Solheim, A., *On gas bubbles in industrial aluminium cells with prebaked anodes and their influence on the current distribution*, Journal of Applied Electrochemistry, vol. 30, pp. 787-794 (2000)

Zukoski, E. E., *Influence of viscosity, surface tension, and inclination angle on motion of long bubbles in closed tubes*, J. Fluid Mech., vol. 25 part 4, pp. 821-837 (1966)



## Chapter 3

# METHODOLOGY

### 3.1 Introduction

In order to obtain information about a new phenomenon, observations and experiments have to be performed. The most evident idea is to observe the real phenomenon and make measurements in the original environment. Unfortunately, in the domain of aluminium electrolysis direct observation is almost impossible due to the non-transparent cell and the hostile environment in the cell. In spite of the difficulties, a few measurements were made in large bench scaled cells (*Aaberg et al, 1997; Gao et al, 2005*) using indirect methods. *Aaberg et al (1997)* measured the fluctuation of the bath level in order to measure the volume flow rate of nucleated bubbles. The flow field of the electrolyte bath was measured using an iron rod which was corroded in the cell (*Grjotheim, 1993*). Both methods were highly limited and gave only limited information. Moreover, the rod method disturbed the flow field, thus reduced the precision of the results. To understand bubble nucleation, anode and cathode wetting and to measure the wetting angle in the cell, small and transparent models were built, using real electrolytes and carbon anodes (*Cassayre et al,*

2002; Haupin, 1975; Xue et al, 1995; Zhuxian et al 1987). These models provided important information about the process, but they were small: the real bubble layer and flow field could not be modeled using them. Moreover, due to the nature of the electrolyte, the transparency of the cell was lost in a short time; it became opaque in about 5-10 minutes. Thus the experiments were limited to short time observations. Other measurement techniques were also used, such as radiography (Cassayre et al, 2002; Utigard et al, 1988 and 1994) and microscope (Utigard et al, 1994).

Due to the problems arising when performing experiments in real cells and in small models, it is common to use real size air-water models to obtain information about the mass transfer phenomena taking place during the aluminium electrolysis (Utigard et al, 1994; Darnedde et al, 1975; Fortin et al 1984; Zoriç et al, 2000).

The other way to obtain information is using numerical models. Nowadays large computer resources are available and numerous mathematical models and commercial CFD codes exist. The advantage of numerical modeling is that the parameters of the process can be chosen and changed individually and arbitrarily and simulations can be repeated *ad infinitum*. The disadvantage is that a complex simulation demands a lot of computer resources, time and well-written, stable codes.

Information obtained during physical experiments cannot be interpreted without mathematical models nor can the mathematical models be verified and validated without physical experiments. Hence, to accomplish the objectives of this thesis, real-sized air-water models and commercial numerical code were used. The physical models, measuring techniques and image analysis used and partly developed by the author are reviewed in the

following chapter while the idea of numerical modeling and the available numerical methods are presented in detail in section 3.3.

### 3.2 Physical modeling

As mentioned, a physical model serves the purpose of obtaining information about a phenomenon by direct observation and/or measurement. The exact aim of the experiment and the elements of the phenomenon under observation have to be decided in advance in order to design and build the proper physical model. Also, the appropriate measuring technique(s) has to be chosen wisely. We have to be able to perform the selected measurements in the model while the measuring device should disturb the parameter(s) to be measured as little as possible. Since this thesis studies bubbles and their effect on the electrolysis process, an easy and economic physical model was to be selected. For simulating a bubbly flow, liquid and gaseous phases have to be used. It is important that these materials should be cheap, easily available and non-toxic. The physical model of the real phenomenon has to be geometrically and dynamically similar to the real one (*Fortin et al, 1984*). The first can be achieved with a real-size model, while the second necessitates the use of materials with similar kinetic viscosity and kinetic surface tension in the real phenomenon.

### 3.2.1 Objectives of physical modeling

According to the objectives of this thesis a real-size physical model was built and used in order to obtain information about the formation of the large bubbles moving under a slightly inclined surface. Several parameters of the bubbles were investigated, such as dimension, shape, the Fortin head and its evolution, bubble velocity and the effect of bubble volume and angle of inclination on these parameters. The relation between the contact shape and the shape in the vertical plane was also investigated. Later, the formation of the bubble layer under a slightly inclined surface was observed. The formation of the bubble layer, the volume distribution and velocity of the bubbles in the layer, the height of the bubble layer and the covering factor of the bubbles were measured as a function of the bubble nucleation rate and the inclination angle of the surface. As the bubble layer is a direct model of the bubble layer forming under the anode in an electrolysis cell, the bubble induced flow under the anode was measured and the effect of the large Fortin bubbles on the flow were investigated.

### 3.2.2 Air-water model

Measurements using real-size air-water models of the aluminium electrolysis cell are widely accepted in this domain (i.e. *Fortin et al, 1984; Solheim et al, 1989*). Using air and water have several advantages, such as easy availability, cheapness, lack of toxicity and not lastly transparency that helps the visualization. Several previous experiments have shown

that the air-water model is a good and adequate alternative to obtaining information about the two-phase flow in the bath (*Solheim et al, 1989; Cooksey et al, 2006*). Numerical simulations show that even though the parameters of the liquid and gas phases affect the shape and movement of bubbles, the same bubble shapes are observed in water as in molten cryolite. However, the movement and formation of the carbon-dioxide bubbles in the molten cryolite are slower than the movement and formation of the air bubbles in water. This is well explained by the high dynamic viscosity and density of the cryolite. As expected, surface tension has no effect on the shape of a large bubble. Moreover it was shown that the shape of a bubble depends on the Morton number of the liquid (*Perron et al, 2006*). The Morton number of water is  $2.59 \cdot 10^{-11}$  and  $2.15 \cdot 10^{-11}$  for molten cryolite. These values are very close, thus similar a bubble shape is expected in both the real electrolysis cell and the air-water model.

Furthermore, several measuring techniques exist for air and water, where the measured parameters can be the velocity field, the bubble size, temperature or other more sophisticated parameters.

Two experimental set-ups were designed and built respecting study objectives and the criteria mentioned above. A real-size model of an electrolysis cell with two anodes installed was made earlier and was used by others too. This model was used to perform experiments on the bubble layer formed under a slightly inclined anode. Additional to the first set-up a new one was designed and built to investigate single large bubbles moving under a slightly inclined surface.

Real-size model of an electrolysis cell

A real-size, transparent Plexiglas® air-water model of a cell was used to observe the bubble layer formed under an anode. The tank, which represents the cell, was 2.4 m long, 0.5 m wide and 0.6 m high. Two anode models were installed and immersed, even though only one of them was filmed during the experiments. The flow field and the bubble layer under the anodes were assumed to be similar. The anodes were slightly inclined in the tank. Each anode was 1.0 m long and 0.5 m wide. The inclination of the anodes could be changed between  $0^\circ$  and  $10^\circ$ . Only the configuration shown in figure 3.1 can be used, where the inner edges of the two anodes are next to each other in the centre channel, while the outer ones are at the end of the tank at the side channel. Since the bubbles are driven by buoyancy, they leave the anode at its outer edge, in the side channels and only rarely in the central channel. The distance of the inner edge of the anode bottom from the bottom of the tank is 4 cm while the immersion of the anodes can be changed gradually by filling the tank with water. During the experiments the water was 20 cm high in the tank, immersing the anodes to around 15 cm.

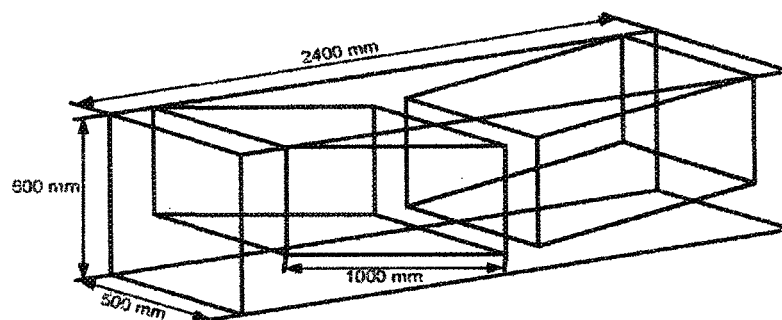


Figure 3.1 – Dimensions of the real-size model

The anode models are made of a porous bronze surface. High pressure air is pressed through the plates to generate the bubbles under the anode. This bubble nucleation is slightly different from the nucleation taking place in a real cell, but it has been shown that the main mechanism of the bubble growth in the real cell is coalescence and that small bubbles do not affect the motion of the large ones (*Ngoya et al, 1985*). Thus bubble nucleation has no significant effect on the bubble layer and bubble movement.

The volume flow rate of air can be controlled gradually between 8 and 150 litre/minute (lpm). The rate of bubble nucleation in a real electrolysis cell can be simulated by choosing the appropriate flow rate. The rate of nucleation in a Hall-Héroult cell depends on the current density and can be calculated from the chemical reaction balance in the cell as follows:

$$air_{inlet} [lpm] = \frac{i \cdot A \cdot R_{gas} \cdot T}{p \cdot z \cdot F}, \quad (3.1)$$

where  $i$  is the current density,  $A$  is the area of the surface for nucleating the bubbles,  $R_{gas}$  is the gas constant,  $T$  is the temperature,  $p$  is the pressure,  $z$  is the number of the charged electrons involved in the chemical reaction and  $F$  is the Faraday constant.

The volume flow rates of air used during the experiments and the corresponding current density can be seen in table 3.1.

Even though the available maximal volume flow rate is 150 lpm, the measurements were intentionally limited to 105 lpm. For the reason that at high volume flow rates large

numbers of bubbles are nucleated under the anode. While leaving the anode, the bubbles create significant frequencies that can seriously damage the set-up.

Volume flow rate of air [lpm]	Mass flow of air [kg/s]	Current density of the real cell [A/cm <sup>2</sup> ]
6	0.00012	0.0572
18	0.00036	0.1717
24.75	0.000495	0.2360
51	0.00102	0.4864
75	0.0015	0.7152
105	0.0021	1.0013

Table 3.1 – Volume flow rates used in the experiments

Gas is injected under the anode by pressing air through the porous plate. This simulates gas nucleation, whose rate depends on the current density of the cell. The nucleated gas moves under the anode where its movement can be characterized by the superficial velocity [ $\text{m}^3/\text{s m}^2$ ], which depends on the rate of nucleation. According to the naming convention in this domain, the “volume flow rate of air” terminology can be replaced with any of the above mentioned ones. Keeping in mind that this work is in the aluminium electrolysis field, therefore the term “gas generation rate” is used in this thesis.

Tap water and pressurized air were used as the liquid and gas phases in the experiments. Their exact composition and specific parameters, such as temperature, density, viscosity and interfacial tension, were not measured. The water was cold water at approximately 7 °C. Its density at that temperature is  $999.856 \text{ kg/m}^3$ , its dynamic viscosity is  $1.43436\text{e-}3$



kg/m·s and its surface tension is  $7.28 \times 10^{-2}$  N/m. The air was assumed to be at room temperature (21 °C).

The different parameters of the experiments can be seen in table 3.2.

Angle of inclination [°]	1 2 4
Length of the tank [cm]	240
Width of the tank [cm]	50
Depth of the tank [cm]	60
Anode size [cm]	100 x 50
Anode cathode distance [cm]	~4.5
Immersion of the anodes [cm]	~15
Lateral channel [cm]	10 x 50
Centre channel [cm]	16 x 50

Table 3.2 – Parameters of the experiments in the real-size set-up

#### Set-up for observing single large bubbles

The simple set-up designed and built to observe single large bubbles moving under a solid surface is built from Plexiglas®. The tank is 1.5 m long, 0.5 m wide and 0.6 m high. A large, 1.5 m long, 0.5 m wide and 1 cm thick inclined Plexiglas® plate is installed in the tank. The inclination of the plate can be changed gradually between 0° and 8°. The setup can be seen on figure 3.2.

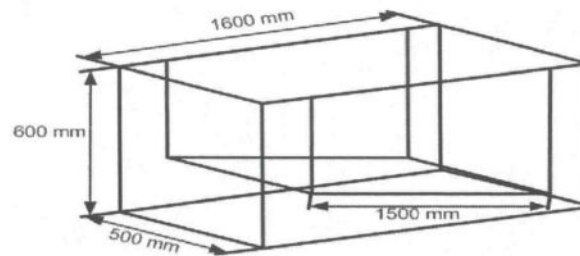


Figure 3.2 – Dimensions of the setup for single bubbles

The bubbles are nucleated by injecting air through a pipe into a half-cut pipe which is fixed at the deepest part of the surface (figure 3.3). This technique is similar to the inverted cup technique. The half pipe is kept downward while the air is injected into it. When the pipe is full of air an arm is turned which turns the pipe. The bubble is released and starts to glide under the surface. The half pipe is turned around its center to cause least possible disturbance in the water. In order to model different bubble sizes, different sized half pipes were created and installed in the set-up.



Figure 3.3 – Device used to inject the bubble under the surface

Once again tap water and pressurized air were used as the liquid and gas phases in the experiments without measuring their specific parameters.

The different parameters used during the experiments can be seen in table 3.3.

Angle of inclination [°]	1 2 4 8
Volume of bubble [ml]	50 150 250
Distance between the surface and the bottom [cm]	11 ÷ 30
Length of the tank [cm]	180
Width of the tank [cm]	50
Depth of the tank [cm]	60
Surface size [cm]	160 x 50

Table 3.3 - Parameters of the experiments in the single bubble set-up

### 3.2.3 Measurement techniques

Since the objectives of the physical experiments are mainly the observation of the formation and movement of large bubbles and bubble layers, digital image recording techniques were used to record the phenomenon and later the recorded videos were analyzed to obtain different parameters. All the desired information about the bubbles can be obtained from the digital images with the exception of the bubble induced flow under

the anode. To measure the velocity field in the cell model, Particle Image Velocimetry (PIV) techniques was used. The different measurement techniques used during the experiments are explained in the following sections.

### **3.2.3.1 Digital image recording**

As much as the air and water model is advantageous for direct observation, the digital image processing the system is not straight forward. The human eye can easily distinguish between the bubbles and the water in the images, even though air, water and Plexiglas® are all transparent. The goal was to record videos that could be analyzed using numerical codes instead of manual techniques. To differentiate between the two phases, the bubbles have to be darker or lighter than the surrounding water. This effect was achieved by special illumination of the set up. Several high-performance lamps were used placed at different locations around the model. Two examples from the recorded videos in figure 3.4 show clearly that the bubbles are a different shade from the water. The image on the left was made from the side of the anode, while the one on the right shows the bubbles at the bottom of the anode.

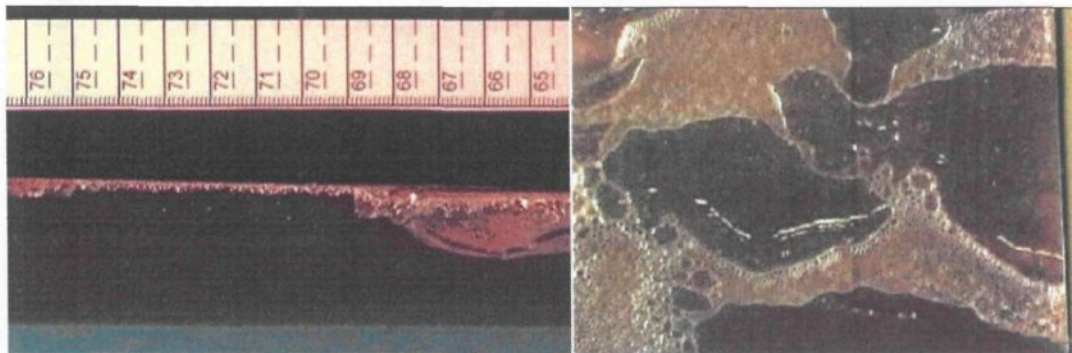


Figure 3.4 –Showing colour difference between air and water in the recorded videos

Two different digital cameras were used to record the videos, a Canon GL2 and a Sony digital camera. The parameters of the cameras can be adjusted manually and the following parameters were used during the experiments (table 3.4).

<b>Real-size model, video recorded from the side and from the bottom (Canon GL2)</b>	
Shutter speed	1/600 sec
Aperture (iris diameter)	f/3.7
Gain	6dB
Misc.	Manual focus
<b>Single bubble set-up</b>	
Shutter speed	1/2300 sec
Aperture (iris diameter)	2.2
Gain	12
Misc.	Manual focus

Table 3.4 – Parameters of the camera

The Canon camera was directly connected to a computer and the recordings were captured directly onto it using VirtualDub® open-sourced software. The videos recorded with the Sony camera were recorded to a HD cassette and later was transferred onto a computer. The videos are kept in uncompressed AVI format. Their frame size is 720x480

pixels and their recording frequency is 29.97 fps. The recordings were decomposed into single images before image analysis. These images were later analyzed as explained in section 3.2.4.

Different recordings were made of the set-ups. In the real size model videos were first made perpendicular to the direction of bubble movement in order to view the contour of the bubble layer in the vertical plan, perpendicular to the camera (figure 3.5).

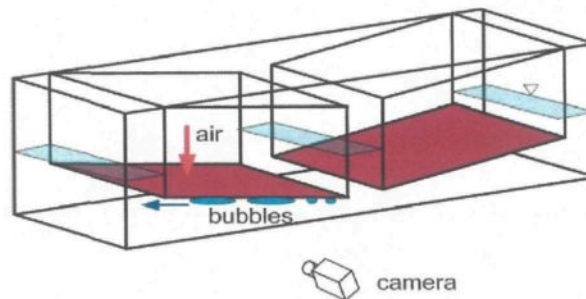


Figure 3.5 – Recording the bubbles from the side

Later videos were also made of the bottom of the anode as seen in a mirror placed slightly inclined under the tank (figure 3.6). This way the contact shape of the bubbles can be seen in the recordings. In both cases the width of the field of view was restricted to no more than 20-25 centimetres to obtain the appropriate resolution. Several recordings were made along the anode and later joined together to visualize the whole bubble layer under the anode. A video was also made of the complete side and bottom of the anode, even though the resolution of these videos is not necessarily adequate for analysis.



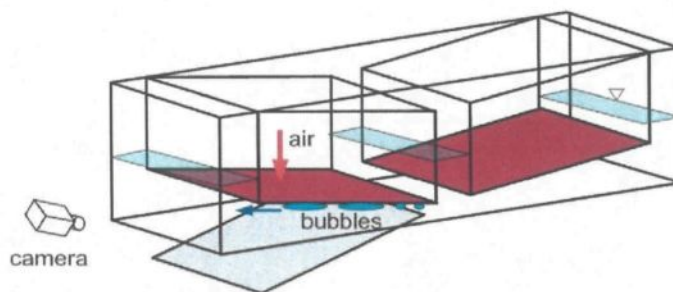


Figure 3.6 – Recording the bubbles from the bottom

Similar videos were made in the single bubble set-up, one perpendicular to the direction of bubble movement in order to view the contour of the bubble and one in a mirror placed inclined under the tank in order to view the contact shape of the moving bubble. The two videos were made simultaneously, thus recordings the shape of the bubble in three dimensions. Two digital cameras were placed onto a rail parallel to the longer side of the set-up, where they could glide following the moving bubble (figure 3.7). The width of the field of view was again restricted to no more than 20 centimetres to obtain the appropriate resolution.

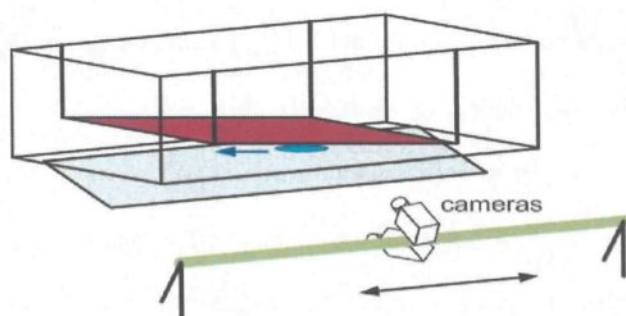


Figure 3.7 – Recording the bubbles in the single bubble setup with the movable cameras

### 3.2.3.2 High speed camera

In addition to the two digital cameras, a high speed camera was also used. While a simple camera records 30 images per second, a high speed camera – as its name suggests - can record up to 1000 images per second. A high speed camera is usually used for velocity measurements, but can be used for simple image recording too. The length of a video depends on the chosen recording frequency. Our high speed camera registers the video directly into its memory, thus the number of images and consequently the length of the video depends on the size of the memory. The memory of our camera is 1024 Mb. An image with a resolution of  $1280 \times 1024$  pixels and 8 bit color depth is 1289 Mb. With the chosen 1000 fps recording frequency maximum 815 images can be recorded onto the memory of the camera and thus the length of the video is limited to 0.814 second. Choosing a lower resolution or recording frequency gives longer videos but with a loss of information.

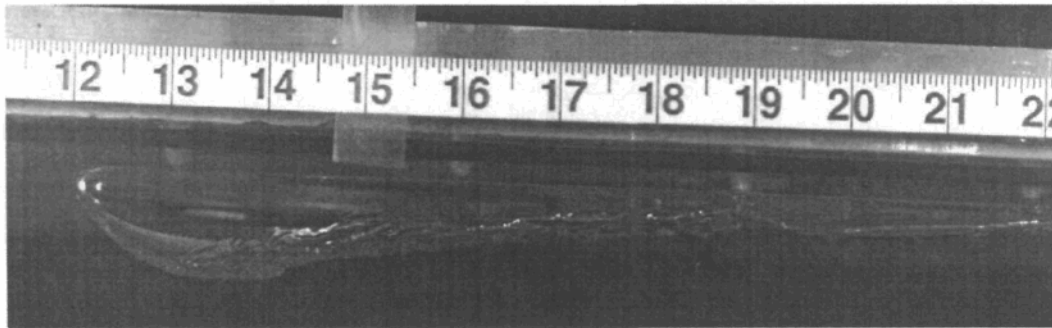


Figure 3.8 – Example from the video made with the high speed camera



The high speed camera was used to make short videos in the single bubble set-up to observe the evolution of the Fortin head and the exact form of a large bubble. An example can be seen on image 3.

### **3.2.3.3 Particle Image Velocimetry**

The Particle Image Velocimetry is an optical method used to measure flow velocities and other properties of a moving fluid. The fluid is seeded with particles which are assumed to follow the motion of the fluid well. The fluid is illuminated by a laser sheet. The particles are chosen to scatter the light in the wavelength of the laser. Only the seeding particles are seen in the digital recordings of the fluid motion. The videos are then analyzed; at least two frames are needed to calculate the velocity field of the fluid. The frames are split into interrogation areas and using the techniques of signal processing (i.e. auto or cross correlation) the displacement vectors are determined in each area. If the particles are well chosen and follow faithfully the motion of the fluid, the determined vectors using the time between the two frames give the velocity of the fluid. With advanced techniques related properties of the fluid can also be measured and determined.

A PIV system was used to qualitatively measure the velocity field of the water induced by the bubble layer. A high speed camera was put perpendicular to the direction of the movement of the bubbles, while a vertical laser sheet was directed toward the middle of the shorter side of the model (figure 3.9).

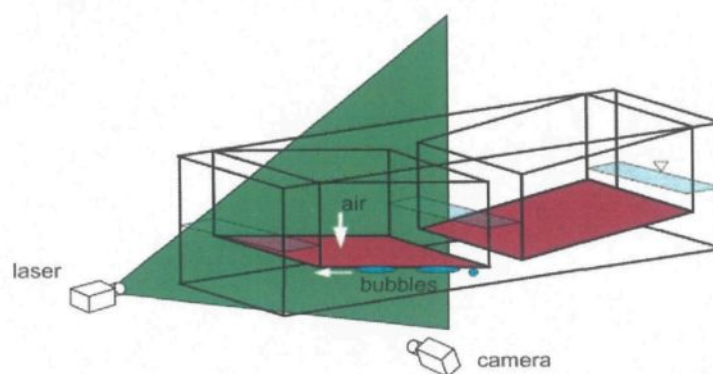


Figure 3.9 – PIV measurement in the real-size model

Our PIV system comprises a time resolved Nd: YAG laser, a high speed camera and a computer. Recordings were made directly onto the computer where they were later analyzed. The width of the field of view was again restricted to no more than 20 centimetres. The separated recordings were later joined together to visualize the entire fluid flow under the anode. Considering that an anode is one meter long, six separate videos were made with enough overlap for matching.

For a PIV measurement the right seeding particle has to be chosen. The particles must reflect enough light from the laser to be seen in the recordings, and must follow the motion of the fluid reliably. Small particles with a density similar to that of the fluid are known to follow the motion of the fluid exactly. Unfortunately they do not reflect too much light, thus it can be difficult to record their motion or to identify them in the video. On the other hand, larger particles reflect enough light, but they may not follow the fluid reliably. If particle weight is too high, the particle will follow only the time-average motion of the fluid, but not the high frequency turbulences. To choose the appropriate particle the

following properties have to be considered: the density of the fluid and the particle, the dynamic viscosity of the fluid and the mean particle size. If the density ratio of particles to fluid is small, the particles are expected to follow the motion of the fluid well, even at a greater particle size. On the other hand, at a high density ratio even the small particles may not follow the small turbulences. According to *Melling (1997)*, the maximal turbulence frequency the seeding particles are able to follow in high density ratio turbulent flows can be calculated as follows:

$$\frac{\overline{u_{particles}^2}}{\overline{u_{fluid}^2}} = \left(1 + \frac{f_c}{C}\right)^{-1}, \quad (3.2)$$

where  $f_c$  is the maximal turbulence frequency,  $\overline{u_{particles}^2}, \overline{u_{fluid}^2}$  are the time average velocities of the fluid and the particles and  $C$  can be calculated as follow:

$$C = \frac{18\mu}{\rho_p \cdot d_p^2}, \quad (3.3)$$

where  $\mu$  is the dynamic viscosity of the fluid,  $\rho_p$  is the density of the seeding particles,  $d_p$  is the particle size.

If our criteria for acceptable flow tracking is the relative fluctuation intensities of the particle and fluid motions to limit  $\overline{u_{particles}^2} / \overline{u_{fluid}^2} = 0.99$ , then we get (3.4).

$$\left(1 + \frac{f_c}{C}\right)^{-1} = 0.99 \quad (3.4)$$

Two different seeding particles were used for the experimental measurements. Alumina powder was used for the trial runs due to its low cost. The alumina particles had a large mean size, around 7-50  $\mu\text{m}$  (average size: 28.5  $\mu\text{m}$ ) and a high density (3.97  $\text{g/cm}^3$ ). This powder formed a high density ratio flow with the water (density ratio was 3.9779). Fine hollow glass spheres were used for the final measurements. This material with a smaller, 8-12  $\mu\text{m}$  mean size (average size: 10  $\mu\text{m}$ ) and density close to that of the water (1.1  $\text{g/cm}^3$ ), gave a small density ratio (1.1022). As it was expected, the first could be illuminated easily, while the second followed the motion of the fluid well.

According to equation (3.4), the maximal frequency the alumina powder can follow in the water is  $f_c=80.87$  Hz. This value is too small to visualize small turbulences in the flow. However it can give a satisfactory image of the time average flow. The maximal frequency of the hollow glass spheres is  $f_c=2366.11$  Hz  $\approx 2.3$  kHz, a fair frequency response. If we accept a lower limit to the relative intensities, 0.95, then we get a better frequency response. The maximal frequency will be  $f_c=12328.68$  Hz  $\approx 12$  kHz, which is a good frequency response.

### 3.2.4 Digital image processing

There are two ways to analyze the recorded videos; either manually, or using a computer either automatically or semi-automatically. Our digital recordings made with the digital cameras could be analyzed automatically using several home written numerical codes developed in MATLAB®. The analysis of the PIV results is much easier using the software originally developed for this purpose and supplied with the PIV system.

The key to digital image processing is to identify the bubbles in the images using either the bubble contours, or the bubble volumes. Knowing the exact position of the bubbles, several parameters can be measured or calculated from the images.

#### Coordinate systems

During the experiments several different coordinate systems were used. These coordinate systems have to be defined so that the results can be clearly understood. The first coordinate system is the real world coordinate system (black lines in figures 3.10 and 3.11). When the video was made from the side, the x coordinate of the world coordinate system is the length of the anode, which starts at 0 and ends at 100 cm, while the y coordinate is the height of the bubble expressed as a positive number. When the videos were made from the bottom, the x axis is aligned with the width of the anode, while the y is aligned with the length of it. As explained earlier, several separated videos were made and

one video shows only a small part of the anode, either from the side or from the bottom. Two examples are shown in the figures 3.10 and 3.11. The image coordinate system - shown in red - is in pixels and has the origin in the bottom-left corner of an image. When an image is read into MATLAB®, it is represented by a matrix of the same size as the image - 720 x 480 x 3 in our case. The 3rd dimension of the matrix represents the color of a pixel point in RGB code. Unfortunately MATLAB® does not use the same image coordinate system. The origin of the MATLAB® image coordinate system is at the top-left corner of the image (light green in the figures). Thus each  $y$  coordinate has to be converted from the image coordinate system into the MATLAB® image coordinate system using (3.5).

$$y_{\text{matlab image coordinate system}} = 480 - y_{\text{image coordinate system}} \quad (3.5)$$

Unless stated to the contrary, our results are given in the world coordinate system in chapters 4 to 7, while the methodology and most of the digital image analysis method is explained in the image coordinate system.

The relationship between the different coordinate systems can be seen in figures 3.10 and 3.11, where the black coordinate system [cm] with an ordinate looking down is the system of the real phenomenon, while the red colour represents the system of the image and the light green belongs to its MATLAB® interpretation. The white arrows show the direction of the bubble movement under the surface.

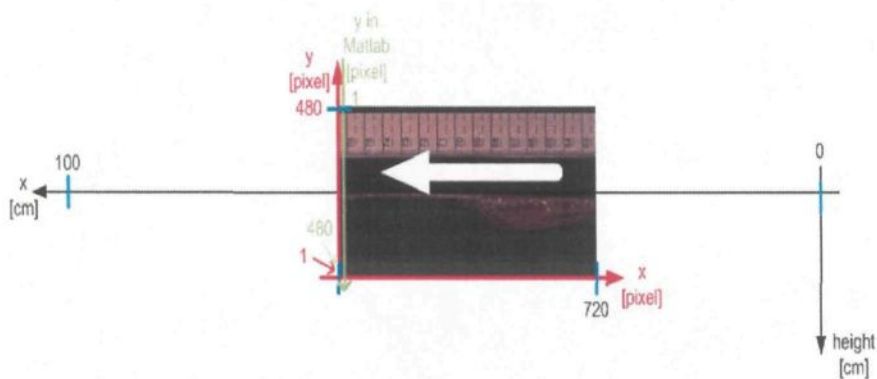


Figure 3.10 – Different coordinate systems used with the video recorded from the side

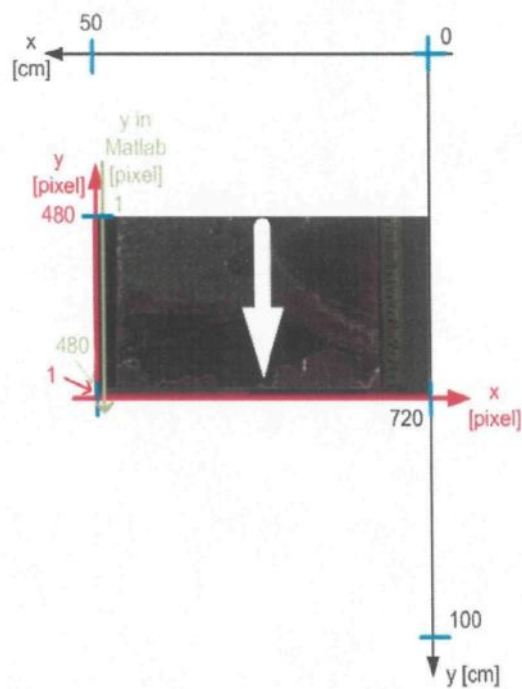


Figure 3.11 – Different coordinate systems used with the video recorded from the bottom

*Image processing of the digital videos*

As already mentioned, the digital video recordings were transferred onto a computer where their qualities were improved and they were decomposed into single pictures using the VirtualDub® software. One of the main problems with recording high speed moving objects is that a simple digital camera records two frames as one, called interlacing (figure 3.12). As a result, a frame we will show two shifted contours instead of one sharp one. In order to improve the quality of the images they have to be de-interlaced by unfolding the two contours into two frames. This way we not just improve the quality of the image but we double our information by having now two images of the moving bubble recorded at different times. The time between the two unfolded images is half the normal time between two frames. Knowing that a digital camera records 30 frames per second, the time shift between two unfolded frames is  $1/60$  ( $\approx 0.0166$ ) second.

The effect of the interlaced recording technique is that the unfolded two fields are not exactly at the same position. One of the unfolded images shows the image with one pixel shifted upward compared to the other. This shifted image has to be re-shifted. Since a digital image is represented by rows and columns of pixels, the re-shifting means that each row of pixels has to be copied one row below. This way the bottom row is lost, while the top row is arbitrary filled with black color. The lost information and despotic filling are not a problem because the first and last rows never contain useful information in these experiments. The pictures are corrected using a home written MATLAB® code.



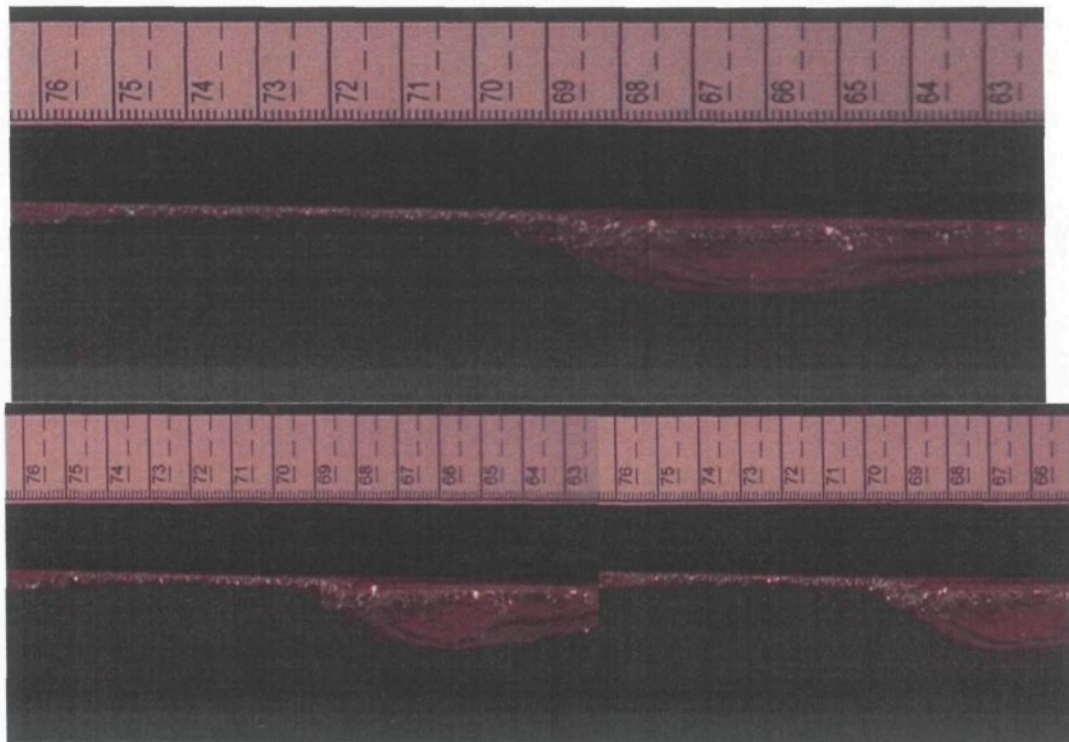


Figure 3.12 – Interlaced image (top) and the two unfolded fields (bottom)

The key to automatic image processing is the identification of the bubbles in the images. As mentioned above, the videos show a colour contrast between the bubbles and their surroundings. A so called threshold filter is then applied to the images. This filter converts a coloured image to black and white; pixels darker than the threshold become black and those lighter than the threshold become white. To obtain good results, the image contrast is increased and the images are smoothed before applying the threshold filter. The contrast is increased by performing fast linear luminance adjustments and the video is smoothed by adaptively blurring it while preserving the edges. The non-useful parts of the images, such

as the ruler, are hidden before the black and white conversion takes place. A resulting black and white image can be seen in figure 3.13.

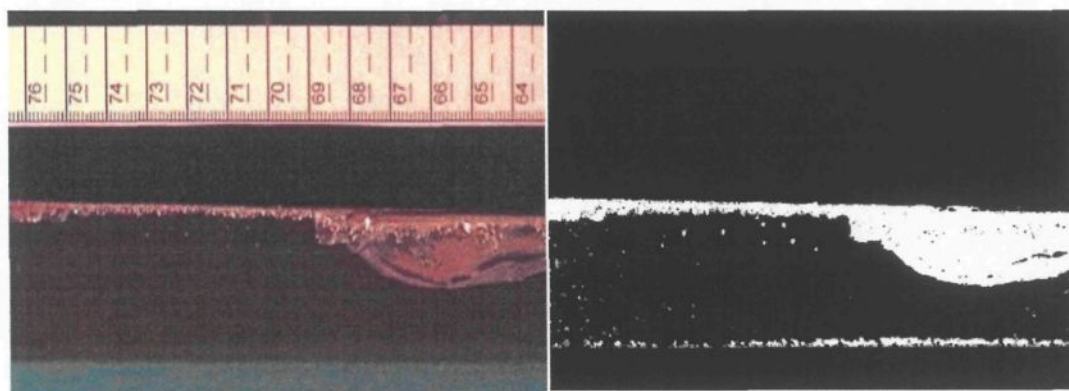


Figure 3.13 – Image before and after using the threshold filter

Following the conversion the bubble is white while everything else is black. Unfortunately the conversion is never perfect. Some small light reflections are always present in the water. These are similar in color to the bubbles, thus after the conversion they are white too. The images have to be cleaned to get rid of these imperfections. These black and white images are read into MATLAB® where they are stored in 720 x 480 matrices. Each element of a matrix represents a pixel of the image, while the value of the element varies between 0 and 255 and represents a tone of gray (figure 3.14). These matrices are then converted into true black and white images, where now an element of the matrix is either one (white) or zero (black). Now checking a matrix element tells us exactly whether the area belongs to a bubble or not.

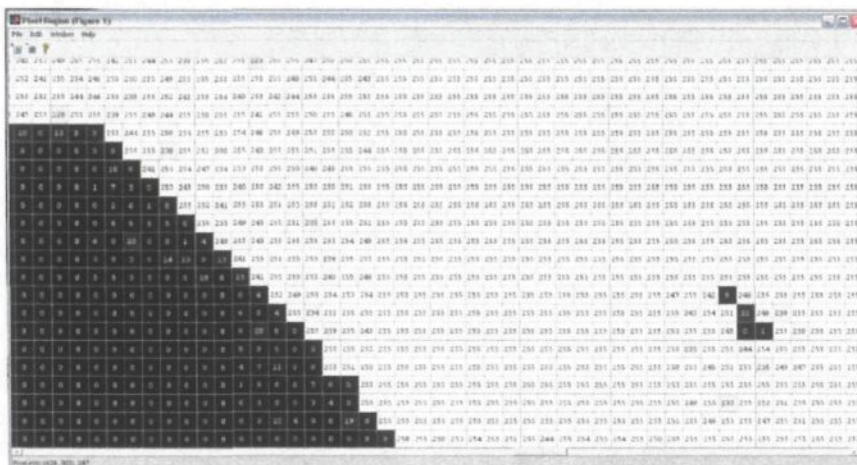


Figure 3.14 – Interpretation of a digital image in MATLAB®

Two methods have been developed to clean the pictures. The first method cleans the picture by finding the largest white area, designating it to be the bubble, and turns all other white areas into black. The second method uses a threshold white area and turns every white area which is smaller than the threshold into black. The first method is used with a continuous bubble layer or with a single bubble. The second method is used when several separated bubbles can be seen in an image and we intend to keep all the bubbles and efface only the non-bubbly white spots.

All the cleaned images are checked for quality. If a problem is found than the image is corrected by hand to make sure that the results obtained from these cleaned images are correct.



The contour of the bubbles or the bubble layer can be determined from the cleaned images. In a first loop, the vertically furthest white pixel from each pixel of the inclined surface is determined (yellow spot in figure 3.15).

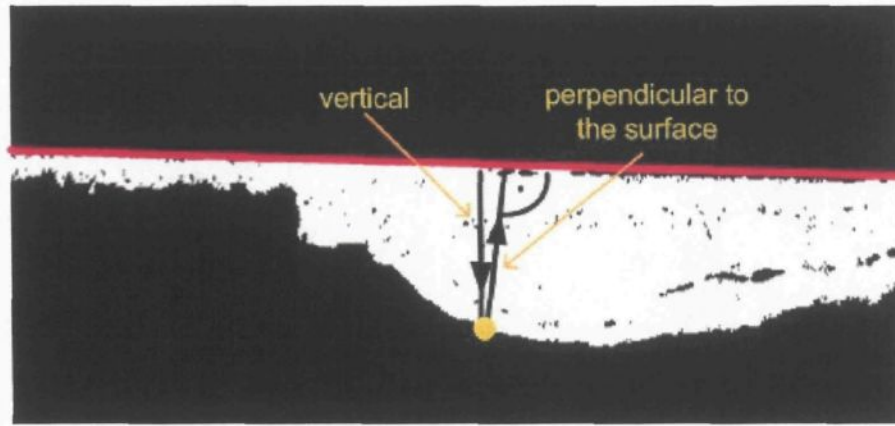


Figure 3.15 – Method to determine the contour of the bubbles

Later the perpendicular distance of these points from the surface are calculated using a simple geometrical formula (3.6).

$$d = \|\vec{r}_2 - \vec{r}_1\| \quad (3.6)$$

where  $d$  is the distance between the surface and a contour point,  $\vec{r}_1$  is the point vector of the contour point and  $\vec{r}_2$  is the point vector of the surface point from which the distance is calculated. The two point vectors are given by (3.7) and (3.8).

$$\vec{r}_2 = \vec{r}_0 + \vec{v} \cdot t_1 \quad (3.7)$$

$$t_1 = \frac{\vec{v} \cdot (\vec{r}_1 - \vec{r}_0)}{\vec{v}^2} \quad (3.8)$$

where  $\vec{r}_0$  is an arbitrary point on the surface,  $\vec{v}$  is the direction vector of the red line representing the surface. The  $\vec{r}_0$  and  $\vec{v}$  are determined from the first frame of a video and stay constant in every other frame.

Since the distance in an image is given in pixels it has to be converted into centimetres. The conversion parameters are from the rulers which can be seen in the original images.

The identified contours are smoothed out using a simple exponential smoothing filter as follows:

$$y[n] = k \cdot x[n] + (1-k) \cdot y[n-1], \quad (3.9)$$

where  $n$  is the sample number,  $k$  is the smoothing factor,  $x$  is the input sign and  $y$  is the smoothed sign. The smoothing factor was chosen empirically to be 0.1.

Having a smooth bubble contour, the maximum and average heights can be easily determined. The definition of the bubble velocity is not as evident. It is known that a bubble gliding under an inclined surface can reach a maximum velocity called the terminal velocity. For a small bubble this velocity can be measured anywhere in the bubble since the shape of the bubble does not change significantly during displacement. However, if the volume of a bubble is large enough, the bubble obtains the Fortin shape, which is changed by dynamic forces. The head is seen to form as the bubble gains volume and the length of the head changes as the bubble moves under the surface. In our experiments it cannot be determined whether these large Fortin bubbles reach their terminal velocity, nor whether the heads are fully formed before the bubbles leave the anode. Thus the velocity of the

Fortin bubble is not explicitly determined. It is defined as the velocity measured at the highest point of the bubble head. In addition, the cross-section of the bubble head was approximated with a segment of a parabola and the velocity of the intersection point of the parabola and the surface was also measured (figure 3.16).

The 2<sup>nd</sup> order parabola was chosen to approximate the head after observing numerous Fortin bubbles. In cross-section, the leading half of the Fortin head fits a 2<sup>nd</sup> order parabola almost perfectly, while the trailing half is close, but it never fits. The applied parabola is defined by a second order equation in the Cartesian plane. The equation consists of a linear element in order to allow for asymmetry.

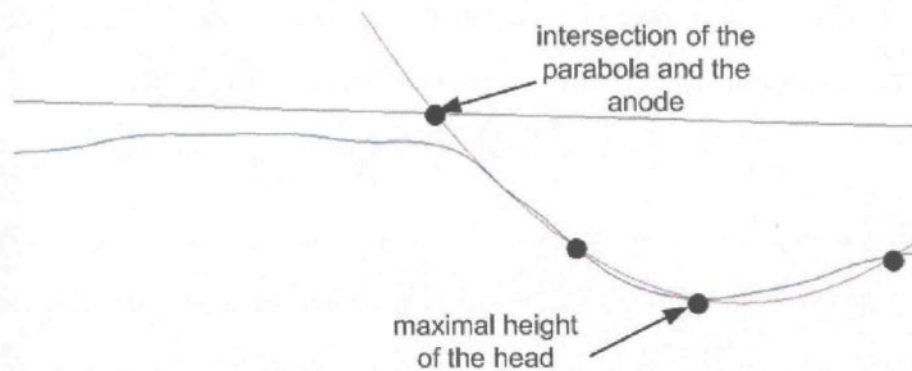


Figure 3.16 – Fortin head approximated by a 2<sup>nd</sup> order parabola

The equation of a second-order parabola in Cartesian plane is

$$y = A \cdot x^2 + B \cdot x + C \quad (3.10)$$

where  $A$ ,  $B$  and  $C$  are constants of the parabola which can be calculated as follow:

$$A = \frac{(y_3 - y_1) + (y_2 - y_1) \cdot \frac{(x_1 - x_3)}{(x_2 - x_1)}}{x_3^2 - x_1^2 - (x_1 + x_2) \cdot (x_3 - x_1)} \quad (3.11)$$

$$B = \frac{(y_2 - y_1)}{(x_2 - x_1)} - A \cdot (x_1 + x_2) \quad (3.12)$$

$$C = y_1 - A \cdot x_1^2 - B \cdot x_1 \quad (3.13)$$

where  $x_1, x_2, x_3, y_1, y_2, y_3$  are the coordinates of three arbitrary points of the parabola.

The parabola approximating the head is open up and has an axis parallel to the y axis, making the  $A$  parameter always positive. Three points of the head have to be chosen to determine the constants. The easiest to choose is the maximal point of the head. The other points are chosen at half height between the max height of the head and average height of the bubble or bubble layer: one to the left of the head and the other one to the right of the head (figure 3.16).

### PIV image processing

The velocity field was obtained from the images using an auto correlation function given by the software provided with the PIV system. Later several parameters were obtained from the velocity field using home written MATLAB<sup>®</sup> codes. The mean velocity,

the standard deviation, the turbulence kinetic energy and turbulence intensity were calculated using the following equations. The mean velocity is given by:

$$\bar{u} = \frac{1}{N} \sum_{i=1}^N u_i, \quad (3.14)$$

where  $u_i$  is either the length of the velocity or one of its components and  $N$  is the sample number.

Standard deviation, also known as the root mean square deviation of values from their arithmetic mean, was calculated as follows,

$$\sigma = \sqrt{\frac{1}{N} \sum_{i=1}^N (u_i - \bar{u})^2}, \quad (3.15)$$

where  $\bar{u}$  is the mean velocity.

The turbulence kinetic energy can be calculated from the square of the standard deviations ( $\overline{u'^2}, \overline{v'^2}$ ) as

$$k = \frac{1}{2} (\overline{u'^2} + \overline{v'^2}). \quad (3.16)$$

And finally, the turbulence intensity is given as

$$\hat{u} = \frac{\sqrt{\overline{u'^2}}}{u_\infty}, \quad (3.17)$$

where  $u_\infty$  is the free stream mean velocity.



### 3.3 Mathematical modeling

Nowadays computational fluid dynamics (CFD) is important because in a lot of processes or circumstances the development and testing of real models are very expensive or not possible. For example, the experimental measurement of bubble movement in aluminium electrolysis cells is almost impossible. In such a case well developed and reliable CFD software can take the place of real experiments. Moreover, computer science has been developing very rapidly. The available computer resources are more powerful and more complex fluid flows can be simulated by CFD than before.

Generally CFD software is built up from the following components:

- Physical model of the physical phenomena. Usually the physical model is an approximation of a real situation. It neglects several physical aspects which are not significant to the case under investigation. A physical model is represented as integral or differential equations with appropriate boundary or initial conditions and necessary restrictions.
- Mathematical method to find the solution of the system of equations. While in the simplest case analogous solution of the physical model may exist, a complex physical model can be solved only using special mathematical methods. Usually it involves the spatial and/or temporal

discretization of the physical model which results in a set of mathematical equations soluble by an appropriate computer code.

- Pre-processor to create the geometry, mesh, to apply the boundary and initial conditions, etc.
- Visualization tools. Although this is not an essential part of CFD software, it helps us visualise the results of our calculations.

In order to be able to use a mathematical method to obtain a solution of the physical model, the set of equations describing the physical phenomenon has to be closed: the number of independent equations has to equal the number independent variables to be calculated. The physical model thus consists of the principal equations describing the motion and state of the continuum, plus as many additional equations as required to close the set of equations.

### 3.3.1 Objectives

The goal of the numerical simulation is to simulate one or many arbitrarily shaped bubbles. The code can be developed in order to simulate the real behaviour of bubbles in a real electrolysis cell including their effect on the electrical resistance.

The code developed can be used to investigate the effect of different factors - density, viscosity, surface tension, bubble volume and angle of inclination - on the behaviour and shape of the bubble. The advantage of using a numerical code is the ease with which the different factors of a system can be changed and thus their effects can be examined independently.

As the physical experiments in a real electrolysis cell is almost impossible, the real shape and movement of a carbon-dioxide bubble gliding under the anode can be investigated only by an appropriate numerical code.

The results of the simulations and the set-up model can be integrated into the bubble layer simulator developed by *Kiss et al (2005)*.

### **3.3.2 Available numerical methods for two-phase bubbly flows**

#### **3.3.2.1 Physical models**

The literature overview of numerical simulations gives a large number of methods which can be used efficiently for simulating the movements of bubbles in different liquids. Hence the most important challenge is to choose the best method to apply to the problem. Even knowing the various physical, numerical and free surface models, the set-up of a complete numerical simulation is not straightforward.

There are two ways of describing the movement and state of a continuum, microscopic and macroscopic. While the microscopic approach describes the motion and state of single molecules which form the continuum, the macroscopic approach concentrates only on the collective motion of the particles as a continuum. There are two methods which belong neither to the microscopic, nor to the macroscopic approaches. The Lattice Boltzmann and Smoothed Particle Hydrodynamics describe the motion and state of the particles forming the continuum, but those particles are much larger than a molecule. The particles in these two methods are a set of molecules. Thus the first decision is which approach should be used: the macroscopic, such as the well-known Navier-Stokes equations along with an interface tracking or capturing method; the microscopic, such as the less used Molecular Dynamics or the mesoscopic, such as the Smoothed Particle Hydrodynamics or the Lattice Boltzmann Method. The majority of the available numerical simulations are based on the Navier-Stokes equations or the Lattice Boltzmann method, which is a very promising new but rapidly developing method.

Another classification of the physical model bases on the presence of numerical mesh. This classification cannot be separated from the mathematical model because the necessity of a mesh is significant in the numerical method not in the physical model. Generally it can be stated that to solve the Navier-Stokes equations mesh is needed while among others the Lattice Boltzmann, Smoothed Particle Hydrodynamics and Spectral methods use no grids to solve the governing equations.

### Macroscopic methods

To solve the governing equations of a physical model at the macroscopic level, the computation domain has to be divided into finite elements/surfaces/volumes which create the computation mesh or grid. The solution of the governing equation is approximated at discrete locations of this grid. These grids can be regular or irregular (structured or unstructured), where the former consists only of certain regular 2D or 3D forms while the later can be build up using any form. Most of the grids are static, but transient grids which are changed by the movement of the continuum can also be used applying an adaptive mesh refinement method.

### *Navier-Stokes equations (NS)*

The most widely used physical model to describe the movement of a continuum at the macroscopic level is the NS equations with additional equations which describe the properties of the continuum, certain restrictions, boundary conditions, etc.

The important issues which arise during the solution of the NS equations is

1. The NS equation is non-linear.
2. The pressure-velocity coupling generally requires special considerations. Many solutions can be found for this problem in the literature.

3. In turbulent flows generally an additional turbulent model is needed. If all the relevant scales can be combined into the computational grid, the NS equations can be solved directly without the turbulence model (Direct Numerical Simulation).

In the case of multi-phase flows with free surfaces additional to the NS equations, further methods are required to track the position of the free surface. The available free surface techniques will be reviewed later.

There are three approaches, the Lagrange-Euler, the Euler-Euler and the fictitious domain approach, to describe a two-phase system at the macroscopic level using NS equations. In the scope of the present review it is assumed that the one of the two phases is continuous, while the gas phase forming the bubbles is dispersed. The Eulerian approach is used when the continuum moves in an absolute, fixed frame of reference while the Lagrangian approach is used when the frame of reference is moving along with the continuum. In our experiment the dispersed phase, the single bubbles, is described by the Lagrangian approach. It means that the bubbles are described by an equation expressed in a coordinate system fixed to the bubble. The difference between the Euler-Euler approach and the Euler-Lagrange approach is that in the first both the continuous and dispersed phase is described by equations expressed in the Eulerian frame, while in the second the dispersed phase is described by the Lagrangian approach. In order to describe the dispersed phase in the Lagrange-Euler approach all the single bubbles have to be tracked while the continuous phase is described on an absolute grid covering the whole fluid domain. In some cases two-

phase flows can be considered as one, fictitious phase. In this fictitious domain approach the governing equations are identical to the single-phase equations, because the dispersed phase occupies the same phase as the continuous one. The dispersed phase surface is taken into account by a penalty technique. This method avoids the expression of the transmission conditions at the boundary of the two phases. This technique is very useful for simulating two-phase flows with complex geometries at the boundaries.

#### Microscopic method

##### *Molecular Dynamics (MD)*

The Molecular Dynamics method is a way to model a system at a molecular level. The method describes and follows the movement of each and every molecule which forms the system. Hence the computation cost can be very high even for a small system. This method is very useful to simulate microscopic phenomena which cannot be observed directly or nanotechnology devices which have not been or cannot yet be created.

The dynamics of the system is characterised by the potential energy function. According to the applied potential function we can distinguish between the empirical potentials, semi-empirical potentials and ab-initio (first principles) MD systems.

### Mesoscopic methods

#### *Smoothed Particle Hydrodynamics (SPH)*

The fluid is divided into a set of discrete fluid elements using a Lagrangian approach. These elements or particles have a spatial distance which is called smoothing length. The properties of the fluid are linked to the fluid elements and are smoothed by a kernel function. The property of an element can be calculated by summing the relevant properties of all the particles which lie within a certain smoothing length of the element. The smoothing length of each element can vary separately in time and space. This variation can be based on density only which does not give a large flexibility to this method. Unfortunately, this method tends to smear out shocks and contact discontinuities. The particle-based nature of this method makes it ideal to model self-gravity combining it with an appropriate gravity solver.

#### *Lattice Boltzmann Method (LBM)*

In the Lattice Boltzmann method one fictitious computational particle consists of a small, but finite part of the fluid and the method describes the state and movement of these particles. The particles are situated on a symmetrical lattice. They have the same mass and move with the same velocity in fixed directions which are the edges of the lattice. The movement of the particles can be divided into two steps. The first step is the streaming in



which each particle moves to the nearest node according to the direction of its velocity and the second is the collision step in which the particles inhabiting the same node collide and their velocity and energy are changed according to the collision rule. From this description the macroscopic Navier-Stokes equation can be recovered fully through the Chapman-Enskog expansion.

### **3.3.2.2 Mathematical methods**

There are three important factors of a mathematical solution, namely uniqueness, existence and stability. The mathematical solution of two-phase models is based on the discretization of the governing equations. We distinguish between spatial, temporal and equational discretizations. According to this discretization the following mathematical methods exist.

#### *Finite Difference Method*

The finite difference method uses finite quantities instead of infinitesimal ones to calculate the value of a difference. This approach requires the temporal and spatial discretization of the computational domain. The differences can be calculated by the forward, the backward or the central scheme. The main disadvantage of the finite difference

method is that it requires structured meshes and coordinate transformation for complicated geometries.

### *Finite Volume Method*

The finite volume method is based on the discretization of the computational space into finite, non-overlapping control volumes. The discretized quantities of interest are located at the centres of the volumes. Values of quantities at other locations than the centre points are given by interpolation profiles. The governing equations are obtained by integrating the differential form of the governing equations over each finite cell. Hence the solution of these discretized equations always satisfies the conservation equations such as mass, momentum, energy and species. This method is the most versatile method in computer fluid dynamics.

### *Finite Element Method*

This method is based on the spatial discretization of the computational domain. The domain is divided into finite elements. The quantities of interest are given at certain nodal points of these elements. These points can be the end points or central point of the elements. The value of the quantities within an element is given by interpolation functions. In the governing equation the exact quantities are approximated by these interpolation functions.

### *Boundary Element Method*

This method based on the integral form of the governing equation. It only requires the dividing into elements the boundaries within or of the computational domain. This method can be applied to problems only for which the green's functions can be calculated. Since the solutions of the governing equations are calculated only on the boundaries the computation cost of this method is much smaller than the other methods.

### *Fundamental Solution Method*

This numerical technique belongs to the class of boundary methods, just like the Boundary Element Method. This method is useful in the situation where a fundamental solution of the partial differential equation in question is known. Contrary to the previous method it requires only the pointisation of the boundary thus avoiding any integral evaluations. Also, the coding does not differentiate between the 2-D and 3-D cases. The disadvantage of the method is that if the Laplace operator is involved, the method requires an artificial boundary. The location of this artificial boundary is a serious problem.

### *Spectral Method*

The spectral method is used to solve partial differential equations numerically using a Fast Fourier Transform.

### 3.3.2.3 Surface handling methods

Modelling the free surface is the crux of two-phase flow modelling. It is very important to calculate the exact position of the sharp surface while including the effect of the surface on the movement of the two phases. Free surface methods can be classified using different aspects. The following classification is made to suit the needs of the author.

We can distinguish between the free surface methods as explicit or implicit methods. The explicit methods keep tracking the exact position of the surface while the implicit methods do not track the position or movement of the interface but track other parameters from which the position of the surface can be determined implicitly.

We also can classify free surface methods based on the kind of grid they use. A method can require the usage of Lagrangian or Eulerian mesh. The Eulerian mesh does not move with the surface and so it is much easier to implement and handle, while the Lagrangian mesh moves with the surface, thus it automatically tracks the free surface but it is difficult to implement and the re-meshing requires additional techniques.

The key to free surface modelling is the proper surface tension model because the use of an improper surface tension model can cause spurious currents which can destroy the surface. These currents are vortices occurring in the neighbourhood of the surface despite the absence of external forces.

### Explicit – Surface tracking methods

#### *Discrete Particle Model*

This method identifies and tracks the dispersed phase as singular, unique particles. The shape of the particle can be determined by a simple function or class shape where only a limited deformation of the surface is possible through several coefficients of the surface. Widely used shapes are the sphere and ellipsoid. More difficult shapes can be described by using a family of surfaces when the surface is represented by polynomials, but the change of the shape is still restricted to the same family.

#### *Moving or adapting boundary fitted grid method*

The free surface is associated with nodal points of a mesh. In order to follow the motion of the surface the mesh has to be moved and/or re-meshed as the surface moves. If the interface undergoes a large deformation, the re-meshing can be very difficult and time consuming. This method is not capable to track surfaces with break-up or coalescence.

#### *Surface Marker Method*

This method is a variation of the Marker Cell Method. In this method only the surface elements and not the whole volume of the dispersed phase are marked to avoid the high

memory cost of the Marker Cell Method. The surface is tracked by the marker and can be recovered using different techniques in two or three dimensions. In two dimensions the surface may be recovered using a piecewise linear function or spline function. The disadvantage of this method is that when the surface expands there are no markers to fill the space. This problem can be overcome by adding further markers.

#### *Immersed Boundary Method*

This is an Eulerian-Lagrangian approach, where the equations of the continuous phase are solved in a fixed Eulerian grid, while the free surface is represented by a set of points and is advected in a Lagrangian manner. The information between the interface and the fixed Cartesian grid is exchanged through interpolation.

#### *Implicit - Surface capturing methods*

These methods track the motion of the particle marked either with weightless particles or by an indicator function such as volume fraction, level set or a phase-field. This method does not define the interface as a sharp surface. To recover the sharp interface from the result of this method further techniques have to be applied.

### *Volume of Fluid Method*

This method is a volume tracking method, where the motion of the particle is tracked by using a volume function as the indicator function. The value of the volume function gives the percentage of the volume occupied by the dispersed phase in each cell. In order to stay inside the physical value of the indicator function, the interface is recovered using convection schemes before advecting it. The slope and curvature of the surface can be calculated by using the fluid volume fraction in neighbouring cells and the movement of the surface is determined by the movement of the volume fractions through the grid.

### *Marked Cell Method*

This method can describe the motion of time dependent arbitrary free shapes. The location of the dispersed phase in the fluid is determined by a set of marked particles which moves together with the cells, but has no mass or volume. The marked cell is occupied by the dispersed phase and the empty cell is occupied by the continuous phase. Therefore the markers are tracking volume and not the position of the surface. The movement of the dispersed phase is determined by the movement of the markers. The surface can be recovered from the marked cells; the surface exists in a marked cell if there is a void neighbour cell next to it. The advantage of this method is that since it tracks volume it naturally handles break-up, coalescence and disappearance of bubbles. The disadvantages are the high computational cost and that converging or diverging flows cannot easily be modeled.

### *Level Set Method*

This is an Eulerian method for tracking closed interfaces and shapes. The surface is described by the level set function, which can have a positive value inside the surface, negative outside it and zero at the interface. This method handles easily the deformation, coalescence and break-up of surfaces.

### *Surface Height Method*

This method can be assumed to be a simplification of the Level Set Method. The limitation of this method is that the surface has to be horizontal and it cannot deviate too far from horizontal. The deviation of the surface from a horizontal reference surface is given by an indicator function. Time evolution of the height can be calculated from the fact that the surface must move with the fluid. The advantage of the method is the low computational cost even in 3 dimensions because of the limitation of the movement.

### *Ghost Fluid Method*

This method tracks the interface using the Level Set Method in an Eulerian framework. This method easily captures the interface boundary conditions or jump conditions. The movement of two fluids is described by the Eulerian equations and difference equations of state. The discretization of the Euler equation is done using ghost cells. These cells are



associated with each point of the computational domain. Each ghost cell, and thus each point of the computational domain consists of the mass, momentum and energy of the fluid which occupies that cell. In addition, each ghost cell consists of the mass, momentum and energy of the other phase which is not at that cell at that moment. With the help of the ghost cells the solution of the Euler equations can be solved and the level set function can be updated. The updated level set function indicates which spatial discretization should be used at a certain point. The main advantages of this method are that it is easy to maintain and extend to multi-dimensions, and that it is possible to maintain a sharp interface without smearing.

### 3.4 References

- Aaberg, R.J., Ranum, V., Williamson, K. and Welch, B.J., in R. Huglen (ed.), *The gas under anodes in aluminium smelting cells. II. Gas volume and bubble layer characteristics*, TMS Light Metals, pp. 341-346 (1997)
- Bilek, M. M., Zhang W.D. and Stevens, F. J., *Modeling of electrolyte flow and its related transport processes in aluminium reduction cells*, TMS Light Metals, pp. 323-331 (1994)
- Cassayre, L., Utigard, T.A. and Bouvet, S., *Visualizing gas evolution on graphite and oxygen-evolving anodes*, JOM, vol. 54, pp. 41-45 (2002)
- Choi, H.M., Kurihara, T., Monji, H. and Matsui, G., *Measurement of particle/bubble motion and turbulence around it by hybrid PIV*, Flow Measurement and Instrumentation, vol. 12, pp. 421-428 (2002)
- Cooksey, M. A. and Feng, Y., *PIV measurement on physical models of aluminium reduction cells*, TMS Light Metals, pp. 359-366 (2006)

- Dernedde, E. and Cambridge, E.L., *Gas induced circulation in an aluminium reduction cell*, TMS Light Metals, pp. 111-122 (1975)
- Fortin, S., Gerhardt, M., and Gesing, A.J., *Physical modelling of bubble behavior and gas release from aluminium reduction cell anodes*, TMS Light Metals, pp 721-741 (1984)
- Gao, B., Li, H., Wang, Z. and Qiu, Z., *A new study on bubble behaviour on carbon anode in aluminium electrolysis*, TMS Light Metals, pp. 571-575 (2005)
- Grjotheim, K., et al, *Aluminium electrolysis: Fundamentals of the Hall-Héroult process*, 2<sup>nd</sup> edition, p. 146 (1993)
- Hauptin, W. and McGrew, W.C., *See-through Hall-Héroult cell*, Aluminium, vol. 51, pp. 273-275 (1975)
- Kiss, L. I., Poncsák, S., and Antille, J., *Simulation of the bubble layer in aluminum electrolysis cells*, TMS Light Metals, pp. 559-564 (2005)
- Liu, Z.-C., Landreth, C. C., Adrian, R. J. and Hanratty T. J., *High resolution measurement of turbulent structure in a channel with particle image velocimetry*, Experiments in Fluids, vol 10, pp 301-312 (1991)
- Melling, A., *Tracer particles and seeding for particle image velocimetry*, Meas. Sci. Technol., vol. 8, pp 1406-1416 (1997)
- Ngoya, F.N. and Thonstad, J., *On mass transfer effect due to electrolytically evolved gas*, Electrochim. Acta, vol. 30, pp. 1659-1664 (1985)
- Perron, A. and Kiss, L. I., *Rise velocity of single bubbles moving under a slightly inclined surface in various liquids*, personal communication, UQAC (2006)
- Purdie, J. M., Bilek, M., Taylor, M. P., Zhang, W.D., Welch, B. J. and Chen, J. J. J., *Impact of anode gas evolution on electrolyte flow and mixing in aluminium electrowinning cells*, TMS Light Metals, pp. 355-360 (1993)
- Solheim, A., Johansen, S., Rolseth, S. and Thonstad, J., *Gas driven flow in Hall-Héroult cells*, TMS Light Metal, pp. 245-252 (1989)
- Utigard, T.A., Toguri, J.M. and Ip, S.W., *Direct observation of the anode effect by radiography*, TMS Light Metals, pp. 703. (1988)
- Utigard, T.A., Costa, H. and Popelar, P., *Visualization of the Hall-Héroult process*, TMS Light Metals, pp. 233 (1994)
- Xue, J. and Öye, H., *Bubble behaviour – cell voltage oscillation during aluminium electrolysis and the effects of sound and ultrasound*, TMS Light Metals, pp. 265-271 (1995)

- Zhuxian, Q et al, *Formation of metal fog during molten salt electrolysis observed in see-through cell*, J. Appl. Electrochem., vol 17., pp. 707 (1987)
- Zorić, J. and Solheim, A., *On gas bubbles in industrial aluminium cells with prebaked anodes and their influence on the current distribution*, Journal of Applied Electrochemistry, vol. 30, pp. 787-794 (2000)

## **Chapter 4**

# **A LARGE BUBBLE MOVING UNDER A SLIGHTLY INCLINED SURFACE**

This chapter is based on the following article:

Vékony, K. and Kiss. I.L., *A large bubble moving under a slightly inclined solid surface*,  
submitted to Journal of Multiphase Flow

### **4.1 Objectives**

Large bubbles with special shapes have been observed under inclined anodes in aluminium electrolysis cells. These large Fortin bubbles play a significant role in the heat and mass transfer in the cell. The formation of this special shape and its movement under slightly inclined solid surfaces are not yet fully understood. Small bubbles and bubble layers moving under inclined surfaces have been observed, even though no quantitative

measurements of the large Fortin bubbles can be found. One of the main objectives of this work is to understand the formation and movement of Fortin bubbles completely.

A single set-up with an inclined surface is used to observe single large Fortin bubbles gliding under the surface. In order to characterize the movement and shape of a large bubble, the dimensions of the bubble and its terminal velocity are measured; the evolution of the shape is observed; different parameters, for example the drag coefficient, are calculated in order to explain the movement of the bubble; several correlations are determined between the different parameters; and the formation of the shape is explained theoretically.

#### **4.2 Series of experiments**

The formation of single large bubbles is observed using the second set-up introduced in chapter 3.2.2. Bubble formation is observed using four different angles of inclination (1,2,4 and 8°) and three different bubble volumes (50, 150 and 250 ml). Videos are made using the two digital cameras from the side and from the bottom as seen in the mirror placed under the tank. At each angle and volume several measurements are taken and presented as an average in order to decrease the uncertainties linked with them.

The recordings are transferred onto a computer where they are analyzed as explained in chapter 3.2.4 and the different dimensions of the bubbles and their velocities are measured from the recordings. Further parameters are calculated as explained below.

### 4.3 Results and discussion

#### 4.3.1 Characterization of the Fortin shape

The shape of the different sized bubbles is observed in two planes; in the plane perpendicular to the surface and parallel to the direction of the bubble movement, which is called transversal plane and in the plane of the surface, which is called surface plane. The shape observed in the transversal plane is the cross-section, while in the surface plane is the contact shape. The bubble shape is characterised in these two planes also. Keeping in mind that this work concentrates on the Fortin shape, the different geometrical parameters used to describe a bubble in the transversal and surface planes are showed in figure 4.1. The parameter  $W$  is the width,  $L$  is the length,  $H_t$  is the mean thickness of the tail,  $H_h$  is the maximum height of the head,  $L_h$  is the maximum distance of the highest point of the head from the front of the bubble,  $R_f$  is the radius of curvature at the front,  $R_h$  is the radius of curvature at the head measuring at its highest point,  $\Theta_f$  is the half angle of the front and  $\Theta_h$  is the half angle of the head. The mean thickness of the tail is measured in the middle between the end of the head and the end of the bubble.

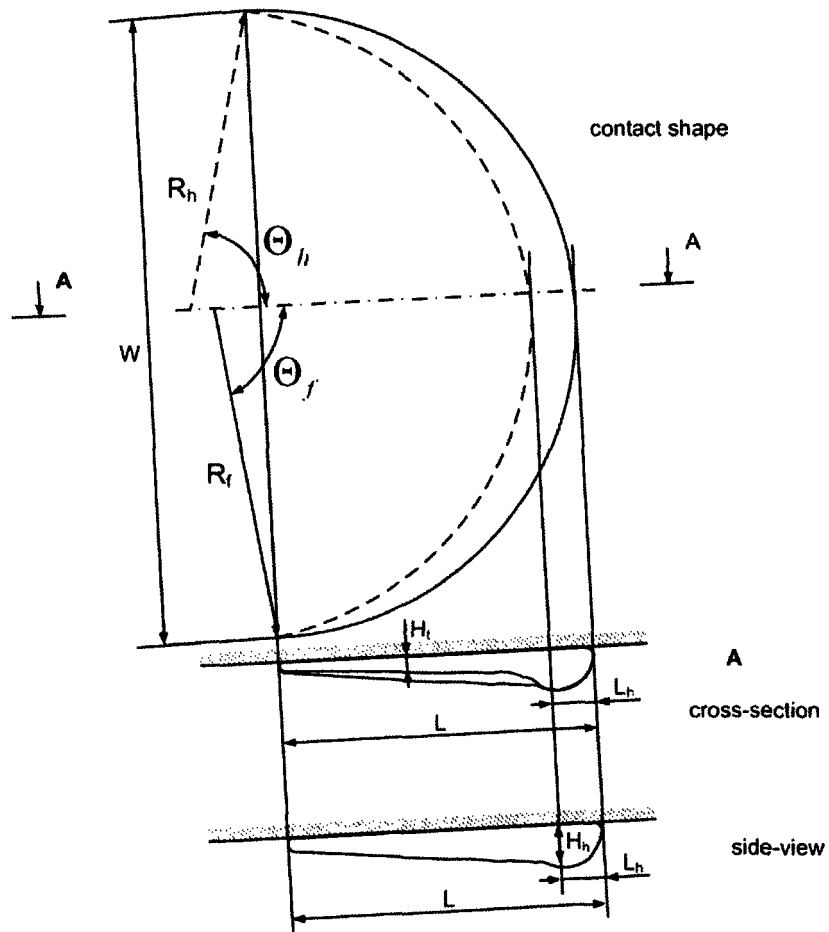


Figure 4.1 – Illustration of the different geometrical parameters used to describe a Fortin bubble

The contact shapes, side-views and cross-sections observed during the experiments can be seen in figures 4.2, 4.3 and 4.4 respectively for each angle and bubble volume.













$\alpha \backslash V$	50 ml	150 ml	250 ml
1°			
2°			
4°			
8°			

Figure 4.2 – Contact shapes at different inclinations and bubble volumes



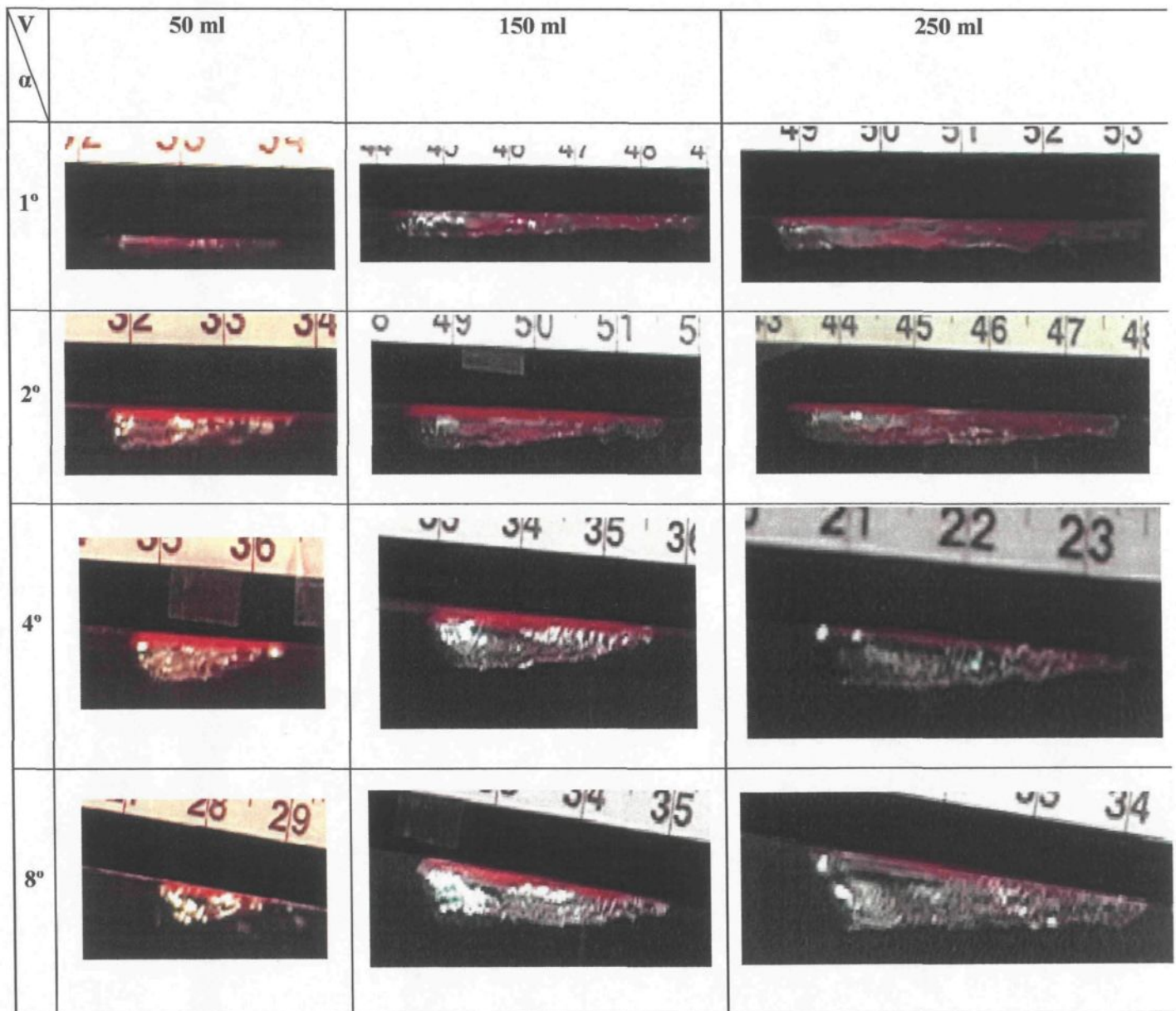


Figure 4.3 – Side views at different inclinations and bubble volumes

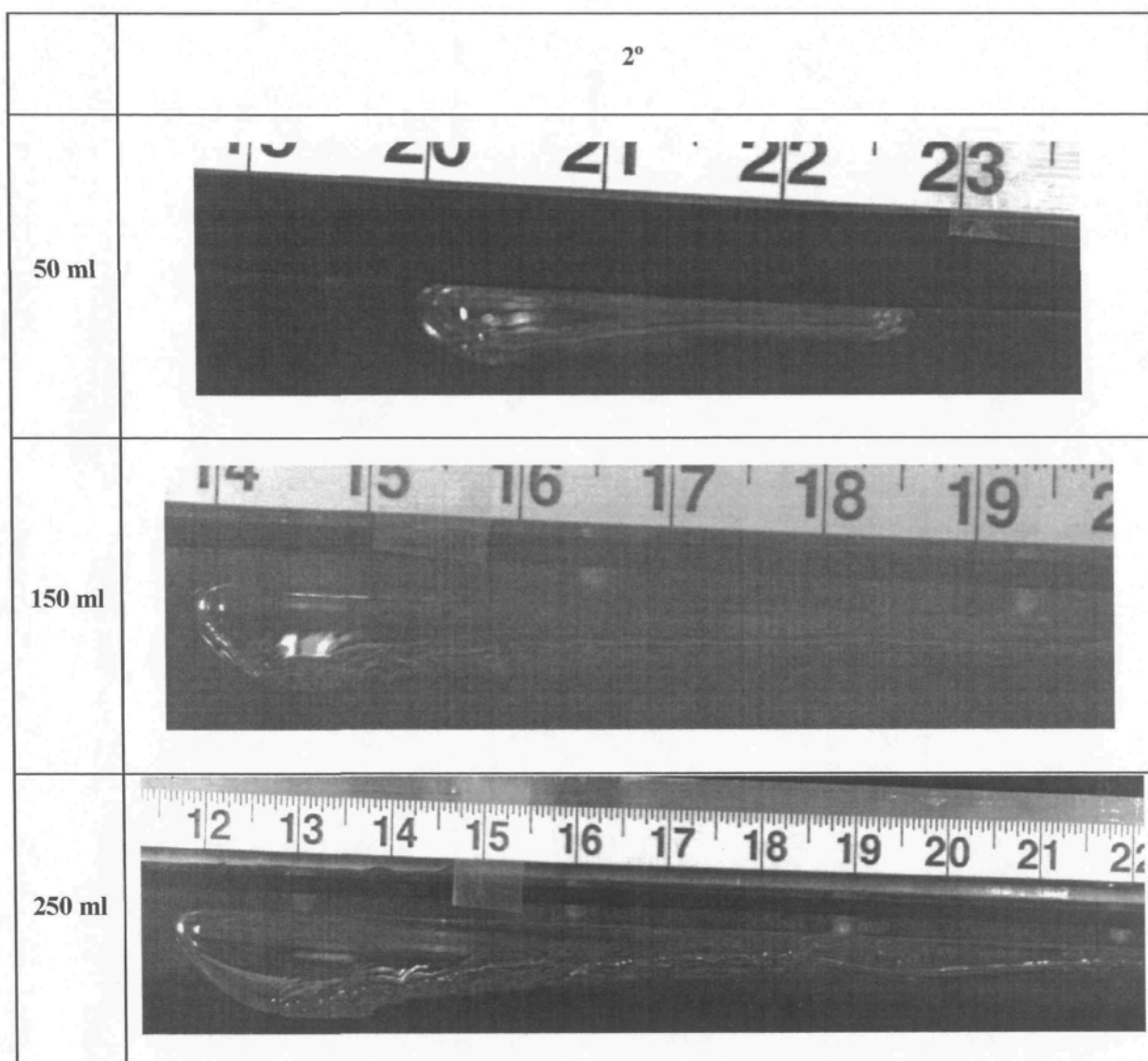


Figure 4.4 – Cross sections for different bubble volumes at 2° of inclination

The same initial contact shape was always observed independent of the velocity of the gas release (figure 4.5). It resembles a butterfly which instantly transforms to the final shape shown in figure 4.2. The transformation from the initial into the final shape takes less

than 1 sec. At high inclination this initial contact shape is closer to the final form but still butterfly like. The volume of the bubble has no significant effect on the initial shape.



Figure 4.5 – Initial contact shape

The Fortin shape was observed in every experiment. The head always formed right after the nucleation of the bubble under the surface and it stayed at the front of the bubble while the bubble was gliding under the surface.

Previously it was thought that the Fortin shape occurs when the “bubble surface became horizontal and the bubble front collapsed” (*Fortin, 1984*) which is not in agreement with our observations. As it will be shown, the Fortin shape is most likely induced by a gravity wave. This sort of wave is usually induced by a gas phase moving fast above a standing liquid phase. If the velocity difference between the two phases is large enough, then the motion of the gas phase disturbs the equilibrium of the liquid phase by displacing a certain quantity of liquid. This disturbance travels in a continuous phase as the gravity restores the displaced parcels toward equilibrium. The Fortin head is formed by the wave-front of the gravity wave which has much larger amplitude than the waves following the front. This wavy motion can be clearly observed at the bottom of the Fortin bubbles (i.e. figure 4.4).

The contact shape of a Fortin bubble at each angle and volume is similar to a sector of a circle. The curvature at the front is always positive while at the rear it is either positive or infinitive, but never negative. The rear is not straight but oscillates during the movement of the bubble. During the transformation from the initial shape to the final shape sometimes two small tails can be observed at the lateral ends of the bubble. The bubble path is always near rectilinear. The head is always at the front of the bubble and its dimensions are very stable, not changing significantly as the bubble glides under the surface. The tallest point of the head is measured at the middle of the front of the bubble. The length of the head is also the longest here. The length of the head is measured at the middle of the bubble front in the transversal plane from the front of the bubble to where the first wave can be observed (figure 4.6). From the middle of the bubble towards the lateral edges the dimensions of the head decreases gradually.

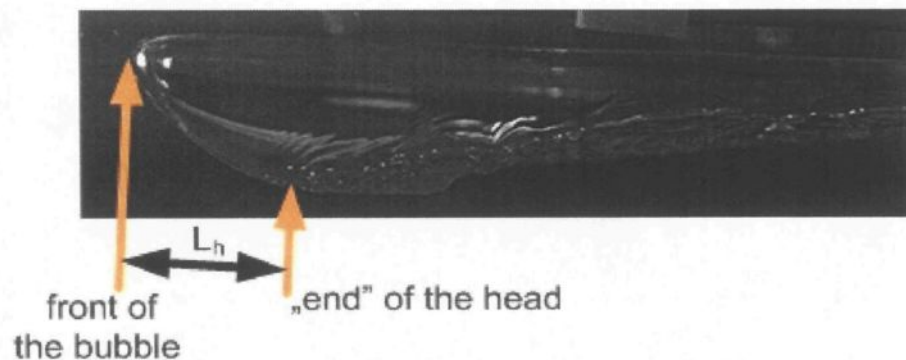


Figure 4.6 – Definition of the length of the Fortin head



### 4.3.2 Effect of the inclination and volume on the bubble dimensions and shape

All the parameters used to characterise the bubble shape are measured or calculated and are presented below. The  $L$  length,  $W$  width,  $H_h$  maximum height of the head and  $L_h$  maximum length of the head for all angles and bubble volumes and  $H_t$  the mean thickness of the tail for all volumes at  $2^\circ$  of inclination can be seen in figures 4.7-4.11.

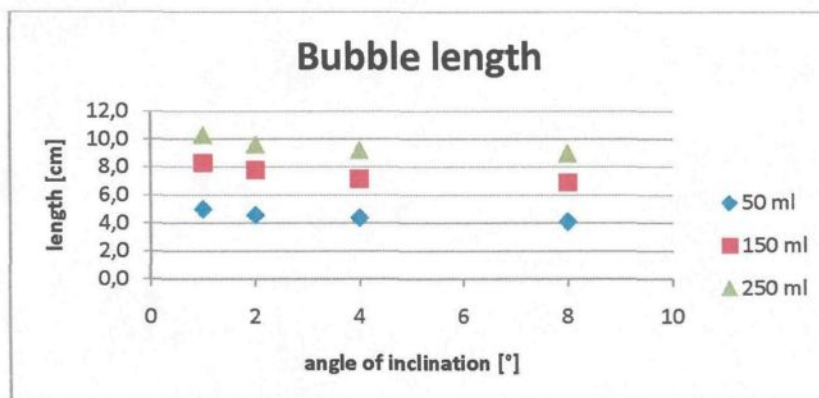


Figure 4.7 – Bubble length measured for all angles and bubble volumes

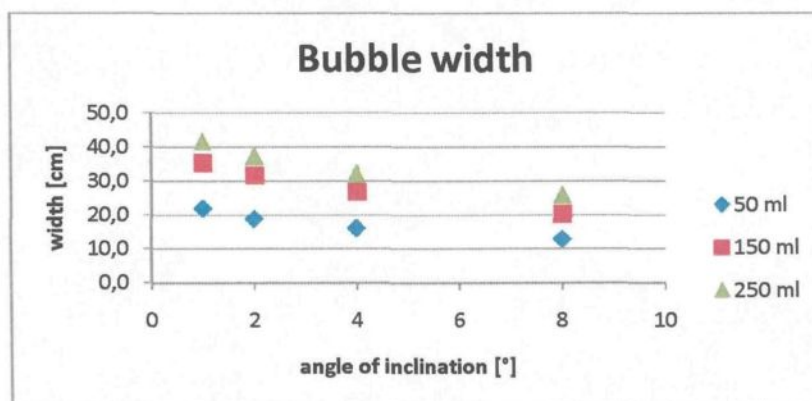


Figure 4.8 – Bubble width measured for all angles and bubble volumes

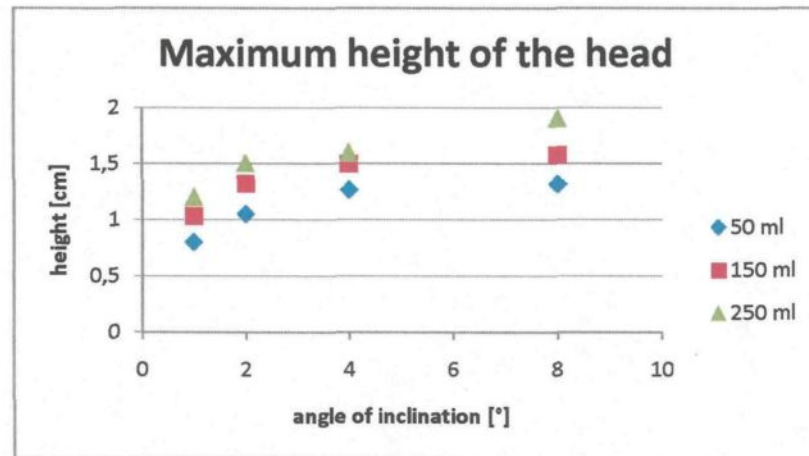


Figure 4.9 – Maximum height of the head measured for all angles and bubble volumes



Figure 4.10 – Maximum length of the head measured for all angles and bubble volumes

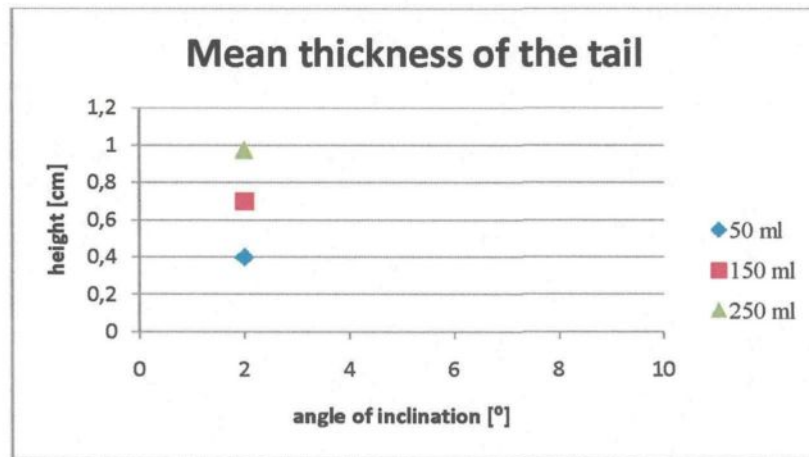


Figure 4.11 – Mean thickness of the tail measured for bubble volumes

The width, length and height depend strongly on the volume of the bubble; increasing the volume increases all these parameters too. As the height of the bubble depends strongly on the movement of the bubble and the balance of the dynamic forces acting on the bubble, it does not increase significantly. The length of the head again depends strongly on the volume of the bubble. This length represents the amount of air which is enclosed before the first wave and thus the wave has to push this amount of air before itself. As the volume increases, it is understandable that the length of the head and thus the volume of the enclosed air increases.

The effect of the angle of inclination is different from the effect of the volume. As the inclination grows, the accelerating part of the buoyancy force becomes more significant and effects the dimensions of the bubble. As the angle increases, the contact size of the bubble decreases because its width and length decrease. However, its height and especially the height of the head increases as the angle increases. A slight increase in the length of the

head can also be measured. But this dimension is hard to measure and the differences are small. Therefore the length of the head for a given volume is treated as constant in this study.

It can be stated that as the volume increase, each dimension of the bubble increases, while as the angle increases, the bubble becomes more compact with a smaller cross-section and a larger height.

Three aspect ratios of the bubble were calculated: the ratio of the width to the length ( $W/L$ ), the ratio of the height of the head to the mean thickness of the tail ( $H_t/H_h$ ) and the ratio of the height of the head to the width ( $W/H_h$ ). The results can be seen as a function of the volume and the angle in figures 4.12-4.14. It was found that these ratios depend on the angle of inclination and in the range of the angles used in our experiments they decrease with increasing angle. On the other hand, the ratios do not seem to depend on bubble volume for really large volumes. This is in agreement with *Perron et al (2006)* who found that the aspect ratio for large bubbles is constant at a given angle.

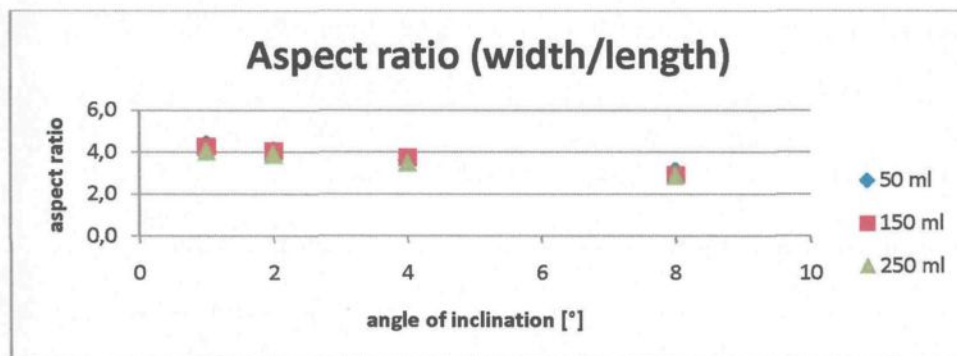


Figure 4.12 – Aspect ratio of width to length as a function of the volume and angle



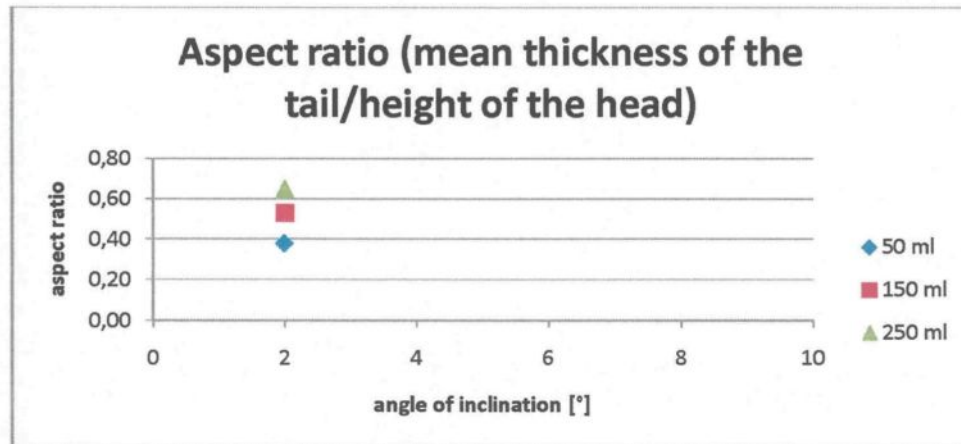


Figure 4.13 – Aspect ratio of mean thickness of the tail to height of the head as a function of the volume and angle

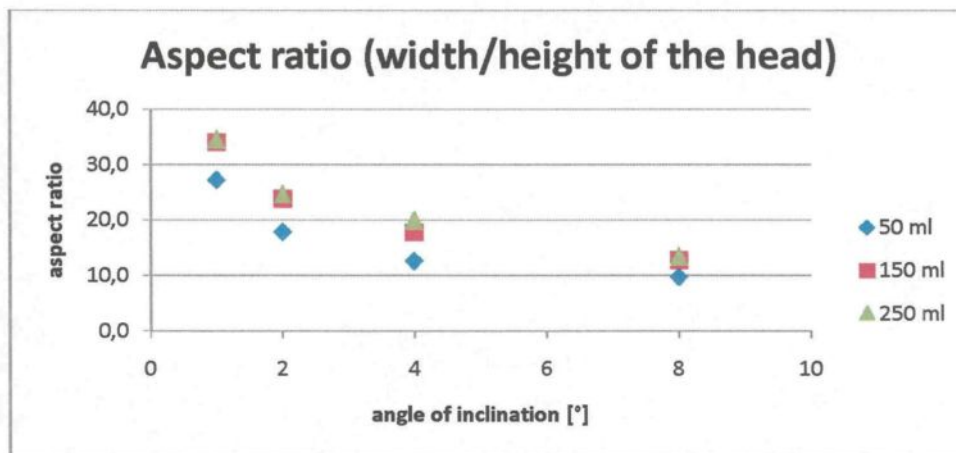


Figure 4.14 – Aspect ratio of width to height of the head as a function of the volume and angle

As mentioned above, a bubble can be characterised either by its length, width and height or by the radii and angles of the front and head and the height of the bubble. The angles and radii can be calculated from the width and length and vice versa. The calculated angles and

radii for the bubble front and head are shown in figures 4.15 and 4.16. The radius of curvature of the front and the radius of curvature at the tallest point of the head decrease with increasing angle and decreasing volume. On the other hand, the angles of the front and head are less dependent on bubble volume while they increase slightly with increasing inclination.

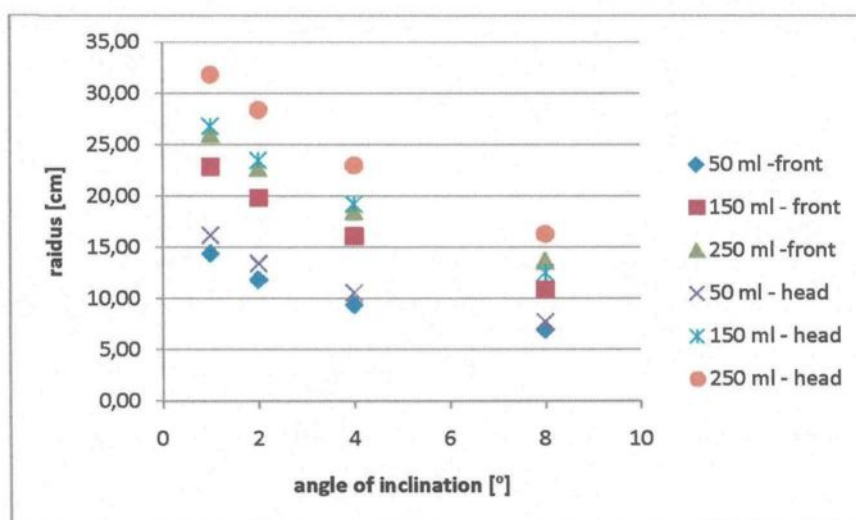


Figure 4.15 – Bubble radii of curvatures as a function of the bubble volume and angle of inclination

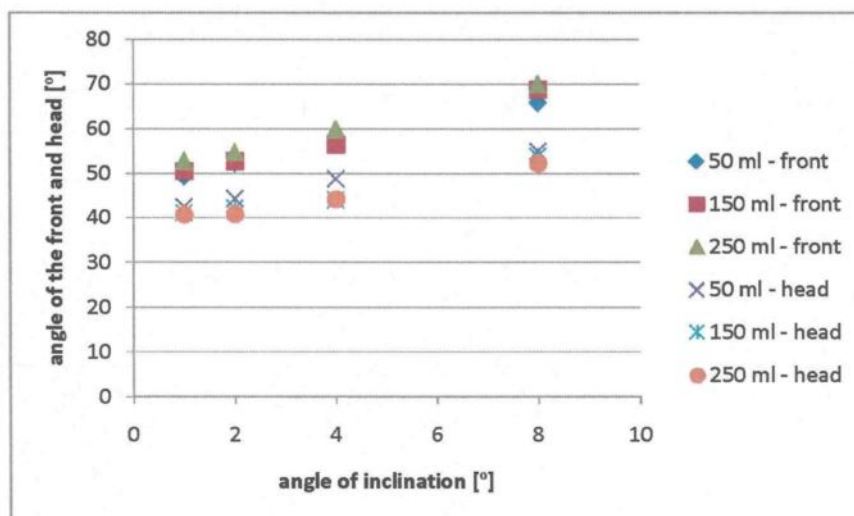


Figure 4.16 – Bubble angles of the front and head as a function of the bubble volume and angle of inclination

#### 4.3.3 Bubble movement along irregularities on the solid surface

A phenomenon observed during non intentional conditions in our experiments helped the understandings of the formation of the Fortin bubble – it is the balance between the accelerating and restraining forces that determines the shape of a bubble. When the bubble is nucleated under a solid surface there is a dry spot between the surface and the bubble. As the bubble starts to glide under the surface, the liquid penetrates between the surface and the bubble. The part of the bubble which is no longer connected to the surface starts to move faster. This either accelerates the whole bubble or leads to its break-up; since the

restraining force of the wetting film is much smaller than that of the dry spot, a bubble on a wetting film can maintain higher velocity. If due to some irregularities on the solid surface the bubble runs onto a dry spot, it eventually loses its momentum and thus slows down. This phenomenon was observed in our experiments. At an angle of inclination of  $1^\circ$  the bubble sometimes slowed down and “lost” its head. This happened mainly at low bubble volumes (50 or 150 ml), when the velocity of the bubble was not too high, certainly not enough to maintain the Fortin shape against an increased restraining force. When the bubble slowed down it thickened, elongated and its height decreased significantly. Sometimes this elongated bubble kept gliding but at a significantly reduced speed. The reduced speed varied from 1 cm/s to 8 cm/s. A moving bubble can maintain a significantly higher height than a standing or a slowly moving one. The limiting height for a standing bubble under a downward facing surface is given by *Pruppacher et al (1978)* and for the air-water-Plexiglas<sup>®</sup> system it is 4.18 mm. Exactly the same height was measured in our experiments for bubbles which slowed down and lost their head. It supports the idea that the higher height and the head are generated by the motion of the bubble and moreover by its fast motion.

As a bubble slows down and loses its head, its contact shape changes too. The new contact shape is no longer circular but becomes more rectangular. Snapshots of the evolution of the contact shape and side-view of a bubble running on a dry spot and losing its height can be seen in figure 4.17.

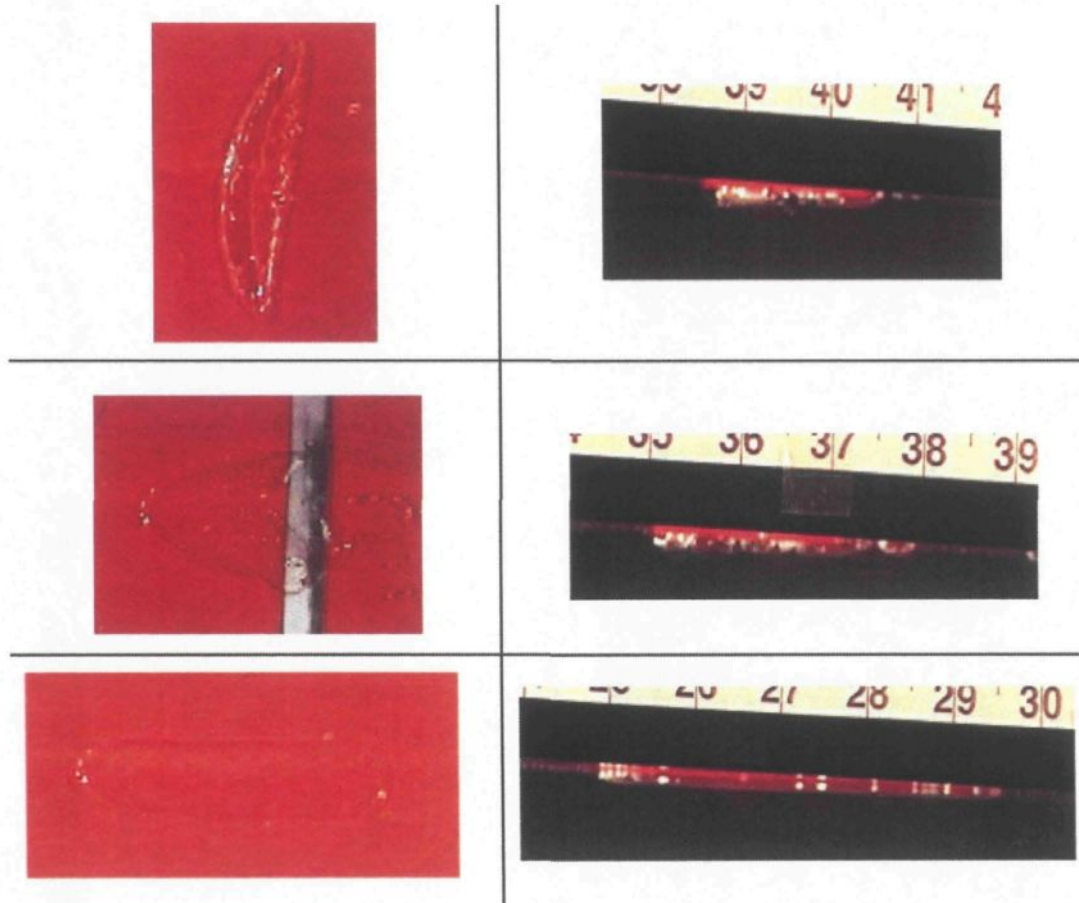


Figure 4.17 – Snapshots of the evolution of the shape of a bubble running on a dry spot

#### 4.3.4 Effect of the bubble volume and surface inclination on the terminal velocity

A bubble reaches terminal velocity when the forces acting on the bubble are balanced. The most important forces effecting the movement of a bubble are surface tension,

buoyancy, inertia, drag force and viscosity. The terminal velocity was determined for each volume and inclination using the following formula

$$u_T = \frac{x(t + \Delta t) - x(t)}{\Delta t} \quad (4.1)$$

where  $x(t)$  is the position of the middle point at the front of the bubble at a certain time. The value of the  $\Delta t$  time step was chosen to be 0.34 sec which corresponds to 10 frames. This value is relatively high compared to previous measurements, but our goal was to measure the mean value and not its oscillation. Several measurements were made at each angle and volume and later the mean value was calculated. The difference between the measured terminal velocities was never greater than 3%. The terminal velocity, just as the final shape, was reached in less than 1 second. The terminal velocities are presented in figure 4.18.

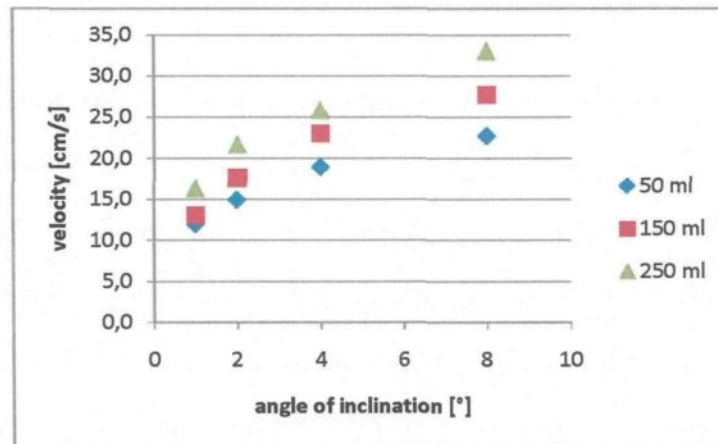


Figure 4.18 – Terminal velocity as a function of bubble volume and inclination angle.

Preliminary estimates of the terminal velocities were made, using linear extrapolation from previous measurements using smaller bubbles. We expected slightly smaller velocities



than the estimates suggested. The Fortin head is thought to be a gravity wave which is induced by the moving gas phase. The wave is induced by a certain amount of momentum transport which consequently decreases the kinetic energy of the bubble and thus leads to a smaller terminal velocity. Our expectations were substantiated by the measurements.

The terminal velocity increases with increasing angle and increases slightly with increasing bubble volume. It has been previously shown that the terminal velocity depends strongly on the shape of the bubble (*Perron et al, 2006*). In our measurements the observed bubble shape was always the Fortin shape and thus monotonous change in the terminal velocity was expected and was indeed observed. To the best of the author's knowledge, the bubbles measured in these experiments are the largest. There are no measurements in the literature to which my data can be compared. *Perron et al (2006)* performed several experiments with smaller bubbles and their results for 2° and 4° of inclination are presented in figure 4.19 along with our results. Our results fit well their prediction that the terminal velocity of a very large bubble increases with increasing volume and angle while it is constant for a moderately large bubble in a deformable bubble regime (figure 2.4).

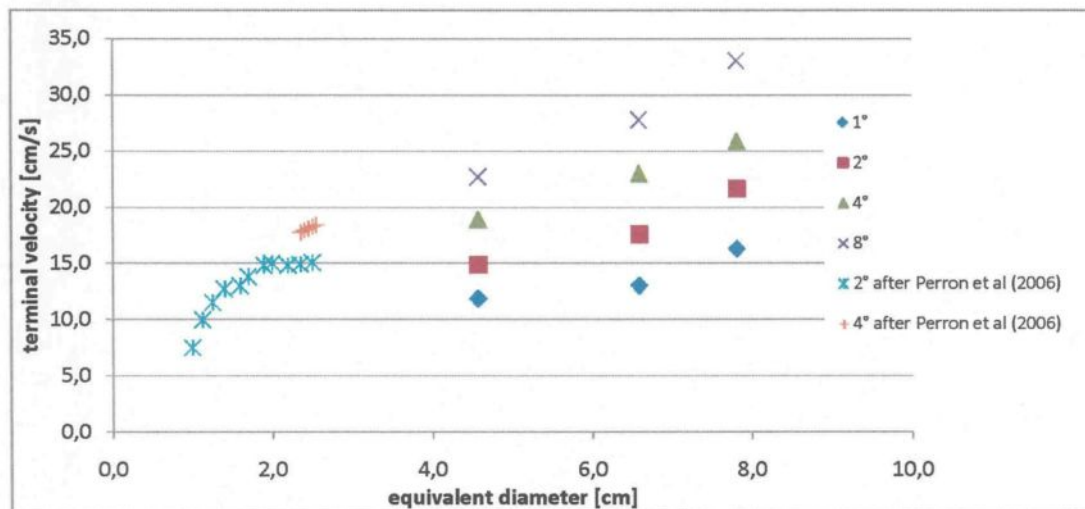


Figure 4.19 – Terminal velocity as a function of the equivalent diameter and angle of inclination

The dimensionless terminal velocity, the Froude number, was calculated using the following formula

$$Fr = \frac{u_T}{\sqrt{g \cdot d_e \cdot \sin \alpha}} \quad (4.2)$$

where  $u_T$  is the terminal velocity,  $\alpha$  is the angle of inclination of the surface,  $g$  is the gravitational acceleration and  $d_e$  is the equivalent diameter of the bubble, which is given as follows

$$d_e = \left( \frac{6 \cdot V}{\pi} \right)^{1/3} \quad (4.3)$$



where  $V$  is the volume of the bubble. The equivalent diameters are 4.57, 6.6 and 7.8 cm for volumes of 50, 150 and 250 ml used in our measurements, respectively.

The dependency of different parameters on the Bond number were also calculated where the Bond number is given by

$$Bo = \frac{\rho_l \cdot d_e^2 \cdot g}{\sigma} \quad (4.4)$$

where  $\rho_l$  is the density of the liquid phase and  $\sigma$  is the surface tension.

The dimensionless velocity as a function of the angle and later as a function of the Bond number can be seen in figures 4.20 and 4.21 respectively. The Froude number is quasi independent of bubble volume but it is inversely proportional to the inclination.

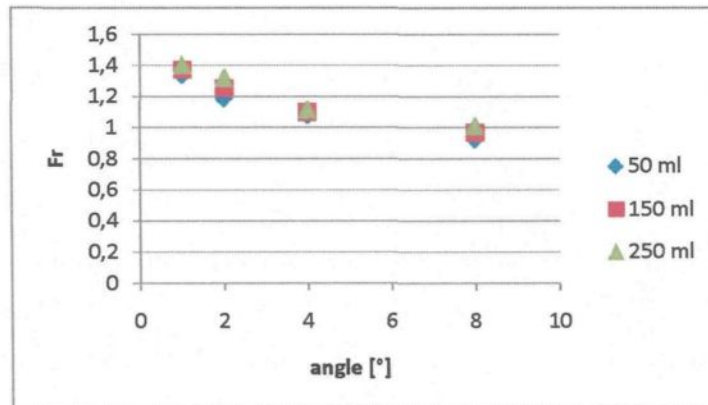


Figure 4.20 – Froude number as a function of the angle and bubble volume

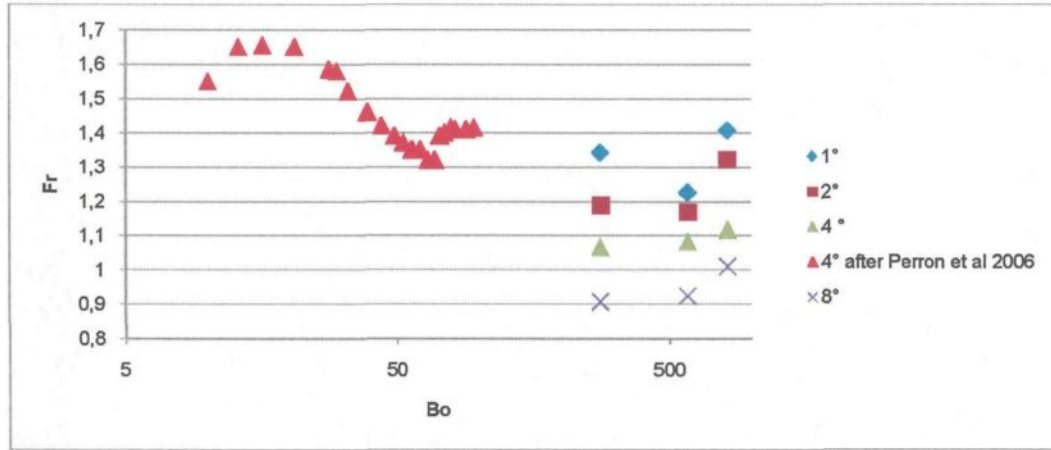


Figure 4.21 – Froude number as a function of the angle and Bond number

#### 4.3.5 Effect of the inclination angle and bubble volume on the drag coefficient

The drag coefficient is calculated from the terminal velocity which is reached when the component parallel to the surface of the buoyancy force equals the drag force. The drag coefficient is given as follow

$$C_D = \frac{2}{A_f} \frac{\Delta \rho}{\rho} \frac{1}{u_t^2} V g \sin \alpha \quad (4.5)$$

where  $A_f$  is the frontal area. According to *Perron et al (2006)* representing the frontal area as a circle does not give rise to a loss of physical sense in the regime of large bubbles, but in our case the difference between the drag coefficients calculated from a circular frontal

area and a rectangular frontal area calculated with the  $W$  width and  $H_h$  head height gives a difference of around 20%. Thus we calculated the frontal area as  $A_T = W \cdot H_h$ .

The drag coefficients calculated are presented in different ways in figures 4.22-4.24. First, the drag coefficient is given as a function of the inclination in figure 4.22. It shows that the drag coefficient depends only slightly on the size of the bubble and increases with increasing inclination. It is likely that due to the dynamic effects taking place in the system, the bubble shape depends more on the inclination than on bubble size.

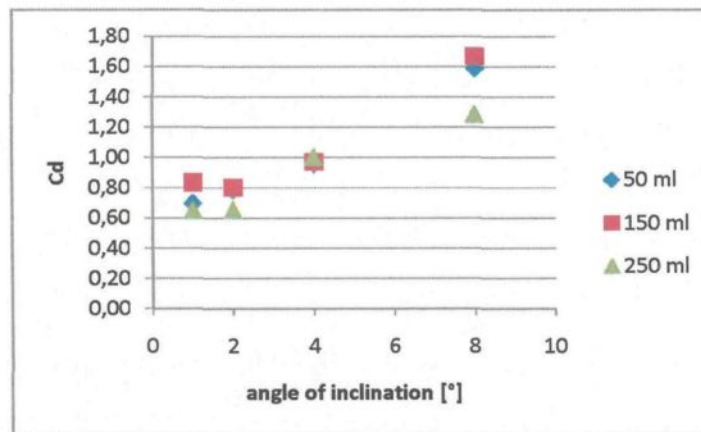


Figure 4.22 – Drag coefficient as a function of the volume and inclination

The drag coefficients are presented as a function of the Reynolds number in figure 4.23. We also make a comparison between our results and standard drag curves found in the literature. Our measurements gave a slightly higher drag coefficient than it is expected from the standard drag curve of rigid sphere, but slightly smaller values than it is expected from the two curves for bubbles rising in contaminated and pure water. The drag coefficient is higher at higher inclination for all Reynolds numbers. In the studied ranges of volume and

inclination it cannot be determined whether the drag coefficient is increasing, decreasing or constant with an increasing  $Re$  number. The maximal difference between the smallest and largest value for one angle is around 15-20% which is relatively high, even though the drag coefficient is expected to be nearly constant in this regime and from the studied range it can be considered nearly constant.

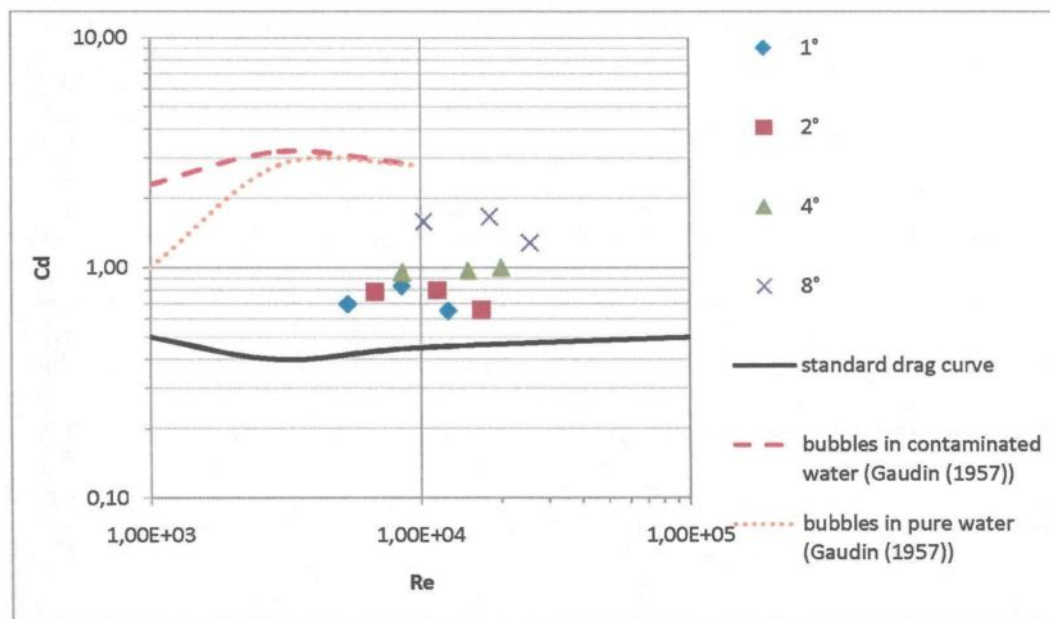


Figure 4.23 - Drag coefficient as a function of the Reynolds number and inclination

The nearly constant drag coefficient with increasing  $Re$  means that the motion of the bubble is principally controlled by inertia, while a decreasing  $C_d$  indicates a viscous regime.

Last, the drag coefficient is presented as a function of inclination and Bond number in figure 4.24.

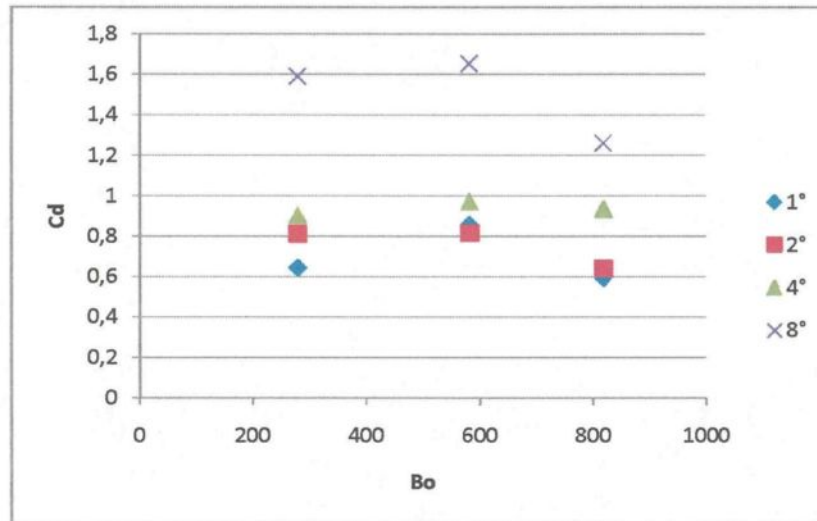


Figure 4.24 – Drag coefficient as a function of the Bond number and inclination

#### 4.3.6 Correlation between the contact size and cross-section size

In the regimes investigated, the bubbles were always large enough to maintain the Fortin shape. The contact shape of this kind of bubble is a circular segment, while in its cross-section a tall head and a long tail can be seen. In order to find a correlation between the dimensions of the contact shape and of the volume of the bubble, two approximations of the cross-section shape are suggested.



#### 4.3.6.1 Approximation with equivalent height

If we do not want to pay attention for the special shape, the bubble can be approximated by a circular segment with a rectangular cross-section, where the length of the rectangle is  $L$ , the length of the bubble in the cross-section and the height of the rectangle is  $H_e$ , the equivalent height (figure 4.25).

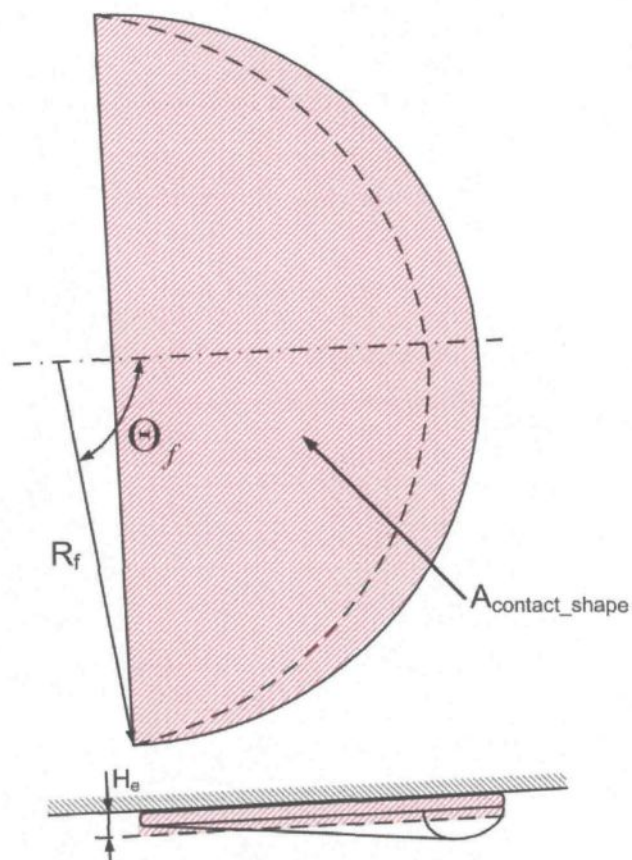


Figure 4.25 – Form approach to the Fortin bubble

The equivalent height is the height which will give an identical volume to real bubble volume by multiplying with the area of the contact shape. It can be calculated as follows:

$$H_e = \frac{V_{bubble}}{A_{contact\ shape}} \quad (4.6)$$

The area of the contact shape for a bubble can be easily calculated from its  $R_f$ , the radius of curvature at the front and  $\Theta_f$ , the angle of the front using the following equation:

$$A_{contact\ shape} = \frac{1}{2} \cdot R_f^2 \cdot \left( \frac{2 \cdot \pi \cdot \Theta_f^\circ}{180^\circ} - \sin 2 \cdot \Theta_f^\circ \right) \quad (4.7)$$

The contact size for all angles and volumes are presented in figure 4.26.

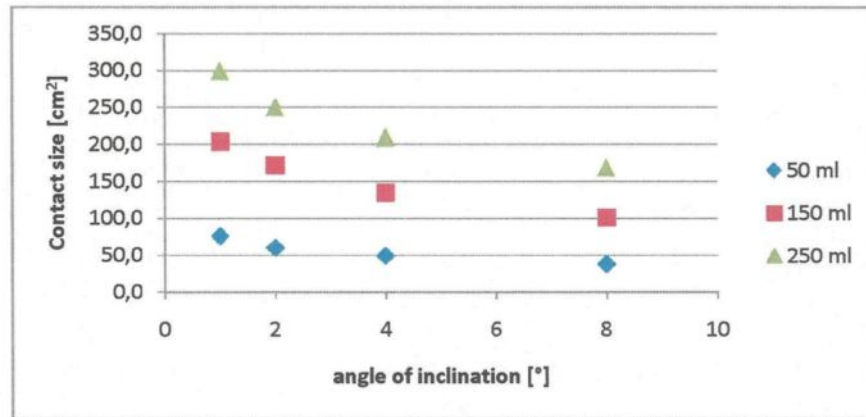


Figure 4.26 – Contact sizes

The calculated equivalent height for all angles and volumes can be seen in figure 4.27. The equivalent height depends on and is proportional to the angle of inclination and the bubble volume.

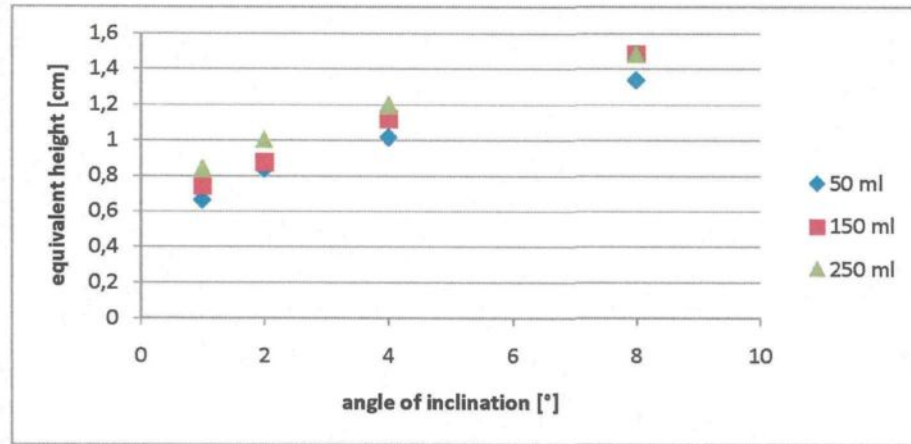


Figure 4.27 – Equivalent height

If the equivalent heights are plotted as a function of the contact size, we get figure 4.28.

This graph lets us calculate the volume of single bubbles in a bubble layer at a certain inclination if we know its contact size.

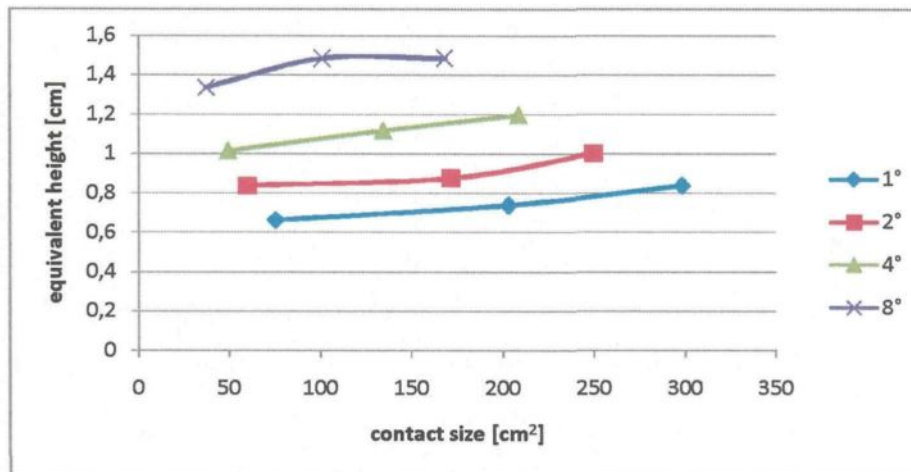


Figure 4.28 – Equivalent height as a function of the contact size



From figure 4.28 the correlation between the equivalent height, the area of the contact shape and the inclination angle can be determined as follows

$$H_e [cm] = (0.54 + 0.1 \cdot \alpha^\circ) + 0.0009 \cdot A_{contact\_shape} \quad (4.8)$$

where  $\alpha$  is the angle of inclination given in degrees and the contact size is given in  $cm^2$ .

#### 4.3.6.2 Exact form approximation with head and tail

An approximation of the equivalent height can be made when only the volume of the bubbles in the bubble layer is important and not the actual shape of them. If the actual shape is important, a more sophisticated approximation has to be applied. The Fortin shape can be approximated by an equivalent high circle segment and a body segment with a parabolic cross-section. The 2<sup>nd</sup> order parabola was chosen to approximate the head after observing numerous Fortin bubbles. In the cross-section, the front half of the Fortin head fits to a 2<sup>nd</sup> order parabola almost perfectly, while the end half part is close but never fits. The applied parabola in the Cartesian plane is defined by a second order equation which consists of a linear element in order to allow for asymmetry.

The volume of the circle segment can be calculated as before from the contact size, only now the height of the body is  $H_t$ , the mean thickness of the tail. The volume of the body

segment is calculated from the integral of the parabola segment along the  $\beta$  axis (figure 4.29).

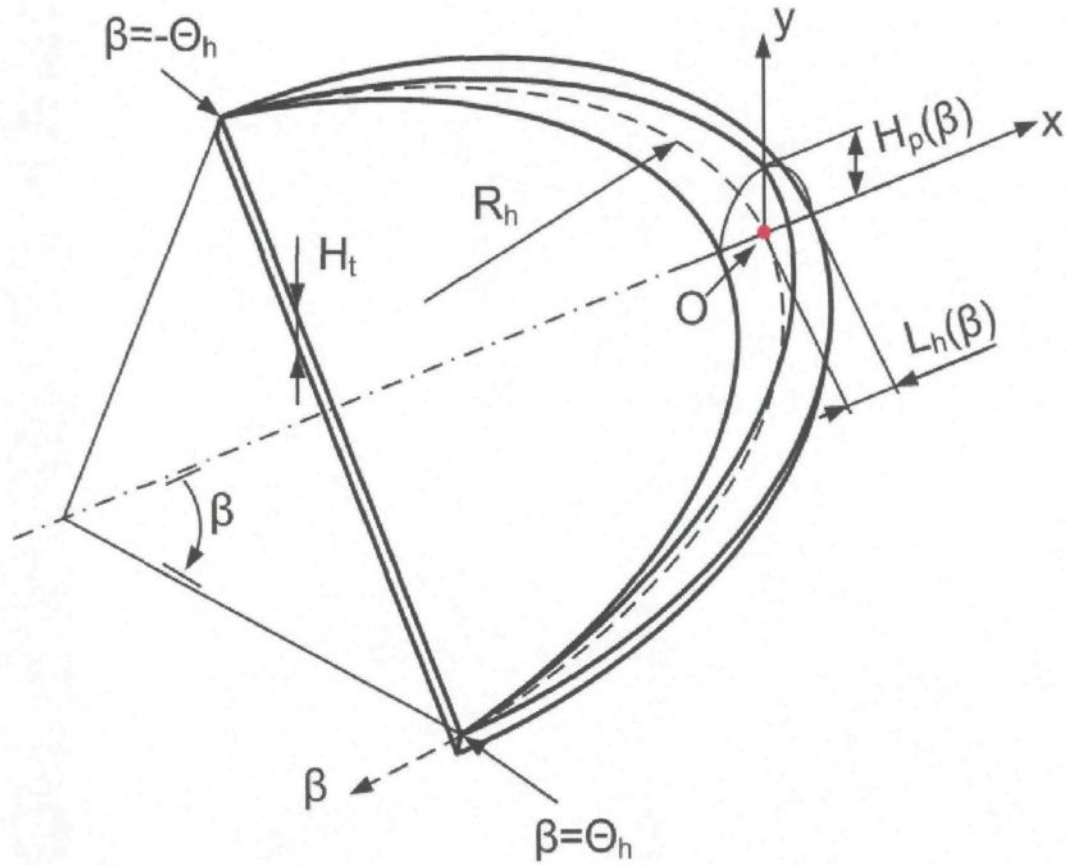


Figure 4.29 – Scheme for the exact form approximation with head and tail

The volume of the bubble can be calculated from the exact approximation as follows (see appendix A for details)

$$V_{bubble} = A_{contac\_shape} \cdot H_t + \frac{32}{21} \cdot H_{p_{max}} \cdot L_{h_{max}} \cdot R_h \cdot \frac{\pi \cdot \Theta_h^\circ}{180^\circ} \quad (4.9)$$

$$\text{where } H_p(\beta) = H_h(\beta) - H_t \quad (4.10)$$

The length and the height of the head changes along a parabola from  $\beta = -\Theta_h$  until  $\beta = \Theta_h$  and has its maximum at  $\beta = 0^\circ$ .

The resulting correlation was verified with measured data for  $2^\circ$  of inclination and the results are given in figure 4.30. The correlation gives a good approximation in the domain of our measurements.

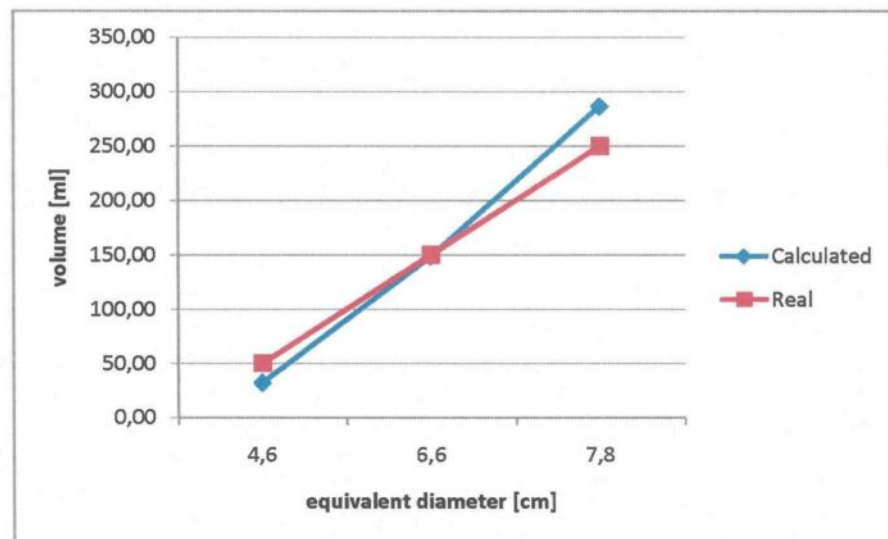


Figure 4.30 –Measured and calculated volumes using the exact form approach

#### 4.3.7 Forces acting on a moving bubble

It is well known that the shape of the bubble depends strongly on the properties of the liquid phase, the relative position of the bubble and the liquid and whether it is moving or stationary. The shape of a standing bubble is formed by the gravity and surface tension while a moving bubble frequently has a complex, three-dimensional shape which may or may not be static and this shape is controlled by several dynamic forces. Not only does the moving bubble create motion in the liquid around it but this bubble induced motion has a back-effect on the shape and velocity of the bubble itself. Among other forces, the inertia, buoyancy, surface tension, viscosity and drag force as well as momentum transfer control the shape and velocity of a moving bubble. The balance and importance of these forces gives the governing equations of the system to describe the motion of the bubble.

The importance of the inertia in controlling the velocity of the bubble becomes more important as the volume of the bubble increases. The role of the buoyancy increases as the volume of the bubble and angle of inclination increases, thus it is also more important for large bubbles. The effect of surface tension is not so evident. It is known that surface tension plays a significant role in the shaping of small bubbles. In the case of large bubbles the surface tension still tries to minimise the bubble surface but its effect may be weaker than the dynamic forces which also play a role in the shaping. The influence of the viscous forces decreases as the volume of the bubble decreases even though it plays an important role in the presence of the wetting film. As a bubble starts to glide under a solid surface the

liquid penetrates between the bubble and the surface and the bubble glides on this film not touching the surface. If the bubble is large enough, as in our experiments, this film evolves fast and it can be stated that the bubble glides only on the film and not on the surface. The viscous drag becomes important if the viscosity of the liquid is high.

To show the importance of the buoyancy force as a function of the angle of the inclination and the volume of the bubble, it was calculated for several volumes and angles and the results can be seen in figure 4.31.

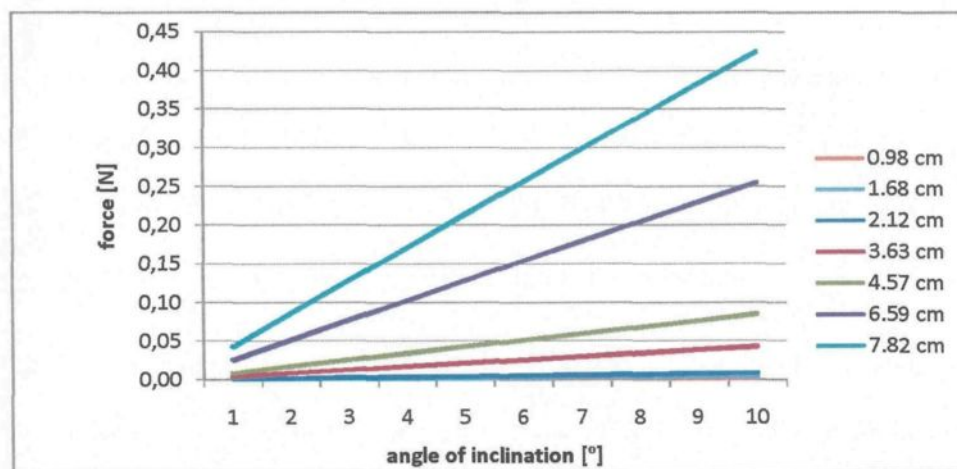


Figure 4.31 – Buoyancy force as a function of the inclination and equivalent diameter

The buoyancy is the force which accelerates the bubble, thus this force is directly proportional to the momentum transfer from the bubble to the bath and thus it plays a very important role in the onset of the Fortin head. As it was observed earlier, this head can be observed at the end of the oval oscillating bubble regime and all the regimes above this one (Perron *et al*, 2006). This means that either the angle of inclination or the bubble volume

has to be large enough in order to have the Fortin head. *Perron et al (2006)* measured different parameters of the moving bubbles and one of their results can be seen in figure 2.4. The different letters represent the different regimes where C is a semi-rigid bubble, D is an oval oscillating bubble, E is a deformable bubble and F is a bulged bubble. The bubble shape and the timing of the hydraulic jump onset depends on the angle of inclination and the bubble volume. For example, at low angles the head onsets at around 1.4 cm equivalent diameter while at higher inclinations the head can already appear on a small bubble with less than 1 cm equivalent diameter.

Combining figures 2.4 and 4.31, the limit for head onset can be calculated and it can be seen in figure 4.32.

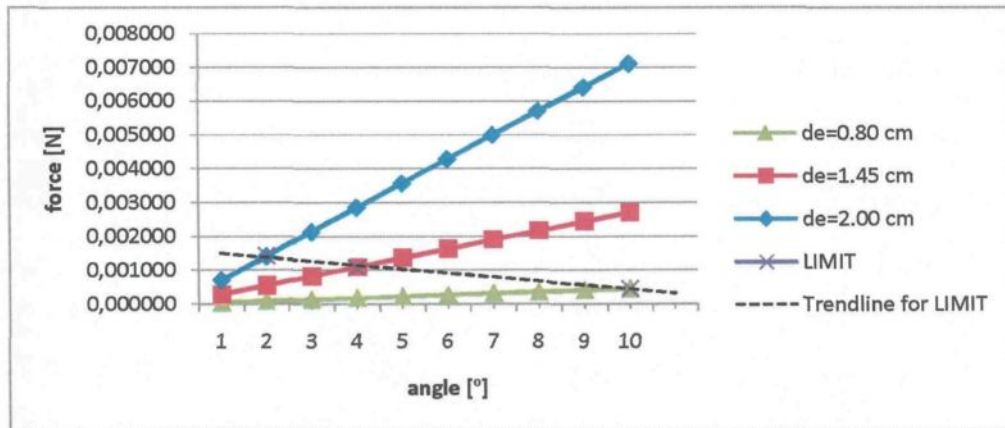


Figure 4.32 – Buoyancy force and limit of the force at head onsets

For the sake of simplicity we assumed that head onsets at the beginning of E regime. Since the head was observed only at the very end of the D regime this does not cause a significant error and makes our calculations easier. The diagram shows that the limit

buoyancy force needed for head onset is not monotonous for a certain size but it depends on the inclination. At a higher inclination smaller bubbles have heads. This implies that forces other than buoyancy are (also) important for head onset. Even though buoyancy is the accelerating force of the bubble, there are other phenomena at higher angles of inclination that lead to a higher velocity than buoyancy alone could achieve. The terminal velocity of a moving bubble under a surface is reached when the component parallel to the surface of the buoyancy force equals the drag force. Therefore, as the inclination grows the drag force decreases and a smaller force is enough to balance the reduced drag and to reach the terminal velocity. It has been shown that viscosity is only important for small bubbles at low inclinations (*Perron et al, 2006*).

#### **4.3.8 Fortin shape induced by a gravity wave**

Gravity waves always occur at the interface of two fluids moving at different velocities and with a significant difference between their velocities. The effect of gravity, which is isotropic in the horizontal plane, is important and the effect of surface tension is negligible for this wave.

This sort of wave is usually caused by a gas phase moving above a liquid phase, like the wind blowing above the ocean. If the velocity difference between the two phases is large enough, than the movement of the gas phase disturbs the equilibrium of the liquid phase by

displacing a certain amount of liquid parcel. This disturbance travels in the continuous phase as the gravity restores the displaced parcels toward equilibrium.

A gravity wave induces mainly a circular flow in the liquid and only a very slight forward movement. Only the momentum is carried forward by the wave. Also, the circular movement induced in the liquid by the wave stops at the depth of half a wavelength.

This wavy motion can be clearly observed at the bottom of the Fortin bubbles. As the air phase moves upwards due to the effect of buoyancy, the gas phase is accelerated. This high velocity disturbs the standing liquid which results in the observed gravity wave. The Fortin head is formed by the wave-front of the gravity wave which has a much larger amplitude than the smaller waves following the front. The circular motions were also observed under the Fortin bubbles in our experiments. The velocity field in our electrolysis cell model was measured using the PIV techniques; and the results are presented in chapter 5.4.

#### **4.3.9 Special shape and height of a Fortin bubble**

As previously mentioned, the large bubbles in our experiments always have the special Fortin shape with head taller than the tail. The bubble head is observed to form dynamically. Its presence depends strongly on the volume of the bubble and on the angle of



inclination. At too high an inclination and too low a volume the head cannot onset. A fast moving air phase induced gravity wave is also observed at the air-water interface.

There is a thick wetting film observed between the bubble and the surface. The bubble glides on this film without touching the surface, which leads to a higher velocity. The thickness of the film is proportional to the volume of the bubble and the angle of inclination.

The exact shape of a Fortin bubble can be seen in figure 4.33 and can be described as follows. The interface between the bubble and the wetting film is parallel to the surface. The movement of this interface is controlled by viscous dissipation.

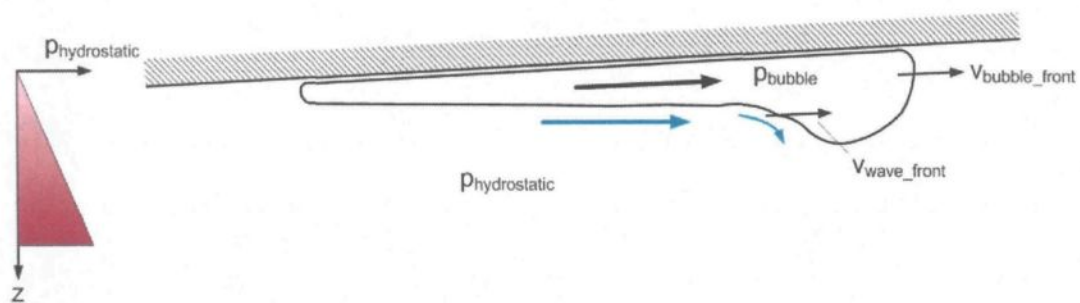


Figure 4.33 – Fortin shape and forces inducing the head

The movement of the bottom interface is vertical and is controlled by inertia. At this interface a gravity wave can be found which is induced by the movement of the air phase. This wave has small amplitude and large wavelength. Depending on the depth of the liquid phase, this gravity wave can be a shallow or deep water wave. If the depth of the liquid is less than half of the wave length it is called shallow water. The velocity of a gravity wave

in shallow water depends only on the depth of the liquid and it is proportional to the depth and is given in *Landau et al (1987)* as

$$c = \sqrt{g \cdot h} \quad (4.11)$$

where  $g$  is the gravitational acceleration and  $h$  is the depth of the water. The velocity of a gravity wave in deep water is proportional to the square of the wavelength and for a gravity wave moving in open water is given in *Landau et al (1987)* as

$$c = \sqrt{\frac{g \cdot \lambda}{2\pi}} \quad (4.12)$$

and for a gravity wave which onsets at the bottom of a bubble gliding under a solid surface is given as (for further details see appendix B)

$$c = \sqrt{\frac{g(\rho - \rho')h'}{\rho \cdot k \cdot h' + \rho'}} \cdot \left[ 1 - \frac{\rho \cdot k \cdot h'}{2 \cdot (\rho \cdot k \cdot h' + \rho')} \right] \quad (4.13)$$

where  $\lambda$  is the wavelength,  $h'$  is the depth of the bubble,  $\rho, \rho'$  is the density of the liquid and air phases respectively and  $k$  is the wave number given as

$$k = \frac{2\pi}{\lambda} \quad (4.14)$$

Figure 4.34 shows the wave velocity in deep water as a function of the wave length and bubble volume at inclination of  $2^\circ$  as calculated from (4.13).

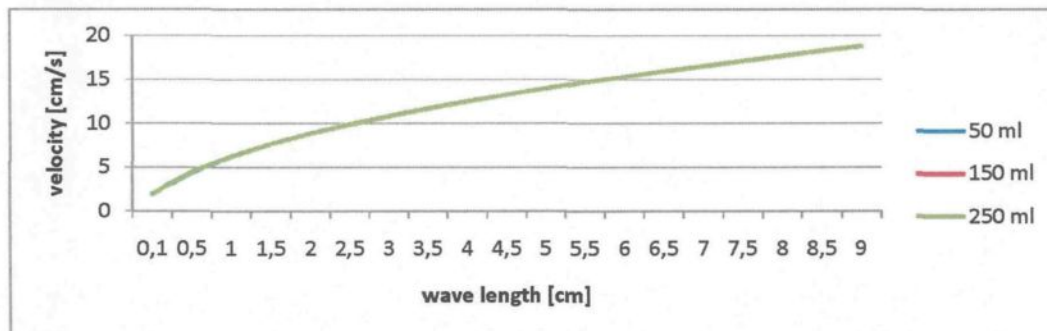


Figure 4.34 – Deep water wave velocity as a function of the wave length

During the measurements the wavelength of the gravity wave moving at the bottom of the bubble was roughly measured to be 6-7 cm for a large 150 ml bubble while moving under a surface with an inclination of  $2^\circ$ . This wavelength gives a wave velocity of around 15-16 cm/s. Similar velocity was measured at the front of the bubble for this size and inclination (figure 4.18).

As equation (4.13) and figure 4.34 shows, the wave velocity is independent of the length of the bubble and thus from the volume of the bubble and from the depth of the liquid, as it is treated as deep water.

The head of the bubble consists of two parts. The front of the head is almost perfectly circular. The back is part of the wave and similar to a moving hydraulic jump, where the hydraulic jump can be treated as example of gravity wave.

As the gas phase gains velocity it induces the gravity wave at the air-water interface and also has to push the water in order to move upward. As it gains velocity it has to push the water faster and thus has to transport higher momentum at the same time. The observed

half-circular shape leads to a smaller drag resistance and thus helps the bubble move faster. As the bubble moves faster, the dynamic pressure increases before the head. The pressure inside the bubble has to counterbalance this increased pressure. The Laplace-Young equation states that the excess pressure across a curved surface is proportional to the interfacial tension and the curvature of the surface. If the surface is flat, the curvature tends to infinity thus there is no pressure difference across the surface. As mentioned above, the bottom surface of the bubble is vertical and even though it is not flat, but disturbed by a gravity wave, the pressure difference is expected to be small. Thus the pressure in the bubble is equal to the hydrostatic pressure just under the bottom surface plus the ambient pressure. As the bubble gains velocity, the height of the front of the bubble, namely the head, increases to counterbalance the increased dynamic pressure at the front. As the pressure inside the bubble is uniform, the increased pressure at the front leads to an increased pressure at the tail too. Since the bottom part of the bubble can be considered flat, the pressure at this part is equal to the hydrostatic pressure. The hydrostatic pressure increases with depth, thus the height of the tail has to increase as the pressure increases inside the bubble. This explains the large heights we measured during our previous experiments and also the height of the tail of a Fortin bubble which is much higher than the height a standing bubble.

The height difference between the head and the tail induces a moving hydraulic jump where the water flows down from the top of the jump. The hydraulic jump moves with the speed of the gravity wave just behind the jump. The speed depends either on the water depth or the wave length. Either way its velocity is higher than the velocity of the bubble

measured at the front of the bubble. This means that the moving hydraulic jump pushes the air before itself thus helping to form the head and the circular shape at the front of the bubble.

#### **4.3.10 Momentum transported by a Fortin bubble**

The bubble induced flow is strongly influenced by the momentum transport between the bubble and the liquid. The momentum the bubble can transport to the fluid is proportional to its mass and velocity. The mass is linearly proportional to the volume, thus the larger bubbles have higher mass. The terminal velocity of a bubble depends on the volume of the bubble and the angle of inclination and is proportional to both. The kinetic energy of the liquid displaced by different size bubbles moving with their terminal velocity can be seen in figure 4.35. The kinetic energy increases with an increasing angle of inclination and bubble volume.

When the bubble is too small, its kinetic energy is too small which restrains the bubble from inducing a gravity wave and thus from forming a Fortin shape.

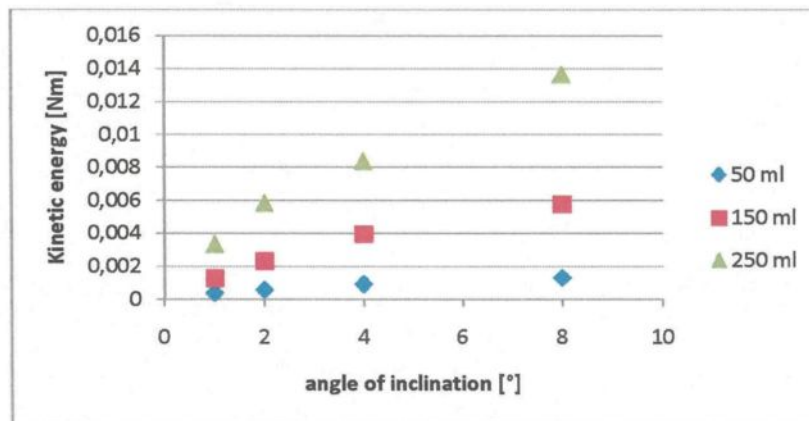


Figure 4.35 – Kinetic energy as a function of the volume of the bubble and the angle of inclination of the surface

#### 4.3.11 Theory of similarity

A similarity study has been performed in order to transfer the experimental results to a real industrial cell conditions. In the given situation two dimensionless groups, the Froude number and the Archimedes number, play an important role.

The Froude number gives the ratio of the inertia force to the gravitational force. For a system where a bubble moves under an inclined plate this number is given as

$$Fr = \frac{u_r}{\sqrt{g \cdot L \cdot \sin \alpha}}, \quad (4.15)$$

where,  $g$  is the gravitational acceleration,  $L$  is the characteristic length of the bubble,  $u_T$  is the terminal velocity and  $\alpha$  is the angle of inclination of the plate. This number is the hydrodynamic equivalent of the Mach number.

The choice of the characteristic length depends strongly on the given system. In the case of a Fortin bubble two Froude numbers should be calculated; one for the tail and one for the head. The ratio of these two Froude numbers gives information about the formation of the head. This is also the characteristic ratio for a hydraulic jump. The characteristic length is the mean thickness of the tail and the height of the head. The ratio of the Froude numbers is as follows

$$\frac{Fr_{tail}}{Fr_{head}} = \frac{\frac{u_{wave\_front}}{\sqrt{g \cdot H_t \cdot \sin \alpha}}}{\frac{u_T}{\sqrt{g \cdot H_h \cdot \sin \alpha}}} = \frac{u_{wave\_front}}{u_T} \cdot \sqrt{\frac{H_h}{H_t}} \quad (4.16)$$

The Archimedes number determines the motion of fluids due to density differences and is given as

$$Ar = \frac{g \cdot L^3 \cdot \rho_l \cdot (\rho_g - \rho_l)}{\mu^2} \quad (4.17)$$

where  $\mu$  is the dynamic viscosity,  $\rho_l$  and  $\rho_g$  is the density of the liquid and gas phases, respectively. The characteristic length for the Archimedes number is the equivalent diameter of the bubble which can be calculated as

$$d_s = \sqrt[3]{\frac{6 \cdot V_p}{\pi}} \quad (4.18)$$

where  $V_p$  is the volume of the bubble.

According to these differences between the real cell and the air-water model, similar bubble shapes and movement are expected in a real electrolysis cell with some changes. Because of the high viscosity and density of the molten cryolite, the amplitude of the gravity wave is expected to be smaller. The terminal velocity is also expected to be smaller in the real cell. The exact values of the different parameters for the two systems can be seen in table 4.1.

	Cell model	Real cell	Dimension
<b>Density</b>	water at 7°C: 999.856 air at 20°C: 1.204	alumina-cryolite melt at 960°C: 2150 CO <sub>2</sub> at 960°C: 0.4	kg/m <sup>3</sup>
<b>Surface tension</b>	water - air: 7.28e-2	cryolite - CO <sub>2</sub> : 6e-2 – 20e-2	N/m
<b>Dynamic viscosity</b>	water: 1.4343e-3 air: 1.83e-5	cryolite: 1.5e-3	kg/m·s
<b>Morton number</b>	water: 1.078e-10	cryolite: 2.15e-11	-

Table 4.1 – Parameters in the model and in the real system



#### 4.4 Conclusions

Experiments with single large Fortin air bubbles gliding in water under a slightly inclined surface were performed. Different angles of inclination and volumes of bubble were used in the experiments. The objectives were to understand the formation and movement of large Fortin bubbles.

The Fortin shape of the different size bubbles was observed in the transversal plane and in the surface plane. The contact shape at each angle and volume is similar to a sector of a circle. The curvature at the front is always positive while at the rear it is either positive or infinitive. The rear oscillates. The head is always at the front of the bubble and its dimensions are very stable. The tallest point of the head is measured at the middle of the front of the bubble. From the middle of the bubble towards the lateral edges the dimensions of the head decrease gradually. Independent of the velocity of the air release, in our experimental setup the initial contact shape was always the same; the initial butterfly shape changed into the final shape in less than 1 sec.

The dimensions of the bubble depend on the volume of the bubble. Increasing the volume increases the width, length and height. The length of the head remains proportional to the volume of the bubble. The effect of the angle of inclination is different from the effect of the volume. As the angle increases, the width and the length of the bubble decrease. However, the bubble height and the head height increase as the angle increases. A slight increase in the length of the head can also be measured. As the volume grows, each

bubble dimension increases. However, as the angle increases, the bubble becomes more compact with a smaller cross-section and a larger height. The aspect ratios ( $W/L$ ,  $H_i/H_h$ ,  $W/H_h$ ) decrease with an increasing angle. On the other hand, the ratios do not seem to depend on the bubble volume if it is  $\geq 150$  ml.

The radius of curvature of the front and at the tallest point of the head decreases with increasing angle and decreasing volume. While the angles of the front and head are less dependent on bubble volume, they do increase slightly with increasing inclination.

If due to some irregularities on the solid surface the bubble runs onto a dry spot, it loses its momentum and slows down. As the bubble slows down, it “loses” its head. This supports the hypothesis that the higher height and the head are induced by the motion of the bubble and moreover by its fast motion.

The terminal velocity increases with an increasing angle, but only increases slightly with an increasing bubble volume. However, the dimensionless terminal velocity, the Froude number does not depend on the volume of the bubble because the increase in the terminal velocity and the increase in volume compensate each other. However, it does depend on and is inversely proportional to the angle of inclination.

It was found that the drag coefficient only slightly depends on the size of the bubble and increases with increasing inclination. The drag coefficient is constant as a function of the Reynolds number in the studied regime. Therefore the motion of the bubble is principally controlled by the inertia.

Two approximations of the Fortin shape were suggested in order to develop a correlation to calculate the volume of the bubble. First the bubble can be approximated by a circular segment by a rectangular cross-section with an equivalent height. The equivalent height is proportional to the inclination but quite independent from the volume of the bubble. Correlation between the equivalent height, the area of the contact shape and the angle of the inclination was determined. The exact form approximation consists of an equivalent high circle segment and a body segment with a parabolic cross-section. Again, the correlation between the contact size and the bubble volume was calculated.

The limit, the buoyancy force needed for head onset is not monotonous for a certain size but depends on the inclination. At higher inclinations smaller bubbles can form heads. As the inclination increases, the drag decreases so a smaller force is enough to balance it.

At the bottom interface of the bubble tail a gravity wave can be found which is induced by the movement of the air phase. The back of the head is part of the wave. As the air moves upwards under the surface it has to push the water away. The observed half-circular shape of the front leads to a smaller drag resistance and thus helps the bubble move faster. As the bubble gains velocity, the height of the bubble increases to counterbalance the increased dynamic pressure at the front.

The height difference between the head and tail induces a moving hydraulic jump where the water flows down from the top of the jump. The hydraulic jump moves faster than the front of the bubble and pushes the air before itself.

Based on a comparison between a real cell and the air-water model, similar bubble shapes and movement are expected in a real electrolysis cell.

#### 4.5 References

- Fortin, S., Gerhardt, M., and Gesing, A.J., *Physical modelling of bubble behavior and gas release from aluminium reduction cell anodes*, TMS Light Metals, pp 721-741 (1984)
- Gaudin, A.M., *Flotation*, 2<sup>nd</sup> ed., McGraw-Hill, New York (1957)
- Landau, L.D. and Lifshitz, E.M., *Fluid Mechanics, Second Edition: Volume 6*, Butterworth-Heinemann, 552 pages (1987)
- Perron, A., Kiss, L. I. and Poncsák, S., *An experimental investigation of the motion of single bubbles under a slightly inclined surface*, Int. J. Multiphase Flow, vol. 32, pp. 606-622 (2006)
- Pruppacher, H. R., and Klett, J. D., *Microphysics of clouds and precipitation*, Boston, D. Reidel, 714 pages (1978)

## **Chapter 5**

# **BUBBLE LAYER AND FLOW INDUCED BY A BUBBLE LAYER IN A REAL-SIZE ELECTROLYSIS CELL MODEL**

This chapter is based on the following articles:

Vékony, K. and Kiss, L., *Velocity measurements in a real size model of an aluminium electrolysis cell using PIV techniques*, submitted to Journal of Applied Electrochemistry

Vékony, K. and Kiss, L., *Morphology of two-phase layers with large bubbles*, submitted to Journal of Metallurgical Transactions

Vékony, K. and Kiss, L., *Experimental study of the morphology and dynamics of gas-laden layers under the anodes of aluminium reduction cells*, submitted to Journal of Metallurgical Transactions

## 5.1 Objectives

The bubbles nucleated during aluminium reduction play a significant role in the mass and momentum transfer in the cell. Thus the understanding of formation and movement of the bubble layer is essential for a good control of the electrolysis process. The anode bottom covered by bubbles reduces the efficient surface to carry current and the movement of the bubbles induces instabilities in the bath. One of the main objectives of this work is to understand the role of the bubbles and especially the large Fortin bubbles in the electrolysis cell and their effect on the process of aluminium electrolysis and most importantly on the resistance of the cell and on the bubble driven flow.

In order to achieve our goals the formation and movement of the bubble layer under a slightly inclined anode is observed and the bubble induced flow is measured qualitatively. During the experiments the volume distribution of the bubbles in the bubble layer as a function of the current density and angle of inclination is measured. The Fortin bubbles, their formation and movement in the bubble layer are observed. Special effects, such as the sweeping effect, the escape of large bubbles are observed and measured qualitatively.

## 5.2 Series of experiments

For these physical experiments the real-size air-water model introduced in chapter 3.2.2 is used. Different current densities and angles of inclination of the anode are used in order to determine the correlation between the angle and current density and different measured parameters of the bubble layer.

Videos using digital cameras from the side and in a mirror showing the bottom are made to observe the bubble layer. Current densities used in the experiments recorded from the side are shown in table 3.1. The angle of inclination is kept at  $1^\circ$ . A recording with the fast camera is also made from the side in order to observe the formation of the Fortin shape. Four different current densities (0.2360, 0.4864, 0.7152 and  $1.0013 \text{ A/cm}^2$ ) and five different angles of inclination ( $1^\circ$ ,  $2^\circ$ ,  $4^\circ$ ,  $6^\circ$  and  $8^\circ$ ) are used for the measurements made in the mirror. The recordings are transferred onto a computer where they are analyzed as described in chapter 3.2.4.

PIV techniques are used at  $1^\circ$  and  $2^\circ$  of inclination and  $1.0013 \text{ A/cm}^2$  current density to observe the bubble induced flow. These measurements are recorded directly onto a computer where they are analyzed as described in chapter 3.2.4.

## 5.3 Bubble layer under a solid surface

Because of the recording method used in the real-size electrolysis cell model with the digital camera, the calculated heights should be handled as statistical data and the

importance of an individual datum should not be overestimated. Moreover, it has to be emphasized that in the video recordings made from the side all the bubbles under the anode can be seen, not only the bubbles at the front. This means that the higher bubbles dominate the videos and increase the average height of the bubble layer. Thus the measurement is a special representation of the bubble layer under the anode model. While this method of evaluation does not seem to have increased the maximal height, the average height is increased significantly.

### **5.3.1 Flow regimes under the anode**

The different flow regimes of the bubbly flow under the anode have not yet been defined in the literature. During our experiments three different regimes, sparse bubble layer, dense bubble layer and gas-pocket dominated bubble layer, were observed which can be seen in figure 5.1.



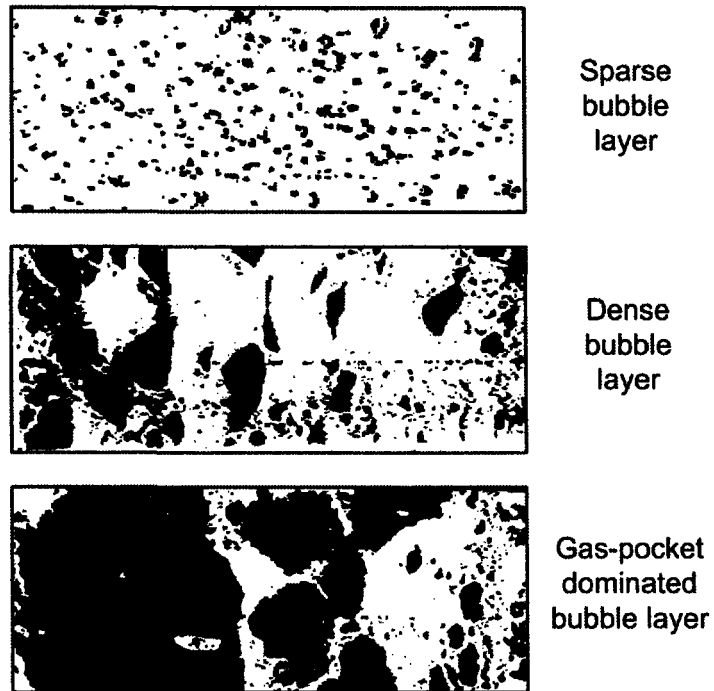


Figure 5.1 – Flow patterns under the anode

The regimes are characterised as follows:

- *Sparse bubble layer.* The liquid phase is continuous under the anode while a dispersion of small gas bubbles flows under the anode. The equivalent diameter of the bubbles is much smaller than the mean distance between two bubbles. The bubbles have no effect on each other since the bubble induced flow in the liquid fades away before the arrival of a new bubble. No Fortin bubble can be observed. Only a small part of the anode bottom is covered by bubbles.

- *Dense bubble layer.* There are several mid to large sized bubbles, usually with Fortin heads, and a large number of small bubbles. The size and shape of the bubbles are diversified. The distance between two bubbles is approximately equal to the mean equivalent diameter of the bubbles. The bubbles and the bubble induced flow have an effect on the other bubbles. A moderate fraction of the anode bottom is covered by bubbles.
- *Gas-pocket dominated bubble layer.* The anode is covered by a few very large bubbles which always have a Fortin head and a large number of small bubbles. A large bubble can cover the fourth or fifth of the anode bottom. Again the size and shape of the bubbles are diversified. The distance between two bubbles is smaller than the mean equivalent diameter of the bubbles. The motion of the bubbles affects strongly the other bubbles. The majority of the anode bottom is covered by bubbles.

The onset of a regime depends on the rate of gas generation and the angle of inclination of the anode.

### **5.3.2 Covering factor as a function of the gas generation and angle of inclination**

The covering factor is known to be important in the aluminium electrolysis process. The area of the anode bottom covered by gas has a higher electrical resistivity. Since the

electrical flow cannot pass through the bubbles, they increase the ohmic resistance of the bath and thus increase the energy consumption of the process. It was shown by *Perron et al (2007)* that overvoltage due to the presence of the bubbles depends on the contact size of the bubbles but not on the shape of single bubbles. The covering factor thus directly shows the decrease of the efficient area of the anode. The covering factor is given by the ratio of the total contact size of the bubbles to the total size of the anode bottom, as follows:

$$C = \frac{\sum_n A_{contact,n}}{A_{anode}} \quad (5.1)$$

where  $n$  is the number of bubbles under the anode. In our experiments the size of the anode bottom is  $A_{anode} = 0.5 \text{ m}^2$ .

As it is expected, the covering factor depends on the current density, the angle of inclination and the position under the anode, where the position under the anode is measured from the inner edge to the outer edge of the anode bottom. Increase in the inclination or decrease in the current density decreases the covering factor. Also, under the inner edge of the anode bottom the covering factor is smaller than under the outer edge, where the bubbles are also larger due to the continuous coalescence. The following three aspects of the covering factor were examined: the minimum and maximum covering factors and the maximum difference between the minimum and maximum values. Since the gas generation is continuous under the anode, large numbers of bubbles are accumulated. These bubbles glide and coalescence, thus forming different sized bubbles. Under the outer edge of the anode, large gas pockets can be observed frequently. Such a large bubble can cover a

fourth of the anode bottom which significantly increases the covering factor. When such a large bubble escapes from under the anode, the covering factor decreases significantly. This change of the covering factor in time can be measured. The minimum and maximum covering factor can be determined from this change in time and also the maximum fluctuation of the covering factor. The maximum fluctuation is calculated as the difference between the maximum and minimum covering factors.

Figure 5.2 shows the minimum covering factor as a function of the current density and angle of inclination, while figure 5.3 shows it as a function of the position under the anode and current density at  $1^\circ$ . The minimum covering factor shows a slight decrease with an increase in the angle of inclination and an even slighter decrease with a decrease in the current density. A decrease of the minimum covering factor with inclination is observable only from  $1^\circ$  to  $2^\circ$ . Further change in the angle of inclination does not change the minimum covering factor significantly at a given current density.

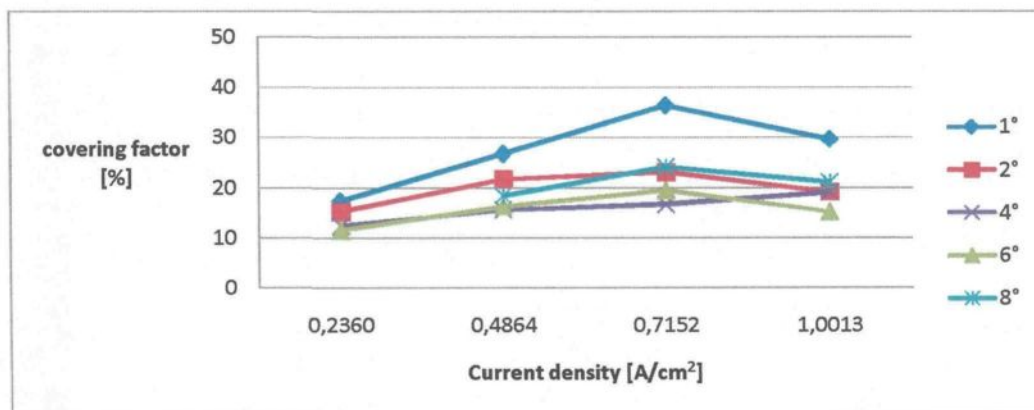


Figure 5.2 – Minimum covering factor as a function of the current density and angle of inclination

On the other hand, the minimum covering factor shows a special dependency on the position under the anode (figure 5.3). It is known that the bubbles are generated at a quasi-uniform rate under the entire anode. There are a large number of small bubbles under the inner edge of the anode. As these bubbles glide and coalesce, they form larger bubbles. The covering factor of the small bubbles depends on the current density and is linearly proportional to it. As the bubbles start to coalesce, larger bubbles form, which are taller than the small bubbles. Even though there is more gas under the second section of the anode, the larger height leads to smaller contact size and thus smaller covering factor in this section. As the gas volume increases further due to the continuous gas generation, the covering factor increases under the third section. Under the last section, the outer edge, of the anode bottom really large gas pockets can be frequently observed. These large bubbles leave the anode periodically. This continuous gas escape leads to a slightly smaller covering factor under the outer edge of the anode, a phenomenon observed at each current density with the exception of the highest one. At the highest density, the bubbles are frequently so large that they easily cover the last section, the outer edge, of the anode. Since the escape of this bubble takes place very fast, it leaves this section almost empty for a short time leading to a small covering factor (see the discussion about the sweeping effect in chapter 5.3.10).

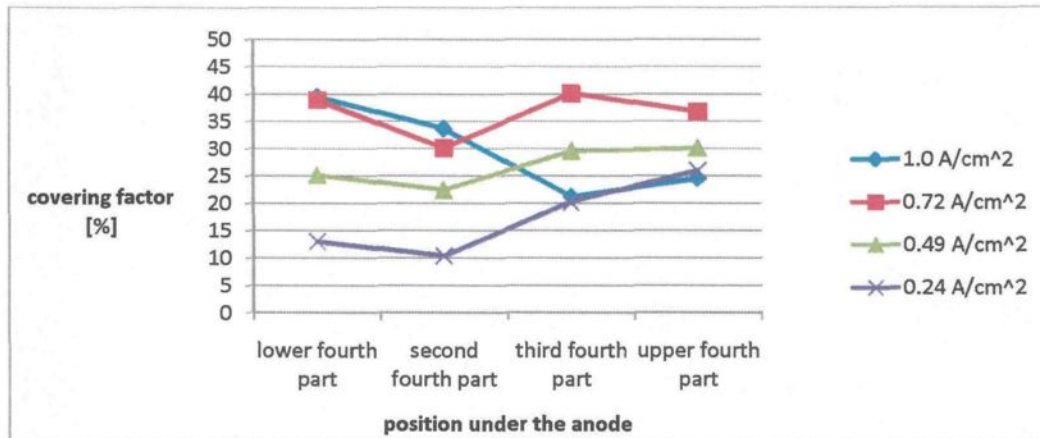


Figure 5.3 – Minimum covering factor as a function of the position under the anode at 1°

Figure 5.4 shows the maximum covering factor as a function of the current density and angle of inclination, while figure 5.5 shows it as a function of the position under the anode and current density at 1°. The maximum covering factor is inversely proportional to the angle of inclination and proportional to the current density. The maximum covering factor depends strongly on the current density. For example, the maximum covering factor is only 35% at 1° at the lowest current density, while it is around 80% for the highest current density. This is a really significant increase. The effect of the current density is stronger at low inclination and an increase in the inclination decreases the influence of the current density. At the highest inclination, the increase in the maximum covering factor with the current density is only around 10 %. The effect of the inclination is also observable at low angles only, between 1° and 4°, while a further increase in the inclination does not change the maximum covering factor.

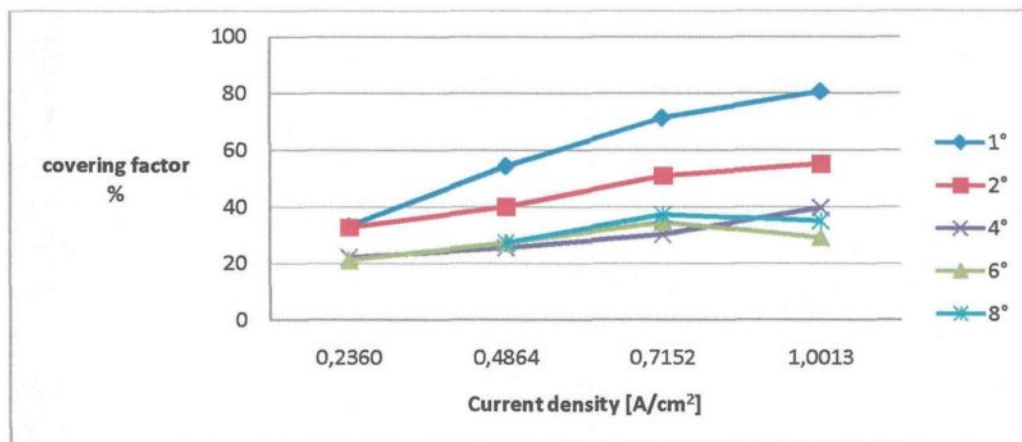


Figure 5.4 – Maximum covering factor as a function of the current density and angle of inclination

Contrary to the minimum covering factor, the maximum covering factor shows a simple correlation with the position under the anode. As the volume of gas increases and the bubbles coalesce, the maximum covering factor increases. Also, the maximum covering factor is proportional to the current density. The more bubbles are nucleated under the anode, the higher the covering factor is.

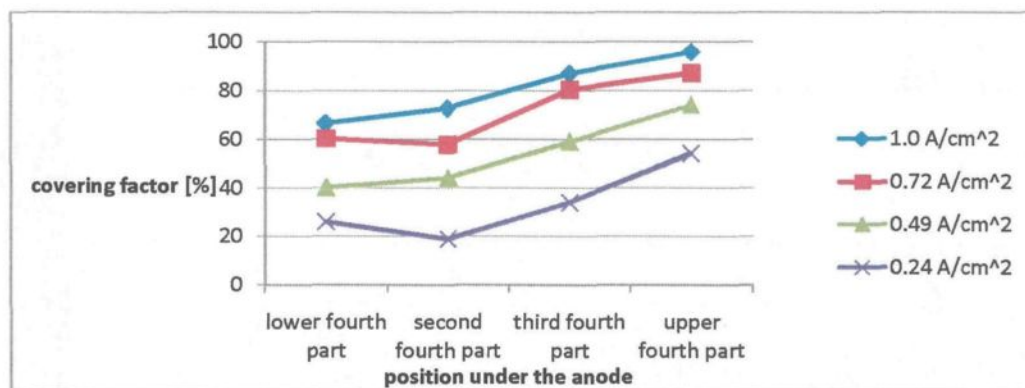


Figure 5.5 – Maximum covering factor as a function of the position under the anode at 1°

The maximum fluctuation in the covering factor shows the same relation with the angle, current density and position under the anode as the maximum covering factor does (figure 5.6). It decreases with increasing angles between  $1^\circ$  and  $4^\circ$ . Further changes in the inclination do not affect the maximum fluctuation. An increase in the current density increases the maximum fluctuation. It is very important to note that the maximum fluctuation can reach as high as 80 % under the outer edge of the anode. It means that at one moment 90% of this section of the anode is covered by bubbles or mostly by one large bubble, while at the next moment only 10% of it is covered. This leads to a very fluctuating magnetic field which has a significant effect on the operation of the electrolysis cell.

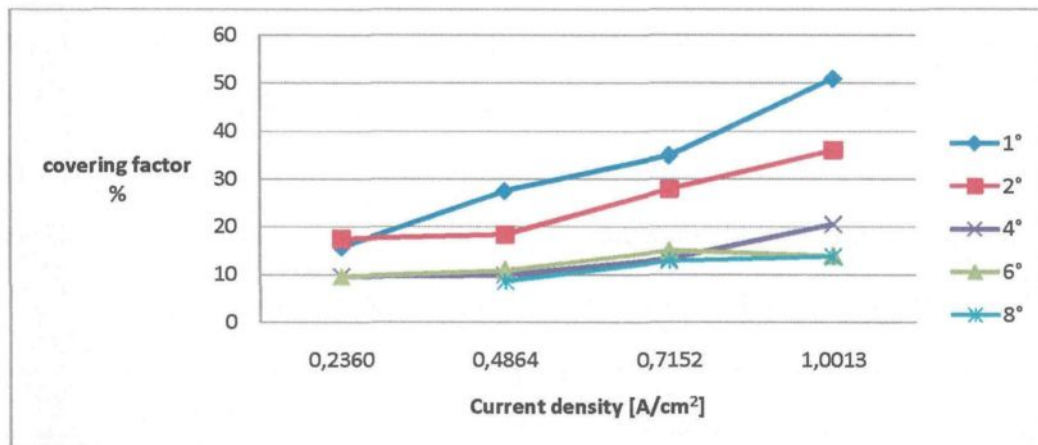


Figure 5.6 – Difference between the minimum and maximum covering factors as a function of the current density and angle of inclination

The fluctuation of the covering factor during time under the outer edge of the anode at the highest current density and at  $1^\circ$  can be seen in figure 5.7. The fluctuation of the covering factor is significant and fast. The peaks show the presence of a large bubble under



this section of the anode, while the troughs correspond to the escape of the bubble. The duration of the formation and escape of a large bubble is short and its frequency for this case is less than 1 Hz.

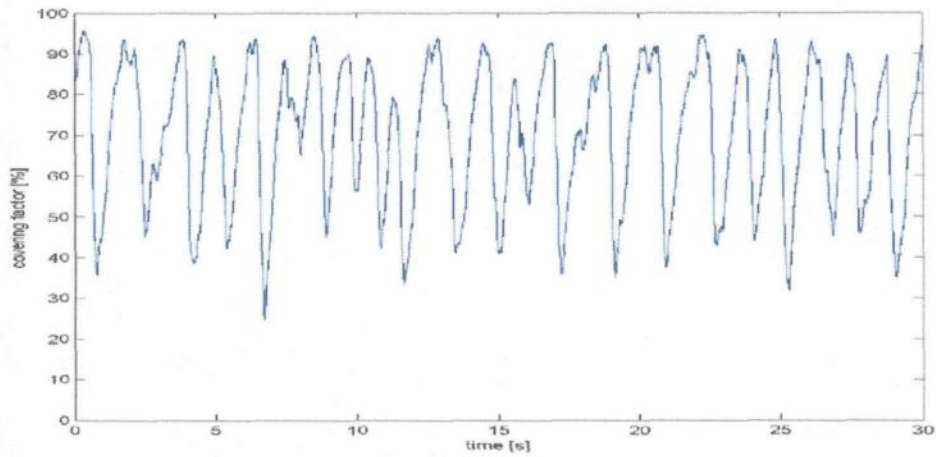


Figure 5.7 – Fluctuation of the covering factor under the outer edge of the anode at the highest current density

The mean value of the covering factor is calculated as

$$\bar{C} = \frac{1}{n} \sum_{i=1}^n C_i \quad (5.2)$$

where  $C_i$  is the value of the covering factor at a moment and  $n$  is the number of samples and the standard deviation, also known as the root mean square deviation of values from their arithmetic mean, which is calculated as

$$\sigma = \sqrt{\frac{1}{n} \sum_{i=1}^n (C_i - \bar{C})^2} \quad (5.3)$$

The mean covering factor and RMS as a function of the current density can be seen in figure 5.8 for 1° of inclination. They are both proportional to the current density and increase quasi-linearly with it.

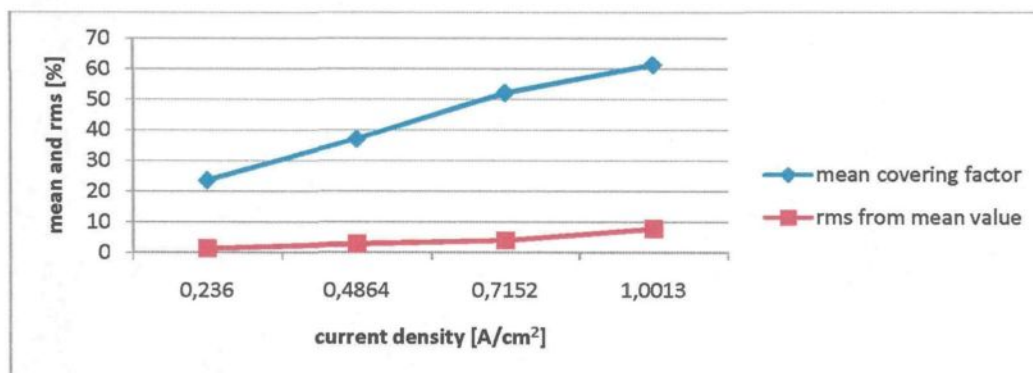


Figure 5.8 – Mean covering factor and standard deviation from its arithmetic mean value (RMS) at 1° of inclination

### 5.3.3 Contact size as a function of the current density and angle of inclination

The contact size of a moving bubble is measured in the contact plane, that is to say the plane of the anode bottom. If a solid spot exists between the bubble and the surface, the contact size is the size of this dry spot. When a bubble moves under a solid surface, there is a thin wetting film between the bubble and the surface and no dry spot. The contact size is now the size of the perpendicular projection of the bubble to the anode bottom. This is what we can see if we look perpendicular to the surface.

The mean contact size of the bubbles and the distribution of the contact sizes depend on the current density, the angle of inclination and the position under the anode.

As mentioned above, four videos were made of the anode bottom and these recordings, each showing approximately one fourth of the anode, were analyzed separately. They were named inner edge, second section, third section and outer edge. The complete size of the anode bottom is  $5000 \text{ cm}^2$ , thus a quarter section of it is  $1250 \text{ cm}^2$  large. Naturally, this limits the maximum contact size which can be seen in a single recording to  $1250 \text{ cm}^2$ . At times, up to a quarter of the anode can be completely covered by a large bubble. This large bubble often has a bigger contact size than  $1250 \text{ cm}^2$ . The maximum area which can be seen in a single recording has to be kept in mind when looking at the results in tables 5.1 and 5.3. A recording was also made of the whole anode bottom and this video was used to obtain the real contact sizes shown in tables 5.2 and 5.4.

As the bubbles are nucleated quasi-uniformly, there are a large number of small bubbles everywhere under the anode. As the bubbles detach from the anode and start to glide, they collide, coalesce and form larger and larger bubbles. This leads to a non-uniform contact size distribution under the anode. Table 5.1 shows that there are a large number of small bubbles under the inner edge of the anode where the maximum contact size is not too large. As the bubbles coalesce, they form larger bubbles under the second section of the anode, but still the small bubbles prevail. Under the third section, the contact size of the bubbles is quite uniform and the maximum contact size increased. As the bubbles keep coalescing, a few but huge bubbles dominate the outer edge of the anode bottom.

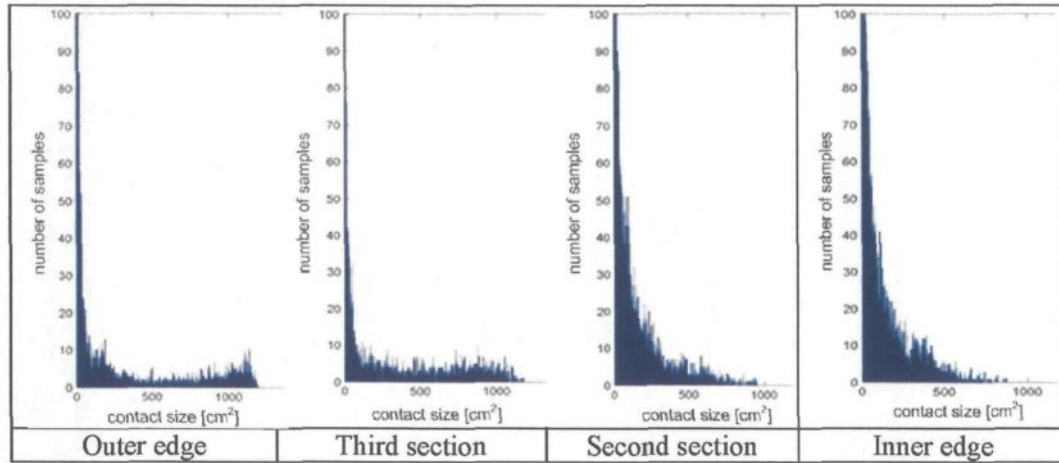


Table 5.1 – Contact size [ $\text{cm}^2$ ] distribution under the anode bottom (current density= $1.0 \text{ A/cm}^2$ ; angle= $1^\circ$ )

As it was expected, the volume of the bubbles and thus their contact sizes are proportional to the current density. Table 5.2 shows the contact size distribution under the whole anode for each current density at  $1^\circ$  of inclination. The maximum contact size decreases with decreasing current density. Also, the pattern of the contact sizes changes with decreasing gas generation. As the gas generation decreases, fewer large bubbles form, consequently large bubbles do not dominate, not even under the outer edge of the anode. Additionally, the small bubbles dominate the outer edge of the anode at the two lowest current densities.

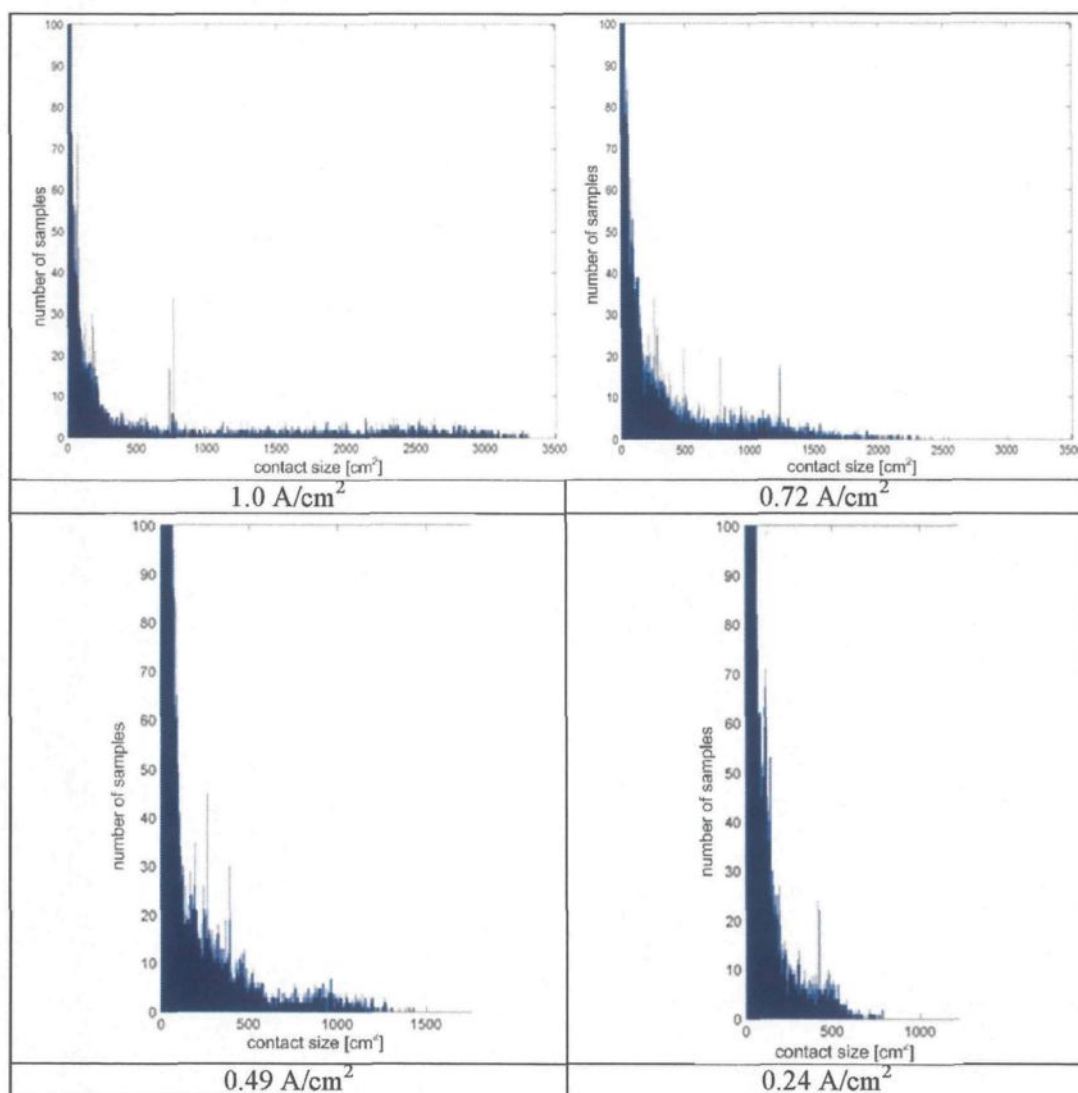


Table 5.2 – Contact size [ $cm^2$ ] distribution under the anode bottom (angle= $1^\circ$ )

The contact size distribution also depends on the angle of inclination of the anode. An increase in the angle decreases the maximum contact size significantly (tables 5.3 and 5.4). As the angle increases, the bubble moves faster due to the larger buoyancy force and less coalescence occurs. This leads to smaller sized bubbles. Also, as with the current density,

the pattern of the contact size distribution changes with the angle. At high inclination, again, the small bubbles dominate the outer edge of the anode.

Once again, inclination only has an effect at low angles, whereas changes in the angle over  $6^\circ$  have only a minor effect. As the angle increases from  $1^\circ$  to  $2^\circ$ , the maximum contact size decreases from  $3250 \text{ cm}^2$  to  $1900 \text{ cm}^2$  which is a significant 42% decrease. If we consider the equivalent height of the bubble to be 1 cm for this contact size at  $1^\circ$  and  $1.0 \text{ A/cm}^2$  current density, then the volume decrease is 1.35 liter.

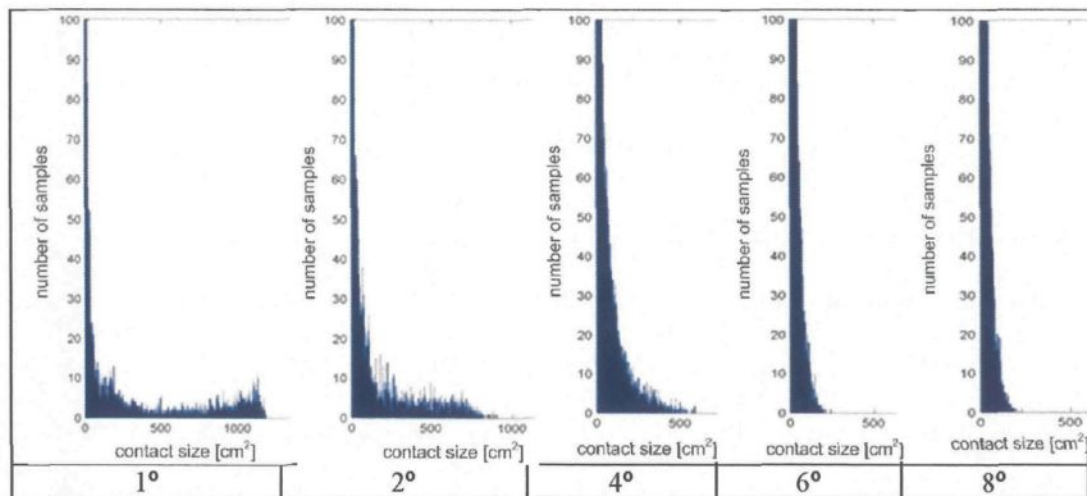


Table 5.3 – Contact size [ $\text{cm}^2$ ] distribution under the outer edge as a function of the angle of inclination (current density= $1.0 \text{ A/cm}^2$ )



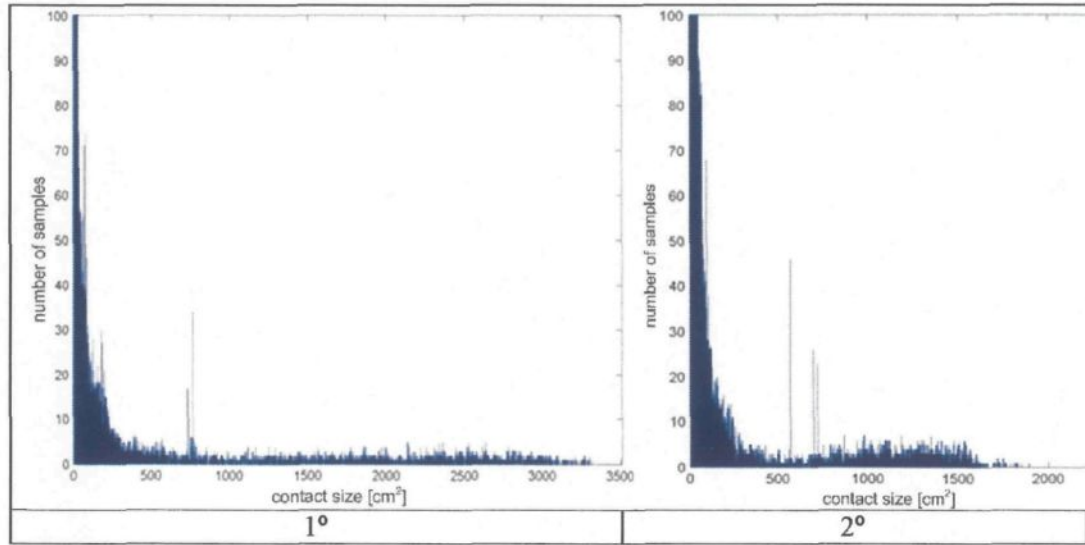


Table 5.4 – Contact size [cm<sup>2</sup>] distribution under the whole anode as a function of the angle of inclination (current density=1.0 A/cm<sup>2</sup>)

#### 5.3.4 Height of the bubble layer and bubbles

The time average and maximum heights of the bubble layer are defined as follows. Approximately 30 second long videos were made at each 20 centimetre segment of the anode. At each image pixel of the anode bottom the average height of the bubble layer was calculated using the following formula.

$$h_{average}^p = \frac{\sum_{i=1}^N h_{measured}^p}{N} \quad (5.4)$$

where  $N$  is the number of the frames in the video,  $h_{measured}^p$  is the height measured at the  $p$ th pixel of the anode bottom and  $h_{average}^p$  is the calculated time average height at the same pixel. This height is calculated in each pixel point of the anode bottom, thus this is the local average height of the bubble layer.

The local maximum height,  $h_{maximal}^p$ , is also measured at each image pixel of the anode bottom. It is chosen to be the maximum measured height value from the  $N$  measured  $h_{measured}^p$  at each pixel.

The local average and local maximum heights were measured and calculated for each gas generation rate used during the experiments and the two heights and their ratio (maximum to average height) can be seen in figures 5.9-5.14.

#### **5.3.4.1 Local average height and terminal value of the average height of the bubble layer**

As it is shown, the height of a stationary bubble under a downward face increases with increasing bubble volume until it reaches its maximum height, beyond which the bubble cannot grow. Should the volume continue to increase, the bubble will grow horizontally instead of vertically. At first thought similar behaviour is expected from the moving



bubbles - after reaching the maximum height, the height of a moving bubble will not increase, even if its volume increases.

At a high gas generation rate, a large number of small bubbles are nucleated under the anode, which often leads to the formation of large bubbles and air pockets under the outer edge of the anode. The figures clearly show that the bubble heights depend on both the gas generation rate and the bubble position under the anode, just as expected. The position under the anode is measured from the lower point at the inner edge of the anode bottom to the upper point at the outer edge. As the length of the anode is 100 cm, the position varies from 0 to 100 cm too.

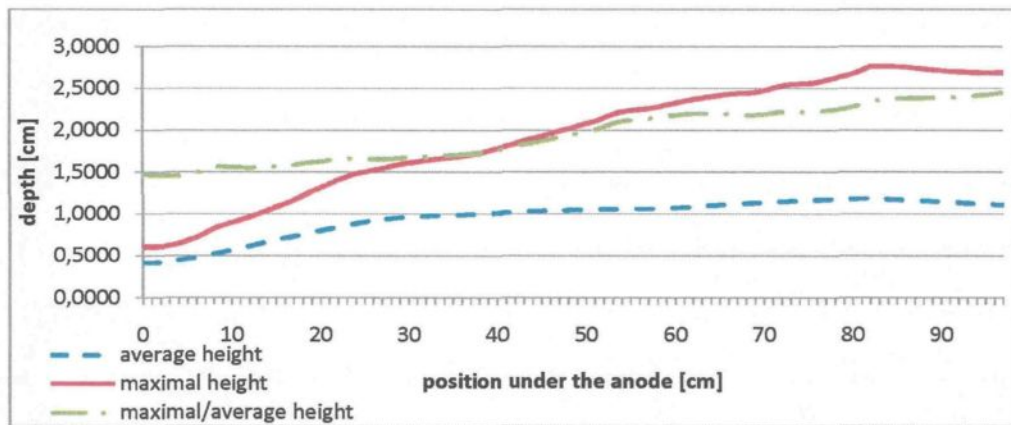


Figure 5.9 – Local average, local maximum heights and their ratio at 105 lpm volume flow rate of air and 1° of inclination

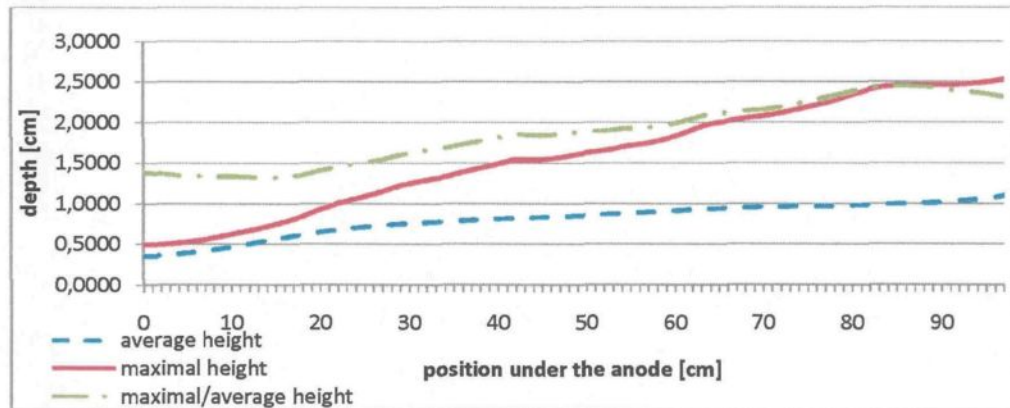


Figure 5.10 – Local average, local maximum heights and their ratio at 75 lpm volume flow rate of air and 1° of inclination

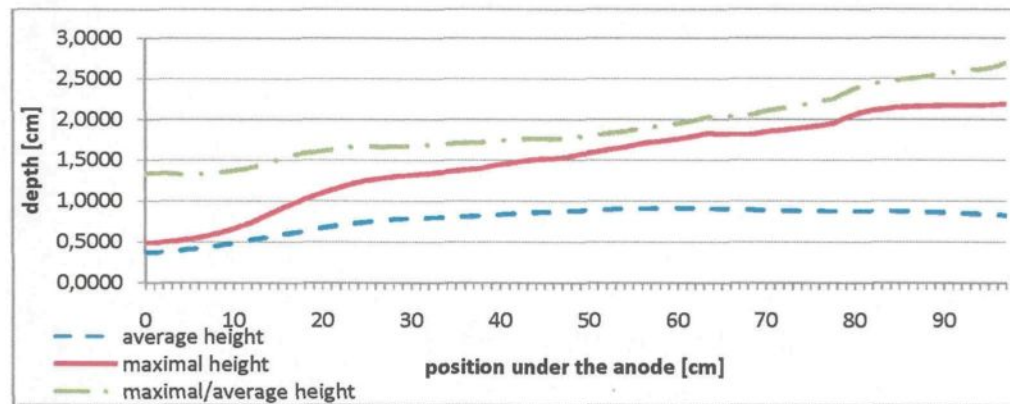


Figure 5.11 – Local average, local maximum heights and their ratio at 51 lpm volume flow rate of air and 1° of inclination

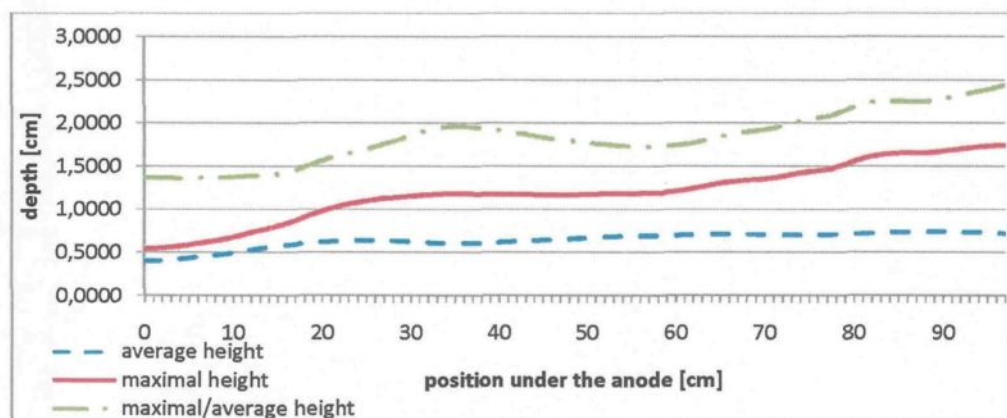


Figure 5.12 – Local average, local maximum heights and their ratio at 24.75 lpm volume flow rate of air and 1° of inclination

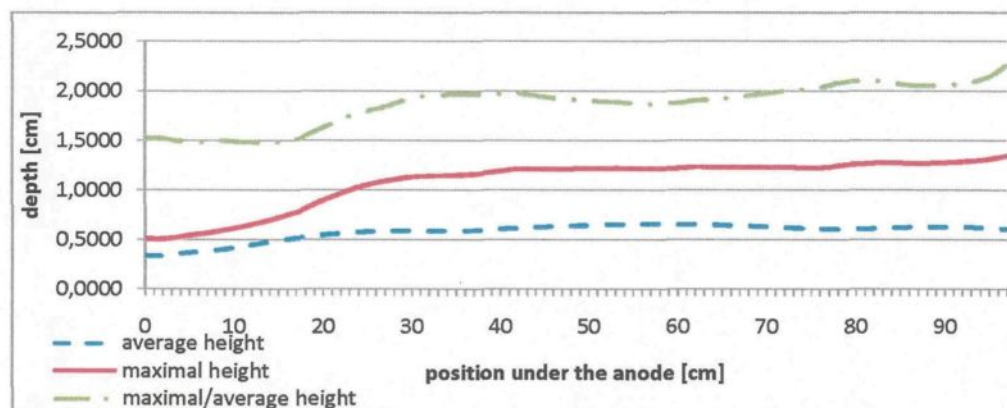


Figure 5.13 – Local average, local maximum heights and their ratio at 18 lpm volume flow rate of air and 1° of inclination

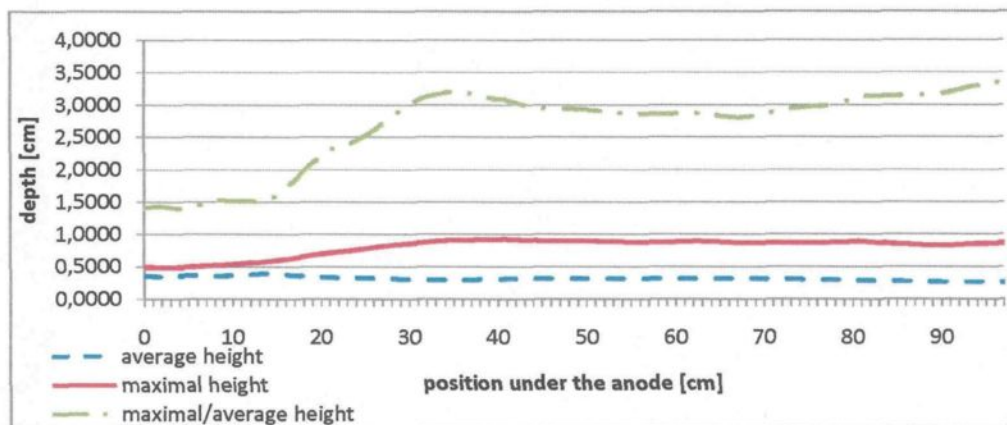


Figure 5.14 – Local average, local maximum heights and their ratio at 6 lpm volume flow rate of air and 1° of inclination

A large numbers of small bubbles can be observed close to the central channel, while close to the side channel there are only a few, but large bubbles. The height of a moving bubble depends, among other things, on its volume. Thus close to the side channel large average height is expected and indeed observed. The maximum height is also greater close to the side channel.

The local average height of the bubble layer starts around 0.4 cm, independent of the gas generation rate. It increases up to 1 cm for the higher gas generation cases. The 0.4 cm starting value is equal to the maximum height of a standing bubble under a downward face. This agreement between the maximum height of a standing bubble and the initial height under the anode is due to the fact that at the inner edge of the anode there are only small, almost still or slowly moving bubbles. As it will be shown later, a bubble moving fast enough can be taller than this maximum height. Thus the local average height close to the

outer edge of the anode, where the bubbles are large and move fast, can reach as high as 1 cm.

The terminal value of the local average height is usually reached under the first third of the anode. This terminal magnitude was reached in all cases and it is proportional to the gas generation rate. In the framework of the experiments it cannot be determined whether a further increase in the gas generation rate would increase this terminal value or if there is a maximum terminal value of the local average height a bubble layer can attain.

Every parameter but the gas generation rate was kept constant during the experiment. Therefore, our results show that an increase in the gas generation rate increases the average height of the bubble layer. This is quite different of what is observed with stationary bubbles.

#### **5.3.4.2 Local maximum height of the bubble layer**

While the local average height seems to reach its terminal value in all cases, the local maximum height seems to grow without limit. The terminal value of the local maximum height was not observed in any of the cases. Moreover, the greatest value of the local maximum height, measured always at the outer edge of the anode, significantly increases

with increasing gas generation rate. It is possible that a further increase in the gas generation rate would increase the local maximum height.

Whether the increase in the local maximum height is caused by the large volume of bubbles or the bubble induced flow is the subject of the chapter 4. It is really important to note that these heights greater than the terminal value of the local average height were always measured at the head of Fortin bubbles. The equilibrium shape of a moving bubble depends on the dynamic forces acting on the bubble. If the volume of a bubble is large enough, these forces most likely help the bubble create a head and thus increase its height significantly.

It is expected that if there is no coalescence, and thus no further increase in the volume, than a bubble can reach a terminal value of the local maximum height which is the height of the head. Since under the anode the volume of a bubble can always increase by coalescence, the terminal value of the local maximum height could not be observed.

#### **5.3.4.3 Ratio of the local maximum height to the local average height**

A surprising agreement can be observed when the curves of the local maximum height to the local average height ratios for all gas generation rates (figures 5.9-5.14) are put into the same graph (figure 5.15). Even though there is a significant difference between the local



maximum heights of the different cases and a slight difference between the local average heights, the ratios are surprisingly similar. The curves of the ratios of local maximum heights to local average heights show that there is a strong connection between the two values. Each curve starts at 1.5 cm and increases up to 2.5 cm. The only exception is the ratio in the case of the lowest gas generation rate. When the gas generation rate is low, there are so few bubbles under the anode that they do not affect each other and there is almost no coalescence and the volume of the bubbles hardly increases. This also suggests that the bubbles have a strong influence on each other and the bubble induced flow has a back-effect on the bubbles themselves.

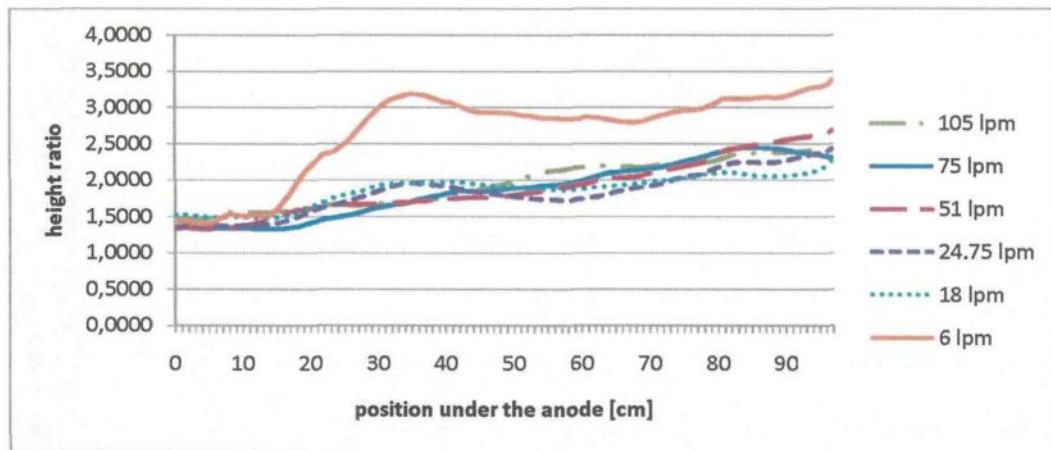


Figure 5.15 – Local maximum/local average height ratios for the six cases

As a bubble glides under the surface, it displaces a certain amount of liquid. If another bubble arrives before the disturbed liquid can return to its equilibrium state, then the velocity field induced by the first bubble affects the newly arrived bubble. It has an effect on its shape and also on its velocity. The velocity field induced by a bubble can be

amplified or weakened by other bubbles. Thus not only does the bubble have an effect on its surrounding liquid, but the moving liquid also affects the bubble. This dynamic connection between the moving bubbles and the disturbed liquid causes the formation of a Fortin head in large bubbles and this connection may be responsible for the strong correlation between the maximum and average heights.

### 5.3.5 Height of the bubble layer as a function of the gas generation rate

The bubble layer formed under the anode has been reported to be around 0.5 cm high. (*Haupin, 1971; Fortin et al, 1984; Xue et al, 1995*). The local average height calculated during our experiment does not correspond to this value, since maximum heights were also included in our local average height calculations. The height of the bubble layer formed in our experiment was not measured directly. Instead the heights obtained from the recordings were analyzed in order to determine the mean height of the entire bubble layer. The value which was obtained most frequently was chosen as the mean height of the bubble layer. The distance of the bubble contour from the anode bottom was measured in each video frame and at each pixel point of the anode bottom in each image. As a large Fortin bubble moves, its height changes dynamically. Moreover, its height is not constant along its interface due to the wavy motion on its surface. Consequently, the height measured at one point does not represent the height of the bubble, but the value which was measured most



frequently can be interpreted as the mean height of the bubble layer. As can be seen in figure 5.16, the most frequently occurring bubble height, and thus the mean height of the bubble layer at the highest gas generation rate is 0.9 cm. This height is almost twice as much as the previously reported values.

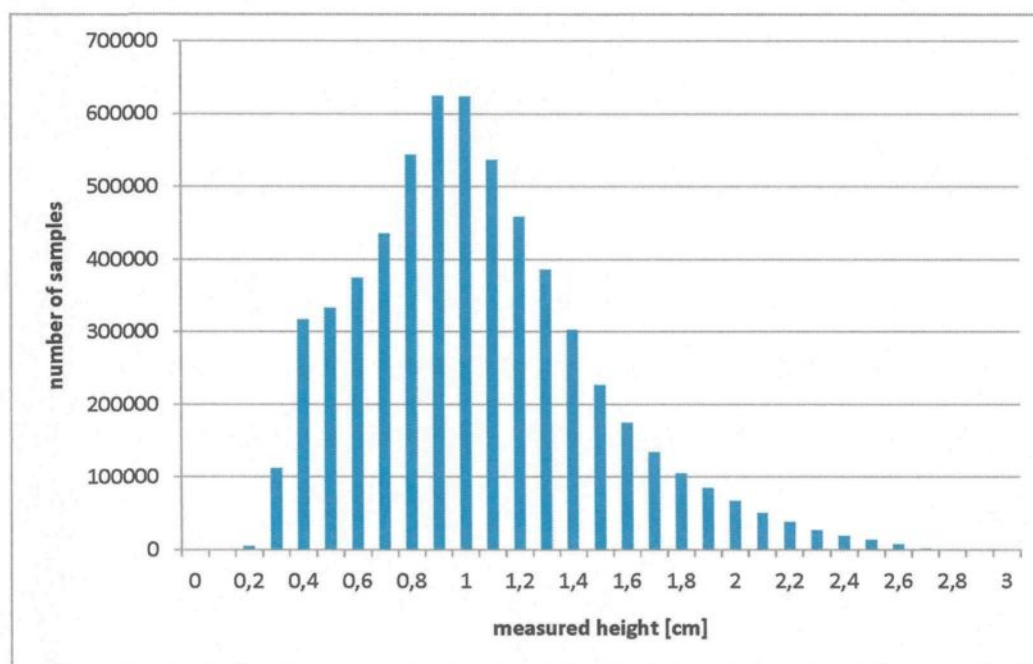


Figure 5.16 – Height distribution at 105 lpm volume flow rate of air

The mean height of the bubble layer for all gas generation rates is shown in figure 5.17. The mean height of the bubble layer is 0.8 cm for all the cases except for the highest and lowest gas generation rates. For the highest rate it is slightly higher, namely 0.9 cm. For the lowest gas generation rate it is only 0.4 cm, which is equal to the maximum height of a standing bubble under a downward facing surface. This is a surprising result, because it shows that the mean height of the bubble layer in this range of gas generation rates is not

dependent on the gas generation rate. Moreover, these values are almost twice as much as previously reported. The only exception is the lowest gas generation rate case, where there were so few bubbles that no bubble layer formed under the anode and thus we cannot talk about height of the bubble layer. At such low gas generation rates, the volume of a bubble is so small that no Fortin head can form, thus the height of the bubble cannot increase above the 0.4 cm limit.

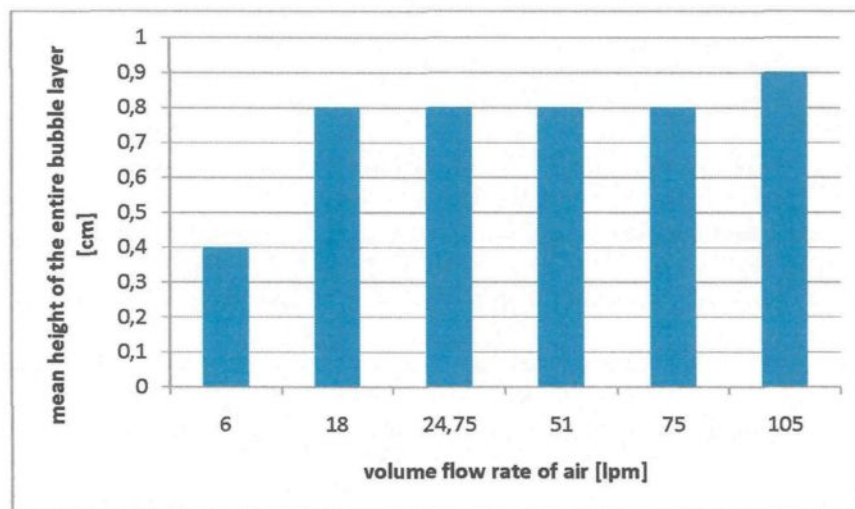


Figure 5.17 – Mean height of the entire bubble layer as a function of the volume flow rate of air

### 5.3.6 Calculation of the volume of a bubble from its contact size

In order to calculate the volume of each single bubble under the anode from the measured contact size, the height of the bubble has to be known. For the calculation of the volume, the knowledge of the average height is sufficient. It is not necessary to know the exact local height, which is highly variable in a Fortin bubble. As *Perron et al (2007)* have shown, the electrical resistance of a bubble does not depend on its shape but on its size. In chapter 4, we determined the correlation between contact size, angle of inclination and equivalent height for a single large bubble moving alone under a solid surface. The correlation is given as

$$H_e[cm] = (0.54 + 0.1 \cdot \alpha^\circ) + 0.0009 \cdot A_{contact\_shape} \quad (5.5)$$

where  $\alpha$  is the angle of inclination given in degree and  $A_{contact\_shape}$ , the area of the contact shape is given in  $cm^2$ . The equivalent height as a function of the contact size can be seen in figure 4.21. This correlation is certainly valid for a contact size smaller or equivalent to  $300\ cm^2$ . As can be seen in tables 5.1-5.4, much larger contact sizes were measured in these experiments. Thus either the above correlation has to be validated for these contact sizes, or a new correlation has to be determined.

As mentioned, the average height of the entire bubble layer under the anode as a function of the current density and the position under the anode was measured. Using the results shown in figures 5.9-5.14, the following new correlation is determined

$$H_{average} = B \cdot x^a \quad (5.6)$$

where  $x$  is the position under the anode in cm, where 0 cm is the lowest point at the anode bottom and 100 cm is the highest one and the two parameters,  $a$  and  $B$ , are given in figure 5.18 as a function of the gas generation rate at 1° of inclination. This correlation is independent of the contact size, but gives the average height of an entire bubble layer at a given inclination. It is valid only for 1°.

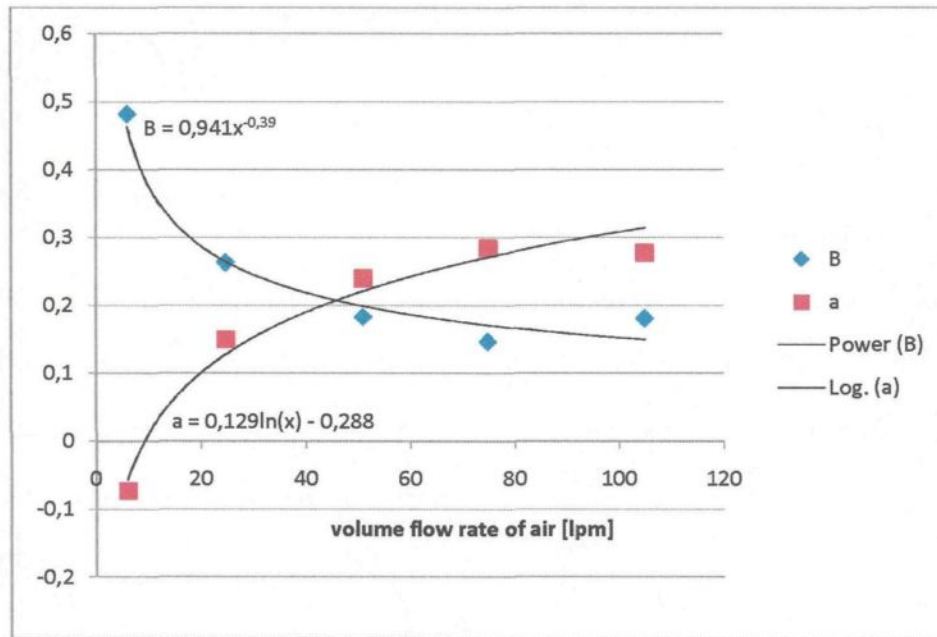


Figure 5.18 – Two parameters to calculate the average height as a function of the volume flow rate of air at 1° of inclination

The overall volume of bubbles under the anode at a certain time is calculated for 1° using the two correlations. It was found that with a measured contact size of up to 1000 cm<sup>2</sup>

the second correlation gives better results. The bubble volume calculated with the second correlation is presented below in figure 5.19 for 1° of inclination. The variation of the accumulated gas volume is almost linearly proportional to the gas generation rate.

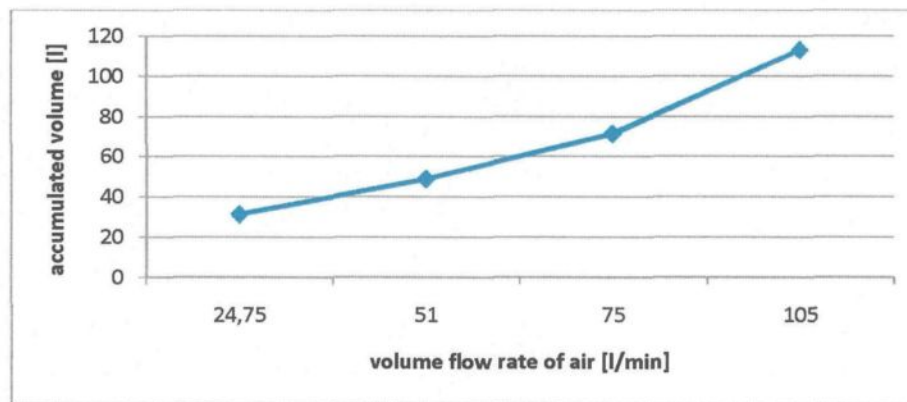


Figure 5.19– Accumulated gas volume under the anode (sum of 60x60 frames)

The specific bubble volume under the different sections of the anode bottom for the highest current density can be seen in figures 5.20-5.23 and the mean specific bubble volume as a function of the position under the anode is shown in figure 5.24. The specific bubble volume under the whole anode for each current density can be seen in figures 5.25-5.28 and the mean specific bubble volume as a function of the current density is shown in figure 5.29.

The specific bubble volume calculated from the measured contact sizes and the experimental correlation for the average height of the bubble layer agrees well with previous results (*Aaberg et al, 1997*). The specific bubble volume increases with increasing current density and increases towards the outer edge of the anode. Also, the difference

between the maximum and minimum specific bubble volume increases towards the outer edge of the anode and with increasing gas generation rate. The mean specific bubble volume as a function of either the position under the anode or the volume flow rate of air is quasi linearly proportional to these two parameters (figures 5.24 and 5.29).

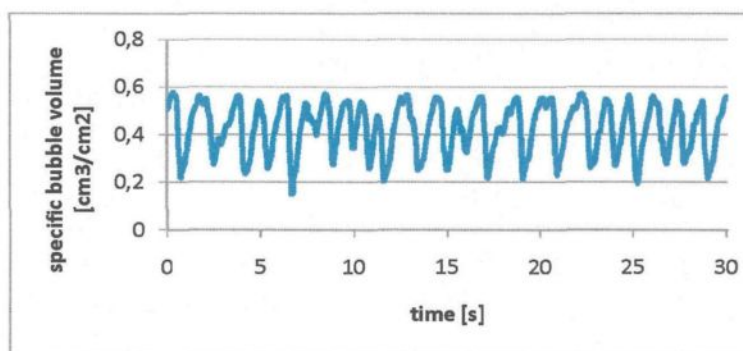


Figure 5.20 – Specific bubble volume under the outer edge of the anode at 1° and at 1.0 A/cm<sup>2</sup> current density

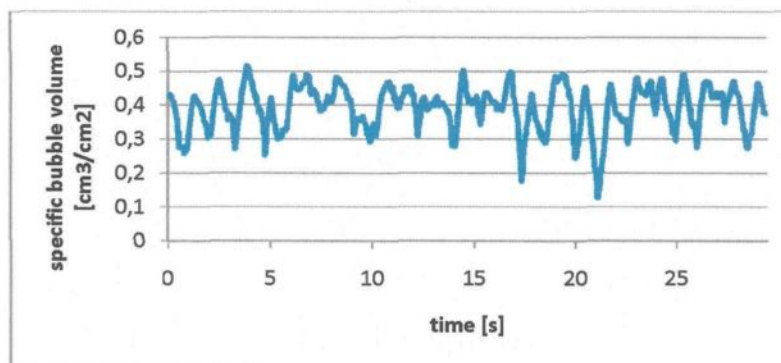


Figure 5.21 – Specific bubble volume under the third section of the anode bottom at 1° and at 1.0 A/cm<sup>2</sup> current density



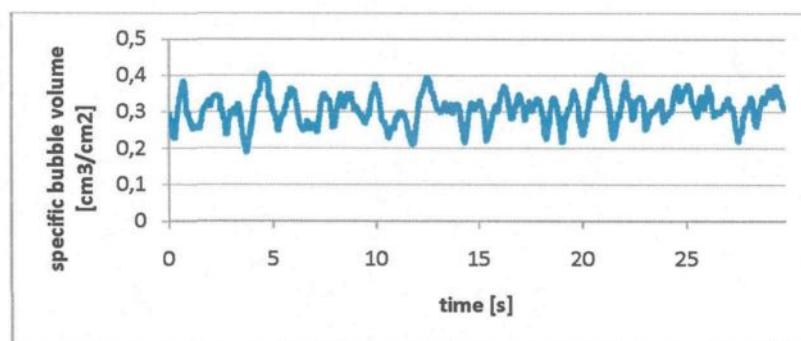


Figure 5.22 – Specific bubble volume under the second section of the anode bottom at 1°  
and at 1.0 A/cm<sup>2</sup> current density

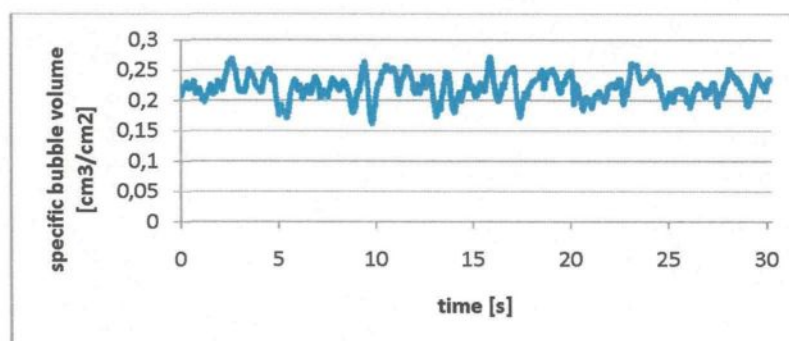


Figure 5.23 – Specific bubble volume under the inner edge of the anode at 1° and at 1.0  
A/cm<sup>2</sup> current density

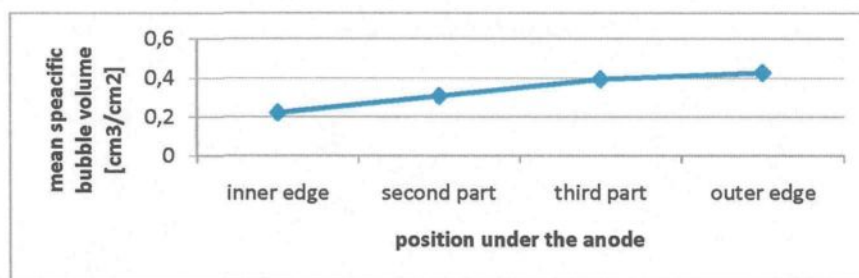


Figure 5.24 – Mean specific bubble volume as a function of the position under the anode at  
1° and at 1.0 A/cm<sup>2</sup> current density

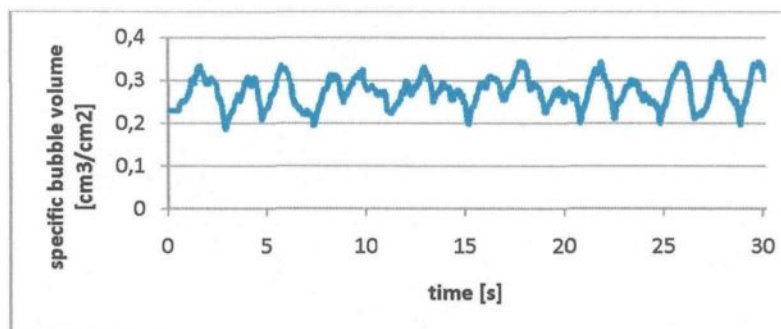


Figure 5.25 – Specific bubble volume under the whole anode at 1° and at 1.0 A/cm<sup>2</sup> current density

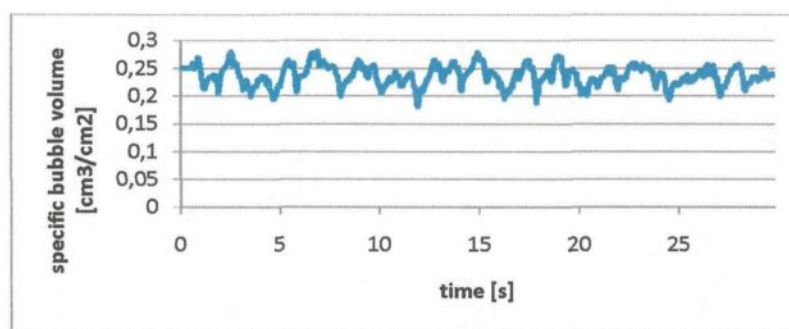


Figure 5.26 – Specific bubble volume under the whole anode at 1° and at 0.72 A/cm<sup>2</sup> current density

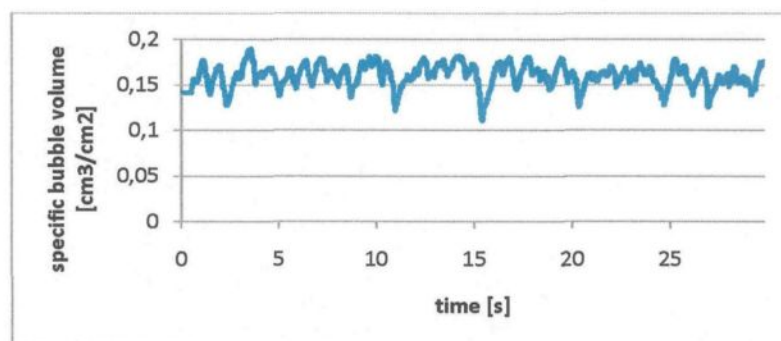


Figure 5.27 – Specific bubble volume under the whole anode at 1° and at 0.49 A/cm<sup>2</sup> current density



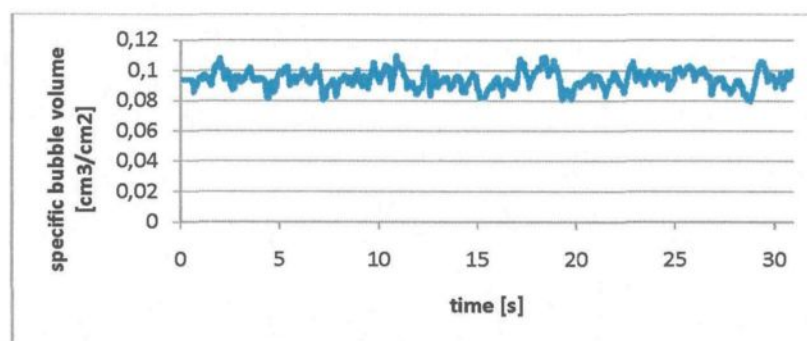


Figure 5.28 – Specific bubble volume under the whole anode at 1° and at 0.24 A/cm<sup>2</sup>

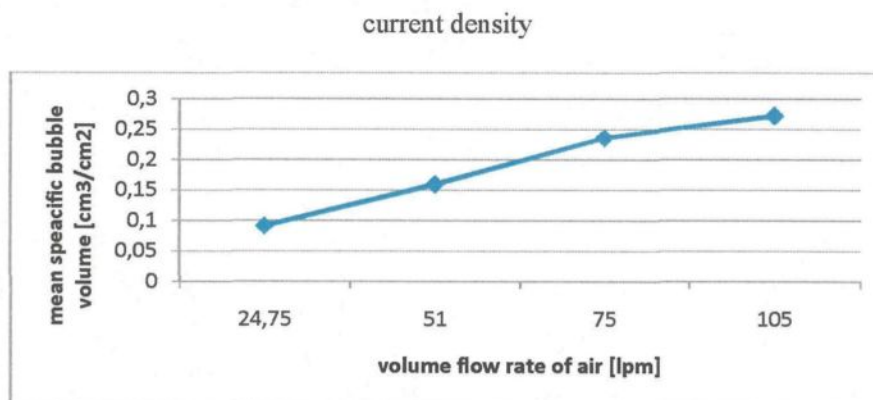


Figure 5.29 – Mean specific bubble volume for the whole anode as a function of the  
volume flow rate of air at 1°

### 5.3.7 Formation of the Fortin bubble

The frequently observed large Fortin bubbles can even dominate the bubble layer at high volume flow rates. Often only one large bubble covered from one third to one half of the

anode bottom. The shape of a Fortin bubble in the contact zone is similar to the shape of a bulged-bubble. In this zone the curvature at the front is always positive while at the end the curvature tends to be infinite.

The typical “head and tail” shape of the Fortin bubble is illustrated in figure 5.30. The bubble is moving from right to left under the slightly inclined surface. The semi-circular thick head and the thin tail can be seen clearly. Note that the height of the tail is not uniform and the contour of the bottom of the tail is neither horizontal nor parallel with the surface, but wavy. Indeed, the wavy motion of the tail can be clearly seen in the videos. This motion and the phenomenon of the head are most likely induced by a gravity wave. This sort of wave is usually induced by a gas phase moving above a liquid phase. If the velocity difference between the two phases is large enough, then the movement of the gas phase disturbs the equilibrium of the liquid phase by displacing a certain amount of liquid parcel. This disturbance travels in a continuous phase as the gravity restores the displaced parcels toward equilibrium.

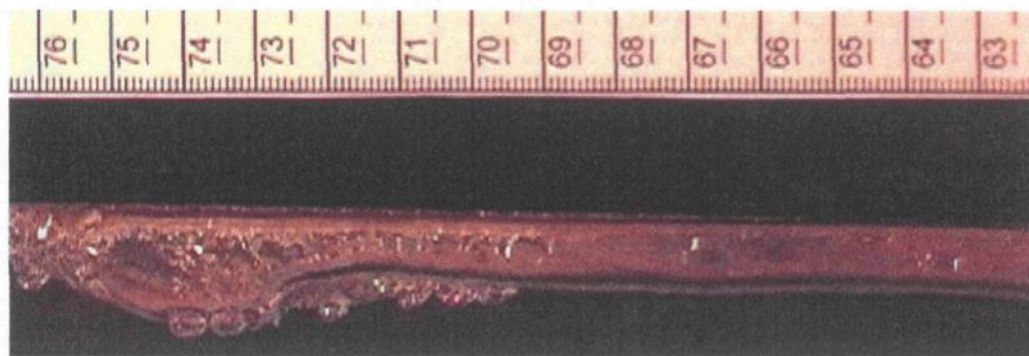


Figure 5.30 – Cross-section of a Fortin bubble

This wavy motion can be clearly observed at the bottom of the Fortin bubbles. As the air phase moves upward due to buoyancy, it accelerates. This gas moving with a high velocity disturbs the standing liquid which results in the observed gravity wave. The Fortin head is formed by the wave-front of the gravity wave which has larger amplitude than the waves following the front. The phase velocity of a gravity wave grows with the depth thus the top of a wave propagates faster than the bottom. After a certain time the top of the wave can break into what is called a foaming front, a phenomenon. A foaming front was not observed during our experiments, perhaps because our bubbles were enclosed in the liquid phase, where different forces affected the gravity wave than in the open air.

A gravity wave induces circular flow in the liquid with only a very slight forward movement. Only the momentum is carried forward by the wave. The circular movement induced in the liquid by the wave stops at a depth equalling half of the wavelength. All these phenomena were observed in our experiments where the velocity field in an electrolysis cell model was measured using the PIV techniques and are presented in chapter 5.4.

#### **5.3.7.1 Dynamic formation of the Fortin head**

It was thought that the Fortin shape formed as the bottom of a large bubble became horizontal and collapsed (*Fortin et al, 1984*). This was not borne out by our observations.

We found that the head of the bubble forms dynamically. The idea of the dynamic formation was strengthened by a special “resonance” observed during the experiment. This phenomenon always started right after the tank was filled with water and the experiment began. The direction of the movement of the bubble layer under the two anodes oscillated. While under one anode the bubbles moved toward the outer edge – as it is well expected – at the same time under the other anode the bubbles moved downslope. After a certain time, the direction of the movement under the two anodes reversed. This phenomenon continued until a parameter of the system, such as gas generation rate, was changed, after which the normal behaviour of the system was observed.

The Fortin head was always observed when the volume of the bubble was large enough, independent of the direction of the movement of the bubble layer. Moreover, at times the head also changed direction. As a large bubble moved in one direction and gained enough velocity, a head formed. This head travelled with the bubble until the bubble changed the direction sharply due to oscillation. The wave that formed the head continued its movement in the original direction until it reached the end of the bubble which was moving in the opposite direction. As the wave “left” the bubble and the bubble reached a velocity high enough, a new head formed, now moving in the same direction as the bubble.

### 5.3.7.2 Onset of the Fortin shape as a function of different parameters

The onset of the Fortin shape was observed during the experiment as a function of the gas generation rate, the angle of inclination and the position under the anode; the size of the head was measured.

The onset of the Fortin shape depends on the volume of the bubble, which depends on the gas generation rate and the angle of inclination, as it was mentioned earlier. The formation of the head depends also on the velocity difference between the liquid and gas phases. The velocity of the bubble depends on its size, shape and the angle of inclination. On the other hand, the velocity field of the liquid is induced by the bubbles. The bubbles form continuously under the anode and they induce a continuous flow in the liquid phase. The velocity difference between the gas and liquid phase is reduced by the induced flow, which reduces the chance of forming a head.

Smaller bubbles form at low gas generation rates and at high inclinations. An increase in the angle accelerates the bubbles and even though large bubbles form occasionally (with an approximately 200 cm<sup>2</sup> contact size), the Fortin shape is rarely observed. This shape was not observed regularly above 4° of inclination. This is explained by the reduced velocity difference between the liquid and gas phases.

Depending on the flow pattern in the liquid, most precisely the absence of it, the Fortin shape may onset at a contact size as small as 30 cm<sup>2</sup>. The velocity of a bubble in a bubble

layer has a strong effect on the onset of the head. If the velocity of the bubble is too high, the head does not form, while at a low velocity a larger volume is necessary for head formation. At a moderate velocity, a smaller bubble forms the head.

The dimensions of a Fortin head change gradually as the bubble grows while gliding and coalescing under the anode. The length and height of the head depend on the volume of the bubble and on the flow pattern around the bubble. At a small volume, the initial length of a head is around 1-2 cm which can grow up to 5-6 cm as the bubble grows. The average length of the head is around 2-3 cm.

#### **5.3.8 Escape of large bubbles**

Before leaving the anode, a large bubble contracts under the effect of buoyancy. This sometimes leads to a break-up of the bubble, forming one larger bubble and one or more smaller ones. During the contraction the height increases significantly. Up to three centimetre thick bubbles were observed close to the side channel. The first bubble escapes at a high speed. The escaping part always stays close to the anode side and it is shapeless. As it escapes, a large amount of liquid has to flow back in order to fill the space left by the escaped bubble. The effect of this backflow was investigated and measured in our PIV experiments. It was found that this backflow transports a large amount of momentum which induces a large fluctuation in the liquid velocity moving in the inter-electrode space.

Sometimes this backflow stops all bubble movement under the anode. A few snapshots of an escaping large bubble can be seen in figure 5.31.

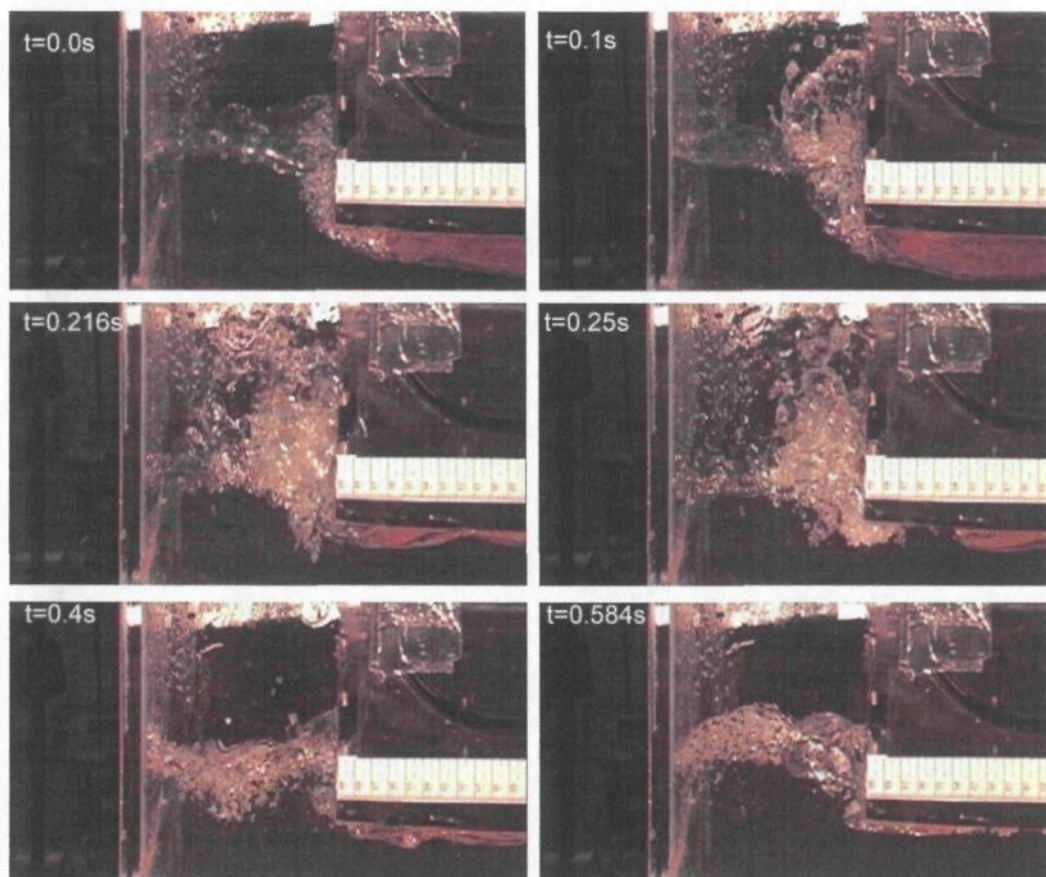


Figure 5.31 - Escape and break-up of a large bubble

The number of bubbles a large bubble breaks into during its escape depends on the size of the original bubble. The larger the initial bubble, the more bubbles it forms. As a large bubble approaches the end of the anode it contracts. It happens because the front of the bubble cannot start escaping as fast as the rest of the bubble is gliding under the anode.



While the end continues to move forward, it pushes air into the front of the bubble, thus decreasing the length of the bubble while increasing its height. When the front part of the bubble leaves the anode it sucks with itself a large quantity of air. The part of the bubble which is no longer connected to the bottom of the anode can rise fast. However, the rest of the bubble which is still under the anode cannot follow with the same velocity. Therefore, when the bubble is large enough and consequently the velocity difference between the two sections, the first freely-rising and the second gliding-under-the-anode, is also large enough, the bubble inevitably breaks into two parts. After the first part escapes, a new section is separated from the bubble and leaves the anode. This continues as long as there is air left under the anode. The first bubble is the largest and transports the greatest momentum.

### **5.3.9 Momentum transfer by the escaping large bubbles**

The movement of the bubble layer under the anode, the magnetic field and the temperature gradient in the bath induce a continuous flow in the cell. A circular flow can be observed under the anode and in the side channels. The liquid moves under the anode with the bubbles at the top and flows backward at the bottom of the inter-anode space. At a low gas generation rate and a high angle of inclination the bubbles induce a quasi-monotone flow in the bath. As the maximum volume of the bubbles increases, the escape of the large bubbles disturbs this monotone flow. When a large bubble escapes from under the anode at



the outer edge of the anode (figure 5.32, red arrow), a large amount of liquid has to return to fill the space left by the escaped bubble. The movement of this large amount of liquid results in a movement of the bath under the anode against the bubble layer, which is moving from the inner edge towards to the outer edge of the anode bottom. This momentum transport may force almost the whole liquid under the anode to move against the bubble layer. The liquid transports a large energy which causes the whole bubble layer to stop for one second. If the escaping bubble is large enough, its escape even forces the small bubbles under the inner edge of the anode to move backward (figure 5.32, blue arrow).

The intensity of this backflow depends on the volume of the escaping bubble, which itself is proportional to the gas generation rate and inversely proportional to the angle of inclination. At a high inclination and/or a small gas generation rate no large bubble forms and thus this intense backflow cannot be observed. The limit of this effect in our experiments was found to be around  $0.65 \text{ A/cm}^2$  current density (below this value it cannot be observed) and  $2^\circ$  angle of inclination (above this value it cannot be observed either).

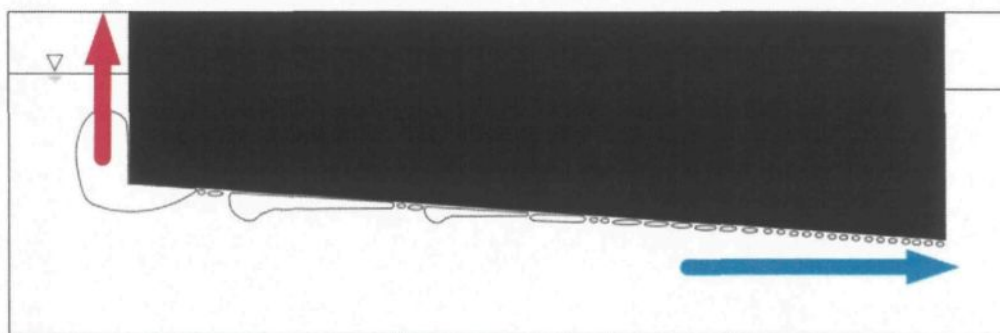


Figure 5.32– Effect of the escape of large bubbles

### 5.3.10 Sweeping effect

*Perron et al (2007)* have shown that the chance for collision and coalescence increases as the volume of the bubble increases; as the size increases, the bubble gains velocity, which further increases its chance for coalescence. Therefore the large bubbles “eat” the smaller and slower ones leaving an empty spot behind. An example of the sweeping effect, observed in our experiments, can be seen in figure 5.33.

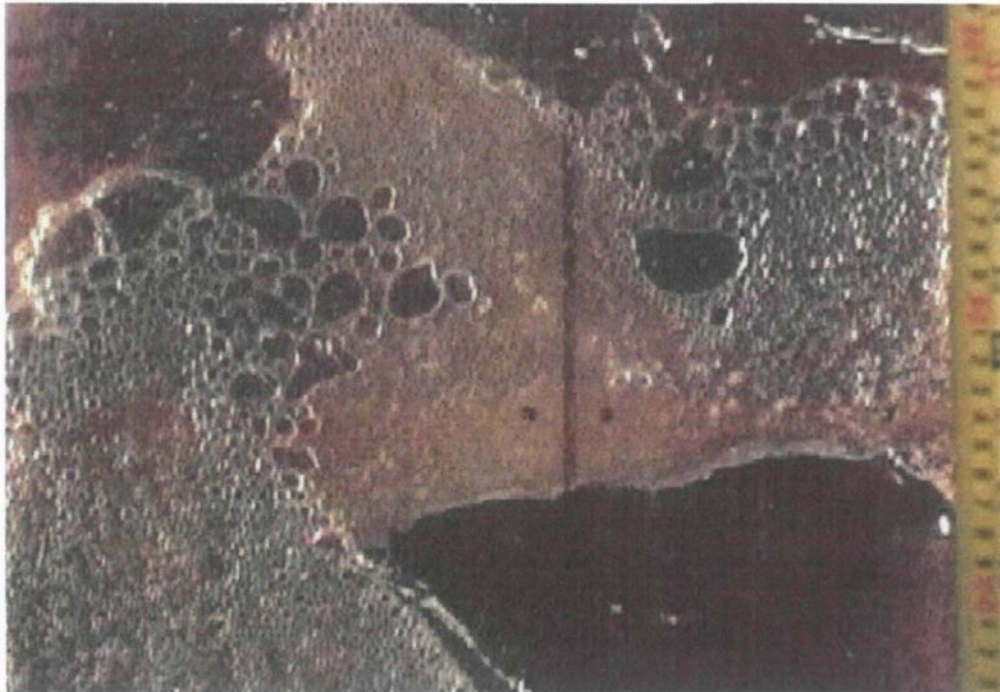


Figure 5.33 – Snapshot showing the sweeping effect of large bubbles

### 5.3.11 Bubble layer in a real electrolysis cell

Our findings are from a real-size air-water model. It is important to examine whether our findings are representative of events in a real cell. The main difference between the two systems is the materials used: cryolite and carbon-dioxide in a real electrolysis cell, water and air in the model. The density of cryolite is almost three times higher than the density of water. The surface tension of cryolite-carbon dioxide is twice as big as the surface tension of air-water. The dynamic viscosity of cryolite is ten thousand times greater than the dynamic viscosity of water.

Both the different parameters of the real cell and the model and our mathematical simulations indicate a very similar volume and contact size distribution in the real cell but with slower moving bubbles. This slow movement further increases the chance of coalescence and consequently increases the volume and contact size of the bubbles. This in turn increases the covering factor of the anode leading to a higher overvoltage of the cell.

Also a very similar bubble shape is expected in the real cell but with the bubbles moving slower. It was observed that the shape of a bubble depends, among other things, on the liquid's Morton number. The Morton number depends only on the physical properties of the working liquid and gives the ratio of the viscosity and gravitational forces to the surface tension force. The Morton number is given by

$$Mo = \frac{g \cdot \nu_l^4 \cdot \rho_l^3}{\sigma^3} \quad (5.7)$$

where  $g$  is the gravitational acceleration,  $\nu_l$  is the kinematic viscosity of the liquid,  $\rho_l$  is its density and  $\sigma$  is the surface tension. Since the Morton number is very similar for the two systems, similar bubble shape is expected.

The exact values of the above mentioned parameters for the two systems can be seen in table 4.1.

## **5.4 Bubble layer induced flow**

### **5.4.1. Fluid flow induced by discrete bubbles and by the bubble layer**

In our experiments the driving force of the fluid flow is created only by the motion of the bubbles. Neither the effect of heat transfer, nor of the magnetic field on the induced flow is reproduced in the experiments. Even though there are a large number of small bubbles under the anode, the effect of a few large bubbles is much stronger than the effect of all the small bubbles together. The bubbles and especially the large bubbles operate in three ways. These three ways are described in the following three subchapters.

#### 5.4.1.1 Vertical motion of the bath

The bubbles pull the liquid in the direction of their movement and thus create movement in the adjacent portion of the liquid layer underneath. The thickness of the affected layer depends on the height of the bubbles. The bubble layer is known to reach a maximum height of around 0.4-0.6 cm under the anode (*Fortin et al, 1984; Haupin, 1971; Aaberg et al, 1997*). Thus the liquid layer which moves with the bubble layer is expected to have a maximum thickness also. But it was observed that if the volume of a bubble grows larger than a limit, the bubble turns into the so called Fortin shape. The Fortin shape consists of a head and a tail, where the height of the head is greater than the maximum bubble layer height. We observed heads as high as 2 cm in our experiments. Such a large bubble head can put significantly more liquid into motion than a small bubble. The thickness of the liquid layer which moves with the bubble layer can be four times thicker below a head than below a small bubble. This is around the top one third of the bath in the inter-electrode space moving with the bubble layer. The thickness of this layer depends on the volume of the single bubbles in the bubble layer, thus it keeps changing. In addition, the bubble layer is not uniform under the length of the anode. Even though the bubbles are nucleated quite uniformly at the bottom of the anode, after detaching they collide and coalesce, thus forming a non-uniform bubble distribution. At the inner edge of the anode there are a large number of small bubbles, while closer to the side channel there are only a few large bubbles. Accordingly, the thickness of the liquid layer moving with the bubble layer is larger closer to the side channel, than to the centre channel (figures 5.34 and 5.35).



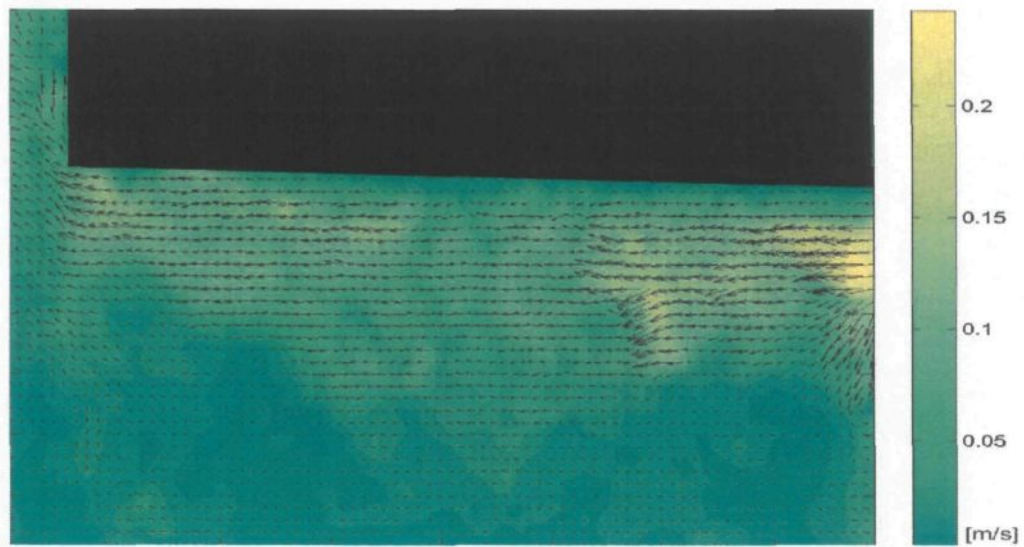


Figure 5.34 – Instantaneous velocity field close to the side channel

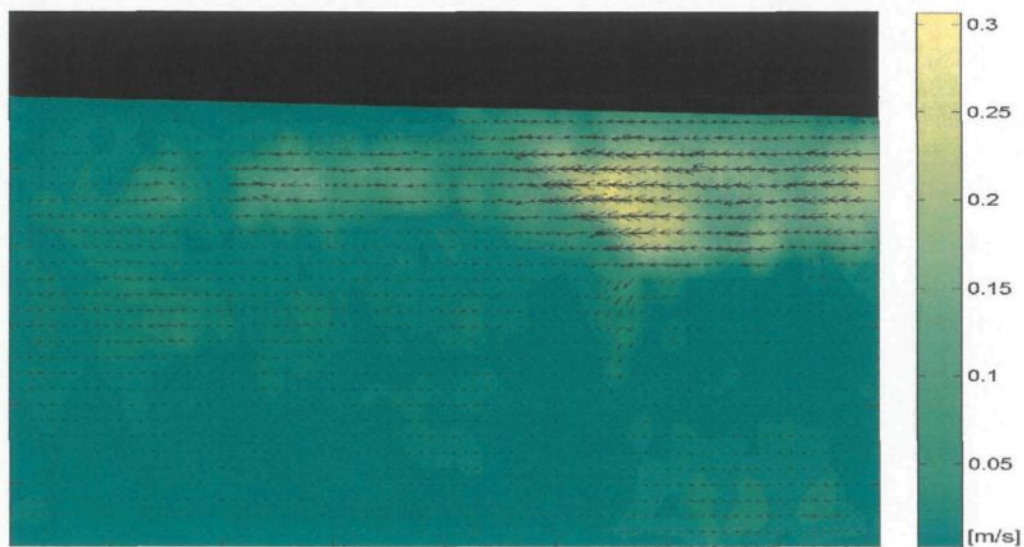


Figure 5.35 - Instantaneous velocity field close to the centre channel

The velocity of the moving liquid layer also depends on the volume of discrete bubbles in the bubble layer. Depending on the volume distribution, the mean velocity of the fluid

close to the centre channel is around 3 cm/s, while close to the side channel it fluctuates between 2 and 10 cm/s. Furthermore, the instantaneous velocity of the bath just before a bubble head can easily reach values as high as 20 cm/s.

#### **5.4.1.2 Fortin head as a gravity wave**

The second way large bubbles operate on the fluid is by creating vortices in the fluid and thus creating vertical motion. Our previous experiments indicated that the shape of a Fortin bubble is induced by a gravity wave. The gravity wave is a surface wave always occurring at the interface of two fluids. This kind of wave is frequently produced by a fast moving light gas phase above a heavy liquid phase, such as the wind blowing across the ocean. Since the Fortin shape is assumed to be formed by a gravity wave, the movement of the fluid under this kind of bubble is expected to be similar to the one found under a gravity wave. The path of the individual fluid parcels under a gravity wave is circular in deep fluids and elliptical in shallow fluids where the depth of the fluid is less than half of the wavelength of the wave. There is only a small forward motion in the fluid. The motion of the individual fluid parcels at a depth of half a wavelength approaches zero. The momentum and energy are carried forward by the wave not the mass. The crest of a wave in shallow fluids always propagates faster than the trough because phase velocity grows with depth. In open fluids the fast propagating top of the first wave can pass over its bottom and the wave breaks into what is called a foaming front. In an enclosed fluid, such as in the

electrolysis cell, the first wave cannot break into a foaming front. One of the reasons may be that the ratio of the depth of the crest to the depth of the trough is too small. If the depth ratio of the crest to trough is smaller than 1.3, the front wave has a smooth profile which is stable against further change and the foaming front does not form.

The first wave of a gravity wave has the largest amplitude. The velocity of the fluid and the radius of the circular path of the fluid parcels under a gravity wave depend on the amplitude of the wave. Thus a large vortex is expected under the first wave which is followed by several smaller ones depending on the volume of the bubble. The larger the volume, the longer the bubble is under an anode, and thus more wave crests and troughs can occur at the interface of the bubble and fluid. The instantaneous velocity field, measured in a fixed, laboratory coordinate system, shows the propagation of a large vortex induced by a Fortin head in figures 5.36-5.38.



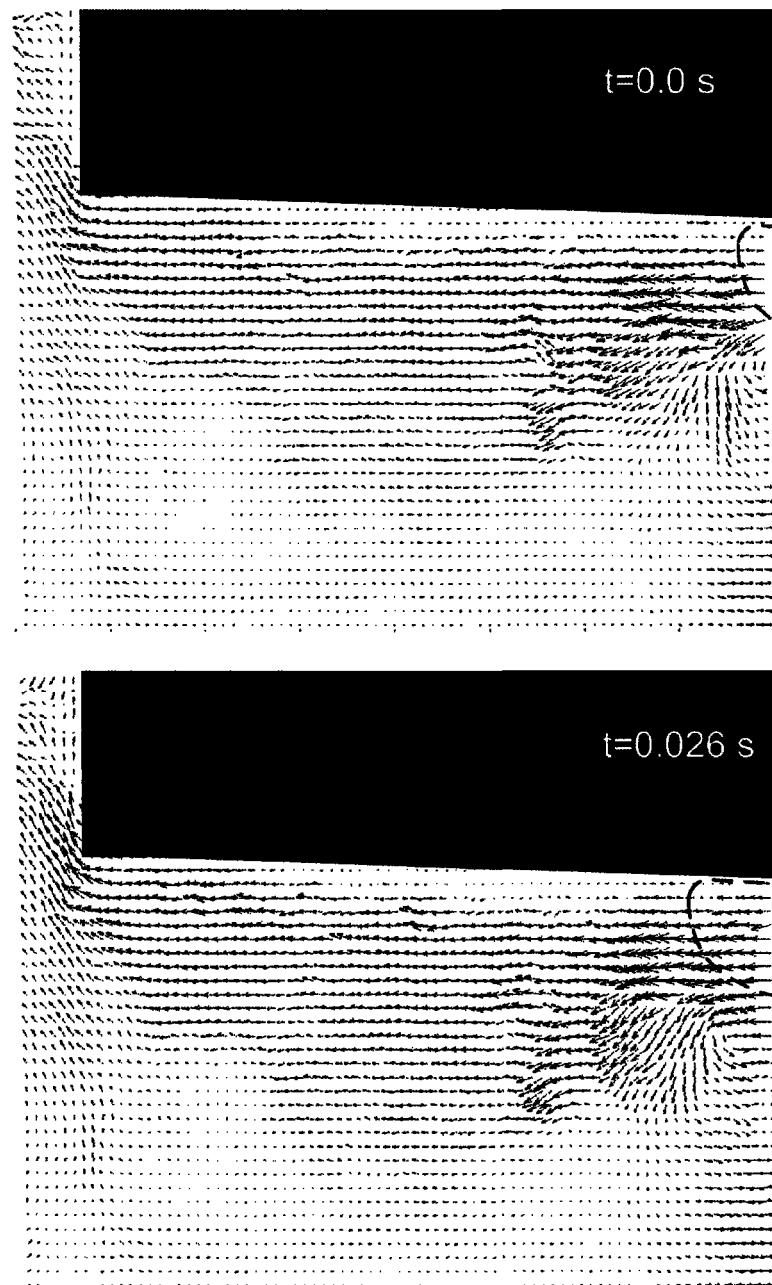


Figure 5.36 – Instantaneous velocity field showing the large vortex created by a Fortin head at 0 and 0.026 seconds.

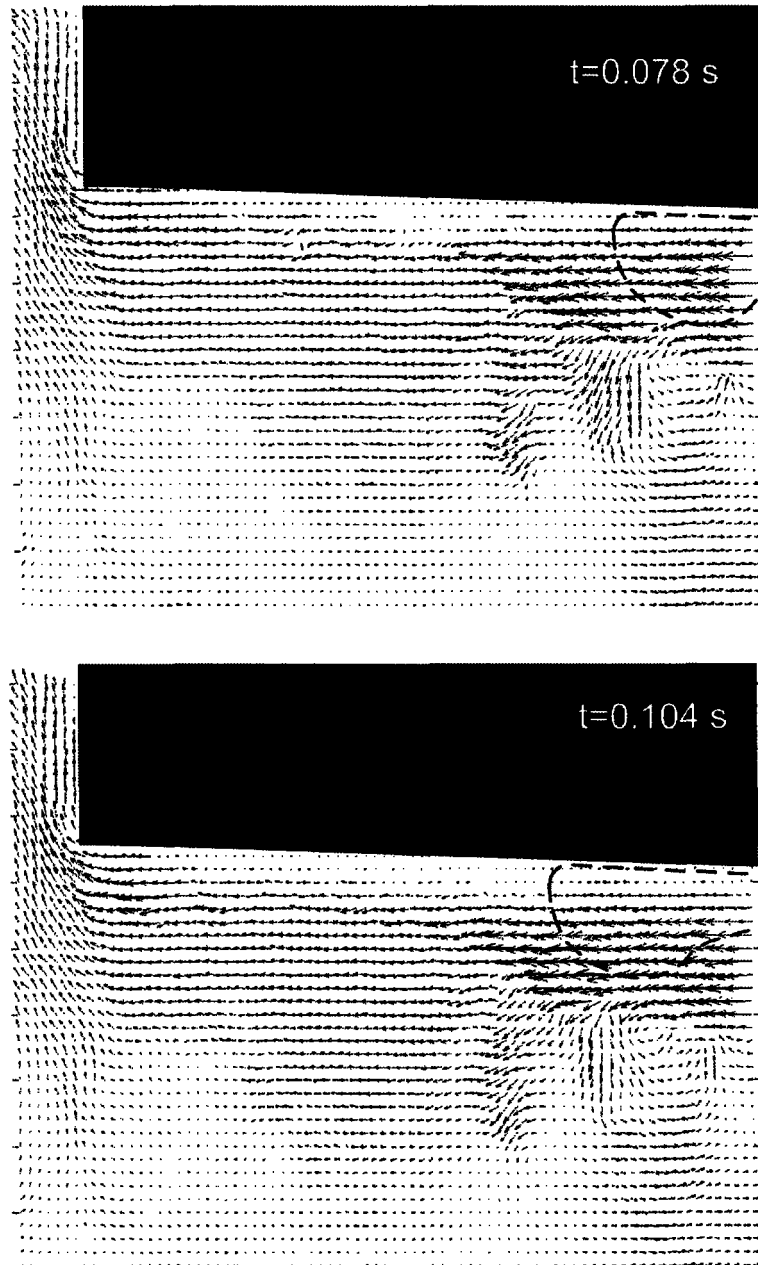


Figure 5.37 – Instantaneous velocity field showing the large vortex created by a Fortin head at 0.078 and 0.104 seconds.

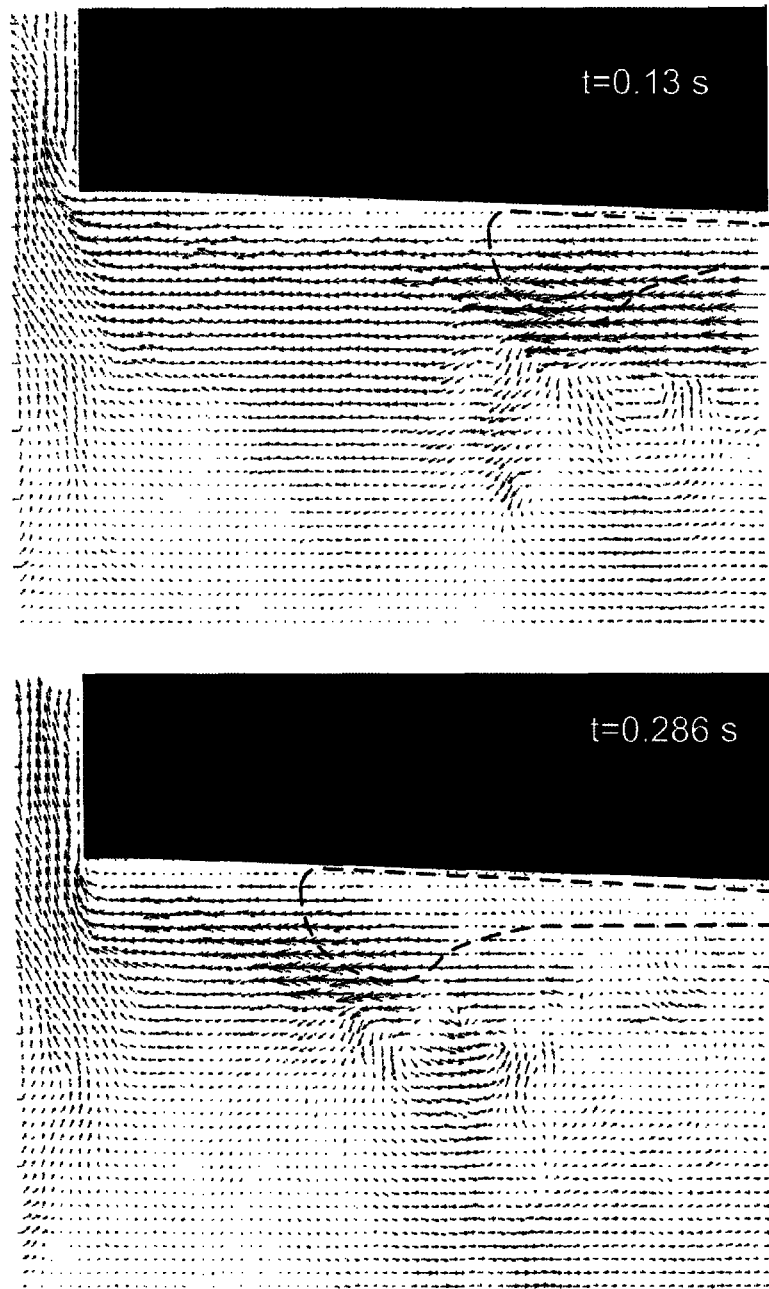


Figure 5.38 – Instantaneous velocity field showing the large vortex created by a Fortin head at 0.13 and 0.286 seconds.

The phenomenon of gravity wave could be observed clearly during our experiments. Under and right behind the head of a Fortin bubble there is always a large vortex followed by one or two smaller vortices created under the tail of the bubble. The radius of the large vortex is about twice the radius of the smaller ones. The instantaneous velocity in a vortex is around a few cm/s but in the large vortex it can reach 10 cm/s. The diameter of the large vortex is easily at least the half of the ACD, and frequently it is as large as the ACD. If the gas generation rate is high enough to form really large Fortin bubbles, the vortices induced by them may disturb the interface between the molten cryolite and the molten aluminium. This can decrease the efficiency of the electrolysis process. On the other hand, the induced vortices help to homogenize the temperature field in the bath and help to transport the alumina to the reaction sites. The instantaneous vertical velocity of the fluid is around or less than half cm/s under the inner edge of the anode bottom where there are only small bubbles. The small, spherical bubbles do not induce vortices, whose presence would increase the vertical velocity. The time-average vertical velocity of the bath under the centre of the anode can be seen in figure 5.39.

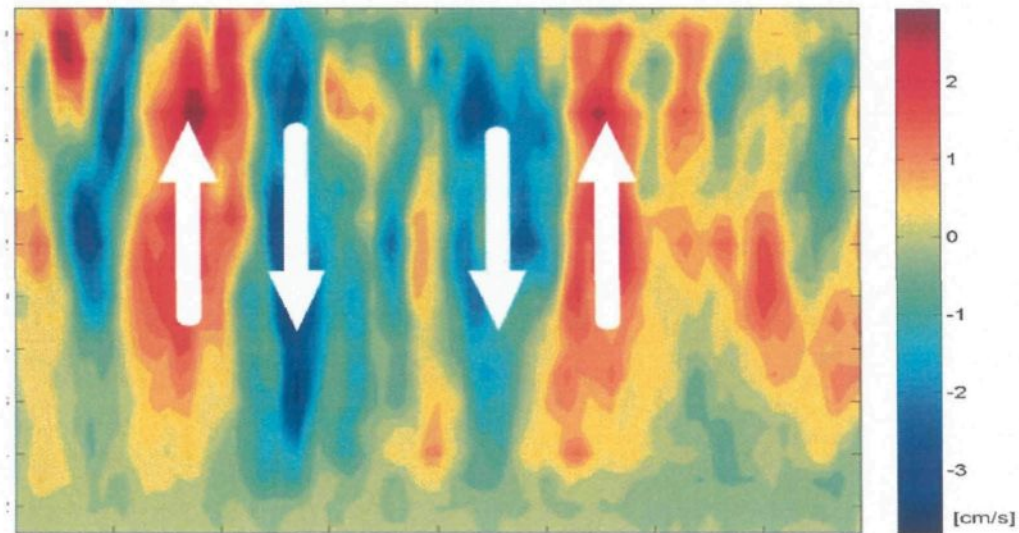


Figure 5.39 – Time-average vertical velocity under the anode showing the mixing effect of Fortin bubbles

#### 5.4.1.3 Backflow caused by escaping bubbles

The third and probably most important effect of the bubbles is the backflow induced by their escape from under the anode: the bigger the bubble, the bigger the effect. Our previous experiments showed that large bubbles escape in two or more fragments, in a larger first part and several smaller ones. When any of the parts escapes, a large amount of liquid has to flow back to fill the space left by the escaped part. According to our experiment, the maximal volume a bubble can have strongly depends on gas generation rate and the dimension and inclination of the anode. At a high gas generation rate, huge bubbles

evolve frequently under a long and only slightly inclined anode. We often observed large bubbles close to the side channel with volumes as high as one litre or more. The backflow induced by such a large bubble contains a really significant volume of liquid. Since the escape of a bubble is quite fast, this amount of fluid has to flow back during a short period of time, thus resulting in high velocities. This high momentum transfer disturbs the flow pattern under the anode and changes significantly the velocity field of the fluid. The instantaneous velocity fields induced by the escape of the first part and the subsequent smaller part can be seen in figures 5.40 and 5.41, respectively.

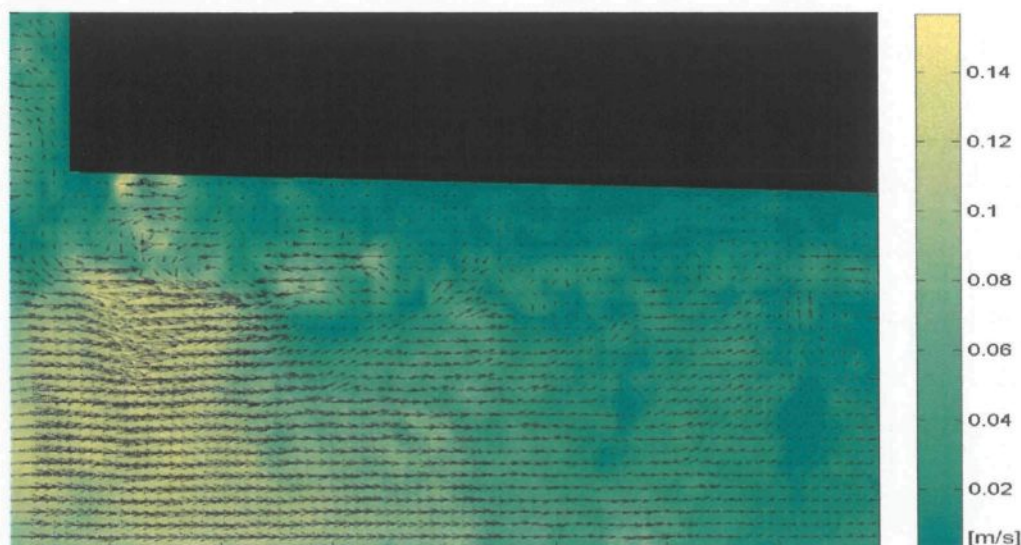


Figure 5.40 – Instantaneous velocity field induced by the escape of the first part of a large bubble



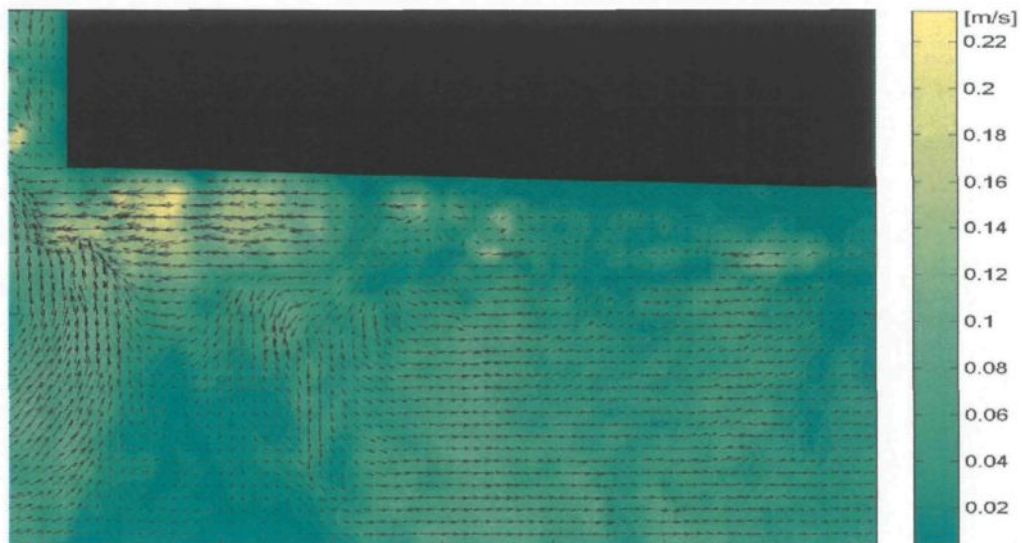


Figure 5.41 – Instantaneous velocity field induced by the escape of the second part of a large bubble

The liquid parcels flowing backward move against both the bubble layer and the fluid layer moving with it. After the escape of a large bubble, the instantaneous velocity of the backflow can reach 15-20 cm/s (figure 5.40). A large amount of liquid moving with such a high velocity can stop the fluid layer from moving with the bubble layer. Should this happen, it would result in an instantaneous cessation of all movement of the liquid, and of the bubble layer. It can even force the whole bath to move backward, toward the centre channel. The escape of a large bubble can easily change the movement direction of small bubbles under the inner edge of the anode. If that happens, these small bubbles move a few millimetres back toward the centre channel.

Because of the principle of continuity, a slow movement takes place from the side channel to the centre channel at the bottom of the inter-electrode space. Moreover, the

abrupt backflows increase the intensity of this movement at the bottom due to the energy transfer from the escaping bubble toward the liquid and cause fluctuations in the liquid velocity. The thickness of the liquid layer moving toward the centre channel is twice as large as the thickness of the fluid layer moving with the bubbles. Consequently, the mean velocity of the fluid layer moving at the bottom is around half of the mean velocity of the fluid layer moving at the top. The magnitude of the mean velocity depends on the position under the anode (figure 5.42). Close to the side channel, where the effect of the backflow is strong but their presence is casual, the instantaneous velocity changes between 0-20 cm/s. Far from the side channel and close to the centre channel, the instantaneous velocity is quite uniform and its value is around 0.5-0.8 cm/s.

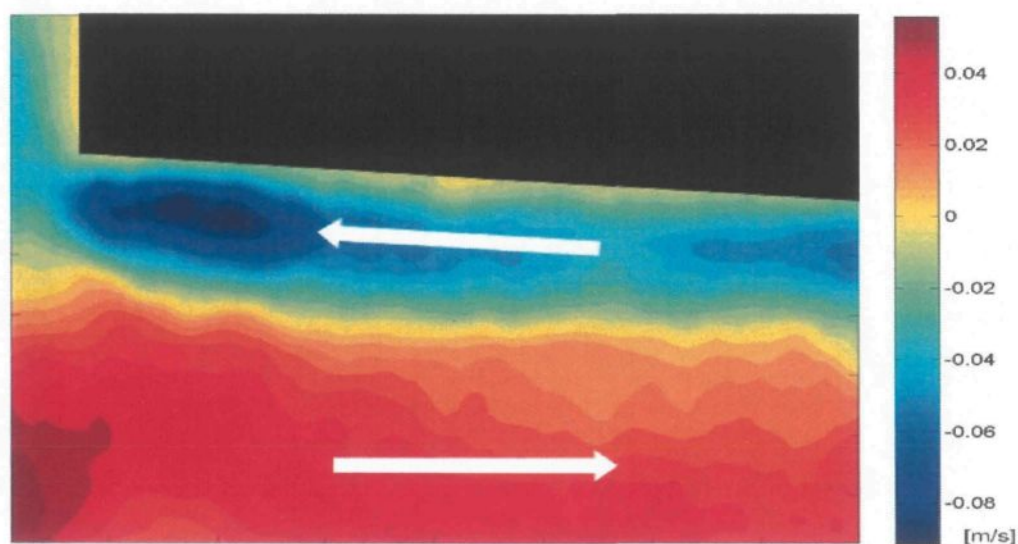


Figure 5.42 – Mean horizontal velocity close to the side channel



#### **5.4.1.4 Momentum transferred by an escaping bubble**

As it was observed earlier, large bubbles escape after breaking up into two or more parts. When the first large part escapes, it induces a strong backflow. This backflow can cause the backward movement of small bubbles under the inner edge of the anode bottom. The escape of the other smaller parts has a similar but less intense effect. The continuous escape of the bubbles induces a fast upward movement in the side channel close to the anode. This naturally results in a downward movement of the liquid close to the side of the cell. The up- and downward movements induce an open circular movement in the lateral channel. The open circular movement means that the liquid parcels pushed before an escaping bubble move upward at the side of the anode, while the liquid at the lateral channel is sucked under the anode in order to fill the void left by the bubble. Then the liquid at the bottom of the inter-electrode space flows toward the centre channel. This circular flow results in good mixing in the lateral channel and under the anode.

The volume and shape of a bubble are known to have a strong effect on the fluid flow induced around the bubble. At the same time, the induced flow has a back-effect on the bubble shape. One example of this back-effect is the Fortin shape which is formed by the dynamic forces appearing in the moving liquid. Thus only a moving bubble can have the Fortin shape. Another example is the four centimetre tall bubbles observed gliding under an inclined anode in forced flow. This height is twice as high as the maximal height observed in our experiments with natural flow in the bath.

In order to quantitatively estimate the energy transfer from the escaping bubble toward the liquid, the sum of the kinetic energy of the horizontal component of the liquid movement was calculated. It was calculated at each time-step in order to visualize its change in time. The effect of an escaping large bubble is easily observable in the results. The escape of a large bubble induces the backflow of a large amount of liquid. This backflow has a significantly larger horizontal velocity than the mean horizontal velocity of the bath. Right after the escape, the horizontal velocity of the bath increases significantly. The amplitude of the increase depends on the volume of the escaped bubble, the larger the bubble, the larger the amplitude. The duration of the increase is rather short, only a few tenths of a second. As the effect of the escape travels toward the inner edge of the anode, the horizontal velocity of the bath returns to its mean value. This return also takes place fast, lasting only a few tenths of a second. The escape of large bubbles is quasi-periodic due to the continuous gas generation under the anode. At  $1^\circ$  of angle of inclination of the anode the period of the large bubble escape is estimated to be around 1.5 seconds.

The abrupt increase and decrease in the horizontal velocity of the bath can be observed under the whole anode but its amplitude decreases toward the inner edge of the anode bottom. An increase in the angle of inclination decreases the volume of bubbles which consequently decreases the amplitude of the change in the velocity. When the inclination of the anode was larger, the effect of the escaping bubble was observed to die away closer to the outer edge of the anode. At  $2^\circ$  of inclination a quite steady horizontal flow was observed under the anode close to the inner edge. The flow at this part was rarely disturbed by the escaping bubbles.

### 5.4.2 Movement in the centre channel

The two anodes were installed with their inner edges side by side, thus the bubbles moved away from the neighbouring anodes and left the anodes at the side channel. The sucking effect of the small bubbles nucleated close to the centre channel is not strong enough to put the neighbouring fluid into movement. Moreover, the effect of a bubble escaping at the side channel is rather weak, if it can be felt at all, in the centre channel. Thus in the absence of additional driving forces, – for example the magnetic field – there is virtually no movement between the two anodes (figure 5.43). Due to the absence of movement in the centre channel the alumina powder fed between two anodes enters under the anodes slowly decreasing the efficiency of the aluminium reduction. Therefore it is very important to feed a cell close to the outer edges of the anode where the bubbles leave. The alumina fed at this point enters under the anode with the liquid and moves along the bottom of the inter-electrode space. It is well mixed and transported to the reaction sites by the vortices induced by the Fortin bubbles.

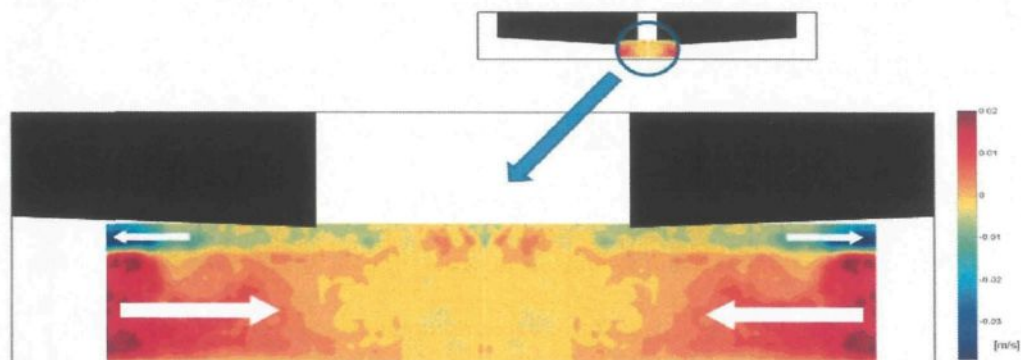


Figure 5.43 – Mean horizontal velocity in the centre channel

### 5.4.3 Flow pattern under the anode

The flow pattern under the anode is determined mainly by the large bubbles. The bubble induced flow can be seen in figure 5.44. A thick liquid layer moves with the bubble layer at the top, while at the bottom of the inter-electrode space the rest of the liquid moves backward, abruptly accelerated by the escaping bubbles. The liquid layer moving along with the bubble layer is not uniform in thickness along the anode. It is thin at the inner edge of the anode bottom, and thicker at the outer edge, where it can reach even to the depth of the inter-anode space.

As the bubbles coalesce and gain velocity while moving toward the outer edge of the anode, the velocity of the liquid moving with the bubble layer also increases. The velocity of the vertical movement also increases toward the side channel. There is a large circular movement in the side channels while at the centre channel there is virtually no movement at all (figure 5.45).

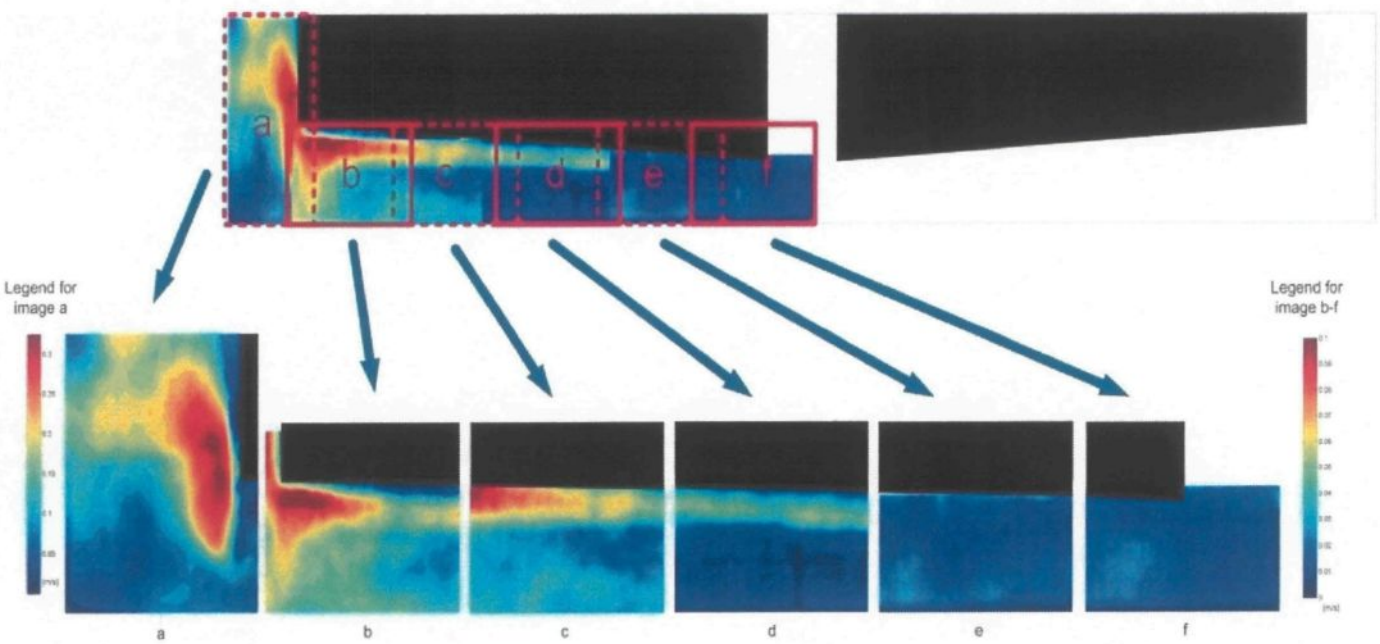


Figure 5.44 – Mean velocity in the cell. The right legend applies to images b-f.

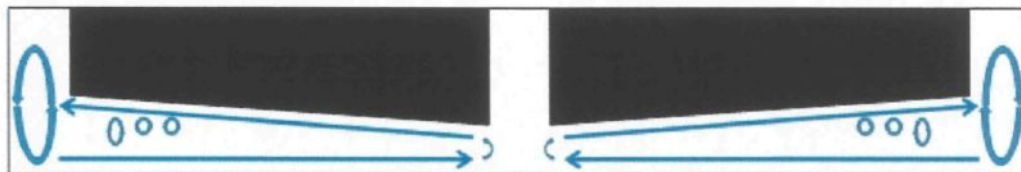


Figure 5.45 – Flow pattern under the anodes

Depending on the flow pattern under the anode, the instantaneous velocity in the top one third of the liquid is horizontal with a very faint vertical component, and it is directed toward the side channels. In the bottom one third of the liquid the magnitude of the velocity is similar but its direction is opposite. It has a significant horizontal component directed toward the centre channel and a weak vertical component. In the centre third of the bath the magnitude and direction of the velocity fluctuate irregularly. The fluid velocity close to the side channels oscillates periodically due to the effect of escaping large bubbles.

#### 5.4.4 The impact of the anodes on each other

The inclination angles of the two anodes were changed together and separately, allowing the observation of the effect of the different configurations. It was found that the inclination angle of the two anodes has a strong effect on liquid movement in the centre channel. When the two anodes have the same inclination, there is almost no movement between the anodes. If the two angles are different, the symmetry of the system is disturbed and a weak, but perceptible movement induced in the centre channel. Liquid flows under the anode that has the smaller inclination, because as the inclination angle increases, the volume of the

bubbles decreases. As already stated, a large bubble puts a large amount of liquid into movement. Thus the bubble layer under an anode whose angle of inclination is smaller, experiences a more intense flow under its inner edge. The alumina powder, which is fed into the cell close to the inner edge of the anode, will most likely enter under the anode which has the smaller inclination. This can leave the other anode alumina-free. In a real electrolysis cell the carbon anodes are consumed at different rates, which may lead to a non-uniform alumina alimentation.

#### **5.4.5 Effect of the inclination angle of the anode on the flow pattern**

The volume distribution of the bubbles in the bubble layer and the velocity of the discrete bubbles depend on the inclination angle of the anode among other things. At small inclination the bubbles move slowly, thus there is a greater probability for them to collide and coalescence. This helps to form large, but slowly moving bubbles. More significantly, it helps to form the Fortin shape. With increasing inclination the bubbles start to move faster, they collide less frequently, and consequently they form smaller bubbles. The larger bubbles force more liquid to move along with them, while the small but fast bubbles can transfer a larger amount of momentum. Thus an increase in the inclination angle generates the movement of a thinner but higher velocity fluid layer. The mean velocity of the bath under the outer edge of the anode can be seen in figures 5.46 and 5.47 for  $1^\circ$  and  $2^\circ$  of angle of inclination, respectively.



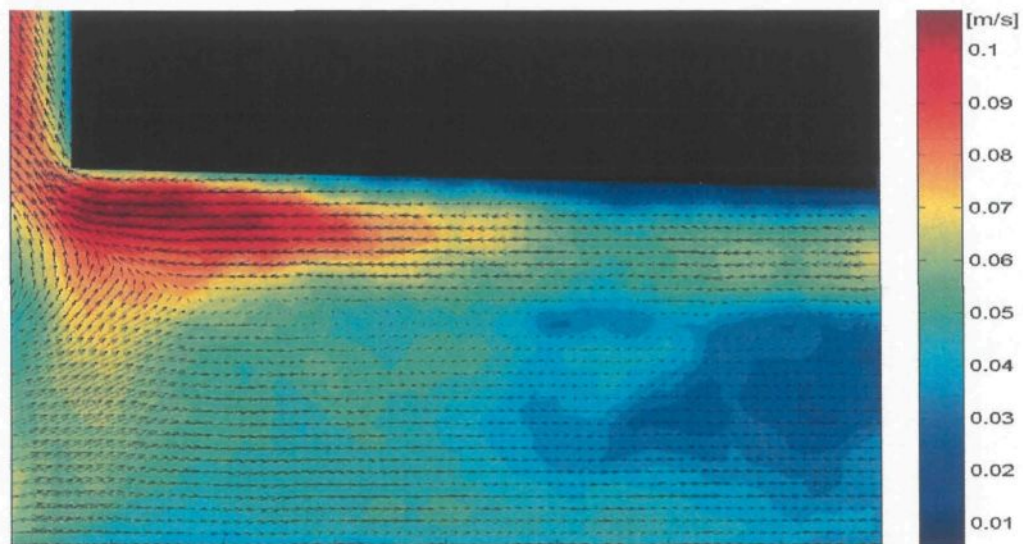


Figure 5.46 – Mean velocity close to the side channel at 1° of angle of inclination

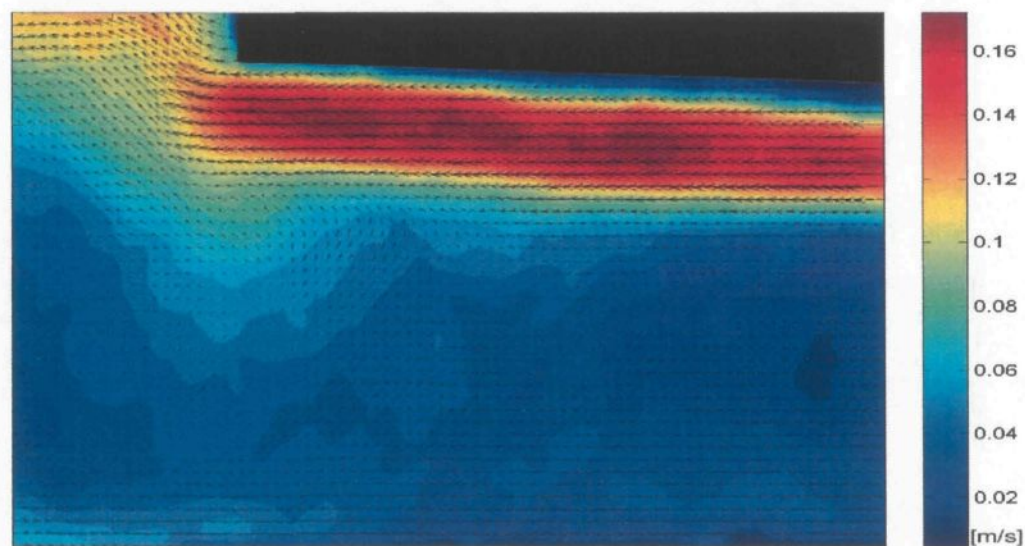


Figure 5.47 – Mean velocity close to the side channel at 2° of angle of inclination

Since the intensity of the backflow induced by an escaping bubble depends strongly on the volume of the bubble, at higher inclination the intensity of the backflow is reduced. At



high inclination the flow at the bottom of the inter-electrode space is slower and quite steady due to the absence of the large abrupt backflows.

The intensity of the mixing caused by the up- and downward movement of the bath depends on the presence of the Fortin shape. This shape forms only if the volume of the bubble is large enough. At high inclination, where the bubbles are smaller, fewer large bubbles and thus fewer Fortin shapes can be observed leading to a decreased intensity of mixing.

#### **5.4.6 Bubble induced flow in a real electrolysis cell**

The experiments were performed in an air-water real-size model. In the real electrolysis cell the fluid phase is molten cryolite-alumina and the gas phase is carbon-dioxide. The main differences between the two systems are density, surface tension and dynamic viscosity. Density is 2.3 times higher in the real cell (water at 7°C: 999.856 kg/m<sup>3</sup>, alumina-cryolite melt at 960°C: 2150 kg/m<sup>3</sup>). Surface tension is twice as high in the cryolite-carbon-dioxide system than in the air-water system (air-water: 7.28e-2 N/m, cryolite-CO<sub>2</sub>: 6e-2 – 20e-2 N/m). Dynamic viscosity is 10 times greater for the cryolite (water: 1.4343e-4 m<sup>2</sup>/s, cryolite: 1.5e-3 m<sup>2</sup>/s).

Thus a similar flow and velocity field are expected in a real electrolysis cell but with some changes due to the differences in the two systems. Because of the high viscosity and density of the molten cryolite, the amplitude of the gravity wave is expected to be smaller,

affecting Fortin bubble formation. Since the vortices induced by the wave depend on the wavelength and amplitude, they are also expected to be smaller and slower in the real bath. It is possible that the mixing effect does not reach the bottom of the ACD in a real cell.

The horizontal movements, both the movement induced by the bubble layer and the movement at the bottom of the inter-electrode space, are expected to be slower in a real cell too. It is still unclear whether the backflow caused by the escaping bubbles transfers the same momentum in the real cell as in the model. The volume distribution of the bubbles depends on the inclination of the anode and on the velocity of the bubbles. The bubbles are assumed to have the same or slower velocity in a real cell, thus they have the same or higher volume than in the model. As the intensity of the backflow depends on the volume of the escaping bubble, similar amount of momentum is expected to be transferred by a same sized bubble in the two systems. On the other hand, the molten cryolite is heavier than the water; thus more energy is needed to move the same amount of cryolite.

## **5.5 Conclusions**

### **5.5.1 Bubble layer formed under the anode**

- The flow regimes formed under a slightly inclined anode were characterised. Three different regimes were found depending on the gas generation rate. In the first regime

the bubbles slightly cover the anode bottom, while in the third regime the majority of the anode bottom is covered by bubbles which significantly decreases the efficient surface of the anode bottom.

- The exact covering at different gas generation rates, angles of inclination and positions under the anode was measured. An increase in the inclination or a decrease in the current density decreases the covering factor. The effect of the current density is stronger at low inclinations. An increase in the inclination decreases the influence of the current density. The effect of the inclination is also only observable at low angles, between  $1^\circ$  and  $4^\circ$ , while a further increase in the inclination does not change significantly the covering factor. Also, the covering factor is smaller under the inner edge of the anode bottom than under the outer edge, where the bubbles are larger due to continuous coalescence.
- Maximum contact size increases from the inner edge of the anode bottom towards the outer edge. This leads to a non-uniform contact size distribution under the anode. There are a large number of small bubbles under the inner edge of the anode, where the maximum contact size is not too large. As the bubbles coalesce, they form larger bubbles under the second section of the anode, but the small bubbles still prevail. Under the third section, the contact size of the bubbles is quite uniform and the maximum contact size is increased. As the bubbles keep coalescing, a few but huge bubbles dominate the outer edge of the anode bottom.

- As it was expected, the volume of the bubbles and thus their contact sizes were proportional to the current density. The maximum contact size decreases with decreasing current density. Also, the pattern of contact sizes changes with decreasing gas generation. The contact size distribution also depends on the angle of inclination of the anode. An increase in the angle decreases the maximum contact size significantly. Once again, small bubbles dominate the outer edge of the anode at a high inclination.
- It was found that the local average height of the bubble layer depends on and is proportional to the gas generation rate. The local maximum height of the bubble layer also increases with increasing gas generation rate, indicating that dynamic forces play an important role in its formation. Terminal value of the local maximum height was not observed in the parameter range of our experiments. The ratios of the local maximum height to local average height are similar for all gas generation rates except for the lowest, where no Fortin head was observed.
- The mean height of the entire bubble layer is independent of the gas generation rate. The mean height is around 0.8 cm for all bubble layers with Fortin bubbles, and around 0.4 cm for bubble layers produced by low gas generation. 0.4 cm is equal to the maximum height of a stationary bubble under a downward facing surface. This implies that the bubble movement plays an important role in the formation of the bubble layer.
- The volume of the bubbles was calculated from the measured contact size and an experimental correlation which gives the average height of the bubble layer at the given position under the anode. It was found that the specific bubble volume increases with

increasing current density and increases towards the outer edge of the anode. Also, the difference between the maximum and minimum specific bubble volume increases towards the outer edge of the anode and with increasing gas generation rate.

- The onset of the Fortin shape was observed and it depends on the bubble volume and the velocity difference between the liquid and gas phase. If this velocity difference or bubble volume is too small, the shape does not form. The Fortin shape was not observed regularly above 4° of inclination. The dimensions of a Fortin head were also observed to change gradually as the bubble grew while gliding and coalescing under the anode. The length and height of the head depend on the volume of the bubble and the flow pattern around the bubble.
- When a large bubble escapes from under the anode at the outer edge of the anode, a large amount of liquid has to return to fill the space left by the escaped bubble. The movement of this large amount of liquid transports a large energy which causes the whole bubble layer to come to a momentary stop. If the escaping bubble is large enough, its escape even forces the small bubbles under the inner edge of the anode to move backward.
- Using the parameters of the real cell and experimental set-up, very similar volume and contact size distribution is expected in the real cell but with slower moving bubbles. This slow movement further increases the chance of coalescence and consequently increases the volume and contact size of the bubbles. This in turn increases the covering factor of the anode leading to a higher overvoltage of the cell.

- Also based on the Morton number, we predict that similar bubble shapes would be produced in a real electrolysis cell. In addition, because of the higher density of the molten cryolite, the Fortin shape induced by the gravity wave is expected to be damped in the real cell.

#### **5.5.2 Bubble layer induced flow**

- It has been found that large bubbles have a strong effect on the flow pattern and velocity field of the bath. The bubbles moving under the anode pull a certain amount of liquid with them. This liquid layer moves toward the outer edge of the anode. The height of the moving liquid layer and its horizontal velocity depend on the volume of the bubbles. As a rough estimate, the vertical dimension is about one third of the ACD. The height of this layer is not uniform. It is four times as great below a Fortin head as below a small bubble. The moving liquid layer is thicker close to the outer edge of the anode bottom than close to the inner edge.
- Large bubbles or gas pockets form at a low inclination angle of the anode, these large bubbles take on the special Fortin shape. The Fortin shape evolves due to a gravity wave induced by the fast movement of the gas phase above the liquid phase. This gravity wave induces a circular movement of the liquid in the vertical plane below the bubble. This movement leads to a better homogenization of the temperature field and it helps to transport the alumina to the reaction sites. The vertical diameter of the circular

movement depends on the volume of the bubble as well as on the wavelength and amplitude of the gravity wave. Due to the non-uniform gas distribution under the anode, a larger circular movement can be observed close to the side channel where large bubbles form than close to the central channel. The vertical diameter of the large mixing can be as large as the ACD. Such a large circulation in the vertical plane can disturb the interface between the molten cryolite and aluminium and can lead to the re-oxidation of the aluminium.

- When a large bubble escapes from under the anode, a large amount of liquid has to flow back in order to fill the liberated space. This backflow results in a large momentum transport which can stop the whole bath for a second from moving toward the side channel. The intensity of the backflow depends on the volume of the escaping bubble. Moreover, these backflows reinforce the effect of the principle of continuity by inducing a slow movement from the side channel to the centre channel at the bottom of the ACD just above the molten aluminium.
- The escape of large bubbles causes an abrupt increase in the horizontal velocity of the bath. The magnitude of the increase is proportional to the volume of the escaped bubble, thus at higher inclination the magnitude is smaller. The effect of an escape is most intense close to the point of escape. Its effect gradually decreases toward the inner edge of the anode. The period of large bubble escapes is proportional to the gas generation rate.
- If two sloped anodes are installed with their inner edges side by side, there is virtually no movement in the gap between the two anodes. If the alumina is fed into this gap, it

enters under the anodes rather slowly, reducing the efficiency of the reduction process.

It has been found that a configuration where the two anodes have different angles of inclination leads to a more intense movement between the anodes. Due to the dissimilar angles, more liquid and thus more alumina powder enter under the anode which has a lower inclination angle.

- It was also found that a higher angle of inclination leads to the formation of smaller but faster bubbles, resulting in a thinner but faster liquid layer moving with the bubble layer and in a more uniform and a slightly slower movement at the bottom of the inter-electrode space.
- Due to the high density and viscosity of the molten cryolite, very similar but slower flow and velocity field are expected in a real electrolysis cell.

## 5.6 References

- Aaberg, R.J., Ranum, V., Williamson, K. and Welch, B.J., *The gas under anodes in aluminium smelting cells. Part II: Gas volume and bubble layer characteristics*, TMS Light Metals, pp. 341-346 (1997)
- Fortin, S., Gerhardt, M., and Gesing, A. J., *Physical modelling of bubble behaviour and gas release from aluminium reduction cell anodes*, TMS Light Metals, pp. 721-741 (1984)
- Hauptin, W. E., *A scanning reference electrode for voltage contours in aluminium smelting cells*, JOM – J. Min. Met. Mater., vol. 23, pp. 46-49 (1971)
- Perron, A., Kiss, L.I. and Poncsák, S., *Mathematical model to evaluate the ohmic resistance caused by the presence of a large number of bubbles in Hall-Héroult cells*, J. Appl. Electrochem., vol. 37, pp. 303-310 (2007)



Xue, J. and Öye, H., *Bubble behaviour – cell voltage oscillation during aluminium electrolysis and the effects of sound and ultrasound*, TMS Light Metals, pp. 265-271 (1995)

## **Chapter 6**

# **NUMERICAL SIMULATIONS OF A SINGLE LARGE BUBBLE MOVING UNDER A SLIGHTLY INCLINED SURFACE**

### **6.1 Introduction**

The experimental measurement of bubble movements in aluminium electrolysis cells is almost impossible because the bath where the bubbles are nucleated and move is very hostile. Even though the bath is transparent, the cell holding the bath is not. In a case like this, a well developed and reliable CFD code can take the place of real experiments and help the understanding of the phenomenon; an appropriate numerical code can be developed and verified. In order to confirm that the simulations represent reality, the numerical code has to be checked against real physical measurements. As it was shown, the two-phase flow in a real electrolysis cell can be reliably simulated using an air-water model; the results of the physical measurements carried out in this model can therefore

prove the reliability of the numerical model. The verified numerical code then can be used to perform simulations using the parameters of the real electrolysis cell.

Moreover, the parameters of the computational domain and the materials in the system can be changed arbitrary and individually in a numerical code. This is almost impossible to perform in a physical measurement. Thus, numerical simulations have the flexibility to investigate the effect of each parameter on the system.

Even though an enormous number of articles have been released lately on the numerical simulation of multiphase flows, no articles can be found simulating bubbles gliding under a solid surface. The majority of work on bubble simulations are concerned with freely rising bubbles, the rising bubble column and two bubbles coalescing under different conditions (i.e.: *Trapp et al, 1993; Yang et al, 2005; Méndez et al, 2005; Ginzburg et al, 2001; Caboussat, 2005; Thürey, 2003*). Simulation of a large, deformable bubble moving under a solid surface hitherto has not been found at all in the literature by the author. The numerical methods used to simulate the different sized bubbles are wide ranging. For the most part, the bubbles do not have an arbitrary shape. Different sized arbitrarily shaped bubbles are extremely difficult to simulate; it is time consuming and requires considerable computer resources.

Several numerical simulations have been performed on mass and heat transfer, and on the magneto-hydrodynamic effects in a real electrolysis cell. The majority of these simulations include the effect of the bubbles only indirectly by using modified parameters of the liquid phase. There are a few simulations where the bubbles are directly included, but

they are always simulated as equal sized (approximately 3 mm) and equal shaped (spherical) bubbles (*Bilek, 1994; Purdie, 1993*). However, the shape and the size of the bubbles gliding under the anode cover a wide range. Their size ranges from a few millimetres up to several centimetres. Neglecting this fact can lead to significant differences between reality and simulation. Some authors have modified certain parameters of the computational system in order to take the effect of the bubbles into account. As it stands now, the effect of the bubbles under the anode on the mass and heat transfer in the bath is not yet completely understood, so these modifications are neither perfect nor verified.

Two numerical simulations were found where the real size but not the real shape of the bubbles was taken into account. *Kiss et al (2005)* developed a numerical code to simulate a large number of bubbles moving and coalescing under downward faces (figure 6.1). In this simulation the simple three dimensional disk shaped bubbles are tracked using the Discrete Particle Model. The shape is considered a rigid body whose volume can grow by coalescence. Hence, the bubble shape and movement can be described by the movement of the centre and the diameter of the bubble in the horizontal plane. The governing equations of the two-phase flow system are derived from simplified force and momentum balance equations. The coalescence process is simulated by a simple model; the two bubbles become one instantaneously if they touch each other.

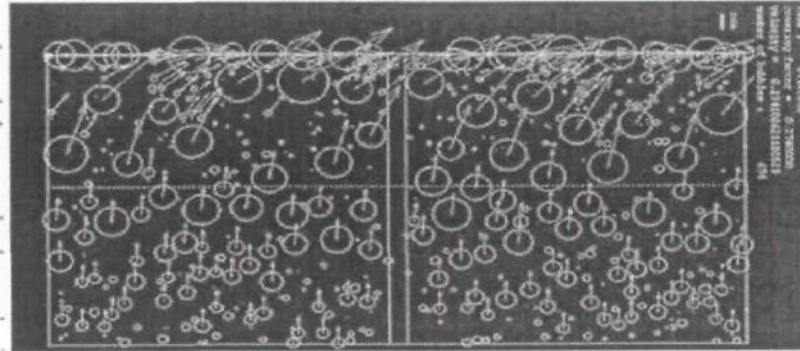


Figure 6.1 - Simulation of bubbles under the anode. After *Kiss et al (2005)*

The simulation of *Lozinski et al (2007)* is based on the above explained idea of simulating a bubble gliding under a slightly inclined solid surface. The bubbles are again described by the DPM, where the shape of a bubble belongs to a family and so its deformation is limited. Hence the motion of the surface is tracked by the motion of the barycentre of the particle and the change of the coefficients used to describe the family of surfaces. The governing equations of the deformable body are derived from the virtual displacements and the Lagrange equations using D'Alembert's principle. The governing equations of the two-phase flow consist of the Navier-Stokes equation, and the conservation of mass for incompressible fluids; the boundary condition is that the velocity has to be the same at the interface. The governing equations are applied using the fictitious domain approach and the Gauge method which introduce two new variables to replace the fluid velocity thus solving the problem caused by the pressure-velocity coupling. *Lozinski et al (2007)* modelled coalescence by using a simple condition to decide when two bubbles are close enough to coalesce. If the distance between two bubbles is smaller than a defined

limit, the two bubbles coalesce; the smaller bubble empties itself into the larger one in a small number of time-steps.

## 6.2 Objectives

The objectives of the numerical simulation is to set-up a numerical code which can simulate arbitrary shaped bubbles and, hopefully, a large number of arbitrary shaped bubbles. The code can be set-up in order to simulate the real behaviour of bubbles rising under a slightly inclined surface including their effect on the electrical resistance caused by the bubbles. A simulation of the real shape of a large bubble gliding under a solid surface is really important for the simulation of heat and mass transfer in an electrolysis cell.

The developed code can be used to investigate the effect of different factors on the behaviour of a bubble, factors such as density, viscosity, surface tension, bubble volume and angle of inclination. Surface tension is believed to have an insignificant effect on large bubbles, while the angle of inclination and bubble volume have an influence on the velocity of the rising bubble and thus on its form because the shape of the bubble depends on the size of the bubble and the forces acting on the moving bubble. The density and viscosity of the electrolysis bath depends on the temperature, but during normal operations they are assumed to be constant. The effects of these parameters are investigated to help our

understanding of the formation and the movement of large bubbles gliding under solid surfaces.

The advantage of a numerical code is that the different factors of a system can be changed separately and thus their effects can be examined. Whereas in an experiment the factors are not independent and to change some of the factors separately is elaborate.

One of the objectives of the physical measurements was to create a database of large bubbles rising under slightly inclined surfaces. The database could then serve to validate the numerical code. As the physical experiments were performed with air and water, the results are used to check against simulations using air and water. If the measurements and numerical simulations are in good agreement for a given material couple, and the shape of the bubble changes with changing certain parameters as it is expected to according to the universal laws of movement, it is assumed that the numerical simulation gives equally good result using materials from a real electrolysis cell.

The method of the numerical simulation set-up can be integrated into the bubble layer simulator developed by *Kiss et al (2005)*. This way the simulator will take into account not only the effect of bubble size, but also the actual bubble shape on the mass transfer in the bath and on the electrical resistance caused by the bubbles.

### 6.3 Simulations using the openFOAM code

OpenFOAM, an open-source code, was chosen to perform the numerical simulations because we wished to be able to freely modify or expand it. OpenFOAM is stable, rapidly developed and it offers several simulation methods. The code is written in C++ language and it is very easily readable and developable. Moreover, there are several FAQs and forums where the problems and questions are quickly answered by experts.

OpenFOAM offers a wide range of solvers, like solver for incompressible flows, compressible flows, multiphase flows, etc as well as different interface tracking/handling methods. A simple geometry and mesh generator is included with the program. Simulation output can be converted into VTK format using a sub-code of openFOAM. This format is widely used and several freely available post-processor codes can be found on the internet in order to visualize any result saved into this format.

#### 6.3.1 Model, mesh and simulations

##### Model

The geometry used during the simulations represents one inclined solid surface and the bath under the anode. This geometry can be seen in figure 6.2.



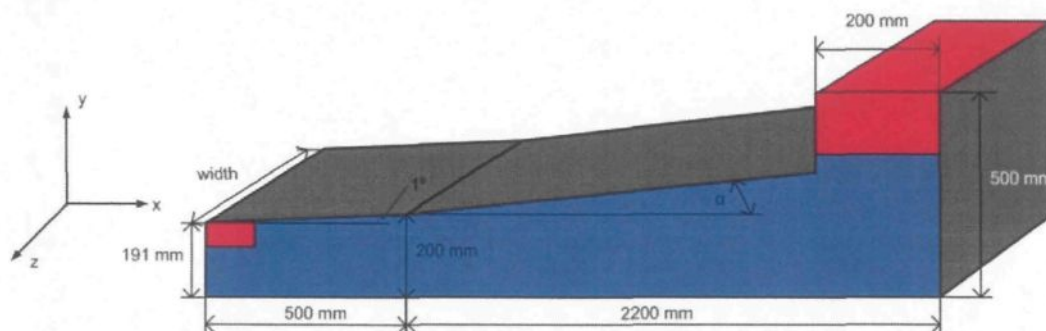


Figure 6.2 - Computational domain

The different colours in the figure 6.2 represent different materials. Red ( $\gamma=1$ ) represents the initial gas area and blue ( $\gamma=0$ ) represents the initial liquid, where  $\gamma$  is the volume fraction of the gas phase in a mesh cell. The initial gas field can be given as a rectangle only. Thus, the red area on the left represents the initial bubble, and the red area on the right represents the ambient air at the outlet.

The surface consists of two sections, the initial section is half-a-meter long with a constant inclination at  $1^\circ$  and the second section is 2 meters long with an inclination that was changed for different runs of the simulation. The first inclined surface with  $1^\circ$  inclination is used to let the bubble evolve from the initial rectangular shape into a more natural bubble shape. This step is necessary because the initial shape of the bubble is very artificial. The second inclined surface represents the bottom of an inclined anode.

The dimensions of the computational domain are given in figure 6.2. The width of the domain is equal to the width of one mesh cell. Since only two-dimensional simulations were performed, the width of the domain was not changed.

Therefore the initial velocity is 0 m/s in all directions and the dynamic pressure is 0 Pa in both liquid and gas phases.

#### *Initial conditions*

The gamma parameter (volume fraction of the liquid phase) is initialized using a sub-code. The volume of the outlet (red area at the top right part of the domain) always has the same dimensions ( $x=200$  mm,  $y=200$  mm and  $z=\text{width}$ ), while the initial bubble area changes according to the bubble volume.

The gas and liquid phases are motionless at the beginning of a simulation. Therefore the initial velocity is 0 m/s in all directions and the dynamic pressure is 0 Pa in both liquid and gas phases.

#### *Boundary conditions*

The boundary conditions used in the simulations can be seen in figure 6.3.

The inclined upper and horizontal bottom side of the domain, just as the vertical most left and most right side of the domain is wall. The vertical left side of the outlet is also wall. The non-slip wall condition means fixed, zero, value for the velocity and zero gradient for the pressure.

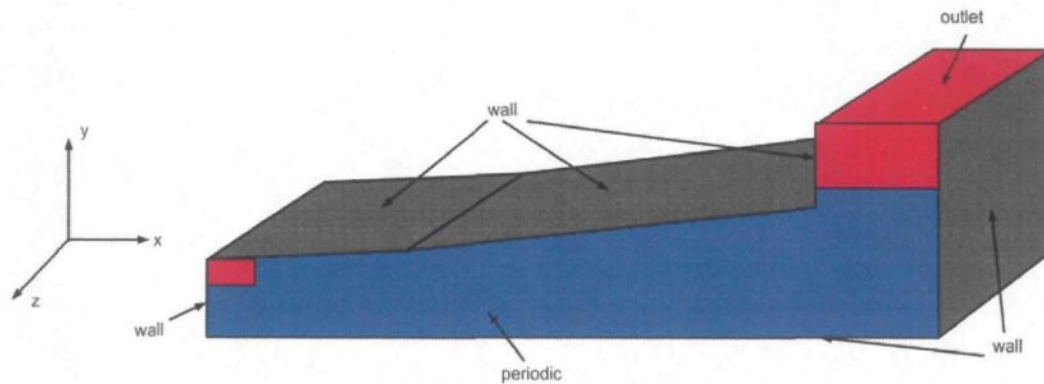


Figure 6.3 - Boundary conditions

The boundary condition on the two vertical sides of the domain in the x-y plane is periodic. The horizontal upper side of the outlet is outlet where the pressure is fixed at 0 Pa.

### Mesh

The geometry and mesh were created using the openFOAM geometry and mesh creator. In order to create geometry, rectangle based blocks were formed and joined together. A block is defined by the three-dimensional position of its corners. The vertices are stored in a separate file as shown in figure 6.4.

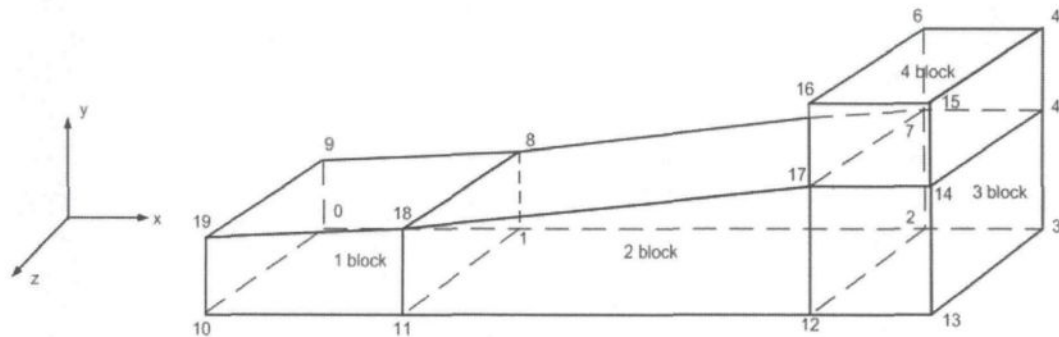


Figure 6.4 –Vertex and block numbers

The meshes were created using the following parameters:

- structured hexagonal cells
- simple grading (equidistant cells)
- 400 cells in x directions
- 70 cells in y direction for the lower blocks and 140 cells for the upper block
- 1 cell in z direction

A segment of the mesh used in the simulations can be seen in figure 6.5.

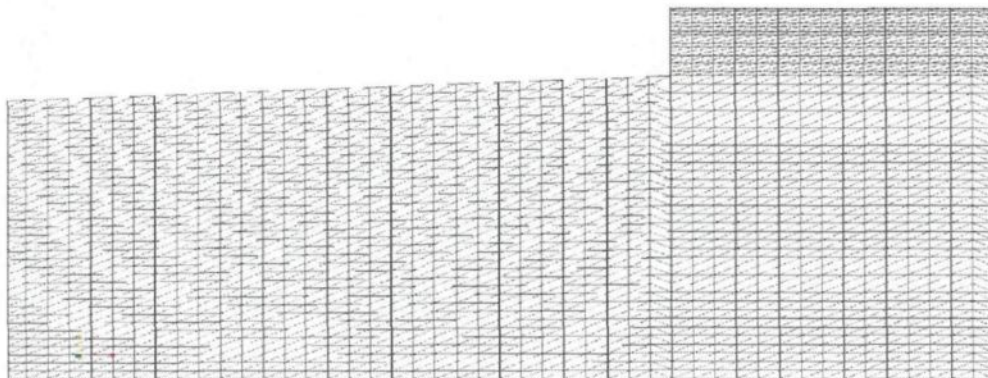


Figure 6.5 – Close up of the mesh used in the simulations

### Simulations

The interFoam solver utility was used for these simulations. It is a “*Solver for 2 incompressible, isothermal immiscible fluids using a VOF (Volume of Fluid) phase-fraction based interface capturing approach*” (from [www.openfoam.com](http://www.openfoam.com)). This code solves a single momentum equation while the momentum itself and the fluid properties are of the “mixture”. The Volume of Fluid method is used to track the interface between the bubble and the liquid. Because of the attitude of the phenomenon, the simulations are transient. Considering that the mass of the liquid is in rest at the beginning and stays in rest during the movement of the bubble, we used a laminar flow model, without prescribing turbulence.

The following Navier Stokes equation was solved for the velocity and pressure fields

$$\frac{\partial \rho \vec{u}}{\partial t} + \nabla \cdot \rho \vec{u} \vec{u} - \nabla \cdot \mu \nabla \vec{u} = -\nabla p \quad (6.1)$$

Air-water and molten cryolite-carbon dioxide phases were simulated using different angles of inclination and bubble volumes. Different surface tensions were also used in order to investigate the effect of surface tension on the movement and shape of the bubble.

Because of the time required to perform a three-dimensional simulation in such a physically large model, only two-dimensional runs were performed.

The parameters used during the simulations can be seen in table 6.1.

Density ratio [-]	2300/0.4 (cryolite/CO <sub>2</sub> ) 998/1 (air/water)
Surface tension [N/m]	0.001 N/m 0.07 N/m (water) 0.5 N/m 0.15 N/m (cryolit)
Angle of inclination [°]	1° 2° 4° 6°
Volume of bubble [cm <sup>3</sup> ]	100 cm <sup>3</sup> 490 cm <sup>3</sup> 750 cm <sup>3</sup> 1000 cm <sup>3</sup>
Dynamical viscosity [m <sup>2</sup> /s]	1.48e-5 m <sup>2</sup> /s (air) 1e-6 m <sup>2</sup> /s (water) 15e-4 m <sup>2</sup> /s (cryolite)
Dimension	2D

Table 6.1 – Parameters used during the simulations

The control parameters of the simulations were chosen as shown in table 6.2.

Timestep [s]	0.001
Physical length of the simulation [s]	100
Time intervals to save results to disc [s]	0.05

Table 6.2 – Control parameters of the simulations

### **6.3.2 Results and discussion**

Several numerical simulations were performed with different gas and liquid phases using the same computational domain and the same mesh, but changing the angle of inclination of the surface. The shape and movement of several different sized bubbles were also simulated. The effect of the different angles of inclination, the volume of the bubble and the parameters of the liquid and gas phases on the movement and shape of the bubble were investigated. The calculated shape and the numerical results are in good agreement with physical observations. These results are presented below.

#### **6.3.2.1 Shape forming from the initial gas pocket**

As mentioned above, the initial shape of the gas bubble is always rectangular in our simulations. In order to let the gas phase form a more natural initial shape before it starts to glide under the investigated surface, a so called “initial surface” is installed before the investigated one (figure 6.6). The angle of inclination of this initial surface is always kept at  $1^\circ$ .

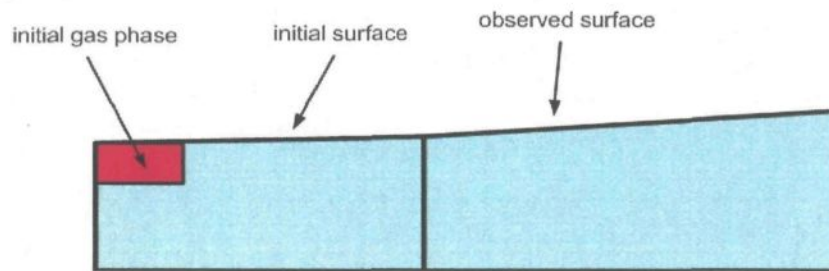


Figure 6.6 – Initial gas phase under the initial surface

The numerical simulations show that a natural shape forms in a short time period, only a few seconds, and well before the bubble reaches the end of the initial surface. Snapshots of the formation of the initial shape of an air bubble moving in water can be seen in figure 6.7. Once again the colours represent the volume fraction of the liquid phase and red means zero volume fraction of liquid.

The most bottom bubble shape seen in figure 6.7 is similar to the initial cross-section observed during the physical experiments. As the numerical simulations were performed only in two-dimension, the contact shape observed during the experiments cannot be compared with the numerical simulations.



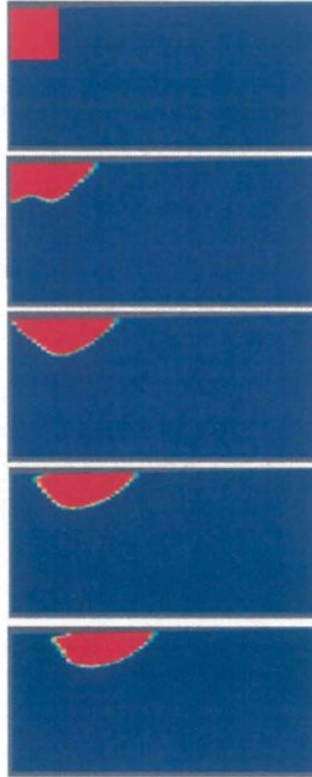


Figure 6.7 – Snapshots of the initial bubble shape evolution

#### 6.3.2.2 Formation of the final Fortin shape

The cross-section of the Fortin shape, described and characterized in detail in chapter 4, could be observed in each simulation. The formation of the simulated Fortin head is similar to the one observed during the measurements. The head starts to form at the back of the bubble and as it gains velocity, it moves forward, toward the front of the bubble. The

physical explication of the formation of the Fortin shape and the movement of the Fortin bubble is explained in chapter 4. Snapshots of the formation of the Fortin shape of an air bubble moving in water can be seen in figure 6.8.

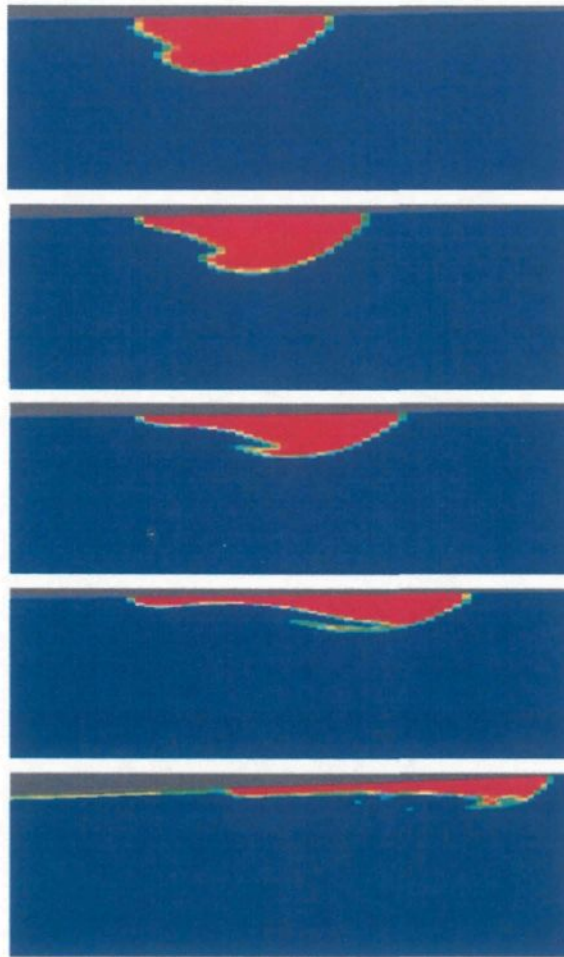


Figure 6.8 – Snapshots of the Fortin shape formation.

The duration of the transformation from the initial into the final shape depends on the bubble volume (figure 6.9) and on the angle of inclination (figure 6.10) while it does not

depend on the surface tension, as it was expected. The velocity of the formation decreases with increasing bubble volume while other parameters are kept constant ( $\alpha_{\text{angle of inclination}} = 4^\circ$ ,  $\rho_{\text{liquid}}/\rho_{\text{gas}} = 998/1$ ,  $\sigma = 0.07 \text{ N/m}$ ,  $\mu_{\text{gas}} = 1.48e-5 \text{ m}^2/\text{s}$  and  $\mu_{\text{liquid}} = 1e-6 \text{ m}^2/\text{s}$ ).

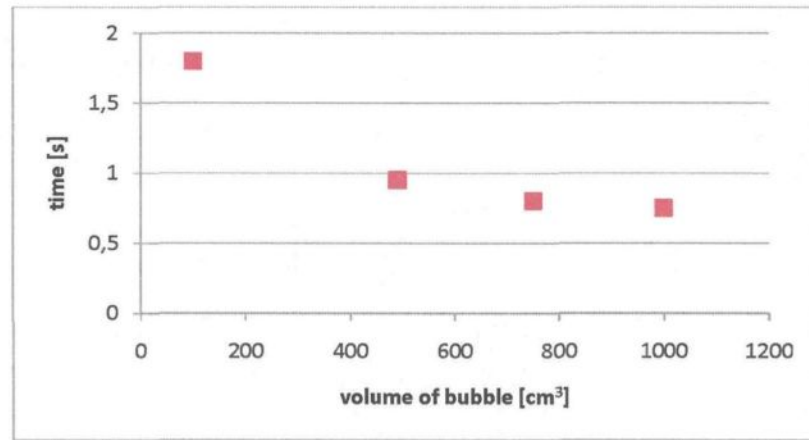


Figure 6.9 – Duration of the formation of the final shape as a function of the bubble volume

The velocity of the formation decreases also with increasing angle of inclination ( $V_{\text{bubble}} = 490 \text{ ml}$ ,  $\rho_{\text{liquid}}/\rho_{\text{gas}} = 998/1$ ,  $\sigma = 0.07 \text{ N/m}$ ,  $\mu_{\text{gas}} = 1.48e-5 \text{ m}^2/\text{s}$  and  $\mu_{\text{liquid}} = 1e-6 \text{ m}^2/\text{s}$ ).

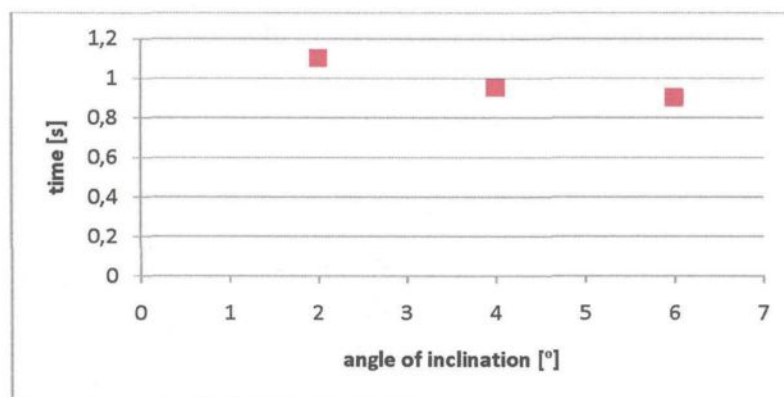


Figure 6.10 – Duration of the formation of the final shape as a function of the angle of inclination

The transformation into the final shape took significantly more time in the real cell simulation, approximately 3.7 seconds, than in the case of an air-water model.

### 6.3.2.3 Effect of the angle of inclination on the bubble shape and movement

The buoyancy force parallel to the direction of the movement of the bubble increases with an increase in the angle of inclination. As a result, the bubble accelerates. On the other hand, as the bubble gains velocity, the drag force increases, this works against the accelerating effect of the increased buoyancy. At a low angle of inclination, the increase in the accelerating force is larger than the increase in the resistance, thus the velocity of the bubble increases with an increasing angle of inclination.

As the shape of the bubble depends on the forces acting on it and these forces depend on the angle of inclination, the angle of inclination plays an important role in the formation of the Fortin shape.

Numerical simulations show similar characteristics to those observed during the physical experiments: the shape of the bubble does not change with an increasing angle but its dimensions do. Increasing the angle of inclination decreases the length and increases the height of the bubble. Diagrams showing the effect of the angle of inclination on bubble dimensions as measured during our experiments can be seen in figures 4.7-4.11 while the simulation results can be seen in figures 6.11 and 6.12. During the simulations to investigate the effect of the angle of inclination the following parameters were used:

$$V_{bubble} = 490 \text{ ml}, \quad \alpha_{angle \text{ of inclination}} = 1, 2, 4 \text{ and } 6^\circ, \quad \rho_{liquid} / \rho_{gas} = 998/1, \quad \sigma = 0.07 \text{ N/m}, \\ \mu_{gas} = 1.48e-5 \text{ m}^2/\text{s} \text{ and } \mu_{liquid} = 1e-6 \text{ m}^2/\text{s}.$$

During our simulations the length of the bubble decreased with increasing angle of inclination just as it was observed during the measurements. Unfortunately, change in the height of the bubble could not be observed with the mesh used for the simulations. A finer mesh is necessary to see small changes in the height. The length of the bubble as a function of the angle of inclination as it was calculated during the simulations is presented in figure 6.11.

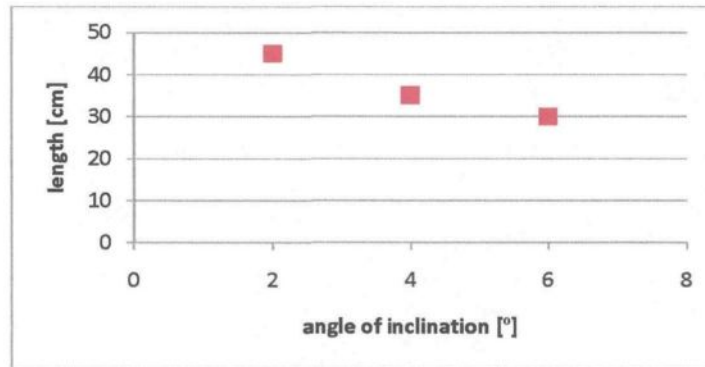


Figure 6.11 – Length of a 490 ml large bubble as a function of the angle of inclination

The terminal velocity of a 490 ml large bubble was calculated as a function of the angle of inclination and is presented in figure 6.12 while the velocities measured during the experiments can be seen in figure 4.18.

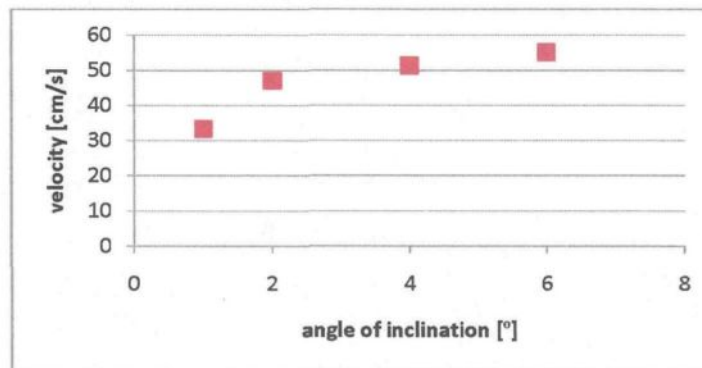


Figure 6.12 – Terminal velocity of a 490 ml large bubble as a function of the angle of inclination

The velocities calculated during the simulations are much higher than those measured during the experiments but show the same relationship with the angle of inclination. The

reason for these higher velocities is the much larger bubble size used during the simulations. The volume of our two-dimensional simulated bubble can be calculated as

$$V_{bubble} = A_{cross\ section} \cdot z \quad (6.2)$$

where  $z$  is the dimension perpendicular to the transversal plane

$A_{cross\ section}$  is the area of the cross section

Since the simulations were performed only in two dimensions,  $z$ , the width of the bubble, was equal to the width of the mesh cell in this direction. The simulated two-dimensional geometry corresponds to a small body segment of the central part (around the nose) of the real bubble (see figure 6.13).

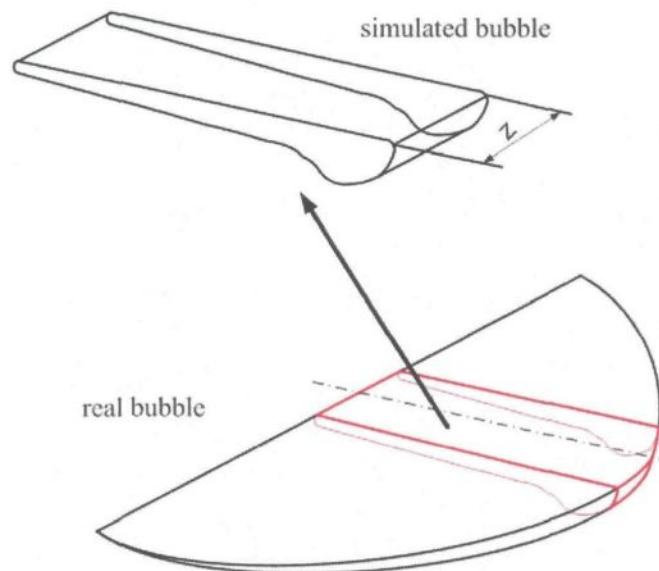


Figure 6.13 – Relationship between the simulated and the real bubble

According to (6.2) and to the width of a mesh cell, the size of the cross section of a 490 ml large bubble is approximately  $50 \text{ cm}^2$ . According to our experiments a cross-section as large as  $50 \text{ cm}^2$  may belong to a bubble as large as 1 litre or more. This is a much larger bubble than it was used during our experiments thus much larger dimensions and higher velocities were expected and indeed calculated during the simulations.

One effect observed during the experiments was not reproduced in the simulations. In the experiments the Fortin shape does not form at a high angle of inclination. This phenomenon was observed because the motion of the liquid layer decreases the difference in velocity between the gas and the liquid phases at a high angle and thus reduces the force forming the Fortin shape. During the numerical simulations the liquid phase was assumed to be initially motionless, therefore the Fortin shape was observed at each angle of inclination. Even the highest angle of inclination simulated,  $6^\circ$ , was not high enough to prevent the formation of the Fortin shape.

#### **6.3.2.4 Effect of the liquid properties on bubble shape and movement**

The properties of the liquid and gas phases investigated were the surface tension, dynamic viscosity and density ratio of the liquid to gas phase. Their investigation is essential to find out more about the formation and movement of carbon-dioxide bubbles in molten cryolite.



### Effect of surface tension

Surface tension is expected to be important and dominant for small sized bubbles, where the surface tension tries to minimize the interface between the bubble and liquid phases and forces the bubble to be spherical. As the volume of the bubble increases, the effect of the surface tension decreases and the effect of other forces, such as buoyancy or different dynamic forces acting on a moving bubble increases. Thus a large bubble has a complex three-dimensional shape. As only large bubbles were simulated, the surface tension was not expected to effect the shape and the movement of the bubble significantly. No notable change in the dimensions of the bubble or in its velocity was observed during the simulations even though three different surface tensions (0.001, 0.07 and 0.15 N/m) were used while all other parameters of the simulations were kept constant ( $V_{bubble} = 490 \text{ ml}$ ,  $\alpha_{angle \text{ of inclination}} = 4^\circ$ ,  $\rho_{liquid} / \rho_{gas} = 998/1$ ,  $\mu_{gas} = 1.48e-5 \text{ m}^2/s$  and  $\mu_{liquid} = 1e-6 \text{ m}^2/s$ ).

### Effect of viscosity and density

Viscosity is expected to have a bigger effect on large bubbles. The viscosity plays an important role in mass transfer through the interface between the gas and liquid phases thus it is important in the formation of the induced flow field around the bubble. In a more viscous liquid a damped flow field is expected.

The density ratio between the two phases is also important for the momentum transfer in the bath. A denser fluid transports larger kinetic energy but it requires more energy to put it into movement.

Simulations were performed with different viscosities and density ratios though their effect separately was not investigated. Two simulations were done, one with air-water and one with CO<sub>2</sub>-molten cryolite materials. The parameters of these two simulations were as follows

$$\text{Air-water: } V_{\text{bubble}} = 490 \text{ ml}, \quad \alpha_{\text{angle of inclination}} = 4^\circ, \quad \rho_{\text{liquid}} / \rho_{\text{gas}} = 998/1, \\ \mu_{\text{gas}} = 1.48e-5 \text{ m}^2/\text{s} \text{ and } \mu_{\text{liquid}} = 1e-6 \text{ m}^2/\text{s}$$

$$\text{CO}_2\text{-molten cryolite: } V_{\text{bubble}} = 490 \text{ ml}, \quad \alpha_{\text{angle of inclination}} = 4^\circ, \quad \rho_{\text{liquid}} / \rho_{\text{gas}} = 2300/0.4, \\ \mu_{\text{gas}} = 1.48e-5 \text{ m}^2/\text{s} \text{ and } \mu_{\text{liquid}} = 15e-4 \text{ m}^2/\text{s}.$$

The effect of the density ratio and viscosity is discussed below in chapter 6.3.2.6.

#### Effect of the Morton number

The higher viscosities of the gas and liquid phases and higher density ratio between the gas and liquid are expected to lead to a similar but slower motion. As it was explained in the chapter 4, the Fortin head forms dynamically. The dynamic forces depend strongly on the fluid parameters. Therefore, these two parameters play an important role in the formation of the Fortin shape.

Bubbles are less deformable in high Morton number fluids (*Perron et al 2006*), where the Morton number depends on the properties of the liquid and it is proportional to viscosity and density and inversely proportional to the surface tension. As the Morton number of a more viscous and denser fluid is higher, a less deformed bubble shape is expected with increasing viscosity and density.

These expectations were verified by simulations. The velocity of the bubble was slower in a denser and more viscous fluid (chapter 6.3.2.6), as was its formation from the initial shape (chapter 6.3.2.2).

#### **6.3.2.5 Effect of the bubble volume on the bubble shape and movement**

Bubble volume is expected to influence bubble dimensions directly. As the volume increases, the dimensions of the bubble have to increase in order to compensate the increased volume. As it was observed during the physical measurements the increase in the volume increases the length, width and height of the bubble. The intensity of the increase in the width and length decreases at higher volumes. The average height of the bubble increases moderately with increasing volumes. The height of the head increases even less, while the length of the head increases more intensely, thus the increased volume seems to be compensated with a longer head, while the aspect ratio between the width and length is independent from the volume of the bubble. The experimental results can be seen in figures

4.7-4.11 while the results of the simulations performed with the following parameters  $V_{bubble} = 100, 490, 750 \text{ and } 1000 \text{ ml}$ ,  $\alpha_{\text{angle of inclination}} = 4^\circ$ ,  $\rho_{liquid} / \rho_{gas} = 998/1$ ,  $\mu_{gas} = 1.48e-5 \text{ m}^2/s$  and  $\mu_{liquid} = 1e-6 \text{ m}^2/s$  are presented below, in figure 6.14. During the simulations all the above mentioned phenomena were observed. It has to be emphasized that the bubble volumes used in the simulations represent much larger bubbles in the reality. For example a 490 ml large bubble in the simulations corresponds to a bubble as large as 1 litre or more in the reality. Moreover, a small increase in the dimensions of the bubble was impossible to measure due to the coarse mesh. The simulated maximum height and mean thickness as large as 8 cm and 5 cm, respectively, are the consequences of the quality of the mesh.

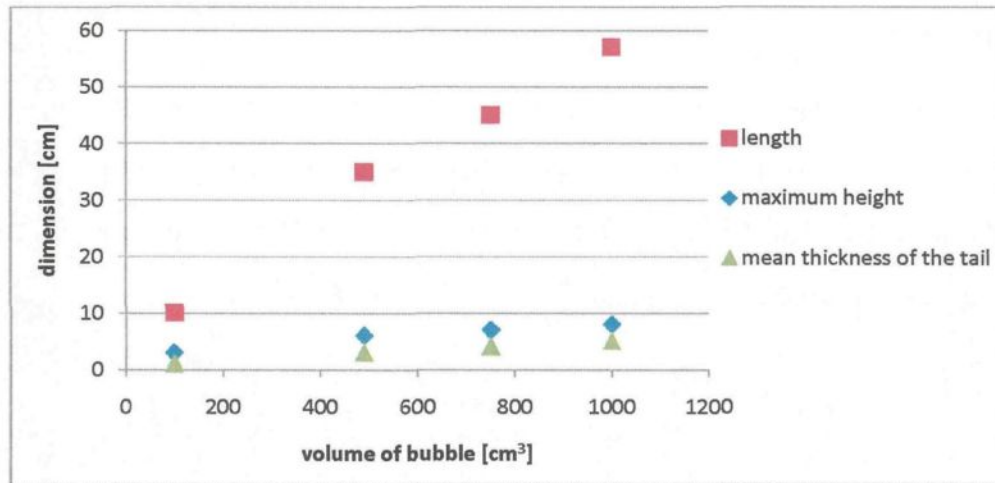


Figure 6.14 – Effect of bubble volume on the dimensions of the gliding bubble

The larger volume accelerates the bubble due to increased buoyancy. This larger velocity shifts the balance of the dynamic forces acting on the bubble resulting in a changed shape.

The terminal velocity as a function of the angle of inclination is presented in figure 6.15. Considering that the bubble volumes used during the simulations represent much larger volumes in the reality, the simulated velocities are in good agreement with the experiments. The terminal velocity increases with bubble volume and angle of inclination.

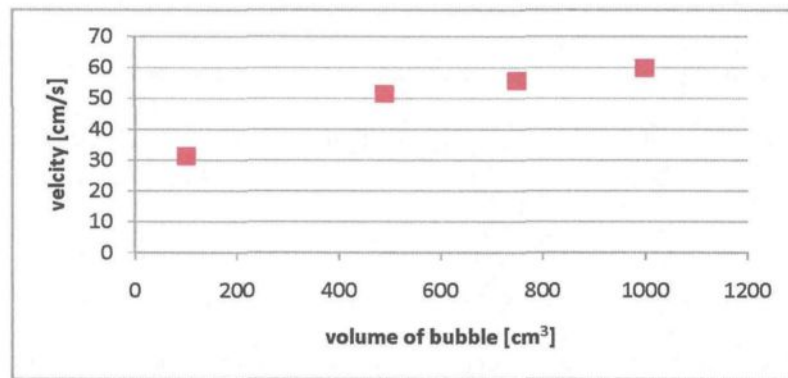


Figure 6.15 – Terminal velocity as a function of the bubble volume

The increase in both the angle of inclination and the volume of bubble strengthen each other's effects on the shape and movement. Increasing both the volume of the bubble and the angle of inclination increases the velocity of the bubble. This in turn changes the balance of the acting forces and the dimensions of the bubble. The faster moving larger bubble limits the increase in its velocity by the increased resistance it causes.

### 6.3.2.6 Air bubble in water vs. carbon-dioxide bubble in molten cryolite

Numerical simulations with the two material groups were performed in order to see the bubble formation and movement in a real electrolysis cell. The different parameters of air, water, carbon-dioxide and molten cryolite materials are shown in chapter 6.3.2.4.

The simulation using the parameters of a real cell showed that the liquid phase has a strong effect on the shape and formation of the bubble. The simulated bubble was much more elongated where the Fortin head could be hardly identified due to the poor quality of the mesh. The formation of a CO<sub>2</sub> bubble into the final shape took more than four times as it took for an air bubble moving in water (figure 6.16). In addition, the terminal velocity of the CO<sub>2</sub> bubble was much smaller than that of an air bubble.

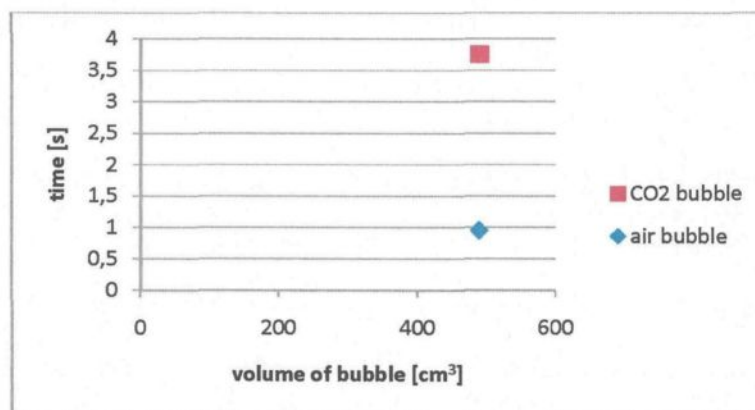


Figure 6.16 – Effect of the material properties on the duration of the formation of a bubble

#### **6.3.2.7 Comparing measurements with the results from the simulations**

All the simulation results show a good agreement with the physical experiment results. The expectations were met about the effect of the bubble volume, angle of inclination, surface tension, density and viscosity on the formation and movement; similar dimensions and velocities were obtained as a function of the above mentioned parameters.

The numerical simulations were also performed on much larger bubbles than in the physical measurements. These simulations also confirm expectations about the shape and movement of the bubble.

Numerical simulations for air and water and carbon-dioxide and molten cryolite systems confirmed yet again the expectations about the effect of the liquid properties. However, we cannot analyse the effect of the existence of a liquid layer separating the bubble and anode bottom because of the relatively coarse mesh used in the simulations. As the hypothetical thickness of such a layer is in the order of a few hundred micrometers, it cannot be visible in our results. Neglecting this layer can effect the calculated terminal velocity.

The good agreement between the physical measurements and numerical simulations show that the simulation of the arbitrarily shaped large bubble gliding under a slightly inclined solid surface is possible. With the availability of large computer resources, the simulations can be performed in a reasonable time.

A cross-section of an air bubble moving in water observed during the physical experiments can be seen in figure 6.17. Figure 6.18 shows the calculated cross-section of an air bubble rising under an inclined surface in water.

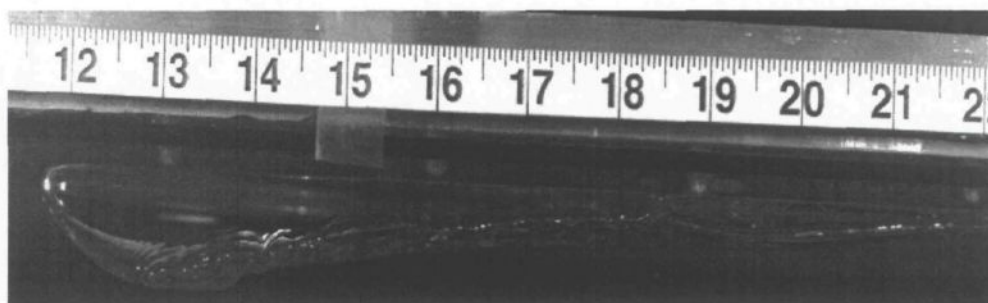


Figure 6.17 – Cross-section of air bubble gliding under an inclined surface in water

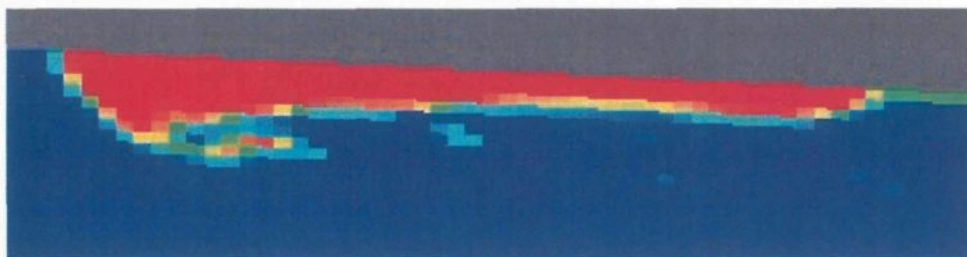


Figure 6.18 – Cross-section of a numerically simulated air bubble gliding under an inclined surface in water

#### 6.4 Conclusions

The numerical simulations were performed in order to investigate the effect of different parameters, such as surface tension, viscosity, density, angle of inclination and bubble



volume, on the formation and movement of a bubble. The objective of these simulations was also the investigation of a carbon-dioxide bubble moving in molten cryolite. These objectives were achieved and the results of the simulations show a good agreement between the expectations and the results of the physical experiments. In light of the results of the numerical simulations, the following conclusions can be drawn.

- Increasing the volume of the bubble increases the dimensions, the average and the maximal heights and the length of the bubble.
- Increasing the volume of the bubble and/or the angle of inclination increases the velocity of the bubble.
- Increasing the angle of inclination increases the height of the bubble and decreases its length; further increasing the angle prevents the bubble from forming the Fortin head.
- Surface tension has no effect on the results.
- The simulation using the parameters of a real cell showed that the liquid phase has a strong effect on the shape of the bubble; the bubble formed much slower in cryolite and the form of the bubble was much more elongated with a much smaller head, has the head formed.

## 6.5 References

- Bilek, M. M., Zhang W.D. and Stevens, F. J., *Modeling of electrolyte flow and its related transport processes in aluminium reduction cells*, TMS Light Metals, pp. 323-331 (1994)
- Caboussat, A., *A numerical method for the simulation of free surface flows with surface tension*, Computers and Fluids, vol. 30, pp. 1205-1216 (2006)
- Ginzburg I., and Wittum, G., *Two-phase flows on interface refined grids modelled with VOF, staggered finite volumes and spline interpolants*, Journal of Computational Physics, vol. 166, pp. 302-335 (2001)
- Kiss, L. I., Poncsák, S., and Antille, J., *Simulation of the bubble layer in aluminum electrolysis cells*, TMS Light Metals, pp. 559-564 (2005)
- Lozinski, A. and Romerio, M.V., *Motion of gas bubbles, considered as massless bodies, affording deformations within a prescribed family of shapes, in an incompressible fluid under the action of gravitation and surface tension*, Mathematical Models and Methods in Applied Sciences, vol. 17, pp. 1445-1478 (2007)
- Méndez, C. G., Nigro, N. and Cardona A., *Drag and non-drag force in numerical simulations of metallurgical ladles*, Journal of Material Processing Technology, vol. 160, pp. 296-305 (2005)
- Perron, A. and Kiss, L. I., *Rise velocity of single bubbles moving under a slightly inclined surface in various liquids*, personal communication, UQAC (2006)
- Purdie, J. M., Bilek, M., Taylor, M. P., Zhang, W.D., Welch, B. J. and Chen, J. J. J., *Impact of anode gas evolution on electrolyte flow and mixing in aluminium electrowinning cells*, TMS Light Metals, pp. 355-360 (1993)
- Thürey, N., *A Lattice Boltzmann method for single-phase free surface flows in 3D*, Master thesis (2003)
- Trapp, J. A. and Mortensen, G. A., *A discrete particle model for bubble-slug two-phase flows*, Journal of Computational Physics, vol. 107, pp. 367-377 (1993)
- Yang, B., and Prosperetti, A., *A second-order boundary-fitted method for free-surface flow computations*, Journal of Computational Physics, vol. 213, pp. 574-590 (2006)

## **Chapter7**

# **CONCLUSIONS**

### **7.1 Conclusions**

The objectives of the doctoral thesis were to gain knowledge about the Fortin bubble; to characterise its shape and movement; to understand the role this bubble plays in the formation of the bubble layer and the bubble induced flow formed under an anode in an electrolysis cell; and to set-up a numerical simulation to simulate large, arbitrarily shaped bubble moving under a solid surface. These objectives were achieved by physical experiments and numerical simulations.

Two set-ups were used for the physical experiments: a life-sized air-water model of an electrolysis cell with two anodes and an air-water model with a single inclined surface. The first set-up was used to investigate the Fortin bubbles in the electrolysis cell while the second was built to observe large, single bubbles gliding under inclined surfaces. Air and water were used as gas and liquid phases, respectively. Measurements were performed using different bubble volumes, gas generation rates and angles of inclinations.

The physical experiments gave the following results about the Fortin shape:

- The contact shape of a Fortin bubble at each angle and volume is similar to the sector of a circle. The rear oscillates. The head is always at the front of the bubble and its dimensions are really stable. The tallest point of the head is measured at the middle of the bubble front.
- The dimensions of the bubble depend on the volume of the bubble and the angle of inclination of the surface.
- The terminal velocity increases with an increasing angle of the anode and increases slightly with the increasing volume of the bubble. The drag coefficient depends only slightly on the size of the bubble and increases with increasing inclination.
- Two approximations of the Fortin shape were suggested in order to calculate the volume of the bubble, one using exact approximation and another using the equivalent height.
- The Fortin shape was observed and its onset was described. At the bottom interface of the tail of the bubble a gravity wave can be found which is induced by the movement of the air phase. The back of the head is part of the wave. The observed half-circular shape of the front leads to a smaller drag resistance. As the bubble gains velocity, the height of the bubble increases to counterbalance the increased dynamic pressure at the front. The height difference between the head and tail induces a moving hydraulic jump where the water flows down from the top of the jump.

The physical experiments gave the following results about the bubble layer formed under the anode and the role of the Fortin bubbles in the layer:

- Three different flow regimes were found under the slightly inclined anode depending on the gas generation rate.
- An increase in the inclination or a decrease in the current density decreases the covering factor. The effect of the current density is stronger at low inclinations. Under the inner edge of the anode bottom the covering factor is smaller than under the outer edge.
- A non-uniform contact size distribution can be observed under the anode. There are a large number of small bubbles under the inner edge of the anode. The second section of the anode is still dominated by small bubbles. Under the third section the contact size of the bubbles is quite uniform. A few, but huge, bubbles dominate the outer edge of the anode bottom.
- When the large bubbles appear, the local average height of the bubble layer is proportional to the gas generation rate. The local maximum height of the bubble layer also increases with increasing gas generation rate, indicating that dynamic forces play an important role in its formation. The ratios of the local maximum height to local average height are similar for all gas generation rates except for the lowest.
- The specific bubble volume increases with increasing current density and increases towards the outer edge of the anode. Also, the difference between the maximum and

minimum specific bubble volume increases towards the outer edge of the anode and with an increasing gas generation rate.

- When a large bubble leaves the anode, it breaks up into two or more smaller parts and these parts leave the anode one after the other. When the parts escape, a large amount of liquid has to return to fill the space left by the escaped bubble. This liquid movement, called backflow, transports a large energy which causes the whole bubble layer to stop for a second or even to move backward. The intensity of the backflow and of the momentum transport depends on the volume of the escaping bubble.
- The onset of the Fortin shape depends on the bubble volume and the velocity difference between the liquid and gas phase. If this velocity difference is too small, the shape does not form. The Fortin shape was not regularly observed above 4° of inclination.

The physical experiments gave the following results about the bubble layer induced flow under the anode in an electrolysis cell:

- Large bubbles have a strong effect on the flow pattern and velocity field of the bath. The bubbles moving under the anode pull a certain amount of liquid with them. The height of the moving liquid layer and its horizontal velocity depend on the volume of the bubbles. The height of this layer is not uniform.
- The gravity wave formed at the surface of the Fortin tail induces a circular movement of the liquid in the vertical plane below the bubble. The vertical diameter

of the circular movement depends on the volume of the bubble as well as on the wavelength and amplitude of the gravity wave. The vertical diameter of the large mixing can be as large as the ACD.

- If two sloped anodes are installed with their inner edges side by side, there is virtually no movement in the gap between the two anodes. If the alumina is fed into this gap, it enters under the anodes rather slowly, reducing the efficiency of the reduction process. It has been found that a configuration where the two anodes have different angles of inclination leads to a more intense movement between the anodes.

In order to investigate the effect of different parameters of the geometry and liquid properties, numerical simulations were performed using the freely available open-source code, openFOAM. The formation and movement of carbon-dioxide bubbles in molten cryolite were also simulated. The simulations gave the following results:

- Increasing the volume of the bubble increases the dimensions of the bubble, such as the average and the maximal height and also the length of the bubble. An increase in the volume of the bubble also increases its velocity.
- Increasing the angle of inclination increases the height of the bubble, while decreases its length.
- The surface tension has no effect on the results.
- The simulation using real cell parameters showed that the liquid phase has a strong effect on the shape of the bubble and on the rate of its formation; a bubble forms

much slower in cryolite than in water and the form of the bubble is much more elongated with a much smaller head, has the head formed.

- Similar flow and velocity fields are expected in a real electrolysis cell as compared to the air-water model. However, the amplitude of the Fortin shape forming gravity wave is expected to be smaller because of the high viscosity and density of the molten cryolite. The vortices induced by the wave are also expected to be smaller and slower in the real bath because they depend on the wavelength and amplitude.
- The horizontal motion induced by the bubble layer and the one at the bottom of the inter-electrode space are expected to be slower in a real cell too. The bubbles are assumed to have the same or slower velocity in the real cell, thus they have the same or higher volume than in the model. As the intensity of the backflow depends on the volume of the escaping bubble, similar amount of momentum is expected to be transferred by a same sized bubble in both systems. On the other hand, the molten cryolite is heavier than the water, thus more energy is needed to move the same amount of cyrolite.

## 7.2 Suggestions for future work

The work presented above serves as a strong foundation in the understanding of the large, so-called Fortin bubbles. The detailed description and characterisation of the shape



has been done. Its formation and movement has been explained. Correlations to calculate its volume have been proposed. Numerical simulations have been performed to simulate the Fortin shape. In addition, the role of the Fortin bubble in the formation of the bubble layer and in the formation of the bubble layer induced flow has been quantitatively and qualitatively observed and described.

The following work is proposed in order to deepen the understanding of the Fortin bubble and its role in the aluminium electrolysis process.

- Perform experiments with single large bubbles using different gas and liquid phases in order to investigate the effect of different materials.
- The correlation between the real cell and the air-water model can be determined from the results of the above proposed experiments.
- In order to quantitatively determine the gas-liquid phase interaction of single large bubbles, PIV measurements are suggested using different materials.
- Also, PIV measurements of the flow field just under and behind the head would allow the confirmation of the theory about the formation of the Fortin head. Such measurements require improvements to the existing PIV techniques available at the university.
- It is suggested that further experiments are performed with the bubble layer, but using a different anode geometry. This would lead to a better understanding of the effect of the anode on the bubble layer and the bubble induced flow.

- Also, physical experiments, including the magneto-hydrodynamic and thermal effects, should be performed for a better understanding of the role of the bubble layer in the reduction process.
- It is recommended to perform three dimensional (3D) numerical simulations in order to verify the influence of the width of the bubbles on the shape and flow pattern.
- The results obtained using the code can be incorporated into the bubble layer simulator developed earlier at the university. Up to now it uses the RPM method to simulate the shape of the bubbles.

# APPENDIX A

## DERIVATION OF THE CORRELATION TO CALCULATE THE VOLUME OF A LARGE FORTIN BUBBLE USING THE EXACT FORM APPROXIMATION

The exact approximation of the Fortin shape consists of an equivalent high circle segment and a body segment with a 2<sup>nd</sup> order parabolic cross-section. The aspect view of the form approximation can be seen in figure 4.29, while figure A.1 shows its cross-section.

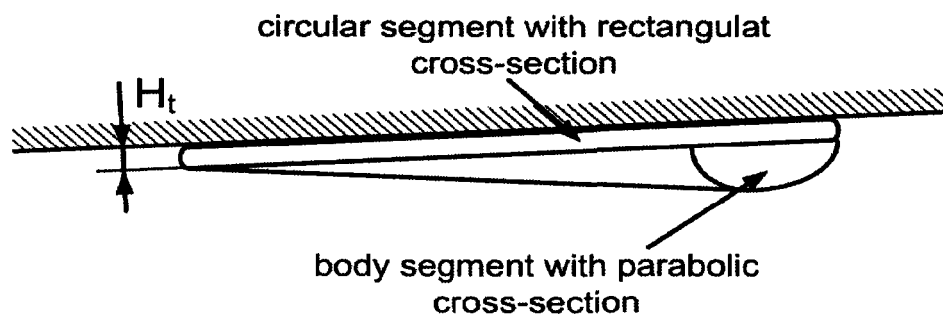


Figure A.1 – Cross-section of the exact approximation

The entire volume of the bubble is given as the summation of the volume of the circular segment and the body segment.

$$V_{Fortin\_bubble} = V_{circular\_segment} + V_{body\_segment} \quad (A.1)$$

The volume of the circular segment with the rectangular cross-section is given as

$$V_{circular\_segment} = A_{contact\_shape} \cdot H_t \quad (A.2)$$

where  $H_t$  is the mean thickness of the tail and  $A_{contact\_shape}$  is the contact size given as

$$A_{contact\_shape} = \frac{1}{2} \cdot R_f^2 \cdot \left( \frac{2 \cdot \pi \cdot \Theta_f^\circ}{180^\circ} - \sin 2 \cdot \Theta_f^\circ \right) \quad (A.3)$$

where  $R_f$  is the radius of the front and  $\Theta_f^\circ$  is the half angle of the front given in degrees.

The parabolic cross-section of the head is given by the following equation:

$$y = -\frac{H_{p_{max}}}{L_{h_{max}}^2} \cdot x^2 + H_p(\beta) \quad (A.4)$$

where  $H_p(\beta) = H_h(\beta) - H_t$ , and the maximum value of the height of the body segment

and the length of the parabola is measured at  $\beta = 0^\circ$  thus  $H_{p_{max}} = H_p(\beta = 0^\circ)$  and

$$L_{h_{max}} = L_h(\beta = 0^\circ).$$

The volume of the body segment with the parabolic cross-section is calculated from the double integral of (A.4) as a function of the  $x$  and  $\beta$  axes as follows:

$$V_{body\_segment} = \int_{i=-R_h \cdot \hat{\Theta}_h}^{R_h \cdot \hat{\Theta}_h} \int_{x=-L_h(\beta)}^{L_h(\beta)} \left[ -\frac{H_{p_{max}}}{L_{h_{max}}^2} \cdot x^2 + H_p(\beta) \right] dx \cdot di \quad (A.5)$$

where the  $i$  is the length of the arc at the bottom middle of the parabolic cross section and is given as  $i = R_h \cdot \hat{\beta}$ , where  $\hat{\beta}$  is given in radians.

After performing the integral as a function of the  $x$  parameter we get:

$$V_{body\_segment} = \int_{i=-R_h \cdot \hat{\Theta}_h}^{R_h \cdot \hat{\Theta}_h} \left[ -\frac{2}{3} \frac{H_{p_{max}}}{L_{h_{max}}^2} \cdot L_h^3(\beta) + 2 \cdot H_p(\beta) \cdot L_h(\beta) \right] di \quad (A.6)$$

In (A.6) the  $L_h$ , length of the head and the  $H_p$ , height of the body segment is a function of the  $\beta$  parameter, while  $R_h$ , the radius of the head, is constant.  $L_h$  and  $H_p$  have their maximum at the middle of the arc at  $\beta = 0^\circ$ . The two parameters decrease gradually from this point towards the two ends of the arc. The value of the two parameters is zero at  $\beta = \pm \Theta_h$ , where  $\Theta_h$  is the angle of the head. The change of these two parameters are approximated with a parabolic function in the  $\beta - L_h$  and  $\beta - H_p$  planes, where the vertex of the parabola is at  $L_{h_{max}}(\beta = 0^\circ)$  and  $H_{p_{max}}(\beta = 0^\circ)$  respectively. Thus the functions of the two parameters are as follows:

$$L_h(\beta) = -\frac{L_{h_{max}}}{\Theta_h^2} \cdot i^2 + L_{h_{max}} \quad (A.7)$$

$$H_p(\beta) = -\frac{H_{p_{max}}}{\Theta_h^2} \cdot i^2 + H_{p_{max}} \quad (A.8)$$

Inserting (A.7) and (A.8) into (A.6) we get:

$$V_{body\_segment} = \int_{i=-R_h \cdot \hat{\Theta}_h}^{R_h \cdot \hat{\Theta}_h} \left[ -\frac{2}{3} \frac{H_{p_{max}}}{L_{h_{max}}^2} \cdot \left( -\frac{L_{h_{max}}}{\Theta_h^2} \cdot i^2 + L_{h_{max}} \right)^3 + 2 \cdot \left( -\frac{H_{p_{max}}}{\Theta_h^2} \cdot i^2 + H_{p_{max}} \right) \cdot \left( -\frac{L_{h_{max}}}{\Theta_h^2} \cdot i^2 + L_{h_{max}} \right) \right] di \quad (A.9)$$

After simplifying (A.9) we get:

$$V_{body\_segment} = \int_{i=-R_h \cdot \hat{\Theta}_h}^{R_h \cdot \hat{\Theta}_h} \left[ H_{p_{max}} \cdot L_{h_{max}} \cdot \left( \frac{4}{3} - 2 \frac{i^2}{\Theta_h^2} + \frac{2}{3} \cdot \frac{i^6}{\Theta_h^6} \right) \right] di \quad (A.10)$$

After performing the integral we get:

$$V_{body\_segment} = \frac{32}{21} \cdot H_{p_{max}} \cdot L_{h_{max}} \cdot i = \frac{32}{21} \cdot H_{p_{max}} \cdot L_{h_{max}} \cdot R_h \cdot \hat{\Theta}_h \quad (A.11)$$

Thus the volume of a Fortin bubble is given as a function of the radii of the front and head, the angles of the front and head, the maximum height of the head, the maximum length of the head and the mean thickness of the tail as follows:

$$V_{Fortin\_bubble} = \frac{1}{2} \cdot R_f^2 \cdot \left( \frac{2 \cdot \pi \cdot \Theta_f^\circ}{180^\circ} - \sin 2 \cdot \Theta_f^\circ \right) \cdot H_t + \frac{32}{21} \cdot H_{p_{max}} \cdot L_{h_{max}} \cdot R_h \cdot \frac{\pi \cdot \Theta_h^\circ}{180^\circ} \quad (A.12)$$

## APPENDIX B

### DERIVATION OF THE CORRELATION TO CALCULATE THE WAVE VELOCITY FOR TWO SUBSTANCES

Let us assume that we have two different liquids, one is denser than the other with  $\rho$  and  $\rho'$  densities, where  $\rho$  is that of the denser liquid (figure B.1). Let us also assume that the depth of the two liquids is  $h$  and  $h'$  and the liquids are limited by a horizontal solid surface at the top and bottom. If the liquid at the top is light enough then this situation is analogous to the situation of a bubble moving in a liquid under a solid surface. The velocity of the wave which occurs at the interface of these two liquids is derived as follows.

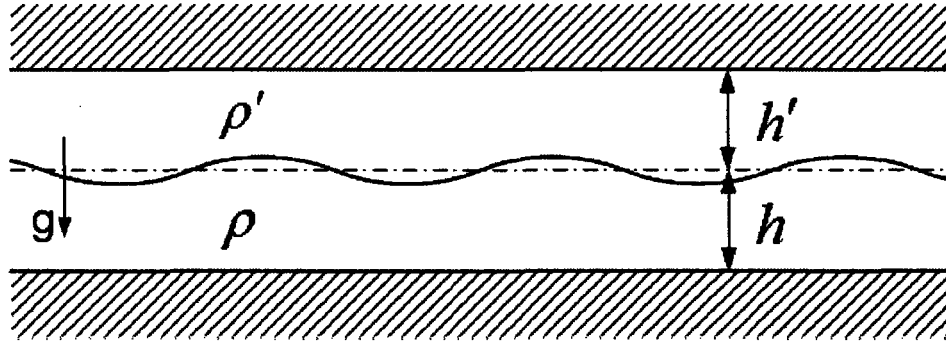


Figure B.1 – Wave onset at the interface of two substances

The wave frequency for the wave onset at the interface of these two substances is given as follows:

$$\omega = k \cdot g \frac{\rho - \rho'}{\frac{\rho}{k \cdot h} + \frac{\rho'}{k \cdot h'}} \quad (\text{B.1})$$

If we consider that the liquid at the bottom is deep and the liquid at the top is shallow, then we get  $k \cdot h \gg 1$  but  $k \cdot h' \ll 1$ . If we substitute this into (B.1) we get:

$$\omega^2 = k \cdot g \frac{\rho - \rho'}{\rho + \frac{\rho'}{k \cdot h'}} \quad (\text{B.2})$$

The velocity of the wave can be calculated from the derivation of the wave frequency:

$$c = \frac{\partial \omega}{\partial k} \quad (\text{B.3})$$



Substituting (B.2) into (B.3) we get the following correlation for the wave velocity for the above described situation:

$$c = \sqrt{\frac{g(\rho - \rho')h'}{\rho \cdot k \cdot h' + \rho'}} \cdot \left[ 1 - \frac{\rho \cdot k \cdot h'}{2 \cdot (\rho \cdot k \cdot h' + \rho')} \right] \quad (\text{B.4})$$

where  $k$  is the wave number given as:

$$k = \frac{2\pi}{\lambda} \quad (\text{B.5})$$